Chapter 19
Thermodynamic Modelling in the Frames of the TRIP-Matrix-Composite Development

Ivan Saenko and Olga Fabrichnaya

Abstract The present chapter is focused on thermodynamic modelling as a part of a complex development of metal-ceramic composite materials. Within this chapter the main examples of successful application of thermodynamic calculation for a solving of technological problems are highlighted, basic theory and methods of thermodynamic investigations and modelling are described in details and the most important results are briefly given. The purpose of this chapter is to give a deep understanding of thermodynamic modelling from basic experiments to modern methods of simulation. There is a set of recommendations for performing thermodynamic assessment and creation of multicomponent thermodynamic databases.

19.1 Introduction

Knowledge of phase equilibria and the underlying thermodynamics play a crucial role in the understanding of development and application of materials. Thereby, phase diagrams represent a kind of roadmaps for materials development and provide important information for understanding of technological aspects of design and usage of materials. However, the most of the modern materials consist of more than two or three components, what makes the graphical representation of these systems challenging and complex. Moreover, there is only limited information for many multicomponent systems. Method of computational thermodynamics is very powerful tool for prediction and extrapolation helping to fill these gaps of the areas without experimental information [1].

In the frame of a development of an innovative composite material, thermodynamic simulation using the CALPHAD method (Calculation of Phase Diagrams) can be used in order to support an optimization of chemical composition of the alloy and to develop a production process.

I. Saenko · O. Fabrichnaya (✉)
Institute of Materials Science, Technische Universität Bergakademie Freiberg, Gustav-Zeuner-Str. 5, 09599 Freiberg, Germany
e-mail: fabrich@ww.tu-freiberg.de

H. Biermann and C. G. Aneziris (eds.), *Austenitic TRIP/TWIP Steels and Steel-Zirconia Composites*, Springer Series in Materials Science 298,
https://doi.org/10.1007/978-3-030-42603-3_19

The TRIP-Matrix-Composite is an example of innovative material, which is based on high-alloyed austenitic TRIP-steel and reinforcing ceramic particles of zirconia partially stabilized by MgO (Mg-PSZ). Thereby, thermodynamic calculations can provide information about the stable and metastable phase formation in the material as well as the accompanying energetic effects and basic information of the physico-chemical parameters of the manufacturing processes.

Metal Matrix Composites containing highly alloyed TRIP-steel as metallic component and MgO partially stabilized ZrO_2 as ceramic component are considered as promising new construction materials with high energy absorption. Under deformation metastable austenite transforms into martensite, which results in an increasing strength. It should be mentioned that MgO stabilized ZrO_2 also shows stress-induced martensitic transformation from tetragonal into monoclinic phase [2]. The increased toughness of this ceramic phase is attributed to a stress-induced transformation. For a good performance of the composite material a strong adhesion between the metallic and the ceramic components is required in order to transmit stresses between the different phases. The infiltration and powder metallurgy/sintering processes selected in the Collaborative Research Center 799 (CRC799) to produce Fe–ZrO_2 based TRIP matrix composites may cause heterogeneous reactions in the matrix materials, in the ceramic particles and at the interfaces that can significantly influence on the mechanical properties of final composite materials. This information can be used to derive the structure development in the constituent materials and their compatibility and long-term stability. Therefore, the CALPHAD method was applied in the CRC 799 for many years as a valuable tool for materials design as knowledge of the phases that are present in a material and their compositions is essential for modelling the behavior and properties. It was widely applied for optimization of chemical composition of steel matrix with following annealing improving of its microstructure [3], for prediction and understanding of the local deformation mechanisms [4], for modelling of interfacial reaction between steel matrix and ceramic particles [5], as well as for understanding of phase transformations of the metastable austenite into martensite in the Fe–CrMnNi–N–C model alloy [6]. Additionally, the CALPHAD method provided a basement for further modelling method concerning the development of the TRIP-Matrix-Composite i.e. thermo-mechanical modelling [7], simulation of electron beam welding [8] and phase field modelling.

This Chapter will consider a basement of computational thermodynamics, reveal experimental side of thermodynamic modelling and present the latest results concerning the TRIP-Matrix-Composite development.

19.2 Experimental Techniques

Since the CALPHAD approach is a phenomenological method, its parametric functions must be assessed using experimental data before any prediction and/or extrapolation can be made. In order to get a maximum of information, all types of experimental measurements that are related to thermodynamic properties must be considered

and assessed. Collected experimental data are applied for adjusting of optimized parameters of the Gibbs energy functions.

Thereby, the reliability and accuracy of the experimental data have to be critically evaluated taking into account, which one of the various experimental techniques was used. Measured experimental data can be roughly classified into a few principal types: "thermodynamic data" and "phase-diagram data" [9]. The most of thermodynamic data can be directly applied to describe Gibbs energy functions of individual phases, while experimental data on the phase relations can be used for optimization of those functions for reproducing of phase diagrams of the system and thermodynamic data within their uncertainty. Since the phase diagram is representing equilibrium states of the system corresponding to minimum of its Gibbs energy being the sum of the properties of the individual phases multiplied to their mole amount respectively [10] at various conditions the phase relations are dependent on thermodynamic properties of the individual phases. Optimization of the Gibbs energy functions is a complex procedure, which will be described further (Sect. 19.3.2).

19.2.1 Sample Preparation

Development of the TRIP-Matrix-Composite requires a multicomponent thermodynamic description, which would include all alloying elements of the matrix, as well as components of ceramics such as ZrO_2 and MgO as well as oxides appearing due to steel oxidation and impurities. Consequently, both type of materials had to be investigated, not only steel matrix but also components of ceramics. Therefore, two different techniques of specimen preparation were applied for investigations of steel and ceramic systems.

In the case of steel systems, two or three components alloys were prepared by arc-melting method in Ar-atmosphere. Chemically pure metals were used as raw materials. Precursors have been weighed in accordance to the nominal compositions using laboratory scale ABJ 120-4M (KERN & Sohn GmbH). In order to achieve good homogeneity of the chemical composition in the bulks, the samples were turned-over and re-melted three times during acr-melting. The melting chamber was evacuated to ~10^{-5} atm and refilled with argon three times. An ingot of Ti (ca. 3 g) was placed in one of the molds and was melted before the melting of the samples in order to adsorb rests of oxygen and prevent possible oxidation. The weight losses due to vaporization should be generally less than 1 mass%. Next, samples obtained by arc melting were encapsulated in quartz tubes with reduced Ar atmosphere. The pressure of Ar was chosen in order to reach 1 atm. at the homogenization temperature. The encapsulated samples were heat treated for a long time afterwards they were quenched into ice-cold water.

For ceramic systems, the co–precipitation method was used for sample preparation. Chemically pure salts of desired metals have been used as the initial materials. In the first step, the salts were diluted and dissolved by distilled water in order to obtain

more suitable consistence for the co-precipitation process (solutions around of 0.4–1.2 mol/l in dependence on precursors). The concentration of obtained initial solutions was determined by Inductively Coupled Plasma-Optical Emission Spectrometry (ICP-OES) spectrometry. Calculated volumes of initial solutions were mixed together in order to get ~2 g of oxide powder of desired molar ratio. The obtained solution was dropped from a burette at a low speed (around 1 ml per minute) into a beaker containing about 500 ml of the aqueous solution of NH_4OH with pH value above 9.0. In order to increase particles in the obtained suspension, it was heated up and held at 333 K for 1–2 h before filtration. In order to control the chemical composition, co-precipitated suspension and filtrates were analyzed by ICP-OES. Since the composition of the samples obtained by ICP deviated significantly from nominal composition, an evaporation process was applied instead of filtration. Then, the substance obtained after filtration/evaporation was dried at 353 K for 2–3 days. Finally, pyrolysis of the dried precipitate powder was performed at 1073–1273 K for 3 h in air. The obtained oxide powder was pressed into cylindrical pellets at 250 MPa and sintered in air atmosphere in Pt-crucibles using NABERTHERM furnace in order to reach equilibrium state. Annealing duration was chosen depending on sintering temperature and on development of microstructures.

19.2.2 Phase-Diagram Data

The quantities measured in phase diagrams are either temperatures of phase boundaries at fixed composition and invariant equilibria determined by thermal analysis or phase compositions at fixed temperatures determined by sample equilibration. There are several experimental methods for measuring the phase-diagram data. They are described in details by Lukas et al. [9]. In the frames of current investigation, X–ray powder diffraction (XRD), scanning electron microscopy combined with an energy dispersive X–ray spectrometry (SEM/EDX) and differential thermal analysis (DTA) were applied in order to get essential information about phase relations, required for thermodynamic assessment of two and three component system. Experimental data for multicomponent systems are usually not used directly in an assessment, but, if the extrapolation from the lower-order systems gives wrong results, one may use these data for modification of parameters describing the lower-order systems or by introducing high-order parameters and new phases. Additionally, if phases are not stable in a binary system the parameters of metastable phases can be assessed from a higher order system.

19.2.2.1 Structural Investigation

After long time annealing, the important step is to determine the phase assemblage of heat-treated samples. The most powerful analytical techniques for identifying the phases is X-ray or neutron diffraction. Moreover, these techniques are also important

for the determination of crystal structures. Lattice parameters and site occupancies as functions of composition and temperature can be obtained to provide detailed information about the internal lattice of crystalline substances, including cite occupancies, unit cell dimensions, bond–lengths and bond–angles. This information is necessary to find right models for thermodynamic description.

In the frames of current investigation, X-ray powder diffraction (XRD) was applied using URD63 diffractometer (Seifert, FPM, Freiberg, Germany) equipped with graphite monochromator and CuKα radiation ($\lambda = 1.5418$ Å). The goniometer of the diffractometer has the Bragg-Brentano geometry. Powder samples were measured placed on monocrystalline silicon substrate with (510) orientation. In this case, the orientation of the substrate does not show any peak on the XRD patter in the range of 15°–110° of 2θ. The Rietveld refinement was applied for the characterization of all measured diffraction patterns in order to obtain the volume fractions of present phases as well as lattice parameters. This method allows determining the site-occupancy parameters by analyzing the polycrystalline samples. Each solid phase has its own characteristic diffraction pattern, as a function of intensity in dependence on the diffraction angle 2θ. The program Maud [11] was used for Rietveld refinement.

19.2.2.2 Microstructural Investigation

A very useful tool in phase-diagram determination is micrography at higher magnification using a scanning electron microscope (SEM), or a transmission electron microscope (TEM). Equipped with an energy dispersive spectrometer (EDS), these devices allow measuring the chemical composition of the microstructural features. For example, boundaries in phase diagrams, which are often deduced from results of characterization of sample series with different compositions after equilibration at fixed temperatures, can be plotted as composition versus a temperature. Afterword, these results can be applied for modelling of homogeneity ranges of solid phases etc.

The microstructures of the samples were analyzed using Scanning Electron Microscopy (SEM). The investigations were carried out on the LEO 1530 Gemini (Zeiss, Germany). The microscope was equipped with a field emission cathode, used at the acceleration voltage of 20 kV with working distance of 8–10.5 mm. In addition, energy–dispersive X–ray spectroscopy (EDX) was used in order to verify chemical compositions of samples, to determine phase compositions which are also used for identification of phases, as well as to estimate composition of liquid in eutectic reactions. An uncertainty range for EDX measurement is around 2–4 at.%.

For imaging in the SEM, samples must be electrically conductive, at least at their surface, and electrically grounded in order to prevent the accumulation of electrostatic charge at the surface at the interaction with the electron beam. Therefore, samples composed of oxides were grinded and polished and then coated with an ultrathin graphite layer.

19.2.2.3 Thermal Analysis

Differential thermal analysis (DTA) was applied in order to detect temperatures of phase transitions and reactions occurring in the sample as well as melting temperatures. The technique of thermal analysis is based on the measuring of the temperature difference between the sample versus a reference as a function of time and temperature during programmed heating and cooling cycles. Any exothermic or endothermic changes occurring in the sample is registered by comparison with the reference as the temperature difference of the thermocouple signals in μV (thermal voltage). The inert material, which does not react with crucible and does not have phase transformations in the investigated temperature range can be used as a reference. However, it should be noted that empty crucibles are mostly used as reference at present.

In the frame of this work, DTA was performed using SETARAM SETSYS EVOLUTION 1750 (SE 1750) and SETARAM SETSYS EVOLUTION 2400 (SE 2400). The SE 1750 device equipped with a type B thermocouple (Pt/Rh 70%/30%—Pt/Rh 94%/6%, by weight) works in an inert atmosphere of argon or helium in the interval of temperatures up to 2023 K. The SE 2400 device equipped with a type C thermocouple (W/Re 95%/5%—W/Re 74%/26%, by weight) works in an inert atmosphere of helium up to 2673 K. As the crucible's materials Pt/Rh10% was used for SE 1750 and pure W was used for SE 2400 in the case of ceramic materials. For metallic samples, ceramic crucibles should be used. Thereby, corundum is the most common ceramic material.

Both if these devices have an opportunity for thermogravimetric analysis (TGA), which is very useful tool for measuring the mass change of a material as a function of temperature and time during heating and cooling program.

Calibration procedure of the apparatuses was systematically carried out by using pure reference elements with known melting temperatures. Measured temperatures were recounted according to a correction function acquired at the last correction procedure. Temperature calibration of SE 1750 was performed using melting points of Al, Ag, Au, Cu and Ni. The correction procedure for SE 2400 was carried out using melting points of Al, Al_2O_3 from literature and temperature of solid phase transformation in $LaYO_3$ measured in SE 1750. These materials were chosen because of their passivity concerning to crucible's materials. Correction polynomials were obtained by fitting derived points using the least–squares method. The temperatures of transformations were determined as on–set point i.e. intersection of the tangent line constructed in the point of highest slope and baseline. Since correction procedures were carried out using on–set point, temperatures of transformations should be also determined by on–set points.

19.2.3 Thermodynamic Data

There are many different techniques for determining thermodynamic properties of individual phases directly. They are described in the book of Lukas et al. [9]. In

this chapter, only two types of measurements will be discussed further, namely drop solution and differential scanning calorimetry that were used in the frames of current work.

19.2.3.1 Differential Scanning Calorimetry

In the present work, differential scanning calorimetry (DSC) measurements were carried out in order to obtain the heat capacity of single phases in the investigated systems. This information is important for the thermodynamic assessments and modelling of multicomponent systems. The heat capacity measurements in the temperature range from 235 to 675 K were carried out using the device DSC 8000 (Perkin Elmer, Pt/Rh crucible, Ar or He flow, heating rate 10 K/min). The measurements in the temperature range from 235 to 675 K were divided into small intervals of 100–150 K. The DSC measurements in the temperature range from 623 to 1220 K were performed in one temperature range using the device DSC Pegasus 404C (NETZSCH, Pt/Rh crucible, Ar flow, heating rate 10 K/min).

The classical three-step continuous method [12] with a constant heating rate was used to measure specific heat capacity:

- The determination of the heat flow rate of the zero–line (with empty sample and reference sides). This step takes into account the heat capacity of inner parts of the device.
- The calibration step—a sample of the material, whose heat capacity is precisely defined (synthetic sapphire), is measured in the sample crucible.
- Calorimetrical measurement of an unknown sample.

Calibration was performed using a certified sapphire standard in the case of ceramic materials. For metallic systems, calibration was performed using certified standard materials depending on the reliable temperature range of their heat capacity: copper standard was used in the temperature range from 100 to 320 K; molybdenum from 300 to 673 K and platinum from 573 to 1473 K. The mass and radius of sample pellets were kept the same as for standard materials. The measurements of two different samples were repeated two times with maximal uncertainty 3%. It should be mentioned that the C_P measurements at high temperatures using DSC equipment are becoming less reliable due to increase of heat radiation which decreased registered signal. This effect was considered during fitting of the experimental data. Fitting of the obtained results was performed using the Maier-Kelley equation. In order to exclude any phase transformation during the heat capacity measurement, XRD analyses of the obtained samples were performed before the heat capacity measurements and afterward.

19.2.3.2 Drop Solution Calorimetry

The principle of this method is that two (or more) different well-defined samples are combined in the calorimeter and react to give a single sample, which again must be well defined. Well defined means that all the variables upon which the enthalpy depends must be known: each sample must be in internal equilibrium; its temperature and composition must be known. Drop solution calorimetry method was applied in order to determine the enthalpy of formation of oxide compounds. These measurements were performed using an Alexis 800 heat-flux micro calorimeter (SETARAM, France). The samples pressed into pellets (Ø 1 mm, mass 3–9 mg) were dropped directly from room temperature into the calorimeter with a solvent at $T =$ 973 K and the enthalpy increments of dropping and solution of a set of 9 pellets were measured. The sodium molybdate $3Na_2O \cdot 4MoO_3$ was used as the solvent. The calorimeter was calibrated by using the molar enthalpy increment of dropping standard sapphire spheres. Error of the measurement was stated to be twice the standard deviation of the mean value.

19.3 CALPHAD Method

Computational thermodynamics is powerful tool for solution of various problems in materials science, particularly used in the construction of phase diagrams [10]. At the beginning of the previous century, a thermodynamic modelling a phase diagrams of a metal-based system was firstly performed by Johannes van Laar using regular solutions models, what has evolved in more recent years to the CALPHAD (Calculation of Phase Diagrams) [13]. The CALPHAD method has been pioneered by American metallurgist Larry Kaufman since the 1970s [9, 14, 15]. Calculation of phase equilibrium is based on minimization of the Gibbs energy of the system which is the sum of the Gibbs energies of individual phases multiplied respectively to their mole amount or from equality of chemical potential for components in the equilibrated phases. The Gibbs energy of individual phase is described by thermodynamic model representing its dependence on temperature, pressure and composition [14]. Therefore, phase diagrams are related to the thermodynamic properties of individual phases which can be also determined experimentally using calorimetry, vapor pressure measurements and electrochemical data. These different kinds of data are used for optimization of thermodynamic parameters simultaneously to reproduce both phase diagrams and experimental thermodynamic data. The obtained set of thermodynamic descriptions of individual phases can be used to calculate different kinds of phase diagrams.

It should be noted that thermodynamic data of some components are very well determined and they are not optimized, the other parameters such as mixing parameters of solution phases and metastable end-members of solid solutions should be optimized. The thermodynamic properties of intermediate phases usually also need to be optimized. The aim of the CALPHAD method is to obtain a consistent description of all phases in the system reproducing the thermodynamic properties

and phase diagrams within uncertainty of measurements. The self-consistent thermodynamic database allows predicting of the phase relations and thermodynamic properties in regions where experimental information is not available as well as calculation of metastable phase diagrams, calculation of diffusion-less transformation and simulations of non-equilibrium processes assuming local equilibration.

Methodology of the CALPHAD method and main principles of thermodynamic databases development are described in many fundamental books [9, 14–16] and basics research [1, 17]. In this chapter, the main information about CALPHAD will be described very shortly.

19.3.1 Methodology

The Gibbs energy is described as a function of temperature, pressure and composition. The thermodynamic descriptions of this function of the pure phases of end members of solid solutions at a certain P and T referred to the enthalpy of its phase at room temperature 298 K are in the following form:

$$G(P,T) = \Delta_f H^0_{298} + \int_{298}^{T} C_P \mathrm{d}T - T\left(S^0_{298} + \int_{298}^{T} (C_P/T)\mathrm{d}T\right) + \int_{1}^{P} V\,\mathrm{d}P \quad (19.1)$$

where S^0_{298} is the standard entropy, $\Delta_f H^0_{298}$ is the enthalpy of formation and C_P is the heat capacity given by

$$C_P = a + bT + cT^{-2} + dT^2 + eT^{-3} + \cdots \quad (19.2)$$

The magnetic contribution $\mathrm{G_{mag}}$ can be taken into account according to Inden–Hillert–Jarl [18] formalism (19.3).

$$\mathrm{G_{mag}} = T\,R\ln(\beta_0 + 1)g(\tau) \quad (19.3)$$

where $\tau = T/T^*$, T^* is the critical temperature (the Curie temperature T_C for ferromagnetic materials or the Neel temperature T_N for antiferromagnetic materials), β_0 the average magnetic moment per atom and $g(\tau)$ is a function depending on τ [19].

The molar volume in (19.1) is calculated as a function of pressure and temperature using the Murnaghan equation,

$$V(P,T) = V(1,T)\left(1 + \frac{K'_P \cdot P}{K_T}\right)^{-1/K'_P} \quad (19.4)$$

where K_T is isothermal bulk modulus, which can be expressed as

$$K_T = 1/\left(\beta_0 + \beta_1 T + \beta_2 T^2 + \beta_3 T^3\right) \tag{19.5}$$

and K'_P is the pressure derivative of bulk modulus which in some cases has a temperature dependency:

$$K'_P = K'_{P298} + K'_{PT}(T - 298)\ln\left(\frac{T}{298}\right) \tag{19.6}$$

K'_{P298} is the pressure derivative of bulk modulus at 298 K, K'_{PT} is its temperature derivative.

The molar volume at 1 bar is expressed as a function of temperature

$$V(1, T) = V^0_{1,298} \exp\left(\int_{298}^{T} \alpha(T)\mathrm{d}T\right) \tag{19.7}$$

where $V^0_{1,298}$ is the molar volume at 1 bar and 289 K. $\alpha(T)$ is the temperature dependent thermal expansion

$$\alpha(T) = \alpha_0 + \alpha_1 T + \alpha_2 T^{-1} + \alpha_3 T^{-2} \tag{19.8}$$

The Gibbs energy $G_{A_aB_b}(T)$ of a stoichiometric phase A_aB_b in case of absence of heat capacity data was modeled using Neumann-Kopp rule as:

$$G_{A_aB_b} = a\mathrm{GHSER}_A + b\mathrm{GHSER}_B + \alpha + \beta T \tag{19.9}$$

where GHSER_i is the Gibbs energy of the pure element i referred to the enthalpy of pure element i at 298 K in its standard element reference (SER) state, α and β are parameters to be optimized.

Solution phases and stoichiometric phases with homogeneity ranges can be described by compound energy formalism [16].

The simplest non-ideal solution model is the substitutional model with the Gibbs energy of expressed as follows:

$$G = \sum_i^n x_i G_i + RT \sum_i^n x_i \ln x_i + \Delta G^{\mathrm{Ex}} \tag{19.10}$$

where x_i are the mole fractions, G_i is the Gibbs energy of an end-member i, $\sum_i^n x_i G_i$ is the surface of reference terms, $RT \sum_i^n x_i \ln x_i$ is the contribution to the Gibbs energy resulting from the configurational entropy of mixing for disordered solution, and ΔG^{Ex} is the excess Gibbs energy of mixing.

The excess Gibbs energy of mixing was modelled using Redlich–Kister polynomials [20], expressed as:

$$\Delta G^{\mathrm{Ex}} = \sum_{i \neq j, i<j} x_i x_j \sum_{v=0}^{n} L_{i,j}^{v} \left(x_i - x_j\right)^{v} \tag{19.11}$$

where $L_{i,j}^{v}$ is the mixing parameter between end-members i and j, while v is integer number.

The sublattice model in the form of compound energy formalism is used for solid phases having several crystallographic sites. The Gibbs energy of solution described by the sublattice model with three sublattices is given by

$$\Delta G^{\mathrm{mix}} = \sum_{i} \sum_{j} \sum_{k} Y_i^s Y_j^t Y_k^u G_{ijk} + RT \sum_{s} \alpha_s \sum_{i} Y_i^s \ln(Y_i^s) + \Delta G^{\mathrm{Ex}} \tag{19.12}$$

where Y_i^s is the mole fraction of constituent i on sublattice s, α_s is the number of sites on sublattice s per mole of formula unit of phase and ΔG^{Ex} is the excess Gibbs energy of mixing expressed as

$$\begin{aligned} \Delta G^{E} = &\sum_{t} y_j^t \sum_{u} y_k^u \sum_{s} y_i^s y_l^s L_{i,l}^s + \sum_{s} y_i^s \sum_{t} y_j^t \sum_{u} y_k^u y_m^u L_{k,m}^u \\ &+ \sum_{s} y_i^s \sum_{u} y_k^u \sum_{t} y_j^t y_n^t L_{j,n}^t \end{aligned} \tag{19.13}$$

$$L_{i,l}^s = \sum_{n} \left(Y_i^s - Y_l^s\right)^n L_{i,l} \tag{19.14}$$

where $L_{i,l}^s$ are binary interaction parameters between species i and l on sublattice s. Higher-order interaction parameters could also be included giving more complicated excess Gibbs energy terms.

19.3.2 Optimization

The optimization process is the most important step of a creation of a thermodynamic database, which gives the best fit of experimental data taking into account the error of every data point. Each individual phase is described by thermodynamic model presenting an analytical function of the Gibbs energy dependence on temperature and composition (pressure is usually fixed at 1 bar) with adjustable parameters. These parameters are optimized using the least-squares method to obtain a description which reproduces experimental data with minimal deviation. However, the least-squares method can work well only if the scatter of experimental data is completely random. Non-randomly distributed deviations of some data may completely destroy the utility of the least-squares method. They must be classified as systematic errors and excluded from the optimization. Therefore subjective judgments are required and decisions have to be taken on the selection of data during the optimization. From

that point of view, the technique can also be called an assessment [9]. Unfortunately, including all available data in optimization does not necessarily lead to satisfactory results. Some experimental data could be in conflict to each other or can show large systematic errors. Thereby, setting different weights for these data points can help to recognize the influence of different experiments on the result of optimization. This procedure helps to identify which data are contradictory. However, it is usually impossible to optimize all parameters simultaneously. There are too many parameters and they have different influence on phase diagrams [17].

The optimization methodology of CALPHAD method can be subdivided into following stages:

1. Collection of diverse experimental information available in literature (crystallographic data for phases, phase equilibria, calorimetry, electrochemical data, vapor pressure measurements).
2. The selection of thermodynamic models based on crystallographic information for phases in the system under investigation. This implies selection of sublattices and their occupancies by constituents in agreement with crystal structure.
3. The consideration of temperature dependence of end-member parameters and introducing of mixing parameters for the Gibbs energy description of phase.
4. The optimization of the thermodynamic parameters using all available experimental as well as theoretical data.
5. The storage of the optimized parameters in computer–readable thermodynamic datasets.
6. The calculation of phase diagrams and various phase equilibria using the thermodynamic datasets.

The principle of the CALPHAD approach is schematically presented in Fig. 19.1.

19.4 The Latest Results Concerning the TRIP-Matrix-Composite Development

In the beginning of the development of the new composite, an extensive thermodynamic database for steel-based materials (Fe, Mn, Cr, Ni, Ti, Mo, W, V, Si, C and N) was created in the frames of CALPHAD method. Therefore the main research point was focused on an optimization of the alloy for the matrix. Afterwards, focus of thermodynamic modelling was shifted to the development of a database for the ceramic materials (ZrO_2, MgO, Al_2O_3, FeO, Fe_2O_3, MnO, Mn_2O_3).

In the beginning of the project, there were currently several thermodynamic databases for Fe-based multicomponent systems that were developed for the modelling of specific processes in the respective steels. They were based on critical assessments of binary and ternary systems available in the literature. For example, the TCFE7 commercial database included 25 elements and many binary and ternary systems (http://www.thermocalc.com/Products/Database). Moreover, this database contains descriptions of some solid oxide phases such as spinel, wustite and corundum in order to predict the tendency of different steels to oxidize. Additionally, there was the

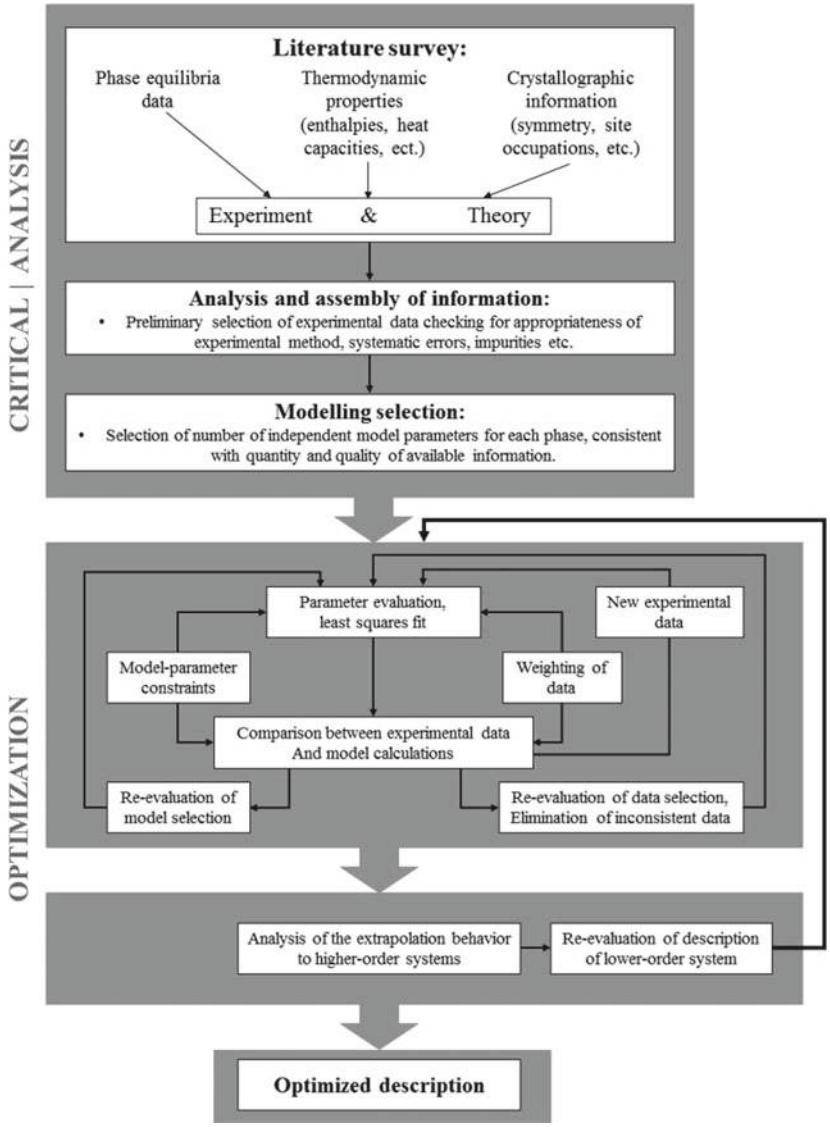

Fig. 19.1 A schematic diagram of the CALPHAD assessment

commercially available database TCOX, which contained 12 elements and descriptions of many oxide phases as well as the ionic melt, which describes both metallic and oxide melting behavior (http://www.thermocalc.com/Products/Database). However, all commercial databases have reproduced most of important binary system such as Fe–Mn, Fe–Ni, Zr–Mn, Zr–Fe very poorly, what could not be accepted for deep process of materials design.

A non-commercial steel database, which was under development in group of B. Hallstedt, contained 8 elements Fe, Al, Mn, Nb, Si, V, C and N and was aimed for modelling phase equilibria in Mn-rich steels [21]. However, this database did not include Cr and Ni, which were very important for highly alloyed TRIP-steels. Therefore, the CRC 799 project required to develop a unique multicomponent steel database, which would fit all specific needs of design process in the fames of the TRIP-Matrix-Composite development.

A new thermodynamic database for steels containing eleven elements (Fe, Mn, Mo, Cr, Ni, Ti, Si, V, W, N, C), has been developed by P. Franke within the first period of the CRC project [22]. Thermodynamic description of one of the most important systems Fe–Cr–Ni was developed based on advanced thermodynamic modelling. Obtained thermodynamic description considered magnetic contribution and chemical ordering in the Fe–Cr–Ni system [22]. This thermodynamic dataset for the ternary system Cr–Fe–Ni which has been reported in the literature for the range from medium to high temperatures has been supplemented with datasets from the binary subsystems at lower temperatures. The magnetic and the chemical ordering transitions which are known from the binary Fe–Ni system were extrapolated into the ternary system Cr–Fe–Ni. The phase diagram of Cr–Fe–Ni alloys at temperatures below 773 K was predicted (Fig. 19.2). The magnetic contribution to the Gibbs energy of Ni-rich alloys induces a miscibility gap which appears in the binary phase diagram of Fe–Ni as a small triangle-like field ending in a tricritical point. In the ternary system, Cr–Fe–Ni the miscibility gap is present as a broad two-phase field in the vicinity of the composition $FeNi_3$. At lower temperatures, this miscibility gap participates in a sequence of changing equilibria when it interferes with the chemically ordered $L1_2$ phase.

Several ternary systems in the Fe–Mn–Cr–Ni–Ti–Si–C–N system were accepted from literature data, checked for the consistency and published in LB series [23].

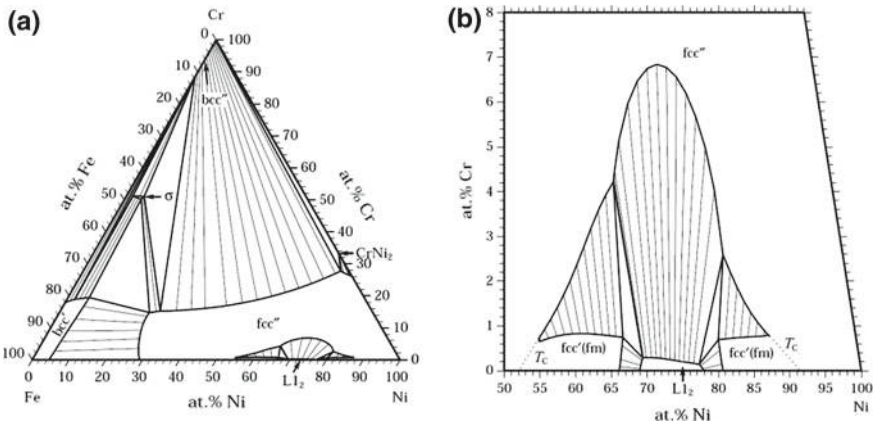

Fig. 19.2 **a** Calculated isothermal section of the Fe–Cr–Ni system at 773 K; **b** Enlarged part of calculated isothermal section at 773 K [22]

With this element selection calculations of the phase equilibria and modelling of the crystallization process using Scheil simulation for austenitic TRIP-steels became possible and reliable. Among the systems published in LB were Fe–Cr–Mn, Fe–Cr–Ni, Fe–Cr–C, Fe–Mn–C, Fe–Ni–C and others. The developed database covers a wide range of evaluated systems in comparison with other available databases. Thus, it also covers non-iron systems.

The second milestone was the interfacial interaction between Mg-PSZ and steel, which was experimentally studied by Franke et al. [5]. Experimental details (SPS pre-sintering, annealing in Ar etc.) were reported in [5]. SEM/EDX investigations demonstrated the formation of Mg_2SiO_4 at the interface between the ceramic component and steel. It was determined that Mg-PSZ contained SiO_2 impurities around of 2.4 mass%. It was stated, that another possible source for the SiO_2 could be the Si content within the TRIP-steel (~0.5 mass%). Thermodynamic calculations were performed to explain destabilization of Mg-PSZ and formation of Mg_2SiO_4 forsterite. The activity of MgO at the investigated temperature and the composition was calculated using the ZrO_2–MgO thermodynamic database available in literature [24]. The SiO_2 activity necessary for formations of silicates Mg_2SiO_4 and $MgSiO_3$ was calculated using the thermodynamic data from literature [25]. Experimental studies of an interaction between steel and pure ZrO_2 and between steel and CaO stabilized ZrO_2 showed that silicates did not form at the investigated conditions [5]. Thermodynamic calculations were also performed for the ZrO_2–SiO_2 and ZrO_2–CaO systems and ranges of the SiO_2 activity were determined at which silicates should form. The oxygen partial pressure was calculated at which the SiO_2 starts to form from Si dissolved in the steel. The corresponding limiting activity of Si in the TRIP-steel and the concentration of Si in the steel were calculated.

The ceramic material used in the present project is ZrO_2 stabilized by 3.4 mass% of MgO. A comprehensive thermodynamic assessment of the ZrO_2–MgO system was available in literature. However, all of the data were based on a substitutional model for the solid and liquid phases. Consequently, re-assessment based on the more advanced modelling using the compound energy formalism had to be performed. Additionally, it was experimentally found that an addition of Titanium can improve bonding between ZrO_2 ceramic particles and austenitic steel containing Mn, Cr and Ni [26]. Therefore, ceramic systems containing TiO_2 became one of the important tasks as well. Moreover, during the investigation of the interfacial interaction between Mg-PSZ and steel [5] it was found that the C–ZrO_2 (fluorite) was destabilized due to reaction between MgO and impurities in ceramic material such as Al_2O_3 and SiO_2. Therefore, systems with Al_2O_3 and SiO_2 became one of the main points.

Thermodynamic descriptions of the systems MgO–Al_2O_3 and MnO–Al_2O_3 based on the compound energy formalism for solid phases and partially ionic liquid model were available in literature [27, 28]. However, the model of the spinel phase in the MnO–Al_2O_3 system had to be extended by introducing an interstitial sublattice to be compatible with the model used for the MgO–Al_2O_3 system.

Many thermodynamic assessments for the systems containing TiO_2, Ti_2O_3, MgO, FeO, MnO and other oxides were performed in the group of A. D. Pelton (http://www.sgte.org/fact/documentation/FToxide). Solid phases were modelled by the compound

energy formalism, while the liquid phase was described by a modified quasi-chemical model [29]. The database for ZrO_2-based systems was set up with the help of very limited experimental literature data. However, the ZrO_2 containing phases do not contain the chemical element Ti, which makes it impossible to calculate the interaction with titanium oxides, which are very important for the planned work. Commercial steel and oxide databases have been developed by the FactSage group (http://www.sgte.org/factsage/fact/factsage/FactSage). Although these databases contain descriptions for the TiO_2–Ti_2O_3–MO systems (M = Mg, Fe, Mn), only very limited data are available for ZrO_2-based systems. Model for liquid is not compatible with models used in the present study.

Therefore, the thermodynamic database of the ZrO_2–MgO–MnO–Al_2O_3 system had to be developed for modelling of the interactions between Al_2O_3 impurities, Mg-PSZ and Fe–CrMnNi-TRIP-steels. In a similar way the SiO_2 containing binary descriptions of the MgO–SiO_2, MnO–SiO_2, ZrO_2–SiO_2 systems had to be combined with databases of the ZrO_2–MgO, ZrO_2–MnO systems and the thermodynamic database of the ZrO_2–MgO–MnO–SiO_2 system had to be developed to model phase relations between SiO_2 impurities, Mg-PSZ and the steel phases.

The thermodynamic description for the quasibinary system ZrO_2–MgO (Fig. 19.3) was based on own experimental investigations with XRD, SEM/EDX and DTA as well as existing literature data [30]. The industrial Mg-PSZ ceramic was also tested in the initial state and after heat treatments at 1523 K with DTA. Differences between

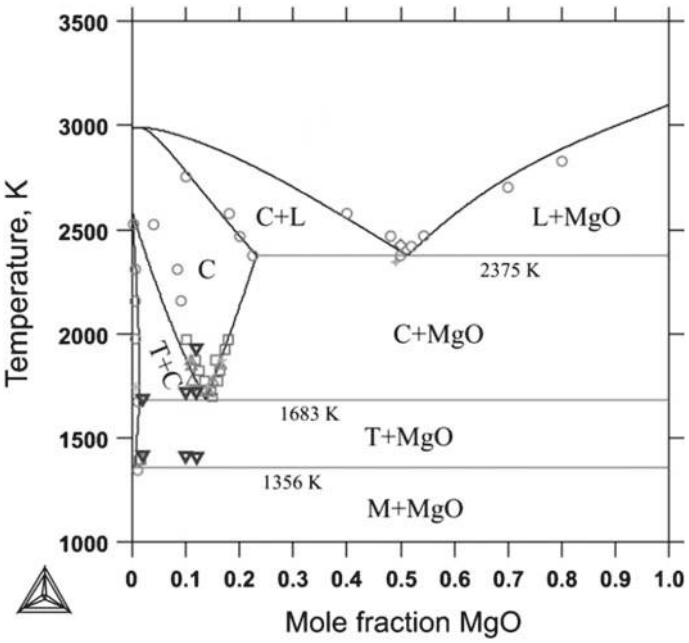

Fig. 19.3 The calculated ZrO_2–MgO phase diagram together with experimental data [30]

the calculations in the ZrO_2–MgO and the experimental data could be attributed to the presence of Al_2O_3 additives in the industrially produced samples. The additives cause the formation of the $MgAl_2O_4$ phase with spinel structure.

As the ZrO_2–MgO–Al_2O_3 quasi-ternary system had only a very limited amount of experimental data available in literature, the phase equilibria were investigated in more detail in the work of Pavlyuchkov et al. [31]. Throughout the composition range, the solid phase equilibria in the ZrO_2–MgO–Al_2O_3 system were investigated using DTA, XRD, and SEM/EDX. Thereby, the isothermal sections at 1523, 1873 and 2023 K have been constructed. Furthermore, the stability of ternary X-phase at 2073 K found by Tassot et al. [32] was confirmed. The temperature limits of the X-phase stability limits were determined in the range between 1894 and 2094 K. In addition, two ternary eutectic reactions and one eutectic maximum could be determined experimentally. The experimental data thus obtained were used to develop a thermodynamic description for this system. Thus, the liquidus and solidus surface projections and the isopleth section ZrO_2–$MgAl_2O_4$ were calculated [31]. The calculations showed that much more complicated phase relations exist in this system in comparison to the literature data [33, 34]. The calculated liquidus and solidus surface's projections of the ZrO_2–MgO–Al_2O_3 phase diagram are presented in Fig. 19.4.

As part of a separate work of Fabrichnaya and Pavlyuchkov [35], a thermodynamic description for the ternary Zr–Fe–O system using the CalPhaD approach was developed based on experimental data from literature. Thermodynamic parameters of ZrO_2–FeO and ZrO_2–Fe_3O_4 systems were assessed using literature data [36–38]. The solubility of FeO and Fe_2O_3 in the ZrO_2 and of ZrO_2 in the Fe_2O_3 and Fe_3O_4 phases were taken into account and described with the compound-energy formalism. The two sublattice model of partially ionic liquid was used for the description of the melt phase. The descriptions obtained for the ZrO_2–FeO and ZrO_2–Fe_3O_4 systems were combined into the description of the ZrO_2–FeO–Fe_2O_3 system. The isothermal section at 1473 K and the liquidus surface projection have been calculated for

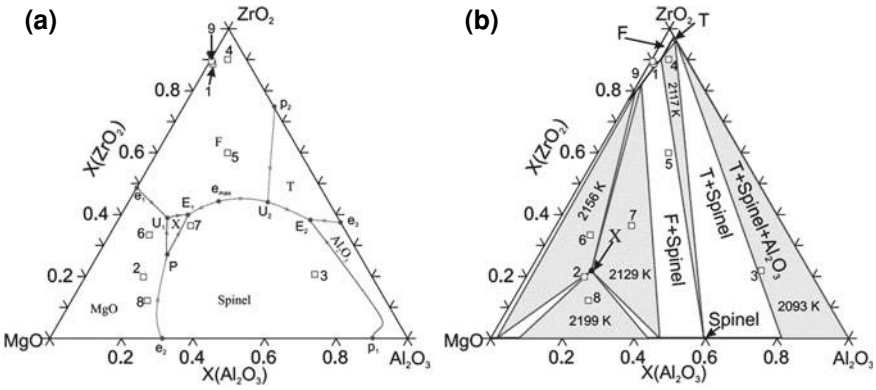

Fig. 19.4 Liquidus **a** and solidus **b** surface's projections of the ZrO_2–MgO–Al_2O_3 phase diagram [31]

the system using the complex data set. The calculated isopleth sections ZrO_2–FeO and ZrO_2–Fe_3O_4 are shown in Fig. 19.5a, b together with the experimental data. Figure 19.6 shows the liquidus surface projection of the ZrO_2–FeO–Fe_2O_3 system. The equilibria between the metallic melt and the solid ZrO_2 phase were calculated and compared with the literature values [39, 40]. Similar to other calculations [41], significant differences between the calculated oxygen solubilities in the Fe–Zr melt and the experimental results were found. New experimental study should be performed to resolve this contradiction.

The phase equilibria in the systems ZrO_2–MnO and ZrO_2–MnO–Mn_2O_3 were investigated experimentally with DTA in Ar atmosphere and by heat treatment in air in the temperature range between 1523 and 1873 K [42]. The reaction temperatures were determined with DTA-TG, the phase compositions in the samples with XRD and

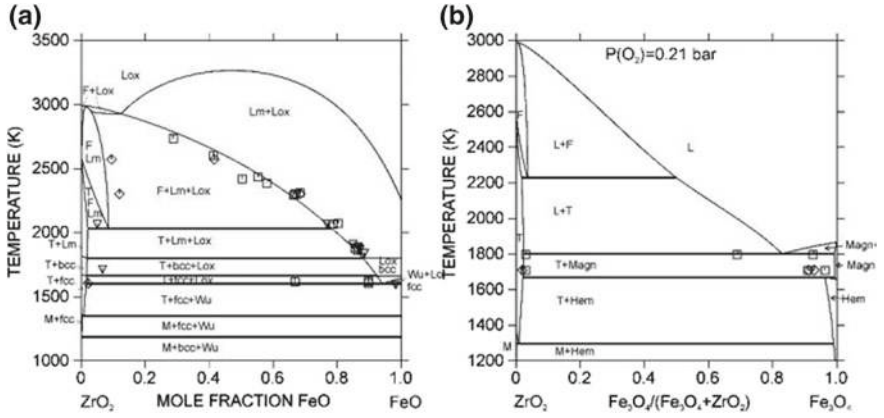

Fig. 19.5 **a** Calculated isopleth section of ZrO_2–FeO; **b** calculated isopleth section of ZrO_2–Fe_3O_4 [35]

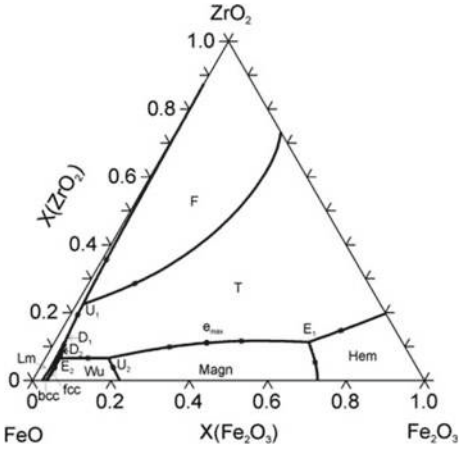

Fig. 19.6 Liquidus surface of the ZrO_2–FeO–Fe_2O_3 system calculated using advanced thermodynamic description of the Zr–Fe–O system [35]

the chemical compositions of the phases with SEM/EDX. Based on the experimental data, the thermodynamic parameters were optimized and phase diagrams at oxygen partial pressures of 10^{-4} bar and in air were calculated. The phase diagrams are shown in Fig. 19.7a, b along with the experimental data.

Phase equilibria in the ZrO_2–MgO–MnO–Mn_2O_3 system were investigated experimentally in air and in Ar atmosphere in the work of Pavlyuchkov et al. [43]. The samples were characterized with XRD and SEM/EDX. The reactions occurring in these systems were determined by DTA-TG experiments under He atmosphere. Isothermal sections constructed at low partial pressure of O_2 are presented in Fig. 19.8.

At the last stage of the TRIP-Matrix-Composite development, the main objective was the further development of the thermodynamic database for ZrO_2-based

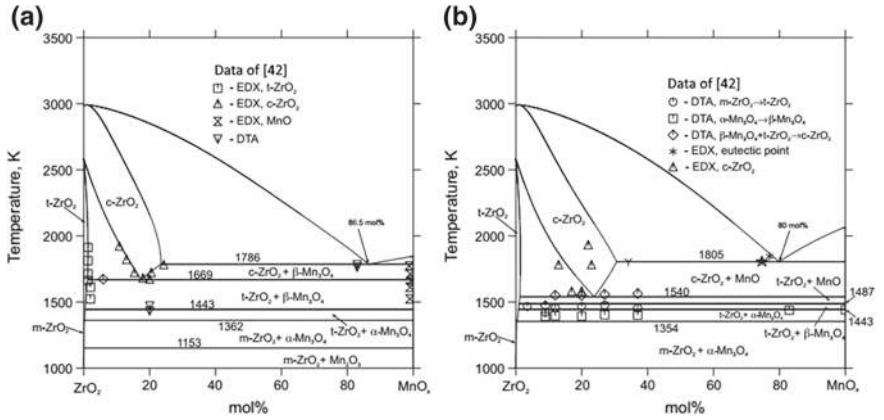

Fig. 19.7 Calculated phase diagrams of the ZrO_2–MnO_x systems at **a** $pO_2 = 0.21$ bar and **b** $pO_2 = 1 \times 10^{-4}$ bar, along with the experimental data [42]

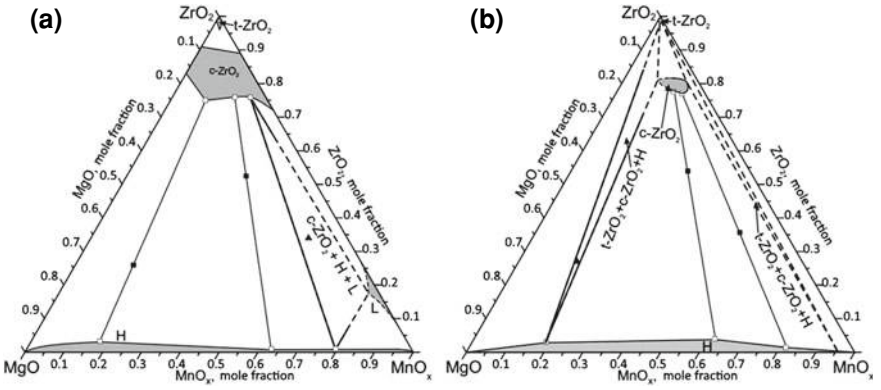

Fig. 19.8 Isothermal section of ZrO_2–MgO–MnO_x under helium atmosphere ($PO_2 = 10^{-4}$ bar) **a** at 1913 K and **b** at 1523 K [43]

ceramic materials and their implementation in the existing steel database. The combined database will make complete simulation of interfacial reactions between steel and ceramics in the TRIP metal matrix composite material possible. Therefore, the following partial goals result:

1. Further development of the thermodynamic database for the ZrO_2–MgO–FeO–MnO–Fe_2O_3–Mn_2O_3–TiO_2–Al_2O_3 system is to be promoted.
2. The next task is to assemble the thermodynamic databases for ceramic materials with the steel database. The main goal of this work is the creation of a thermodynamic database, which allows the calculation of the chemical reactions taking place at the interface between steel and ceramic. This task requires the integration of binary and ternary descriptions from the literature into the newly generated database as well as the adaptation of the thermodynamic parameters. The incorporation of oxygen into the data set requires the implementation of system descriptions such as Fe–O, Mn–O, Cr–O, Ni–O and the associated ternary systems Fe–Ni–O, Fe–Mn–O, Fe–Cr–O, Ni–Cr–O, etc. The integration of Zr requires the thermodynamic modelling of Zr–Fe, Zr–Mn, Zr–Ni systems as well as other Zr-containing systems. Therefore, the expansion of the steel database with Zr was planned. The binary descriptions Zr–O and Ti–O are implemented in the complex steel ceramics database.

First, high-temperature phase transformations in strongly metastable austenitic-martensitic Fe–CrMnNi–N–C cast steels were studied using SEM/EXD and DTA based on preliminary CALPHAD calculations. Our studies of the Fe–15Cr–3Mn–3Ni–0.1N cast stainless steels with five different carbon contents, in particular the SEM imaging and EDX elemental mapping of the segregation of Cr and Ni, have shown that the solidification mode changes from primary ferritic to primary austenitic with increasing carbon content. This is in contradiction to thermodynamic calculations (Fig. 19.9) of a primary ferritic solidification of all alloys, but can be explained by the experimental conditions, e.g. by the solidification rate, which creates a nonequilibrium state and facilitates therefore the austenitic solidification. Melting temperatures determined by DTA measurements showed no clear trend with respect to the carbon content in the investigated steel compositions, probably due to the influence of local chemical inhomogeneities. The experimental temperature range for melting is narrow and lies above the calculated melting range, probably due to an overheating effect. The transformation temperature for the solid-solid phase transformation fcc(γ) $\rightarrow$ fcc(γ) + bcc(δ) was also measured by DTA. In agreement with the calculations, it increases with increasing carbon content for steels NC05 to NC15, but above 0.155 wt% C it remains approximately constant regardless of the further increasing carbon content. Again, several effects can explain the deviation from the calculation in alloys with a higher carbon content: local fluctuations of the chemical composition, but also a reduced overheating due to an increased transformation rate at higher temperatures. The transformation fcc(γ) $\rightarrow$ fcc(γ) + bcc(δ) was found to be fully reversible, that means it occurs during heating and cooling at almost the same temperature, thus the undercooling is very small.

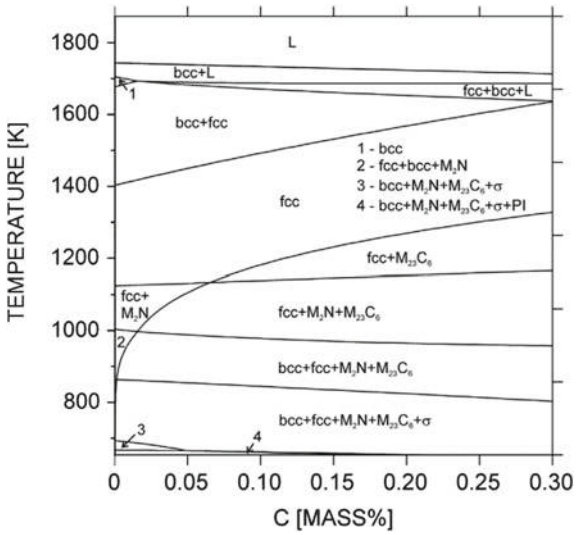

Fig. 19.9 Vertical section of the phase diagram of the steel Fe–15Cr–3Mn–3Ni–0.1N–xC in dependence on the carbon content [6]

Furthermore, the reversion transformation of a thermal martensite $\alpha' \rightarrow \gamma$ was shown for the steels NC05 and NC10, which contain a significant fraction of martensite formed during quenching. For the other alloys, the effect was below the detection limit of DTA because of the low volume fractions (<5 vol%) of martensite present. The onset temperature of the transformation decreased with the carbon content.

Concerning further thermodynamic modelling of the ceramic systems, thermodynamics of the Mg–Mn–O system has been modeled based on new heat capacity measurements of the $MgMn_2O_4$ and Mg_6MnO_8 phases [44]. Phase diagram data, structural information, and thermochemical data were used in the assessment. All solid solution phases were modeled using the compound energy formalism. Mg-solubility in the cubic spinel has been modeled according to the findings in a previous study of Pavlyuchkov et al. [43], which suggests that Mg solubility reported by earlier studies was too low. Thus, the older reports on the Mg solubility in the cubic spinel were not considered. In general experimental data found in the literature was well reproduced. The results presented were significant for further thermodynamic modelling of the Mg–Mn–Zr–O system.

Phase relations in the ZrO_2–TiO_2 system were investigated in the temperature range from 1303 to 1903 K using XRD and SEM/EDX. Melting reactions in this system were studied using DTA followed by microstructure investigation [45]. The Liq = β-$(Zr_xTi_{1-x})_2O_4$ + TiO_2 eutectic and the Liq + T-ZrO_2 = β-$(Zr_xTi_{1-x})_2O_4$ peritectic reactions were determined at 2029 K and 2117 K respectively. Composition of eutectic was determined by SEM/EDX to be 83.2 ± 1.0 mol%. First, the drop solution calorimetry method was applied using AlexSys 800 (SETARAM Instrumentation) in order to measure enthalpy of formation of the β-$ZrTiO_4$ compound from oxides (-18.3 ± 5.3 kJ mol^{-1}). Molar heat capacities of the β-$(Zr_xTi_{1-x})_2O_4$ compound was measured in the range 233–1223 K. Experimental thermodynamic values

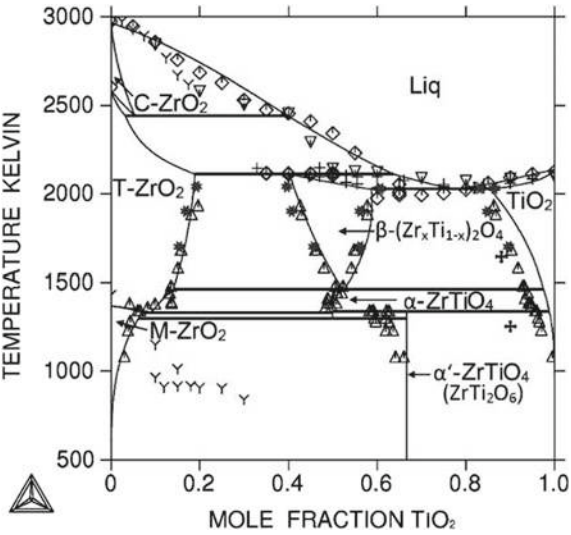

Fig. 19.10 Calculated phase diagram of the ZrO_2–TiO_2 system along with experimental data [45]

(i.e. heat capacity and enthalpy of formation of β-$ZrTiO_4$ compound) determined in [45] were used in order to optimize the description of heat capacity of α-$ZrTiO_4$ and β-$(Zr_xTi_{1-x})_2O_4$, as well as the contribution of the formation enthalpy of the β-$Zr_xTi_{1-x}O_4$ phase, respectively. Using the obtained experimental results together with literature data, the thermodynamic parameters in the ZrO_2–TiO_2 system were derived. Calculated phase diagram is presented in the Fig. 19.10.

Later on, based on the newly obtained results for the ZrO_2–TiO_2 system, the ZrO_2–TiO_2–MgO ternary system was experimentally investigated in the temperature range from 1533 K up to melting temperatures using XRD, SEM/EDX and DTA [46]. Isothermal sections of the system were constructed based on experimental data at 1533, 1683 and 1883 K. It has been determined that TiO_2 doping did not stabilized T-ZrO_2 phase in this system which transformed to monoclinic structure on cooling. Ternary compound described by formula $Zr_4TiMg_2O_{12}$ has been discovered. Homogeneity range of the compound was not established. However, based on experimental results, it was stated that the homogeneity range was insignificant and this compound was practically stoichiometric. The ternary compound has a trigonal structure of the Pr_7O_{12}-structure type. Nevertheless, further crystallographic investigations are necessary to establish the cations occupancies in the crystal structure of the phase. High temperature limit of the phase stability of the ternary compound has been determined to be 1664 K. Using results obtained by DTA and SEM/EDX, liquidus projection for the ZrO_2–TiO_2–MgO system has been constructed. The eutectic reactions Liq = C-ZrO_2 + β-$(Zr_xTi_{1-x})_2O_4$ + $MgTi_2O_5$, Liq = TiO_2 + β-$(Zr_xTi_{1-x})_2O_4$ + $MgTi_2O_5$ and Liq = $MgTi_2O_5$ + C-ZrO_2 + $MgTiO_3$ have been determined at 1800 K, 1851 K and 1872 K respectively. Based on the obtained experimental results, thermodynamic

description of the ZrO_2–TiO_2–MgO system was developed. Comparison of calculated and experimental results shows a good mutual agreement. Experimental and calculated liquidus projection of the system is shown in the Fig. 19.11.

As it was said above, the integration of Zr into steel database was required for combining of thermodynamic databases for ceramic materials with the steel database. Therefore, experimental differential scanning calorimetry measurements and ab initio simulations were carried out to define the heat capacities of Zr_3Fe and C15–$ZrFe_2$ compounds from 0 K up to their maximum stability temperatures [47]. Experimental measurements of heat capacity of each compound were performed for the first

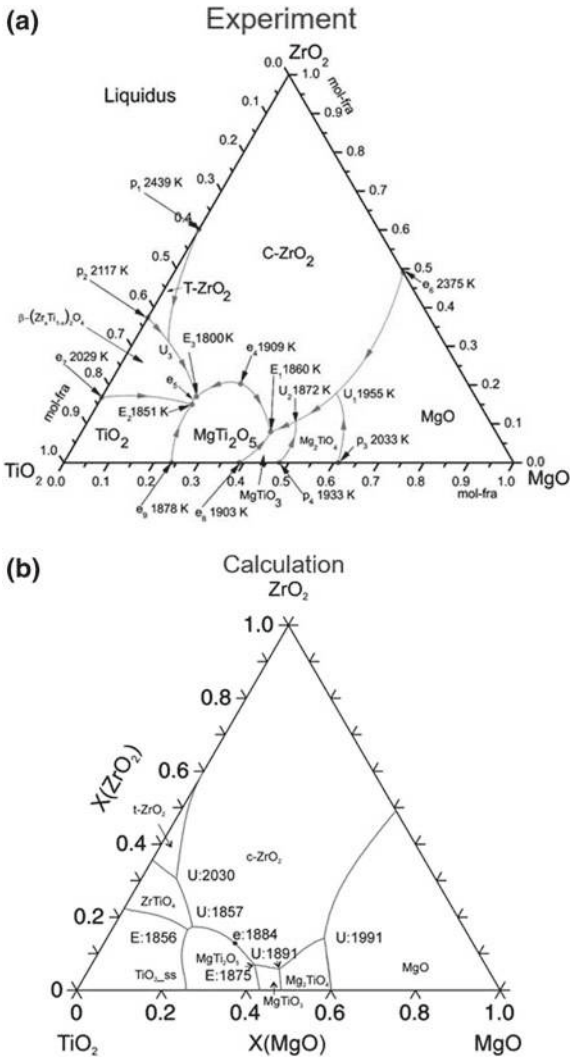

Fig. 19.11 **a** Constructed liquidus projection of the ZrO_2–TiO_2–MgO system [46] and **b** current results of CALPHAD calculation

time in wide range of temperatures. Density functional theory and quasi-harmonic approximation (QHA) were employed to calculate the Gibbs energy of the studied systems as a function of volume and temperature. Using the combination of DFT + QHA approach and experimental DSC analysis the main thermodynamic functions $C_P(T)$ and parameters S^{298} and ΔH^0 for Zr_3Fe and $ZrFe_2$ intermetallic phases were obtained form 0 K up to temperatures of their stability. In addition, experimental measurements of thermal expansion coefficient were performed for verification of DFT calculations. Analysis of theoretical and experimental data on α_V and C_P shows that QHA remarkably underestimates the anharmonic and magnetic effects starting from temperatures ~200 to 300 K. However, for low-temperature regions we observed very good agreement between theory and experiment.

Experimental measurements of heat capacity of Zr_2Fe were performed using DSC in the temperature range from 220 to 450 K for the first time [48]. Obtained results were compared with theoretical calculations of $C_P(T)$ presented by Ali et al. [49]. Using the combination of calculated [49] and experimental results, temperature dependence of heat capacity $C_P(T)$ for Zr_2Fe was described in the temperature range of 0–450 K as well. The standard entropy S^{298} of Zr_2Fe was evaluated using obtained heat capacity data. Taking into account recent experimental data on heat capacity and ab initio calculations of enthalpy of formation for intermetallic compounds and most reliable data for phase diagram [50, 51] thermodynamic re-assessment of the Fe–Zr system has been performed [48]. Liquid and solid solution phases such as bcc, fcc, and hcp have been described using substitutional model. Compound energy formalism has been used in order to describe homogeneity ranges of the C15- and C36–$ZrFe_2$ Laves phases. In the results, it has been demonstrated that the set of obtained thermodynamic parameters describes experimental data better than thermodynamic descriptions published earlier. Calculated phase diagram of the Fe–Zr system is presented in Fig. 19.12 along with experimental data.

Afterwards, the Zr–Mn system was studied using XRD, SEM/EDX, DSC and DTA by Flandorfer et al. [53] and in the present study. The heat capacity of the C14–$ZrMn_2$ phase was measured in the temperature range of 770 to 1320 K. Based on the obtained results, thermodynamic description was developed. The calculated phase diagram is presented in Fig. 19.13.

Newly obtained thermodynamic parameters of the Zr–Mn and Fe–Zr systems were combined together with Fe–Mn parameters [53] into description of Fe–Zr–Mn system based on binary extrapolation. This database was created for calculations of the ternary diagram which was further used for selection of sample compositions. Experimental investigation of Zr–Fe–Mn system included study of quasi-binary C14–$ZrMn_2$–C15–$ZrFe_2$ system and ternary phase equilibria. Quasi-binary section of the ternary system was studied by diffusion couple (DC) method. DC was prepared from single phase C14–$ZrMn_2$ and C15–$ZrFe_2$ samples by spark plasma sintering (SPS) plating. Obtained samples were heat-treated at 1173 and 1373 K in order to examine phase relation at different temperatures. Microstructure of the DCs was then studied using SEM/EDX with engaging of line-scan for analysis of composition gradient. Samples for ternary phase relations investigation, corresponding to three phase regions, were prepared by arc melting. Samples were heat-treated at

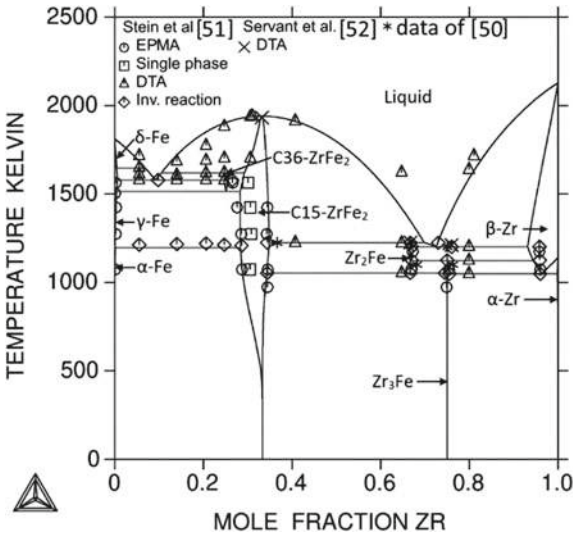

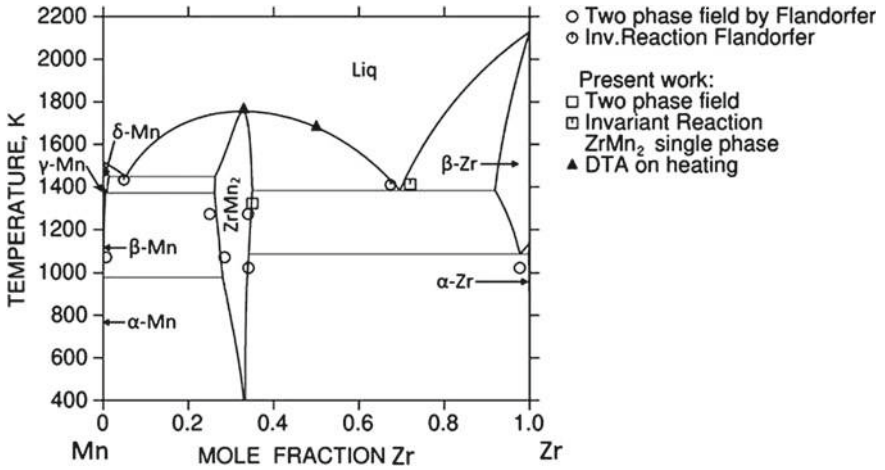

Fig. 19.12 Calculated Fe–Zr phase diagram [50] along with experimental data from the works of Stein et al. [51] and Servant et al. [52]

Fig. 19.13 Calculated Zr–Mn phase diagrams along with experimental data of Flandorfer et al. [53]

1073 K and quenched into water. They were then studied using XRD and SEM/EDX for phase identification and phase relation and chemical composition analysis.

There was contradiction in literature data for this system connected with the area on the phase diagram corresponding to the two-phase region C15–C14. In the work [54] a two-phase region was reported, while in the work [55] an anomaly change of magnetic moment was observed and XRD results indicated formation of C36 Laves phase structure in the composition range between C15 and C14 Laves phases. In

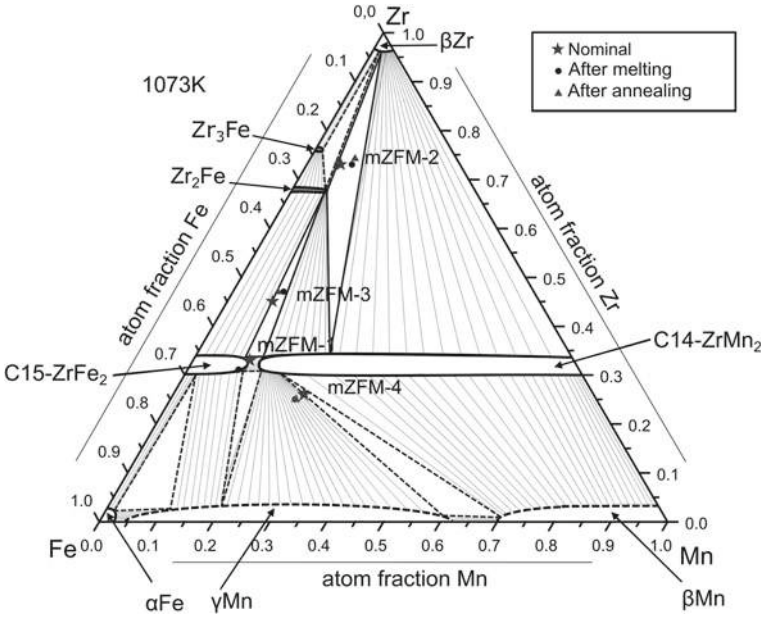

Fig. 19.14 Constructed isothermal section of the Fe–Zr–Mn system at 1073 K

the present work results from SEM/EDX investigation indicated absence of a phase with an intermediate composition. Therefore, it was concluded that two solid solution phases C15 and C14 were present in the system coexisting with each other in the range between 60 and 80 mol% $ZrFe_2$. Measured solubility ranges of the boundaries of the phases are in good agreement with the literature data [54].

It should be mentioned, that ternary Fe–Zr–Mn system was studied the first time. It was partially constructed based on the results obtained on ternary system and thermodynamic assessments of the composing binary systems. Obtained results are presented in the Fig. 19.14.

19.5 Conclusions

Within the present work, substantial amount of results were obtained for thermodynamic modelling of the system related to the TRIP-Matrix-Composite development. Advanced methods of thermodynamic simulations were applied for optimization of chemical composition of steel matrix and ceramic particles, for prediction and understanding of mechanisms occurring in the material, for finding new solutions of technological issues. Additionally, the methods of thermodynamic modelling provided a basement for further development of the TRIP-Matrix-Composite.

Thermodynamic database was developed for 11 elements Fe, Mn, Cr, Ni, Ti, Si, N, C, Mo, W, V. Obtained thermodynamic description reproduces most of the available experimental results. Thereby, it gives more reliable extrapolations in comparison to other commercial or noncommercial thermodynamic descriptions. Concerning development of thermodynamic oxide description, 3 binary, 7 ternary and a quaternary systems were investigated and modeled in cooperation with other projects.

However, the main uncompleted task is the integration of Zr, what requires the thermodynamic modelling of binary systems such as Zr–Ni, Zr–Cr and ternary system of iron, zirconium and main alloying elements of steel matrix. Moreover, the incorporation of oxygen into the data set of the steel database requires the implementation of system descriptions such as Fe–O, Mn–O, Cr–O, Ni–O and the associated ternary systems Fe–Ni–O, Fe–Mn–O, Fe–Cr–O, Ni–Cr–O, etc.

Acknowledgements Current work was funded by the Deutsche Forschungsgemeinschaft (DFG, German Research Foundation)—Projektnummer 54473466–SFB 799. The authors thank Prof. Seifert, Dr. Franke and Dr. Pavlychkov for scientific support and co-working in the sub-project C2 in the frame of SFB 799.

References

1. U.R. Kattner, Tecnol. Metal Mater. Min. **13**(1), 3–15 (2016). https://doi.org/10.4322/2176-1523.1059
2. S. Martin, S. Richter, S. Decker, U. Martin, L. Krüger, D. Rafaja, Steel Res. Int. **82**(9), 1133–1140 (2011). https://doi.org/10.1002/srin.201100099
3. M. Wendler, B. Reichel, R. Eckner, O. Fabrichnaya, L. Krüger, A. Weiß, J. Mola, Metall. Mater. Trans. A **47**(1), 139–151 (2016). https://doi.org/10.1007/s11661-014-2716-0
4. S. Martin, O. Fabrichnaya, D. Rafaja, Mater. Lett. **159**, 484–488 (2015). https://doi.org/10.1016/j.matlet.2015.06.087
5. P. Franke, M. Ksyta, H.J. Seifert, Steel Res. Int. **82**(9), 1149–1157 (2011). https://doi.org/10.1002/srin.201100132
6. O. Fabrichnaya, C. Ullrich, M. Wendler, G. Savinykh, D. Rafaja, J. Alloys Compd. **686**, 511–521 (2016). https://doi.org/10.1016/j.jallcom.2016.06.026
7. M. Hauser, M. Wendler, O. Fabrichnaya, O. Volkova, J. Mola, Mater. Sci. Eng., A **675**, 415–420 (2016). https://doi.org/10.1016/j.msea.2016.08.080
8. L. Halbauer, R. Eckner, M. Wendler, O. Fabrichnaya, A. Buchwalder, L. Krüger, R. Zenker, H. Biermann, Steel Res. Int. **87**(12), 1627–1637 (2016). https://doi.org/10.1002/srin.201600028
9. H.L. Lukas, S.G. Fries, B. Sundman, *Computational Thermodynamics* (Cambridge University Press, Cambridge, 2007)
10. Z.-K. Liu, Y. Wang, *Computational Thermodynamics of Materials* (Cambridge University Press, Cambridge, 2016)
11. L. Lutterotti, Nucl. Instrum. Methods Phys. Res. B **268**(3–4), 334–340 (2010). https://doi.org/10.1016/j.nimb.2009.09.053
12. G. Della Gatta, M.J. Richardson, S.M. Sarge, S. Stølen, Pure Appl. Chem. **78**(7), 1455–1476 (2006). https://doi.org/10.1351/pac200678071455
13. O.B. Fabrichnaya, S.K. Saxena, P. Richet, E.F. Westrum, *Thermodynamic Data, Models, and Phase Diagrams in Multicomponent Oxide Systems* (Springer, Berlin, Heidelberg, 2004)
14. L. Kaufman, H. Bernstein, *Computer Calculation of Phase Diagrams with Special Reference to Refractory Metals* (Academic Press Inc, New York, 1970)

15. N. Saunders, A.P. Miodownik, *Calphad* (Pergamon, Oxford, 1998)
16. M. Hillert, J. Alloys Compd. **320**(2), 161–176 (2001). https://doi.org/10.1016/S0925-8388(00)01481-X
17. R. Schmid-Fetzer, D. Andersson, P.Y. Chevalier, L. Eleno, O. Fabrichnaya, U.R. Kattner, B. Sundman, C. Wang, A. Watson, L. Zabdyr, M. Zinkevich, Calphad **31**(1), 38–52 (2007). https://doi.org/10.1016/j.calphad.2006.02.007
18. M. Hillert, M. Jarl, Calphad **2**(3), 227–238 (1978). https://doi.org/10.1016/0364-5916(78)90011-1
19. A.T. Dinsdale, Calphad **15**(4), 317–425 (1991). https://doi.org/10.1016/0364-5916(91)90030-N
20. O. Redlich, A.T. Kister, Ind. Eng. Chem. **40**(2), 345–348 (1948). https://doi.org/10.1021/ie50458a036
21. D. Djurovic, B. Hallstedt, J. von Appen, R. Dronskowski, Calphad **35**(4), 479–491 (2011). https://doi.org/10.1016/j.calphad.2011.08.002
22. P. Franke, H.J. Seifert, Calphad **35**(1), 148–154 (2011). https://doi.org/10.1016/j.calphad.2010.10.006
23. Scientific Group Thermodata Europe (SGTE), *Thermodynamic Properties of Inorganic Materials* (Springer, Berlin, London, 2000)
24. S. Serena, M.A. Sainz, S. de Aza, A. Caballero, J. Eur. Ceram. Soc. **25**(5), 681–693 (2005). https://doi.org/10.1016/j.jeurceramsoc.2004.02.011
25. B. Hallstedt, Calphad **16**(1), 53–61 (1992). https://doi.org/10.1016/0364-5916(92)90038-Y
26. D. Wittig, A. Glauche, C.G. Aneziris, T. Minghetti, C. Schelle, T. Graule, J. Kuebler, Mater. Sci. Eng., A **488**(1–2), 580–585 (2008). https://doi.org/10.1016/j.msea.2007.11.065
27. B. Hallstedt, J. Am. Ceram. Soc. **75**(6), 1497–1507 (1992). https://doi.org/10.1111/j.1151-2916.1992.tb04216.x
28. A.B. Farina, F.B. Neto, Calphad **33**(4), 711–718 (2009). https://doi.org/10.1016/j.calphad.2009.09.003
29. A.D. Pelton, G. Eriksson, D. Krajewski, M. Göbbels, E. Woermann, Z Phys. Chem. **207**(Part_1_2), 163–180 (1998). https://doi.org/10.1524/zpch.1998.207.part_1_2.163
30. D. Pavlyuchkov, G. Savinykh, O. Fabrichnaya, Adv. Eng. Mater. **15**(7), 618–626 (2013). https://doi.org/10.1002/adem.201200316
31. D. Pavlyuchkov, G. Savinykh, O. Fabrichnaya, J. Euro. Ceram. Soc. **34**(5), 1397–1408 (2014). https://doi.org/10.1016/j.jeurceramsoc.2013.11.038
32. P. Tassot, G. Knig, F. Seifert, F. Liebau, J. Mater. Sci. **21**(10), 3479–3482 (1986). https://doi.org/10.1007/BF00553788
33. A.S. Berezhnoj, R.A. Kordyuk, DAN URSR (4), 506–508 (1964)
34. A.V. Shevchenko, G.I. Gerasimyuk, L.M. Lopato, S.G. Yusupova, Inorg. Mater. **29**, 117–118 (1993)
35. O. Fabrichnaya, D. Pavlyuchkov, Metall. Mater. Trans. A **47**(1), 152–159 (2015). https://doi.org/10.1007/s11661-015-2805-8
36. S.V. Bechta, E.V. Krushinov, V.I. Almjashev, S.A. Vitol, L.P. Mezentseva, Y.B. Petrov, D.B. Lopukh, V.B. Khabensky, M. Barrachin, S. Hellmann, K. Froment, M. Fischer, W. Tromm, D. Bottomley, F. Defoort, V.V. Gusarov, J. Nucl. Mater. **348**(1–2), 114–121 (2006). https://doi.org/10.1016/j.jnucmat.2005.09.009
37. T.S. Jones, S. Kimura, A. Muan, J. Am. Ceram. Soc. **50**(3), 137–142 (1967). https://doi.org/10.1111/j.1151-2916.1967.tb15063.x
38. R.H.G.A. Kiminami, Ceramica (Sao Paulo) (33), 207–209 (1987)
39. R.J. Fruehan, MT **5**(2), 345–347 (1974). https://doi.org/10.1007/bf02644100
40. D. Janke, W.A. Fischer, Archiv für das Eisenhüttenwesen **47**(4), 195–198 (1976). https://doi.org/10.1002/srin.197603805
41. W. Huang, Calphad **28**(2), 153–157 (2004). https://doi.org/10.1016/j.calphad.2004.07.007
42. D. Pavlyuchkov, G. Savinykh, O. Fabrichnaya, J. Euro. Ceram. Soc. **35**(13), 3623–3632 (2015). https://doi.org/10.1016/j.jeurceramsoc.2015.06.005

43. D. Pavlyuchkov, D. Dilner, G. Savinykh, O. Fabrichnaya, J. Am. Ceram. Soc. **99**(9), 3136–3145 (2016). https://doi.org/10.1111/jace.14327
44. D. Dilner, D. Pavlyuchkov, T. Zienert, L. Kjellqvist, O. Fabrichnaya, J. Am. Ceram. Soc. **100**(4), 1661–1672 (2017). https://doi.org/10.1111/jace.14686
45. I. Saenko, M. Ilatovskaia, G. Savinykh, O. Fabrichnaya, J. Am. Ceram. Soc. **101**(1), 386–399 (2017). https://doi.org/10.1111/jace.15176
46. I. Saenko, V. Tsukrenko, M. Ilatovskaia, D. Pavlyuchkov, G. Savinykh, O. Fabrichnaya, Adv. Eng. Mater. **21**(5), 1800655 (2018). https://doi.org/10.1002/adem.201800655
47. B.O. Mukhamedov, I. Saenko, A.V. Ponomareva, M.J. Kriegel, A. Chugreev, A. Udovsky, O. Fabrichnaya, I.A. Abrikosov, Intermetallics **109**, 189–196 (2019). https://doi.org/10.1016/j.intermet.2019.01.018
48. R. Lück, H. Wang, J. Alloys Compd. **191**(2), L11–L12 (1993). https://doi.org/10.1016/0925-8388(93)90055-R
49. K. Ali, P.S. Ghosh, A. Arya, J. Alloys Compd. **723**, 611–619 (2017). https://doi.org/10.1016/j.jallcom.2017.06.154
50. I. Saenko, A. Kuprava, A. Udovsky, O. Fabrichnaya, Calphad **66**, 101625 (2019). https://doi.org/10.1016/j.calphad.2019.05.002
51. F. Stein, G. Sauthoff, M. Palm, J. Phase Equilibria Diffus. **23**(6), 480 (2002). https://doi.org/10.1361/105497102770331172
52. C. Servant, C. Gueneau, I. Ansara, J. Alloys Compd. **220**(1–2), 19–26 (1995). https://doi.org/10.1016/0925-8388(94)06036-3
53. H. Flandorfer, J. Gröbner, A. Stamou, N. Hassiotis, A. Saccone, P. Rogl, R. Wouters, H. Seifert, D. Macciò, R. Ferro, G. Haidemenopoulos, L. Delaey, G. Effenberg, Mater. Res. Adv. Tech. (88), 529–538 (1997)
54. V.V. Petkov, Russ. Metall. **5**, 113–115 (1972)
55. K. Kanematsu, J. Phys. Soc. Jpn. **31**(5), 1355–1360 (1971). https://doi.org/10.1143/JPSJ.31.1355

Chapter 20
Thermodynamic-Mechanical Modeling of Metastable High Alloy Austenitic CrMnNi Steels

Michael Hauser, Marco Wendler, Javad Mola, Olga Fabrichnaya, Olena Volkova and Andreas Weiß

Abstract The deformation-induced formation of α'-martensite was investigated by tensile testing of a X5CrNi18-10 wrought austenitic steel and X3CrMnNi16-7-3/6/9 (Ni contents of 3, 6, and 9 mass%) as well as X15CrNiMnN19-4-3 cast austenitic steels at temperatures between −80 and 400 °C. The results were presented in the form of Stress-Temperature-Transformation (STT) and Deformation-Temperature-Transformation (DTT) diagrams. The diagrams laid foundations for the development of a method for the quantitative determination of strength and elongation contributions by means of induced and often overlapping deformation processes in the austenite. The summation of such contributions yielded the tensile strength and the uniform elongation of the steel. In order to determine the critical Gibbs free energy for the formation of martensite at temperatures between M_s and M_d, the chemical and mechanical contributions to deformation-induced martensite formation were determined by CALPHAD method using Thermo-Calc software. The mechanical contribution was estimated by determining the triggering stress for the formation of martensite using an in situ magnetic measurement device. This was done using the model proposed by Patel and Cohen. The magnitudes of shear strain (γ_0) and dilatational strain (ε_0), required for the calculations, were obtained based on the martensite crystallography theory of Wechsler-Lieberman-Read. The sum of the chemical and mechanical contributions yielded the critical driving force for the martensitic transformation.

M. Hauser (✉) · M. Wendler · O. Volkova · A. Weiß
Institute of Iron and Steel Technology, Technische Universität Bergakademie Freiberg, Leipziger Str. 34, 09599 Freiberg, Germany
e-mail: michael.hauser@iest.tu-freiberg.de

J. Mola
Material Design and Structural Integrity Lab, Osnabrück University of Applied Sciences, 49076 Osnabrück, Germany

O. Fabrichnaya
Institute of Materials Science, Technische Universität Bergakademie Freiberg, Gustav-Zeuner-Str. 5, Freiberg, Germany

H. Biermann and C. G. Aneziris (eds.), *Austenitic TRIP/TWIP Steels and Steel-Zirconia Composites*, Springer Series in Materials Science 298,
https://doi.org/10.1007/978-3-030-42603-3_20

20.1 Introduction

Depending on the chemical composition and deformation temperature, deformation mechanisms such as dislocations cell formation, mechanical twinning, and martensitic transformation may occur in the austenite phase of austenitic high-alloy steels [1–12]. The martensite commonly forms at intersections of glide bands in the austenite. At low temperatures where martensite formation is enabled, glide bands may consist of stacking fault bundles, ε martensite, and mechanical twins [13, 14].

In austenitic steels exhibiting the transformation-induced plasticity (TRIP) effect, the knowledge of the minimum driving force necessary for the martensite formation is of primary importance. The concept of defining a critical driving force for the martensite nucleation was first put forward by Cohen and coworkers [15, 16] and has been extended by Ghosh and Olson to include the effect of alloying elements [17]. This concept enables the thermodynamic modeling of metastable austenitic steels and can be used as a powerful tool to design new engineering materials [18–23]. The accuracy of such calculations will then depend on the reliability of the thermodynamic data. The thermodynamic database is particularly trustworthy in the chemical composition range where it has been calibrated by experimental data [24, 25].

The focus of the present work is the thermodynamic-mechanical modeling of metastable high alloy austenitic CrMnNi steels. To collect the experimental results needed for modeling, several steels were investigated. With the aid of thermodynamic data and flow curve analysis, it is possible to describe the dependence of mechanical properties on deformation mechanisms and phase transformation.

20.2 Experimental Methods

The chemical composition of the investigated steels are shown in Table 20.1. The steel X5CrNi18-10 was produced from BGH Edelstahl Freital GmbH, Germany. The steel X3CrMnNi16-7-6 was molten in an induction furnace and cast into a sand mould by ACTech GmbH, Freiberg, Germany. The steels X3CrMnNi16-7-3/9 were melted in a vacuum induction furnace and cast into a water-cooled copper mould. The steel X15CrNiMnN19-4-3 was melted in the vacuum induction furnace under a

Table 20.1 Chemical composition of the investigated cast steels in mass%

Alloy	C	N	Cr	Mn	Ni	Si	Fe
X5CrNi18-10	0.045	0.018	17.2	1.82	8.8	0.5	bal.
X3CrMnNi16-7-3	0.028	0.009	16.4	7.0	3.1	1.0	bal.
X3CrMnNi16-7-6	0.034	0.033	15.5	6.1	6.1	1.0	bal.
X3CrMnNi16-7-9	0.031	0.013	16.4	6.9	9.0	1.1	bal.
X15CrNiMnN19-4-3	0.154	0.167	18.7	2.9	4.2	0.5	bal.

nitrogen partial pressure of 450 mbar followed by casting into a water-cooled copper mould with a dimension of 230 × 35 × 95 mm^3. To avoid pore formation in the ingot, the nitrogen partial pressure was raised to 1500 mbar during casting.

To ensure the absence of machining-induced martensite near the surface of tensile specimens, solution heat treatments were performed after machining of tensile specimens. The solution heat treatment aimed at the dissolution of carbides and nitrides likely existing in the as-cast microstructure The solution heat treatment consisted of holding the X5CrNi18-10 steel at 1050 °C for 60 min, the X3CrMnNi16-7-3/6/9 steels at 1050 °C for 30 min and the X15CrNiMnN19-4-3 steel at 1150 °C for 30 min under an argon atmosphere.

Using a Zwick 1476-type universal testing machine, tensile specimens were tested at a constant crosshead displacement speed with an initial strain rate of 4×10^{-4} s^{-1}. With the aid of a thermal chamber which surrounded the tensile specimen and the specimen fixtures, different temperatures in the range of −40 and 200 °C were adjusted. The tensile tests below −40 °C were performed with the aid of an Instron S5982 universal testing machine.

An in situ magnetic measurement system was devised to determine the α'-martensite content formed during tensile tests [21]. The experimental setup is shown in Fig. 20.1. The magnetic measurement system consisted of two coils. The

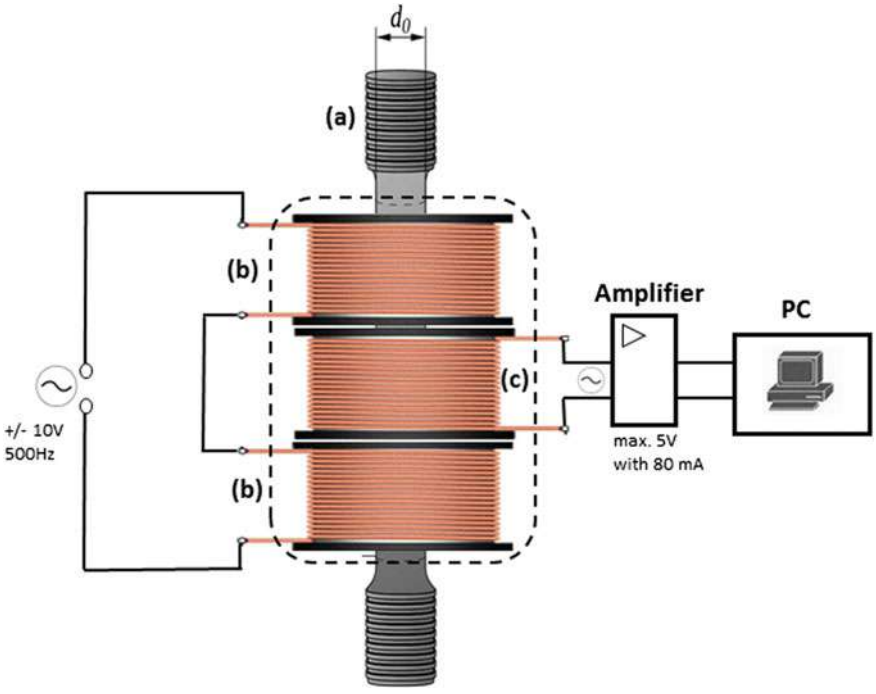

Fig. 20.1 Experimental setup showing tensile specimen and in situ magnetic measurement system with **a** tensile specimen, **b** first coil and **c** second coil

first coil served to generate an electromagnetic field which magnetized the martensite phase as it formed during tensile loading. The magnetization of martensite phase in tensile specimens induced an electrical potential difference (voltage) in the second coil which was recorded. To avoid interactions between the magnetic field and the surrounding components in the thermal chamber, a relatively small current (0.35 A) was used. This led to a magnetic field strength of 15 kA/m in the gauge section of tensile specimens. To avoid thermal degradation of the polymer components of the magnetic coil, in situ magnetic measurements were only conducted in the temperature range −80 to 40 °C.

The conversion of the voltage induced in the second coil to martensite fraction was done by a correlation procedure. The correlation procedure consisted of performing interrupted tensile tests followed by magnetic saturation measurements with an ex situ unit in order to quantify the α'-martensite fractions at the point of interruption. The procedure is described in more detail by Hauser et al. [21].

For the ex situ quantification of the ferromagnetic phase fraction in tensile specimens, a Metis MSAT-type magnetic saturation device equipped with a Lakeshore 480 fluxmeter was used. This equipment enabled the measurement of magnetic flux density after saturation magnetization of specimens cut from tensile specimens. The ferromagnetic phase fraction was calculated after an internal correction for the chemical composition. The correction took the influence of alloying elements on the magnetic moment of pure iron into account. The measurement accuracy with this method is within ±1%. Magnetic saturation measurements prior to tensile tests enabled the quantification of delta ferrite fractions retained after solution annealing. The delta ferrite fraction in solution annealed tensile specimens was also determined by quantitative metallography. These measurements closely reproduced the delta ferrite fraction based on ex situ magnetic saturation measurements. The microstructure was studied by means of electron channeling contrast imaging (ECCI) and electron backscatter diffraction (EBSD) techniques in a Zeiss LEO-1530 GEMINI-type field emission scanning electron microscope (FESEM). To calculate Gibbs free energies for the austenite (fcc) and ferrite (bcc) phases, the thermodynamic database developed by Franke et al. with the Thermo-Calc Software was used [26].

20.3 Theoretical Background

In metastable austenitic steels, martensite formation can occur spontaneously at temperatures below the martensite start (M_s) temperature and completes at the martensite finish (M_f) temperature. Martensite formation can also be triggered by deformation at temperatures up to M_d temperature, which leads to the so-called Transformation-Induced Plasticity (TRIP)-effect. The austenite stability can be described as the sum of energy contributions which are beneficial to the martensitic phase transformation and those which hinder it. Whereas the mechanical energy (W_{mech}), and at sufficiently low temperatures, the chemical driving force ($\Delta G_{chem}^{\gamma \rightarrow \alpha'}$) have a positive effect on the

phase transformation, the non-chemical contribution ($\Delta G_{\mathrm{nc}}^{\gamma\rightarrow\alpha'}$) as defined in the following and the adiabatic heating (Q_{ad}) of the sample delay the phase transformation. When the total Gibbs free energy change ($\Delta G_{\mathrm{total}}$) is negative, thermodynamic driving force is available for the austenite to martensite transformation. Different energy contributions are included in (20.1) [18, 25, 27].

$$\Delta G_{\mathrm{total}} = \Delta G_{\mathrm{chem}}^{\gamma\rightarrow\alpha'} + \Delta G_{\mathrm{nc}}^{\gamma\rightarrow\alpha'} + W_{\mathrm{mech}} + Q_{\mathrm{ad}} \tag{20.1}$$

While the adiabatic heating of the sample can be avoided by applying a low strain rate, the non-chemical energy contributions still need to be taken into account. The non-chemical energy contributions include the energy due to the lattice shear (ΔG_{sh}), surface and interface energies (ΔG_{sur}) and elastic strain energy (E^{str}), see in (20.2). All these energy contributions can be summed up to the critical driving force for the martensite formation ($\Delta G_{\mathrm{crit}}^{\gamma\rightarrow\alpha'}$) [17, 22, 23, 28].

$$\Delta G_{\mathrm{nc}} = \Delta G_{\mathrm{sur}} + \Delta G_{\mathrm{sh}} + E^{\mathrm{str}} \triangleq \Delta G_{\mathrm{crit}}^{\gamma\rightarrow\alpha'} \tag{20.2}$$

In Fig. 20.2, the Gibbs free energy for martensite formation is shown as a function of temperature. The martensitic phase transformation can only occur at temperatures

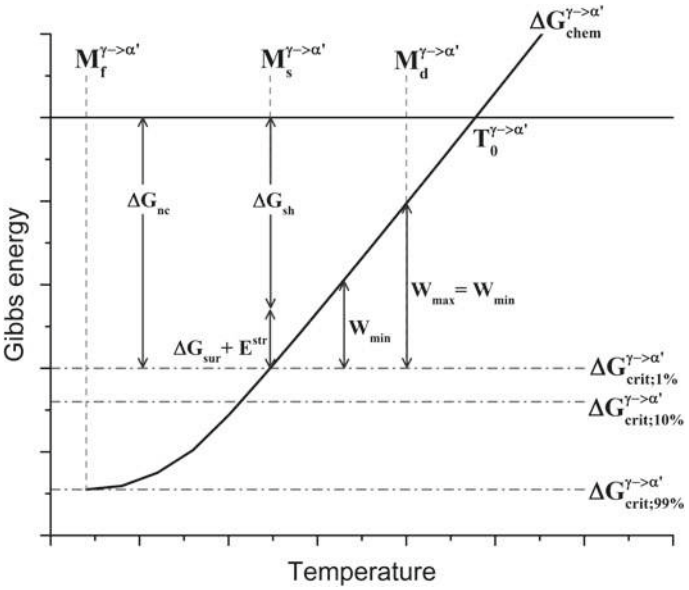

Fig. 20.2 Schematic representation of the temperature dependence of the chemical driving force for α'-martensite formation ($\Delta G_{\mathrm{chem}}^{\gamma\rightarrow\alpha'}$), minimum external mechanical work required to trigger the transformation (W_{min}), maximum applicable mechanical work (W_{max}), and critical driving forces for the formation of various martensite fractions ($\Delta G_{\mathrm{crit}}^{\gamma\rightarrow\alpha'}$), and non-chemical contributions ΔG_{nc}

below $T_0^{\gamma\rightarrow\alpha'}$, where the Gibbs free energies for austenite and ferrite of the same chemical composition are equal. Nevertheless, an additional energy contribution is needed to reach the critical driving force. At the M_s temperature and below, the chemical energy alone is high enough to trigger the martensitic phase transformation spontaneously. In the temperature range between M_s and M_d temperatures, on the other hand, the critical driving force can be reached by an additional energy contribution supplied by mechanical deformation. Therefore, the M_d temperature is the highest temperature where deformation-induced martensite formation can occur and thus the upper temperature limit to achieve the TRIP-effect with the maximum mechanical energy applicable to the material (W_{max}). During uniaxial tensile test, W_{max} denotes the maximum mechanical work applicable to austenite until the onset of localized deformation (necking). The applicable work determines the capacity of material to absorb external energy, thereby the amount of martensite that can be induced by deformation. Below the M_d temperature, one can define a minimal mechanical energy (W_{min}) which is needed to trigger the martensitic phase transformation. W_{min} reaches zero at M_s temperature. The larger the applied mechanical work with respect to W_{min}, the larger the induced martensite fraction [18, 22, 23].

Looking at the spontaneous martensitic transformation from a thermodynamic point of view, three possible cases can arise at low temperatures (Fig. 20.3). Case

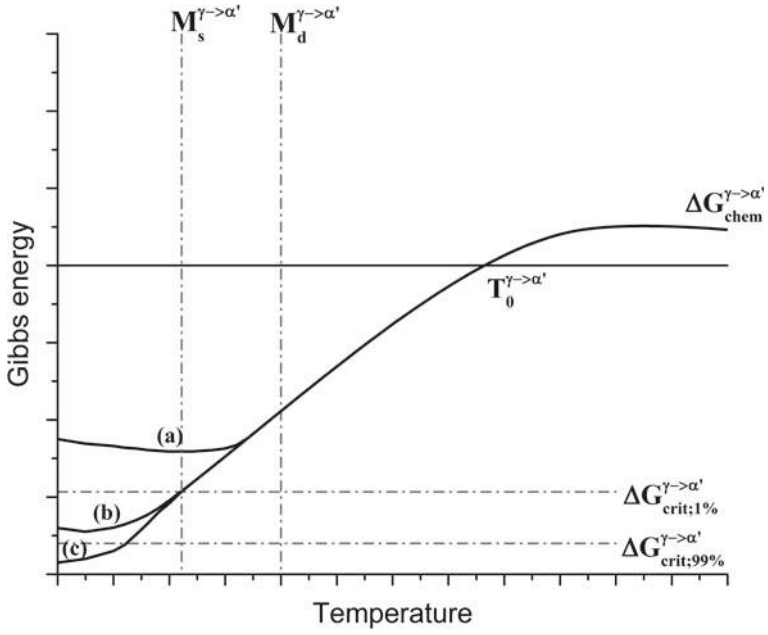

Fig. 20.3 Schematic representation of the temperature dependence of the chemical driving force for α'-martensite formation ($\Delta G_{chem}^{\gamma\rightarrow\alpha'}$), showing cases associated with the absence of spontaneous martensite (**a**), partial formation of spontaneous martensite (**b**), and full transformation to spontaneous martensite (**c**)

(a) describes a metastable austenite without phase transformation. This case arises when the chemical driving force does not reach the critical driving force. Nevertheless, an additional mechanical energy might still enable the deformation-induced martensite formation. In case (b), as-quenched martensite formation occurs. Due to the increasing austenite stability at lower temperatures, caused by magnetic transition of austenite from paramagnetic to antiferromagnetic, the martensite formation might come to a standstill below the Néel temperature. In case (c), the martensitic phase transformation proceeds until completion because the chemical driving force is large enough to supply the critical driving force for the full transformation, namely $\Delta G^{\gamma\rightarrow\alpha'}_{\text{crit;99\%}}$ [11, 22, 28].

The procedure proposed by Patel and Cohen for the calculation of the minimum and maximum mechanical work needed to induce martensite is discussed in detail in the following [29]. When loading metastable austenite, the applied stress leads to unequal resolved shear stresses on glide systems in the austenite, thereby favoring the selective formation of martensite variants [11]. For transformations associated with pure shear, the habit plane for the transformation will make an angle of 45° with respect to the external loading direction. However, due to the dilatational component associated with martensitic transformation [29, 30], the habit plane for the deformation-induced martensite formation does not necessarily make an angle of 45° with the tensile loading direction [23].

The mechanical work W_{mech} which can trigger the martensite formation during the tensile test depends on the molar volume (V_{m}) of the deformed tensile test specimen, the orientation of the habit plane, and the magnitude of the external stress (σ_a). According to (20.3), the mechanical work consists of two terms: the first term is the shear stress (τ_r) responsible for the shear strain (γ_0) parallel to the habit plane and the second term is the normal stress (σ_{N}) responsible for the volume expansion normal to the habit plane (ε_0) [23]. Experimental values of the investigated steels are shown in (Table 20.2).

$$W_{\text{mech}} = V_{\text{m}}\left[\tau_r * \gamma_0 + \sigma_{\text{N}} * \epsilon_0\right] \tag{20.3}$$

Assuming that the tensile load is applied at an angle (θ) to a potential habit plane normal, the normal and shear components of stress can be deduced from the Mohr's circle construction for tension as shown in Fig. 20.4.

Equation (20.4) can be derived by inserting the stress components from Fig. 20.4 in (20.3).

$$W_{\text{mech}} = V_{\text{m}}\left[\sigma_{a/2} * \gamma_0 \sin(2\theta) + \sigma_{a/2} * \epsilon_0(1 + \cos(2\theta))\right] \tag{20.4}$$

The term W_{min} in Fig. 20.2 can be estimated by inserting the triggering stress for martensite formation at temperatures between M_{s} and M_{d} in (20.4). The summation of this term with the chemical driving force for α'-martensite formation ($\Delta G^{\gamma\rightarrow\alpha'}_{\text{chem}}$) gives an estimate of the critical driving force for martensite formation. The maximum applicable mechanical work contributing to the formation of martensite (W_{max}), on

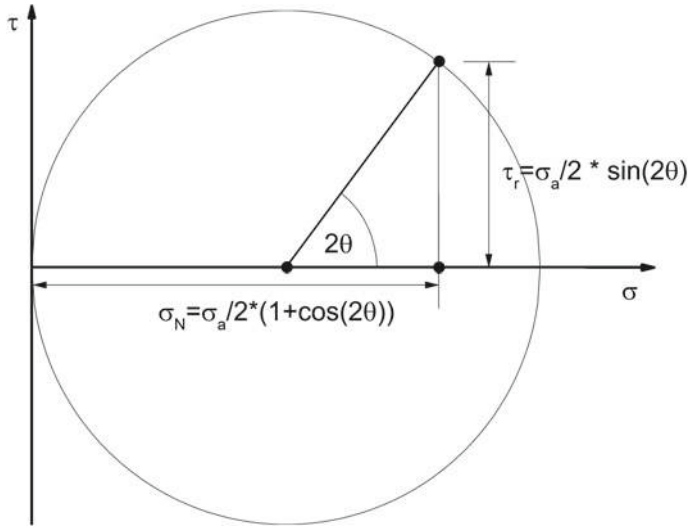

Fig. 20.4 Mohr's circle for tension showing shear (τ_r) and normal (σ_N) components of stress as functions of the applied stress (σ_a) and the angle between the potential habit plane normal and loading direction (θ) [23]

Table 20.2 Lattice parameters of austenite and martensite and the corresponding shear strain (γ_0), volume expansion (ε_0), and the angle θ_{max}

Alloy	a_γ (Å)	$a_{\alpha'}$ (Å)	$c_{\alpha'}$ (Å)	γ_0 (–)	ε_0 (–)	θ_{max} (°)
X5CrNi18-10	3.589	2.873	2.873	0.2260	0.0253	41.81
X3CrMnNi16-7-3	3.596	2.878	2.878	0.2263	0.0230	42.10
X3CrMnNi16-7-6	3.594	2.875	2.875	0.2266	0.0225	42.16
X3CrMnNi16-7-9	3.593	2.873	2.873	0.2318	0.0267	41.72
X15CrNiMnN19-4-3	3.591	2.884	2.858	0.2258	0.0259	41.73

the other hand, can be calculated by inserting the true stress at the onset of necking in (20.4). To calculate the angle θ associated with the maximum value of W_{mech}, the differential of (20.4) with respect to θ must be set to zero. This condition is represented in (20.5) [23].

$$\frac{dW_{mech}}{d\theta} = 0 \Rightarrow \tan 2\theta_{max} = \frac{\gamma_0}{\varepsilon_0} \tag{20.5}$$

The ε_0, γ_0, and θ_{max} values are influenced by the lattice parameters of austenite and martensite, which in turn depend on the chemical composition. To determine these quantities for the investigated steel, the martensite crystallography theory due to Wechsler-Lieberman-Read was used [31–33]. The following equations enable to calculate the shear and dilatational components of the invariant-plane strain based

on the lattice parameters of austenite (a_γ) and martensite (a_α) [31]:

$$\gamma_0 = \left[\left(\frac{2 * a_\alpha^2}{a_\gamma^2} - 1 \right) * \left(1 - \frac{2 * a_\alpha^4}{a_\gamma^4} \right) \right]^{\frac{1}{2}} \tag{20.6}$$

$$\epsilon_0 = \frac{V_\alpha}{V_\gamma} - 1 = \frac{2 * a_\alpha^3}{a_\gamma^3} - 1. \tag{20.7}$$

20.4 Model Development Based on an Austenitic X5CrNi18-10 Steel

Figure 20.5 shows the flow curves (dashed lines) of the X5CrNi18-10 steel (AISI 304) at various temperatures. With decreasing temperature, the flow curves shift to higher stresses. The uniform tensile elongation values, in contrast, pass through a maximum at intermediate tensile testing temperatures. In the temperature range of 140–23 °C, the elongation increases as the temperature decreases. The highest elongation was reached at room temperature and decreased again at lower deformation temperatures. Three solid lines are superimposed on the flow curves in Fig. 20.5. Two of these lines indicate the inflection points on the flow curves, namely where the sign of

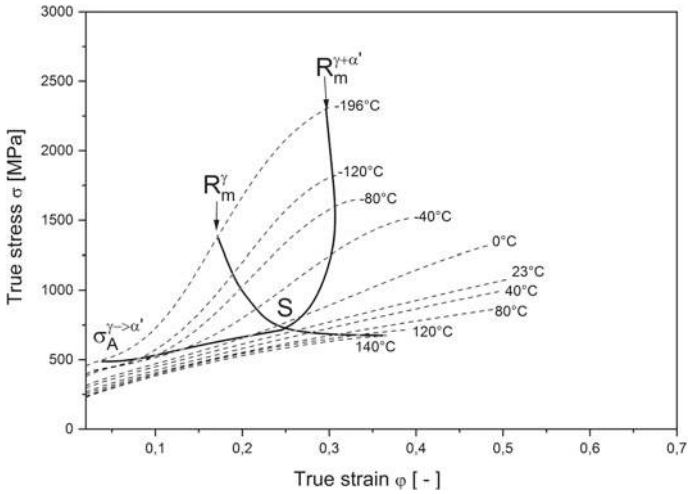

Fig. 20.5 Temperature dependent flow curves for the X5CrNi18-10 steel. Superimposed on the flow curves are the trigger stress $\sigma_A^{\gamma\rightarrow\alpha'}$, the tensile strength of the austenite R_m^{γ} and tensile strength of the steel $R_m^{\gamma+\alpha'}$ with neglected strengthening contributions other than the deformation-induced martensite formation [18]

the second derivative of the flow curves reverses. The inflection points only occur for the stress-strain curves obtained at temperatures below 23 °C. The first inflection point, marked $\sigma_A^{\gamma\rightarrow\alpha'}$ in Fig. 20.5, represents the triggering stress for the deformation-induced martensite formation. According to Weiß et al., the second inflection point, marked R_m^{γ}, corresponds to the tensile strength of the austenite [18, 28]. The first and second inflection points are associated with a minimum and a maximum in the strain-hardening rate, respectively. The third line, marked $R_m^{\gamma+\alpha'}$ in Fig. 20.5, indicates the tensile strength level expected if the strengthening contributions other than the deformation-induced martensite formation are neglected [18, 28].

The point marked with "*S*" in Fig. 20.5 almost lies on the 23 °C curve and may be identified with the approximate stress and strain coordinates of 705 MPa and 0.28, respectively. The point *S* denotes where the first ($\sigma_A^{\gamma\rightarrow\alpha'}$) and second ($R_m^{\gamma}$) inflection points of the flow curve coincide. This means that the triggering stress $\sigma_A^{\gamma\rightarrow\alpha'}$ and the tensile strength R_m^{γ} of the austenite are equal, which defines the $M_{\mathrm{d}}^{\gamma\rightarrow\alpha'}$ temperature. The formation of martensite primarily occurs via $\gamma \rightarrow \varepsilon \rightarrow \alpha'$ formation. However, the martensitic phase transformation via $\gamma \rightarrow \alpha'$ martensite formation is possible too [18, 28].

Figure 20.6 shows the measured fractions of ε- and α'-martensite in tensile specimens tested at various temperatures until the onset of necking. As the testing temperature decreased from 140 to 40 °C, the ε-martensite fraction increased continuously to a maximum level of approximately 17%. At temperatures between 40 and 23 °C, the fraction of ε-martensite decreased, reaching zero at room temperature. In the

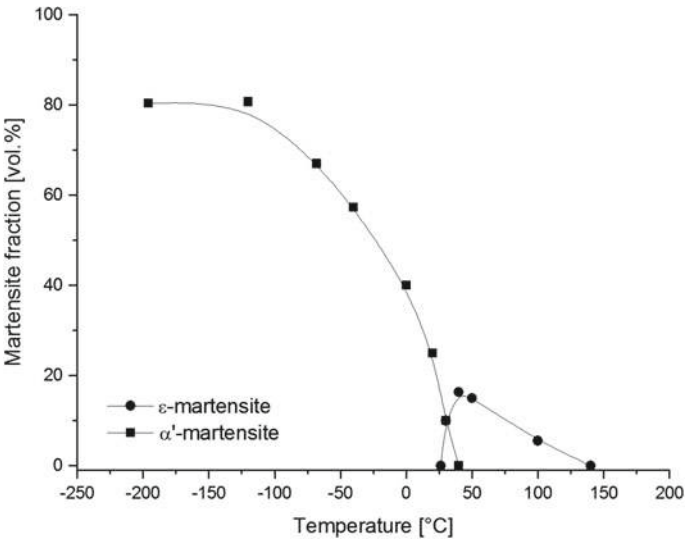

Fig. 20.6 Temperature dependence of ε- and α'-martensite contents in tensile specimens strained in uniaxial tension until the onset of necking [18]

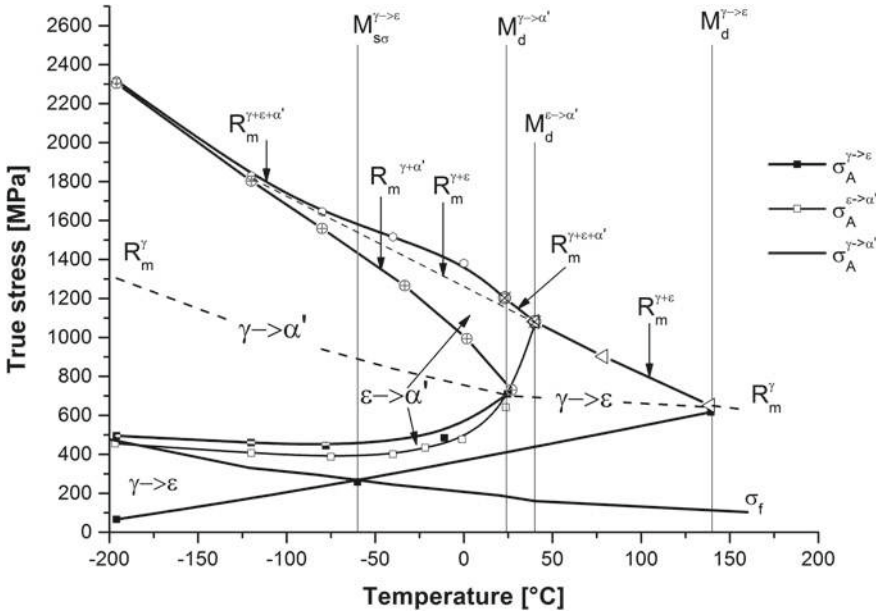

Fig. 20.7 Stress-temperature-transformation diagram (STT) for the X5CrNi18 10 steel [18]

temperature range between 40 °C and room temperature, the decrease in the fraction of ε-martensite was almost equal to the increase in the α'-martensite fraction [18, 28].

Figure 20.7 shows the Stress-Temperature-Transformation (STT) diagram for the X5CrNi18-10 steel. The yield stress σ_f, the triggering stresses $\sigma_A^{\gamma\to\varepsilon}$, $\sigma_A^{\varepsilon\to\alpha'}$ and $\sigma_A^{\gamma\to\alpha'}$ and on the other hand the corresponding tensile strengths $R_m^{\gamma+\varepsilon}$, $R_m^{\gamma+\varepsilon+\alpha'}$ and $R_m^{\gamma+\alpha'}$ are shown in the diagram. The triggering stress $\sigma_A^{\gamma\to\alpha'}$ was estimated from the first inflection point of the flow curve. The triggering stresses for the $\gamma \to \epsilon$ and $\varepsilon \to \alpha'$ martensitic transformations were obtained experimentally through microstructural analyses of interrupted tensile test specimens. The tensile strength of austenite R_m^{γ} was estimated by the extrapolation of the tensile strength values above $M_{\mathrm{d}}^{\gamma\to\varepsilon}$ to lower temperatures. The tensile strength $R_m^{\gamma+\varepsilon}$ below $M_{\mathrm{d}}^{\varepsilon\to\alpha'}$ temperature is a linear extrapolation of the course between $M_{\mathrm{d}}^{\varepsilon\to\alpha'}$ and $M_{\mathrm{d}}^{\gamma\to\varepsilon}$ temperature. The intersection of triggering stress with specific tensile strengths $\left(R_m^{\gamma+\varepsilon};\, R_m^{\gamma+\varepsilon+\alpha'};\, R_m^{\gamma+\alpha'}\right)$ for a given strain-induced transformation defines the $\mathrm{M_d}$ temperature corresponding to that transformation, shown in Fig. 20.7. The $M_{\mathrm{d}}^{\gamma\to\varepsilon}$, $M_{\mathrm{d}}^{\varepsilon\to\alpha'}$ and $M_{\mathrm{d}}^{\gamma\to\alpha'}$ temperatures are approximately 413 K (140 °C), 313 K (40 °C), and 296 K (23 °C), respectively. The $M_{s\sigma}^{\gamma\to\varepsilon}$ temperature is located at the intersection point of yield stress σ_f and the triggering stress $\sigma_A^{\gamma\to\varepsilon}$ near 213 K (−60 °C). The stress region, bounded by the triggering stress and the corresponding tensile strength for each martensitic transformation, marks the stress interval in which the relevant transformation occurs ($\gamma \to \varepsilon/\varepsilon \to \alpha'/\gamma \to \alpha'$). The wider the transformation interval, the

higher are the formed fractions of ε und α' martensite and, hence, the tensile strength of the steel. Below $M_{\mathrm{d}}^{\gamma\rightarrow\alpha'}$ temperature, the ε-martensite only formed before the α'-martensite formation was triggered. As soon as the triggering stress $\sigma_A^{\gamma\rightarrow\alpha'}$ was reached, ε-martensite was replaced by the α'-martensite [18, 28].

The strength contributions due to the induced deformation mechanisms in the austenite could be derived from the STT diagram in the following form. The summation of all strength contributions yields the true stress corresponding to the tensile strength R_m^{steel} of the steel. At temperatures above the $M_{\mathrm{d}}^{\gamma\rightarrow\varepsilon}$ temperature, the strain hardening of austenite occurred only via dislocation glide and increase of dislocation density. Under these circumstances, the tensile strength R_m^{steel} is equal to the tensile strength R_m^{γ} of austenite, as shown in (20.8) [18, 28].

$$R_m^{\mathrm{steel}} = R_m^{\gamma} \tag{20.8}$$

In the temperature range between the $M_{\mathrm{d}}^{\gamma\rightarrow\varepsilon}$ and $M_{\mathrm{d}}^{\varepsilon\rightarrow\alpha'}$ temperatures, two deformation processes are superimposed in the austenite. These were the strain-induced ε-martensite formation and dislocation glide. As (20.9) indicates, the tensile strength of the steel in this temperature range is the sum of the tensile strength of austenite and the strengthening due to the $\gamma \rightarrow \varepsilon$ transformation $\Delta\sigma^{\gamma\rightarrow\varepsilon}$ [18, 28].

$$R_m^{\mathrm{steel}} = R_m^{\gamma+\varepsilon} = R_m^{\gamma} + \Delta\sigma^{\gamma\rightarrow\varepsilon} \tag{20.9}$$

In the temperature range between the $M_{\mathrm{d}}^{\varepsilon\rightarrow\alpha'}$ and $M_{\mathrm{d}}^{\gamma\rightarrow\alpha'}$ temperatures, the dislocation glide, the strain-induced ε martensite formation, and the strain-induced $\varepsilon \rightarrow \alpha'$ martensite formation processes are superimposed. The tensile strength R_m^{steel} can be calculated in this temperature range by using (20.10) [18, 28].

$$R_m^{\mathrm{steel}} = R_m^{\gamma+\varepsilon+\alpha'} = R_m^{\gamma} + \Delta\sigma^{\gamma\rightarrow\varepsilon} + \Delta\sigma^{\varepsilon\rightarrow\alpha'} \tag{20.10}$$

Below $M_{\mathrm{d}}^{\gamma\rightarrow\alpha'}$ temperature, the strain-induced $\gamma \rightarrow \alpha'$ martensite is increasing the tensile strength R_m^{steel} of the steel by an amount equal to $\Delta\sigma^{\gamma\rightarrow\alpha'}$, shown in (20.11) [18, 28].

$$R_m^{\mathrm{steel}} = R_m^{\gamma+\varepsilon+\alpha'} = R_m^{\gamma} + \Delta\sigma^{\gamma\rightarrow\varepsilon} + \Delta\sigma^{\varepsilon\rightarrow\alpha'} + \Delta\sigma^{\gamma\rightarrow\alpha'} \tag{20.11}$$

The behavior described in Fig. 20.7 and (20.8)–(20.11) arises from the interplay between the strain-induced ε or α' martensite formation and the dislocation glide in the austenite. Referring to the STT diagram, the stress increments achieved by various deformation-induced mechanisms can be obtained according to Weiß et al. [18, 28] by a procedure involving mirroring of the triggering stress values with respect to the tensile strength of the austenite (R_m^{γ}).

The strain contributions due to deformation-induced mechanisms can be summarized using the so-called deformation-temperature-transformation (DTT) diagrams.

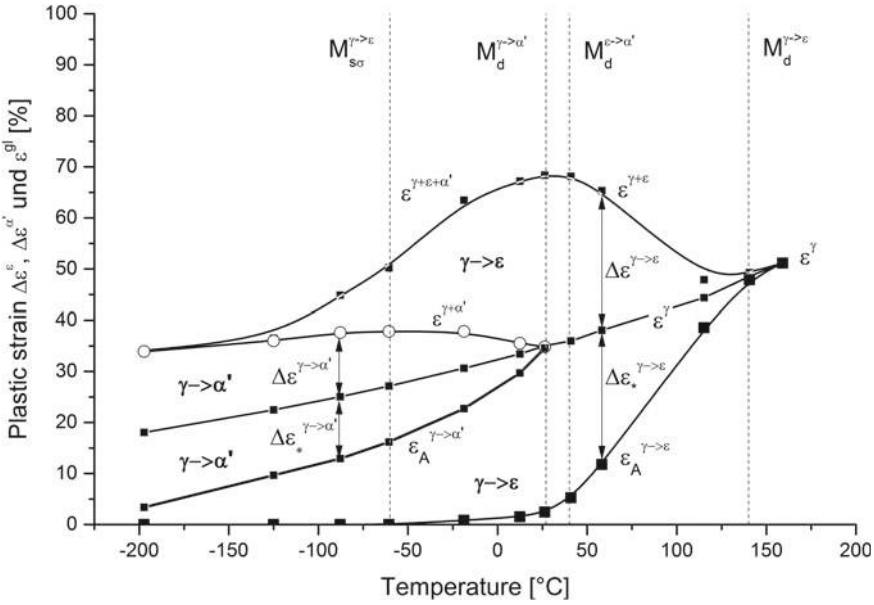

Fig. 20.8 Deformation-temperature-transformation diagram (DTT) of the X5CrNi18-10 steel [18]

Figure 20.8 shows the DTT diagram for the X5CrNi18-10 steel where the plastic elongations associated with the strain-induced $\gamma \rightarrow \varepsilon \rightarrow \alpha'$ and $\gamma \rightarrow \alpha'$ deformation processes are indicated [18, 28].

The uniform elongation of the steel (uppermost curve in Fig. 20.8), uniform elongation of the austenite ε^{γ}, and the elongations $\varepsilon_A^{\gamma\rightarrow\varepsilon}$ and $\varepsilon_A^{\gamma\rightarrow\alpha'}$ corresponding to the tensile trigger stress values $\sigma_A^{\gamma\rightarrow\varepsilon}$ and $\sigma_A^{\gamma\rightarrow\alpha'}$, respectively, are shown in Fig. 20.8. In addition, the plastic elongations $\Delta\varepsilon^{\gamma\rightarrow\varepsilon}$ and $\Delta\varepsilon^{\gamma\rightarrow\alpha'}$ contributed by the strain-induced ε-martensite and α'-martensite formation, respectively, as well as the values $\Delta\varepsilon_*^{\gamma\rightarrow\varepsilon}$ and $\Delta\varepsilon_*^{\gamma\rightarrow\alpha'}$ contributed by the glide in the austenite, are shown in Fig. 20.8. It is also shown that the elongation values $\Delta\varepsilon^{\gamma\rightarrow\varepsilon}$ and $\varepsilon_*^{\gamma\rightarrow\varepsilon}$ as well as $\Delta\varepsilon^{\gamma\rightarrow\alpha'}$ and $\Delta\varepsilon_*^{\gamma\rightarrow\alpha'}$ are equal [28]. The measured plastic elongations are a consequence of deformation-induced martensite formation as well as the plastic elongation pertaining to the induced glide processes in the austenite in the transformation range. Equations (20.12)–(20.14) describe the plastic elongation behavior of the X5CrNi18 10 steel in various temperature intervals with different deformation mechanisms. Equation (20.12) applies above the $M_{\mathrm{d}}^{\gamma\rightarrow\varepsilon}$ temperature, in which the uniform elongation of the steel ($\varepsilon^{\mathrm{steel}}$) is equal to the uniform elongation of the austenite (ε^{γ}) [18, 28].

$$\varepsilon^{\mathrm{steel}} = \varepsilon^{\gamma} \tag{20.12}$$

Between $M_{\mathrm{d}}^{\gamma\rightarrow\varepsilon}$ and $M_{\mathrm{d}}^{\gamma\rightarrow\alpha'}$ temperatures (20.13) applies.

$$\varepsilon^{\text{steel}} = \varepsilon^{\gamma+\varepsilon} = \varepsilon^{\gamma} + \Delta\varepsilon^{\gamma\rightarrow\varepsilon} \tag{20.13}$$

Below the $M_{\text{d}}^{\gamma\rightarrow\alpha'}$ temperature (20.14) applies.

$$\varepsilon^{\text{steel}} = \varepsilon^{\gamma+\varepsilon+\alpha'} = \varepsilon^{\gamma} + \Delta\varepsilon^{\gamma\rightarrow\varepsilon} + \Delta\varepsilon^{\gamma\rightarrow\alpha'} \tag{20.14}$$

At the $M_{\text{d}}^{\gamma\rightarrow\varepsilon}$ temperature, the plastic elongation value $\varepsilon_A^{\gamma\rightarrow\varepsilon}$ coincides with the uniform elongation of the austenite (ε^{γ}). Below that temperature, the anomalous temperature dependence of the uniform elongation ($\varepsilon^{\text{steel}}$), associated with noticeable ductility enhancement at lower temperatures, begins. At the $M_{\text{d}}^{\gamma\rightarrow\alpha'}$ temperature, the uniform elongation of the steel reaches a maximum. Below the $M_{s\sigma}^{\gamma\rightarrow\varepsilon}$ temperature, the stress-induced ε martensite formation begins, which does not lead to a plastic elongation. In the $\gamma \rightarrow \varepsilon \rightarrow \alpha'$ transformation range, the plastic elongation $\Delta\varepsilon^{\gamma\rightarrow\varepsilon}$ contributed by the strain-induced ε-martensite formation equaled the plastic elongation value $\Delta\varepsilon_*^{\gamma\rightarrow\varepsilon}$ contributed by the glide in the austenite. The X5CrNi18-10 steel serves as an example for a method to describe the shear and glide processes occurring in the austenite. It is assumed that no glide processes were activated in the strain-induced ε and α' martensite phases. Strength and ductility contributions by the induced glide processes in the martensitic phases must be taken into account when spontaneous ε- or α'-martensite, which raise the yield strength of the steel, are present in the starting microstructure [18, 28].

20.5 Effect of Nickel on the Deformation Mechanisms of Metastable CrMnNi Cast Steels

To describe the influence of chemical composition on the deformation mechanisms, the X3CrMnNi16-7-3, X3CrMnNi16-7-6 and X3CrMnNi16-7-9 cast steels with primarily austenitic microstructures have been developed [5, 34]. The true-stress versus true-strain curves of the investigated steels are shown in Fig. 20.9. These flow curves, obtained at various temperatures, are the basis for the development of STT and DTT diagrams [19]. The yield strength, tensile strength, and uniform elongation can be determined directly from the flow curves. To determine the triggering stress ($\sigma_A^{\gamma\rightarrow\alpha'}$) for the deformation-induced α'-martensite formation, the first derivatives of the flow curves, namely the work hardening rate, has to be calculated. A typical steel with deformation-induced α'-martensite formation shows two inflection points. The first inflection point corresponds to the triggering stress for the austenite to martensite formation. The second inflection point, on the other hand, can be correlated with the maximum of deformation-induced α'-martensite formation rate [21]. In the case of deformation-induced twinning or ε-martensite formation, no inflection point is observed. Therefore, the triggering stress for twinning or ε-martensite formation has to be determined by microstructural investigations after interrupted tensile tests [19].

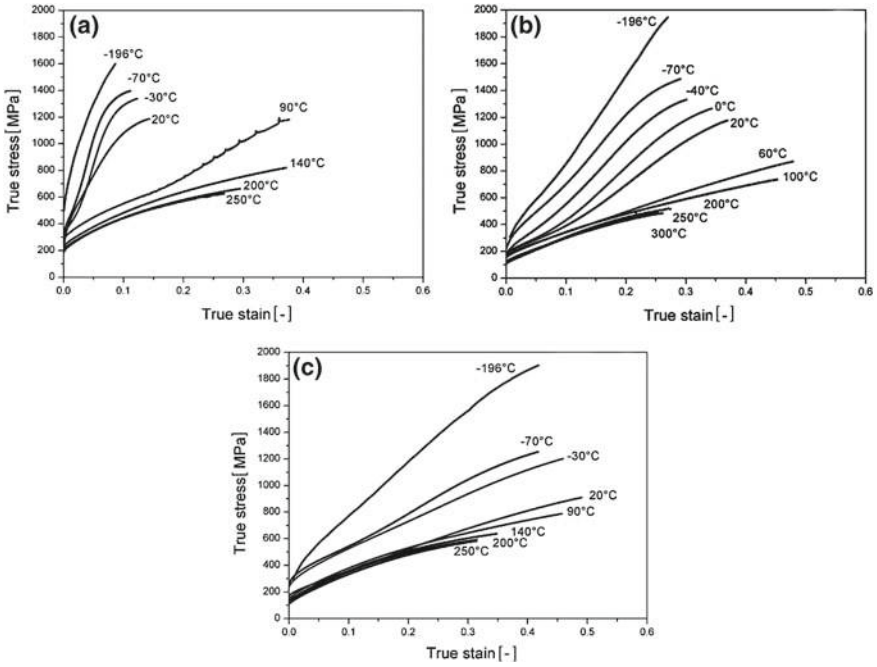

Fig. 20.9 True stress-strain curves for tensile specimens of **a** X3CrMnNi16-7-3, **b** X3CrMnNi16-7-6 and **c** X3CrMnNi16-7-9 steel in the temperature range of −196 to 250 °C [19, 34]

The STT and DTT diagrams for the steel X3CrMnNi16-7-3 are shown in Fig. 20.10. The triggering stresses and the tensile strength of the phases determine the stress-temperature fields for the deformation-induced processes (martensite formation, twinning, dislocations glide, etc.). The location of these fields depends on the chemical composition of the investigated steel [20]. All solid lines in the diagrams are experimentally determined. The dashed lines are predicted or approximated. In contrast to the X3CrMnNi16-7-6 and X3CrMnNi16-7-9 steels, the microstructure of the X3CrMnNi16-7-3 steel prior to tensile tests was not fully austenitic and the low austenite stability, the critical temperatures for deformation-induced twinning $T_{\mathrm{d}}^{\gamma\rightarrow\mathrm{Tw}}$ (300 °C) and deformation-induced α'-martensite formation $M_{\mathrm{d}}^{\gamma+\varepsilon,(\mathrm{Tw})\rightarrow\alpha'}$ (140 °C) were higher compared to the other two steels [5, 20, 34]. According to microstructural investigations, it is assumed that the ε martensite formation occurs in the approximate temperature range 40–300 °C. With increasing temperature and thus increasing stacking fault energy, deformation twinning replaces the ε martensite formation [4]. Due to the low triggering stresses for the strain-induced α'-martensitic transformation at low temperatures, the ε-martensite formation is practically suppressed below room temperature. The maximum true strain of about 0.4 is reached at a temperature of approximately 120 °C. The temperature anomaly of elongation (broad maximum in Fig. 20.11) in the steel X3CrMnNi16-7-3 is mainly caused by the strain-induced ε-TRIP [20]. The elongation contribution caused by the α'-martensite formation is

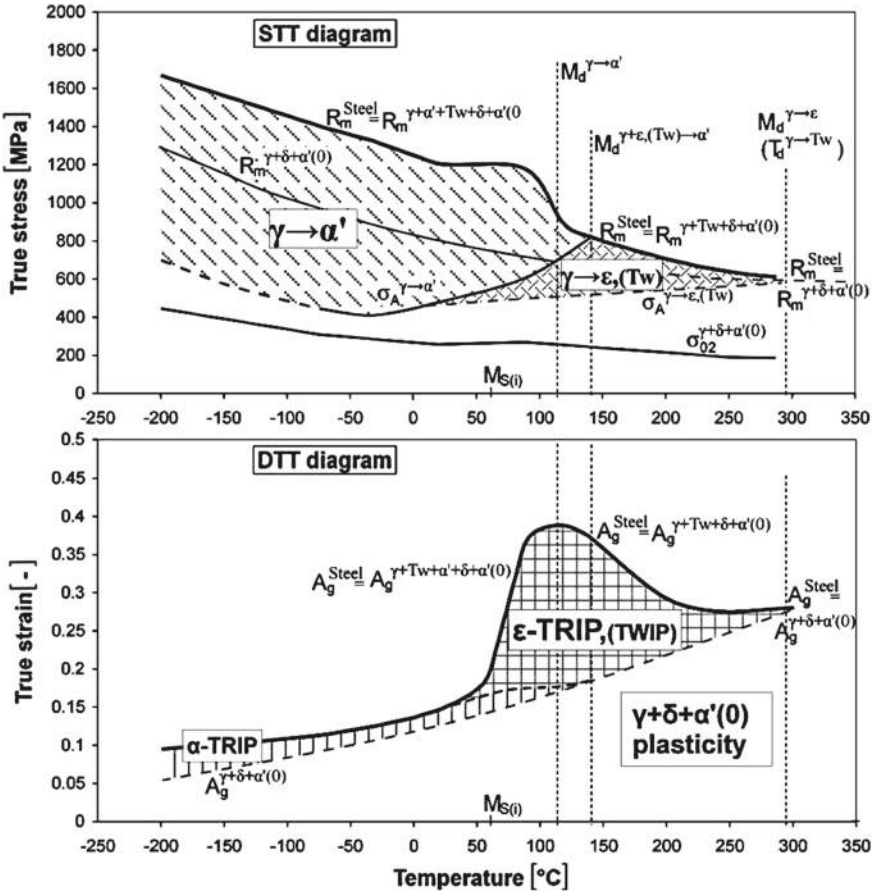

Fig. 20.10 STT and DTT diagrams for the X3CrMnNi16-7-3 steel [19]

negligible, because the α'-martensite after tensile tests is either deformation-induced or formed spontaneously.

Figure 20.11 shows the STT and DTT diagrams for the steel X3CrMnNi16-7-6. Compared to the X3CrMnNi16-7-3 steel, the critical transformation temperatures and the transformation fields are shifted to lower temperatures [35]. The $T_{\mathrm{d}}^{\gamma\rightarrow\mathrm{Tw}}$ temperature and the $M_{\mathrm{d}}^{\gamma+\varepsilon,(\mathrm{Tw})\rightarrow\alpha'}$ temperature are 250 °C and 100 °C, respectively. In the temperature range between 0 and 50 °C, the triggering stress for α'-martensite formation is very low. Therefore, the austenite transforms into martensite practically without twinning or ε-martensite formation. At a deformation temperature of 60 °C, ε-martensite was found in the microstructure [19, 36]. Additionally, the kinetics of the α'-martensite formation is shown in the STT diagram. Therefore, compared to the STT diagram of the X3CrMnNi16-7-3 steel, the STT diagram for the X3CrMnNi16-7-6 steel additionally includes the isolines for α'-martensite fraction as marked in

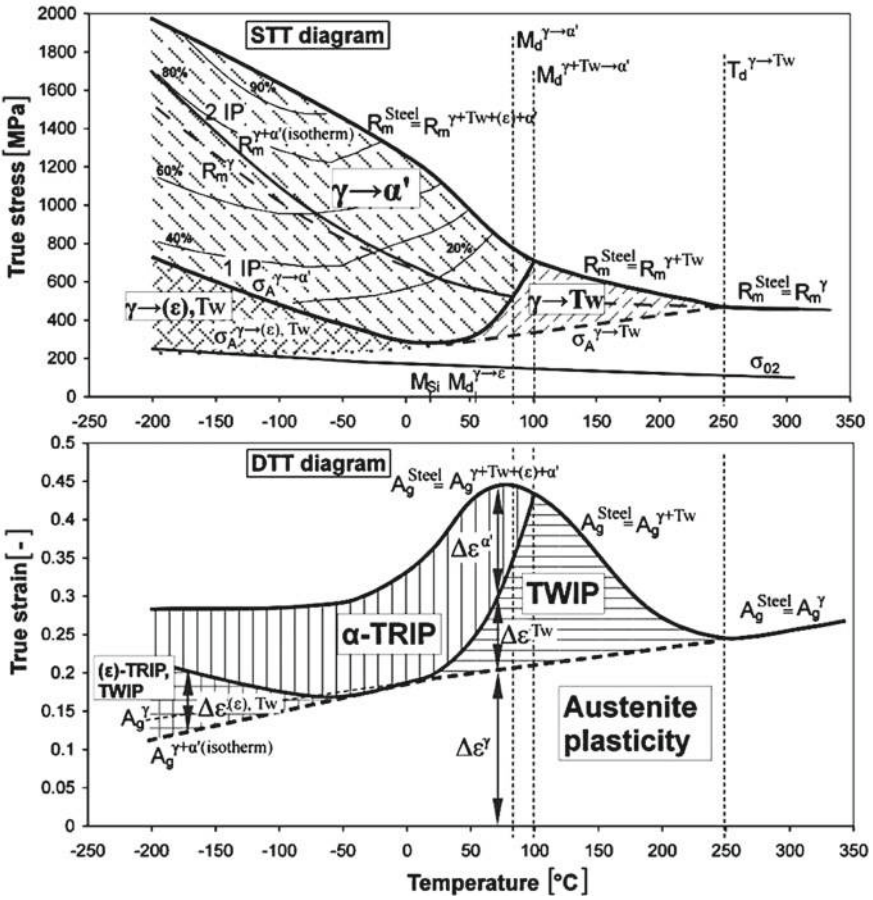

Fig. 20.11 STT and DTT diagrams for the X3CrMnNi16-7-6 steel [19]

the $\gamma \rightarrow \alpha'$ transformation field. Moreover, the X3CrMnNi16-7-6 steel is capable of forming isothermal martensite, which is not taken into account in the STT diagram [20]. Accordingly, the stress values measured at the second inflection point are higher than the R_m^{γ}. This measurable stress $R_m^{\gamma+\alpha'(\text{isotherm})}$ enables an approximation of R_m^{γ}.

The uniform elongation A_g^{Steel} of the X3CrMnNi16-7-6 steel, the uniform elongation of the austenite A_g^{γ} and corresponding deformation mechanisms are shown in the DTT diagram in Fig. 20.11. Additionally, the elongation contributions due to the dislocations glide in the austenite $\Delta\varepsilon^{\gamma}$, deformation twinning $\Delta\varepsilon^{\text{Tw}}$, and strain-induced martensite transformation $\Delta\varepsilon^{\alpha'}$ are included in the DTT diagram. The temperature anomaly starting at 250 °C is a result of the stacking fault formation and twinning, which leads to an enhanced elongation with decreasing temperature [19, 20]. Below the $M_{\text{d}}^{\gamma+\text{Tw}\rightarrow\alpha'}$ temperature (80 °C), the gradual replacement of stacking fault formation and twinning by α'-martensite formation leads a decrease in elongation.

The STT and DTT diagrams for the steel X3CrMnNi16-7-9 are shown in Fig. 20.12. Compared to the steels X3CrMnNi16-7-3 and X3CrMnNi16-7-6, the stability of austenite is increased due to the higher Ni content. Accordingly, the critical temperatures are shifted to lower temperatures. The $T_d^{\gamma \rightarrow Tw}$ temperature is around 200 °C. Austenite, which is deformed by twinning, transforms below $M_d^{\gamma+Tw \rightarrow \alpha'}$ (50 °C) into martensite. In the temperature range between −50 and −70 °C, the triggering stress for α'-martensite formation is very low, and austenite transforms directly into martensite almost without twinning. The maximum true strain of about 0.5 is reached at a temperature of 30 °C. A superposition of three deformation mechanisms—glide deformation of the austenite, TWIP effect, and TRIP effect—takes place at this temperature and causes the highest elongation.

The various austenite stabilities of the dendritic cast structure caused by the segregation of the alloying elements Cr, Mn, Ni during solidification of the austenitic

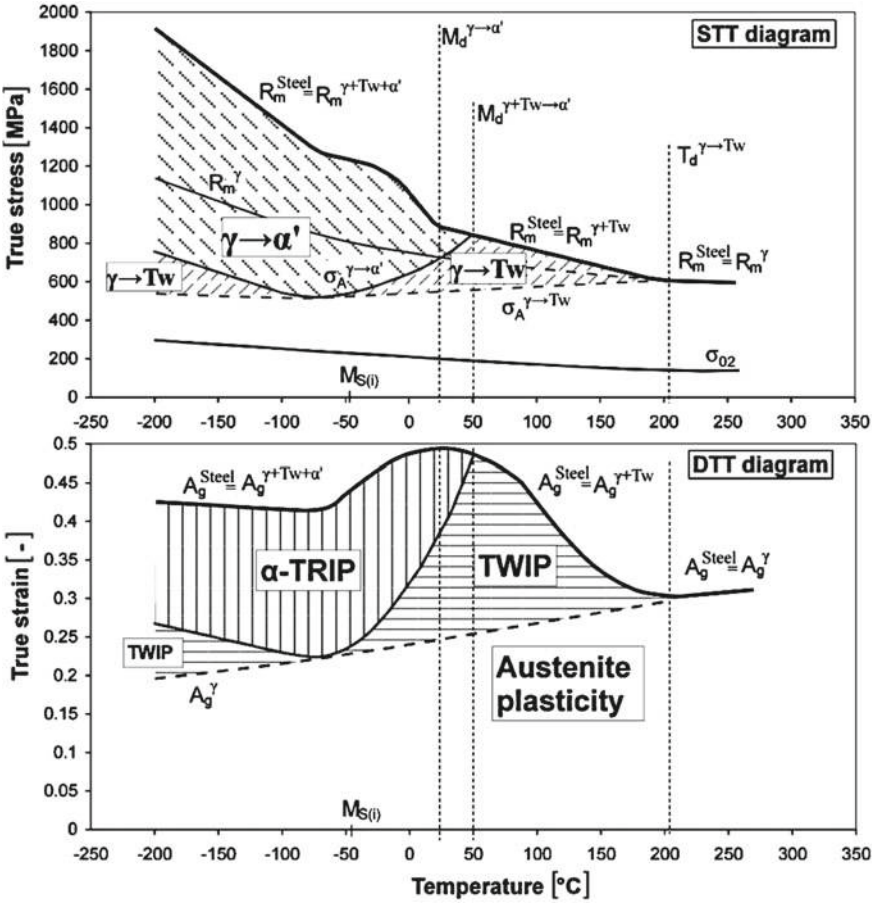

Fig. 20.12 STT and DTT diagrams for the X3CrMnNi 16-7-9 steel [19]

steels X3CrMnNi 16-7-3/6/9 leads to a shift of critical temperatures. Accordingly, the center of dendrites are more metastable than interdendritic regions of austenite.

For further information the reader is revered to read the publication of Martin et al. [37] and Mola et al. [10].

20.6 Thermodynamic-Mechanical Modeling Based on Austenitic CrMnNi–C–N Cast Steel

Figure 20.13 shows the true stress-strain curves for the interstitially-alloyed X15CrNiMnN19-4-3 cast steel deformed until fracture at temperatures between −80 and 400 °C. Carbon and nitrogen were alloyed to the steel to increase the strength by solid solution solidification. The highest elongation of 53% was reached at 60 °C, which is almost equal to the M_d-temperature (70 °C). The formation of α'-martensite at lower temperatures resulted in a pronounced strengthening and a steady decrease in elongation. Reduction of tensile elongation at temperatures below the M_d temperature is a common observation in austenitic stainless steels, including the steels discussed above [22]. The noticeable work hardening at −80 °C resulted in the highest (engineering) tensile strength of 1500 MPa, which correlates to a true tensile strength of 2000 MPa.

The phase fractions of martensite and austenite after tensile deformation until fracture at different temperatures is shown in Fig. 20.14. The steel does not form as-quenched martensite at temperatures as low as −196 °C. Therefore, the martensite contents in Fig. 20.14 represent the deformation-induced martensite only. The highest martensite content of about 81 vol% was formed during deformation at −80 °C.

To determine the deformation mechanisms activated during tensile tests, SEM investigations were carried out on tensile specimens deformed until fracture at −80, 70 and 200 °C (Fig. 20.15). The tensile direction is horizontal aligned to the plane of view. ECCI image of Fig. 20.15a shows the presence of various operating

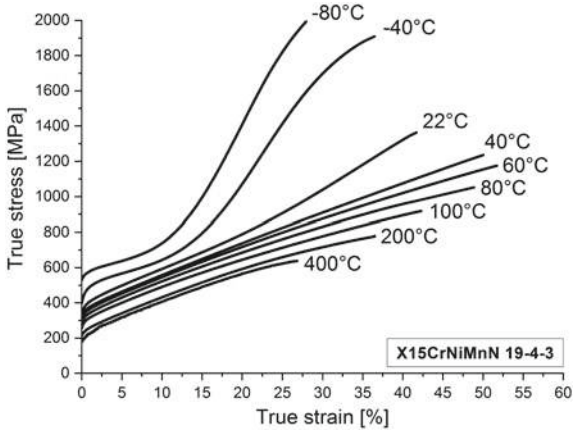

Fig. 20.13 True stress-strain curves of tensile specimens of the X15CrNiMnN19-4-3 cast steel in the temperature range of −80 to 400 °C

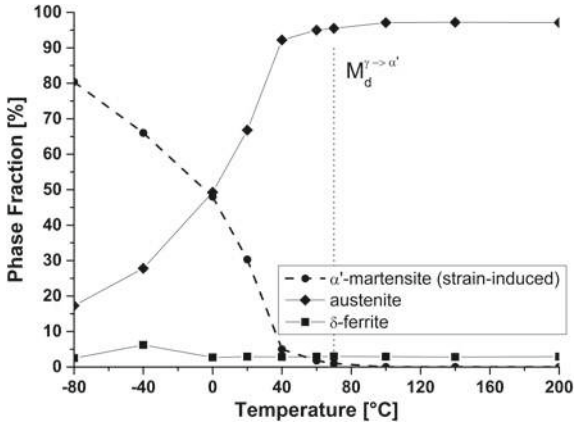

Fig. 20.14 Phase fractions in the microstructure of tensile specimens of the X15CrNiMnN19-4-3 steel tested at various temperatures

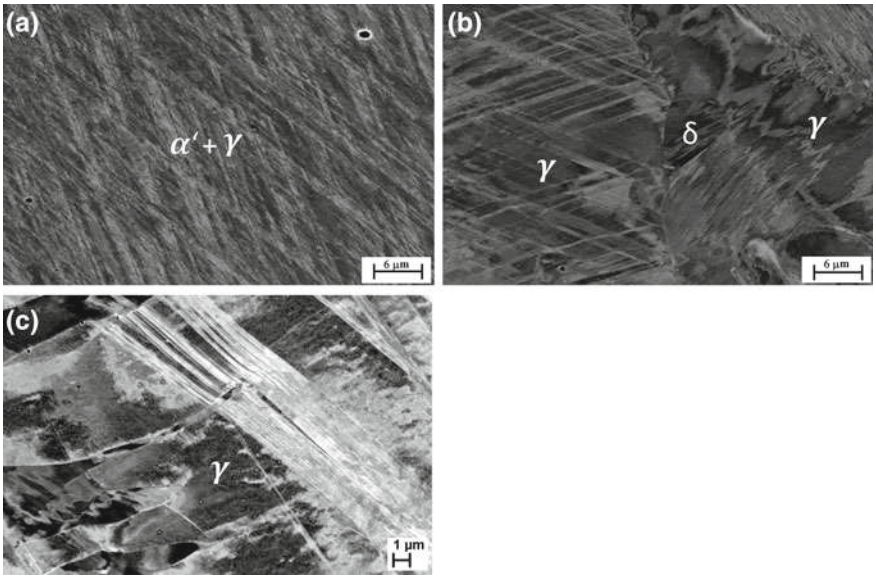

Fig. 20.15 Microstructures obtained after tensile deformation at different temperatures: ECCI micrographs of specimens deformed at −80 °C (**a**), 70 °C (**b**) and 200 °C (**c**) of the X15CrNiMnN19-4-3 steel

straight deformation bands with α'-martensite in the microstructure of the specimen deformed at −80 °C. This indicates the dominance of planar glide due to the high activity of Shockley partial dislocations at −80 °C [9]. According to the MSAT measurement results (Fig. 20.15) a large volume fraction of austenite transformed to

α'-martensite. The ECCI image of the specimen tensile tested at 70 °C (Fig. 20.15b) shows two austenite grains with different microstructural characteristics. Whereas the microstructure of the austenite grain on the left resembles the microstructure shown in Fig. 20.15a, diffuse contrast changes in the austenite grain to the right imply the dominance of wavy glide [8, 38]. Abrupt transition in the glide mode across a grain boundary is more consistent with the differences in the crystallographic orientation of the neighboring grains than with the possible segregation of alloying elements in the cast steel. After all, the forces exerted on the leading and trailing partial dislocations of the primary slip system depend on the crystal orientation [9, 39]. The ECCI image of the specimen deformed at 200 °C in Fig. 20.15c on the other hand shows only a diffuse contrast changes in the austenite grain what a dominance of wavy glide means. This sequence has been similarly observed in the X3CrMnNi16-7-6 steel [4, 5, 40, 41].

To describe the occurring deformation mechanisms during tensile loading, interrupted tensile tests with subsequent microstructure investigations have been performed. ECCI image and EBSD phase map of a tensile sample deformed at 0 °C to 800 MPa are shown in Fig. 20.16. It is well established that the type of deformation-induced processes in austenitic steels depends on the stacking fault energy; as the stacking fault energy decreases, the deformation mechanism changes from perfect dislocation glide to deformation twinning, ε-martensite formation, and α'-martensite formation in that sequence [42]. Due to the coexistence of a small ε-martensite fraction in the deformation bands, the martensitic transformation according to the sequence $\gamma \rightarrow \varepsilon \rightarrow \alpha'$ (Fig. 20.16b) is very likely. The mechanism of formation of deformation-induced twins and ε-martensite is very similar and only differs in the stacking sequence of $\{111\}\gamma$ close-packed planes; thus stacking faults on successive $\{111\}\gamma$ planes generate deformation twins, whereas their overlap on every second $\{111\}\gamma$ plane results in the formation of ε-martensite [4]. Accordingly, these two byproducts of stacking faults have been observed to coexist in the microstructure of deformed austenitic steels [43].

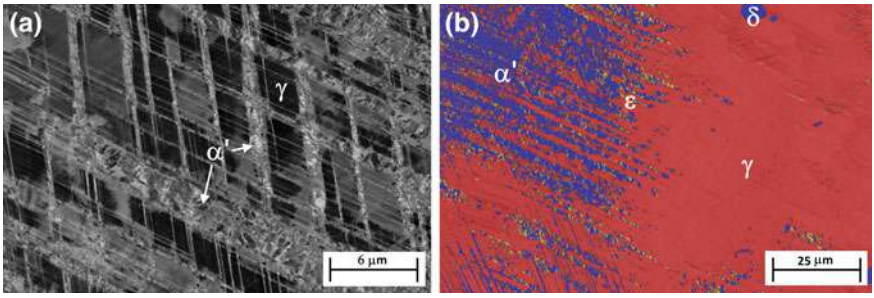

Fig. 20.16 Microstructures obtained after tensile testing at different temperatures: ECCI image and EBSD phase map of a specimen deformed at 0 °C to 800 MPa. In the EBSD phase map, red, yellow, and blue denote phases with fcc, hcp, and bcc crystal structures, respectively

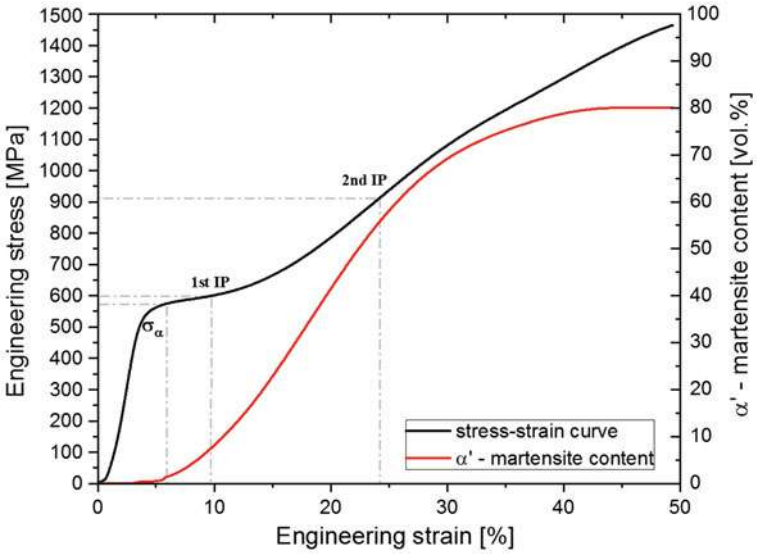

Fig. 20.17 Evolution of deformation-induced α'-martensite fraction during tensile deformation at −80 °C of the X15CrNiMnN19-4-3 steel superimposed on the stress-strain curve

In order to correlate the stress-strain curve with the deformation-induced α'-martensite fraction, the evolution of martensite fraction during tensile test at −80 °C, obtained from in situ magnetic measurements, is superimposed on the stress-strain curve (Fig. 20.17). The evolution of α'-martensite fraction with strain resembles the available literature data on the kinetics of deformation-induced martensite formation in metastable austenitic alloys. The increase in the work hardening rate caused by the deformation-induced formation of α'-martensite is known to cause a first inflection point in the stress-strain curve of metastable austenitic steels [36]. Taking the stress at which almost 1 vol% α'-martensite has formed by deformation as the triggering stress for the deformation-induced α'-martensite formation (σ_A), it does not match the first inflection point (IP) of the stress-strain curve. As marked in Fig. 20.17, the first inflection point during tensile deformation at −40 °C occurs after the formation of almost 3–5 vol% martensite in the microstructure. In other words, the first inflection point gives a slightly overestimated approximation of the triggering stress. Between the first and second inflection points, the martensite formation rate remains almost constant [21].

The STT and DTT diagrams of the X15CrNiMnN19-4-3 are shown in Fig. 20.18. The area between the triggering stress and the tensile strength, marked $\gamma \rightarrow \alpha'$ in Fig. 20.18, denotes the stress-temperature field favorable for the deformation-induced martensitic transformation. In different temperature ranges, different deformation mechanisms are activated. The dominant mechanisms are deformation-induced martensite formation below M_d, deformation twinning between M_d and T_d, and glide of perfect dislocations above T_d temperature. The temperature range where

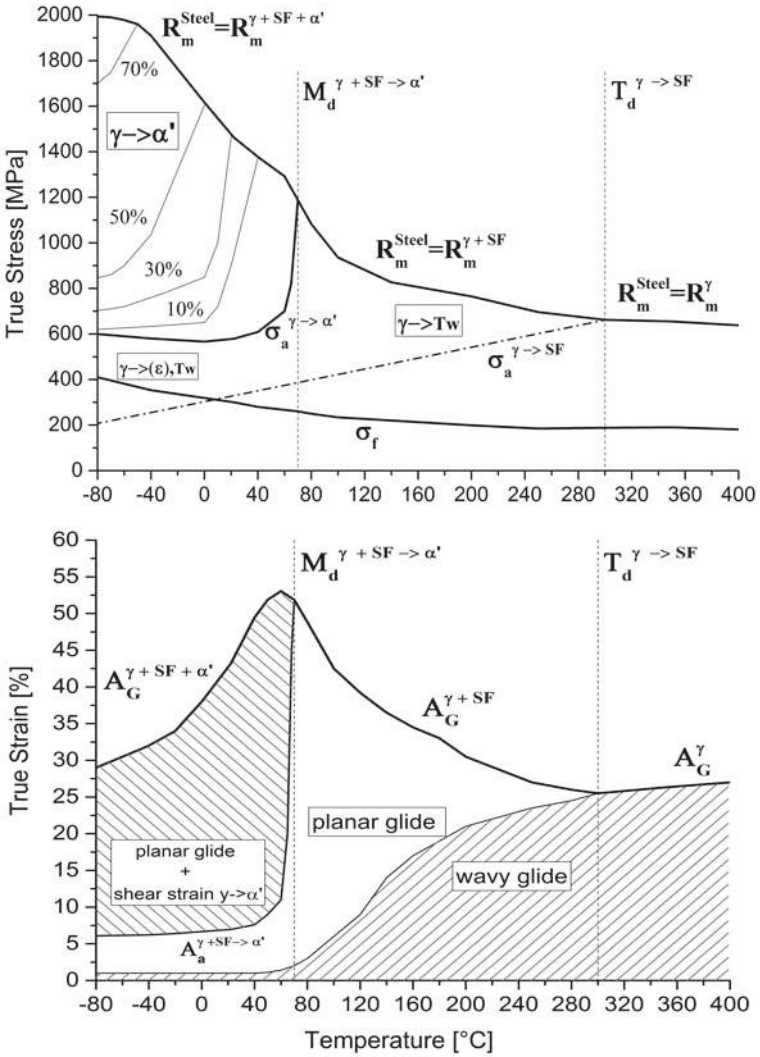

Fig. 20.18 STT and DTT diagrams for the X15CrNiMnN19-4-3 steel

these processes occur depends on the chemical composition. Deformation-induced martensite formation is absent at temperatures above approximately 70 °C, leading to a weak temperature dependence of tensile strength. Upon deformation-induced martensite formation at lower temperatures, the tensile strength increases at a much faster rate. The martensite tends to form within the slip bands in the austenite, thereby restricting dislocations glide within the existing bands. As a result, additional slip bands must be activated to sustain plastic deformation. This explains the high rate

of strain hardening. In the temperature range between 70 and −80 °C, the triggering stress for deformation-induced martensite was determined by in situ magnetic measurements to be in the range 600–1180 MPa.

The DTT diagram enables the separation of strain contributions owing to the glide of dislocations in the austenite as well as those due to the deformation-induced twinning and martensitic transformation. The summation of these strain contributions yields the experimental elongation (A_G^{Steel}) of the steel, which reaches a maximum at 53% in the studied temperature range of −80 to 400 °C. Since the strain contributions of twinning, ε-martensite formation and dislocation glide are difficult to separate, the DTT diagram in Fig. 20.18 shows only the summation of these contributions.

Due to the high amount of interstitial elements, the X15CrNiMnN19-4-3 has a higher yield strength than the X3CrMnNi16-7-3/6/9 steels at equal deformation temperatures. Although the martensite content of the X15CrNiMnN19-4-3 at room temperature is significantly lower (30.3 vol%) than the martensite content of the X3CrMnNi16-7-3 (82 vol%), is the yield strength (342–298 MPa) and the ultimate tensile strength (1663–1198 MPa) is higher. The M_d temperature of the X15CrNiMnN19-4-3 steel (70 °C) is located between the X3CrMnNi16-7-6 (100 °C) and X3CrMnNi16-7-9 (50 °C).

In Fig. 20.19, the Gibbs energy changes for the martensite formation based on the thermodynamic database are compared with the values calculated using the procedure explained in the following and discussed in more detail by Hauser et al. [22]. Whereas the dash-dotted line predicts a continuous increase in the chemical driving force at lower temperatures (down to −196 °C), the chemical driving force

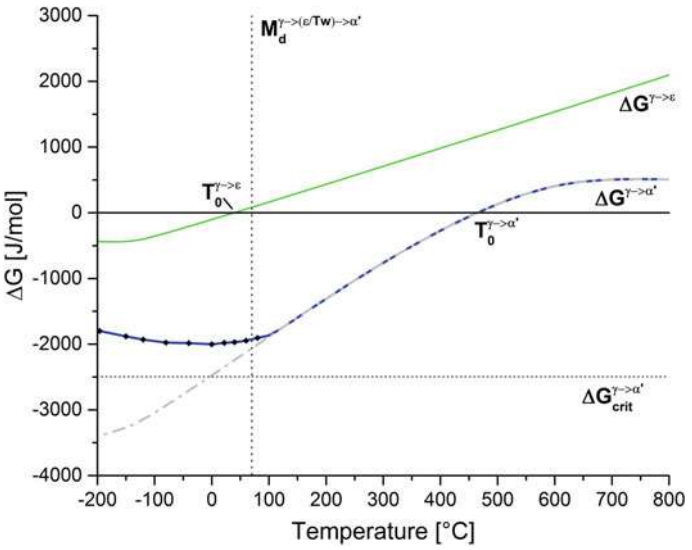

Fig. 20.19 Gibbs energy changes for $\gamma \rightarrow \varepsilon$ and $\gamma \rightarrow \alpha'$ phase transformations calculated by Thermo-Calc and corrected Gibbs energy $\gamma \rightarrow \alpha'$ with the aid of tensile tests with in situ magnetic measurements for the X15CrNiMnN19-4-3 steel [22]

based on the revised values remains almost constant below −80 °C. The observed deviation is most likely caused by changes in the mechanical and physical properties of austenite near the Néel temperature. The critical Gibbs free energies for the formation of martensite at different temperatures were determined by the addition of the chemical and mechanical contributions. The chemical term was obtained from thermodynamic calculations. The mechanical term, on the other hand, was obtained by calculating the mechanical energy supplied to tensile specimens up to the onset of martensitic transformation. The critical driving force for the formation of α' (−2496 J/mol) was obtained by determining the mechanical energy necessary to trigger the deformation-induced α'-martensite formation at 0 °C. Driving forces for the formation of α'-martensite at other tensile test temperatures were then obtained by subtracting the mechanical energies applied to trigger the martensitic transformation from the critical driving force. Additionally, the calculated Gibbs free energy for ε-martensite formation is shown in Fig. 20.19. Due to the low critical driving force of ε-martensite, the ε-martensite formation starts immediately below the $T_0^{\gamma\rightarrow\varepsilon}$. Since the α'-martensite is more stable, the $\varepsilon \rightarrow \alpha'$ phase transformation starts at the moment where the critical driving force for α' martensite is reached.

20.7 Conclusions

The focus of the subproject C3 was the thermodynamic-mechanical modeling of metastable high alloy austenitic CrMnNi steels. To achieve this, several steels were investigated in cooperation with different subprojects of the Collaborative Research Center 799. With the aid of thermodynamic data and flow curve analysis, it is possible to describe the mechanical properties based on the deformation mechanisms and phase transformations. The investigated metastable austenitic steels exhibited the transformation induced plasticity (TRIP) and twinning induced plasticity (TWIP) effects.

First, a new method was developed for the quantitative determination of strength and plastic elongation contributions due to deformation-induced processes during uniaxial tensile loading of austenitic steels. The method was demonstrated using a commercial X5CrNi18-10 steel. For this purpose, the dependence of the overlapping deformation processes in the austenite on the temperature and applied tensile stress was studied in the temperature range of −196 to 40 °C. It was shown that every deformation process leads to a strength and plasticity contribution commensurate with its dominance. The sum of all contributions yielded the tensile strength and the uniform elongation of the steels. Stress-temperature-transformation (STT) and deformation-temperature-transformation (DTT) diagrams were constructed with the aid of flow curve analysis and microstructural examinations. Plastic deformation of martensite was excluded in the developed method. Therefore, the method is only valid for metastable austenitic steels whose initial microstructure is free of as-quenched ε- or α'-martensite.

The influence of the chemical composition on the deformation mechanisms of metastable CrMnNi cast steels was investigated using three high alloy steels, namely X3CrMnNi16-7-3, X3CrMnNi16-7-6 and X3CrMnNi16-7-9. The influence of martensite formation on the mechanical properties of the three steels was studied by tensile tests between −196 and 300 °C. With increasing nickel content, the critical temperatures shifted to lower temperatures. For instance, the M_d-temperature decreased from 140 °C at 3% Ni to 50 °C at 9% Ni. Furthermore, the increase in the Ni content was associated with a change in the deformation mechanism at room temperature from a pronounced TRIP effect to a mixture of TRIP and TWIP effects.

A mathematical model was applied to describe the mechanical work due to uniaxial tensile loading. This enabled to determine the critical driving force for the martensitic phase transformation. The deformation-induced formation of α'-martensite was investigated by tensile testing of X15CrNiMnN19-4-3 cast austenitic steel between −80 and 400 °C. The steel did not exhibit spontaneous α'-martensite formation at temperatures as low as −196 °C. The triggering mechanical energies for the deformation-induced α'-martensite formation were calculated after determining the onset of α'-martensite formation by in situ magnetic measurements during tensile tests. The results enabled to calculate modified driving forces for the occurrence of the $\gamma \rightarrow \alpha'$ phase transformation.

Acknowledgements The authors would like to thank Dr. Alexander Kovalev for the research on the 1st generation steels. Sincere thanks are due to the colleagues at the Institute of Iron and Steel Technology (IEST), Institute of Materials Engineering and the Institute of Materials Science (IWW) for their support and assistance on the experiments: Ms. C. Ullrich and Mr. B. Reichel for the SEM, ECCI and XRD measurements; Dr. T. Kreschel und Mr. G. Franke for the heat treatments; Mrs. G. Schubert for the dilatometry experiments and hardness tests; Mr. P. Neuhold for producing the steels; Dr. R. Eckner and Mr. G. Schade for the tensile tests; Mrs. I. Grahl and Mrs. J. Kreschel for the metallographic sample preparation and light optical microscope observations; Mr. M. Block for the machining of specimens; and all the student assistants for the magnetic measurements. The financial support of the Deutsche Forschungsgemeinschaft (DFG, German Research Foundation) in the framework of Collaborative Research Center 799 (Project number 54473466) subproject C3 was gratefully acknowledged. The authors would also like to thank Prof. P. R. Scheller, the previous director of IEST, for his support on preparing the C3 subproject proposal. Special thanks are extended to all the colleagues from SFB 799 for the valuable and fruitful scientific discussions.

References

1. R.G. Stringfellow, D.M. Parks, G.B. Olson, Acta Metall. Mater. **40**, 1703 (1992)
2. F.D. Fischer, G. Reisner, E. Werner, K. Tanaka, G. Cailletaud, T. Antretter, Int. J. Plast **16**, 723 (2000)
3. F. Lecroisey, A. Pineau, Metall. Trans. **3**, 391 (1972)
4. S. Martin, S. Wolf, U. Martin, L. Krüger, D. Rafaja, Metall. Mat. Trans. A **47**, 49 (2014)
5. S. Wolf, S. Martin, L. Krüger, U. Martin, U. Lorenz, Steel Res. Int. **83**, 529 (2012)
6. M. Wendler, B. Reichel, R. Eckner, O. Fabrichnaya, L. Krüger, A. Weiß, J. Mola, Metall. Mater. Trans. A **47**, 139 (2016)
7. J.F. Breedis, Acta Metall. **13**, 239 (1965)

8. M. Pozuelo, J.E. Wittig, J.A. Jiménez, G. Frommeyer, Metall. Mater. Trans. A **40**, 1826 (2009)
9. R. Rahimi, C. Ullrich, V. Klemm, D. Rafaja, B.C. De Cooman, H. Biermann, J. Mola, Mater. Sci. Eng., A **649**, 301 (2016)
10. J. Mola, M. Wendler, A. Weiß, B. Reichel, G. Wolf, B.C. De Cooman, Metall. Mater. Trans. A **46**, 1450 (2015)
11. M. Wendler, C. Ullrich, M. Hauser, L. Krüger, O. Volkova, A. Weiß, J. Mola, Acta Mater. **133**, 346 (2017)
12. F. Abrassart, Metall. Trans. **4**, 2205 (1973)
13. K. Spencer, K.T. Conlon, Y. Bréchet, J.D. Embury, Mater. Sci. Technol. **25**, 18 (2009)
14. S. Martin, S. Wolf, U. Martin, L. Krüger, Solid State Phenom. **172–174**, 172 (2011)
15. M. Cohen, E.S. Machlin, V.G. Paranjpe, Am. Soc. Metals **242** (1950)
16. L. Kaufman, M. Cohen, Prog. Metal Phys. **7**, 165 (1958)
17. G. Ghosh, G.B. Olson, Acta Metall. Mater. **42**, 3361 (1994)
18. A. Weiß, H. Gutte, J. Mola, Metall. Mater. Trans. A **47**, 112 (2016)
19. A. Kovalev, A. Jahn, A. Weiß, S. Wolf, P.R. Scheller, Steel Res. Int. **83**, 576 (2012)
20. A. Kovalev, M. Wendler, A. Jahn, A. Weiß, H. Biermann, Adv. Eng. Mater. **15**, 609 (2013)
21. M. Hauser, M. Wendler, S. Ghosh Chowdhury, A. Weiß, J. Mola, Mater. Sci. Technol. **31**, 1473 (2015)
22. M. Hauser, M. Wendler, O. Fabrichnaya, O. Volkova, J. Mola, Mater. Sci. Eng., A **675**, 415 (2016)
23. M. Hauser, M. Wendler, A. Weiß, O. Volkova, J. Mola, Adv. Eng. Mater. **21**, 1800676 (2019)
24. M. Palumbo, Calphad **32**, 693 (2008)
25. G. Ghosh, G.B. Olson, J. Phase Equilibria **22**, 199 (2001)
26. S.G.T.E. (SGTE), in *Ternary Steel Systems: Phase Diagrams and Phase Transition Data*, ed. by P. Franke, H.J. Seifert (Springer, Berlin, Heidelberg, 2012), pp. 64–64
27. G.B. Olson, M. Cohen, Metall. Trans. A **7**, 1915 (1976)
28. H. Gutte, A. Weiß, *Spannungs- und verformungsinduzierte Martensitbildungen in metastabilen austenitischen CrNi-Stählen, Habilitation* (TU Bergakademie, Freiberg, 2011)
29. J.R. Patel, M. Cohen, Acta Metall. **1**, 531 (1953)
30. H.K.D.H. Bhadeshia, ISIJ Int. **42**, 1059 (2002)
31. H. Schumann, *Kristallgeometrie - Einfürhung in die Theorie der Gittertransformationen metallischer Werkstoffe*, 1st edn. (Deutscher Verlag für Grundstoffindustrie, Leipzig, 1979)
32. H. Ledbetter, M.L. Dunn, Mater. Sci. Eng., A **285**, 180 (2000)
33. H. Arslan, H. Arslan, T. Dogan, Phys. Metals Metall. **114** (2013)
34. A. Jahn, A. Kovalev, A. Weiß, S. Wolf, L. Krüger, P.R. Scheller, Steel Res. Int. **82**, 39 (2011)
35. A. Kovalev, Thermodynamisch-mechanische Modellierung der verformungsinduzierten α'-Martensitbildung in austenitischen Cr-Mn-Ni-Stählen, Dissertation (TU Bergakademie Freiberg, 2016)
36. A. Kovalev, A. Jahn, A. Weiß, S. Wolf, P.R. Scheller, Steel Res. Int. **82**, 1101 (2011)
37. S. Martin, O. Fabrichnaya, D. Rafaja, Mater. Lett. **159**, 484 (2015)
38. R. Rahimi, C. Ullrich, D. Rafaja, H. Biermann, J. Mola, Metall. Mater. Trans. A **47**, 2705 (2016)
39. H.-J. Kestenbach, Phil. Mag. **36**, 1509 (1977)
40. S. Martin, S. Wolf, S. Decker, L. Krüger, U. Martin, Steel Res. Int. **86**, 1187 (2015)
41. S. Martin, C. Ullrich, D. Šimek, U. Martin, D. Rafaja, J. Appl. Cryst. **44**, 779 (2011)
42. S. Allain, J.-P. Chateau, O. Bouaziz, S. Migot, N. Guelton, Mater. Sci. Eng., A **387–389**, 158 (2004)
43. L. Remy, A. Pineau, Metall. Trans. **5**, 963 (1974)

Chapter 21
Multi-scale Modeling of Partially Stabilized Zirconia with Applications to TRIP-Matrix Composites

Mohan Kumar Rajendran, Michael Budnitzki and Meinhard Kuna

Abstract The understanding of how the microstructure influences the mechanical response is an essential pre-requisite for materials tailored to match specific requirements. The aim of this chapter is to further this understanding in the context of Mg-PSZ-TRIP-steel composites on three different scales using a set of methods ranging from phase-field simulations over micromechanics to continuum constitutive modeling. On the microscale, using a Ginzburg-Landau type phase-field model the effects of cooling- and stress-induced martensitic phase transformation in MgO-PSZ is clearly distinguished. Additionally with this method the role of energy barrier in variant selection and the effect of residual stress contributing to the stability of the tetragonal phase are also investigated. On the mesomechanical scale, an analytical 2D model for the martensitic phase transformation and self-accommodation of inclusions within linear elastic materials has been successfully developed. The influences of particle size and geometry, chemical driving force, temperature and surface energy on the $t \rightarrow m$ transformation are investigated in a thermostatic approach. On the continuum scale, a continuum material model for transformation plasticity in partially stabilized zirconia ceramics has been developed. Nonlinear hardening behavior, hysteresis and monoclinic phase fraction during a temperature cycle are analyzed. Finally, The mechanical properties of a TRIP steel matrix reinforced by ZrO_2 particles are analyzed on representative volume elements. Here the mechanical properties of the composite as function of volume fraction of both constituents and the strength of the interface are studied.

M. K. Rajendran (✉) · M. Budnitzki · M. Kuna
Institute of Mechanics and Fluid Dynamics,
Technische Universität Bergakademie Freiberg,
Lampadiusstrasse 4, 09599 Freiberg, Germany
e-mail: mohan-kumar.rajendran@imfd.tu-freiberg.de

H. Biermann and C. G. Aneziris (eds.), *Austenitic TRIP/TWIP Steels and Steel-Zirconia Composites*, Springer Series in Materials Science 298,
https://doi.org/10.1007/978-3-030-42603-3_21

21.1 Introduction

21.1.1 Aims and Scopes of the Present Work

One central aim of the Collaborative Research Center SFB799 "TRIP-matrix composites" was the development of a particle reinforced composite, composed of a TRIP-steel metallic matrix and ceramic particles of partially stabilized zirconia PSZ. The underlying idea was to exploit the phase transformation capability of both constituents in order to enhance and to optimize the mechanical properties by making such a composite.

In particular, the combination of the strain-induced phase transformation in the TRIP steel and the stress-induced transformation in PSZ offers the opportunity to compensate local stress concentrations at considerably high plastic deformations. This reinforcing effect has been verified by several experiments with these metal-matrix-composites MMC under monotonous [1] loading.

In complementation to the fabrication and characterization of these MMC, a thorough theoretical-numerical modeling of the composite material was necessary to understand and to simulate the phase transformation and the deformation behavior of both constituents.

This work was devoted to the simulation of the phase transformation processes in the PSZ ceramics and the MMC, whereas in another work the behavior of the TRIP-steel was investigated. The aim was to provide proper constitutive equations for stress and temperature controlled tetragonal-to-monoclinic phase transformation of PSZ ceramics, based on physical assumptions accounting for the responsible micromechanical mechanisms. The problem has been approached at various length scales, see Fig. 21.1:

- At the **microscale** level it was needed to simulate the actual kinetics of the transformation process inside of single tetragonal phase particles in PSZ. This task could be best accomplished by using the phase-field method.
- To study the transformation conditions of an ensemble of tetragonal lentils in polycrystalline PSZ ceramics, a semi-analytical thermostatic approach was applied at the **mesoscale**.
- In order to enable quantitative strength analysis of structures made of PSZ and MMC, a phenomenological constitutive law at the **macroscale** was further developed and implemented in a FEM-environment.
- To support the development of tailored particle MMC TRIP-matrix composites, representative volume elements on the **composite level** were simulated, which allow to predict the mechanical properties of the composite as function of volume fraction of both constituents and the strength of the interface.

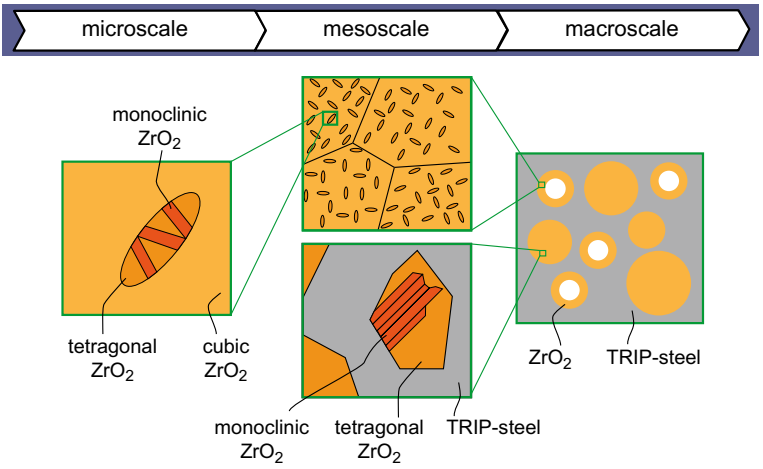

Fig. 21.1 Different scales of modeling partially stabilized zirconia

21.1.2 Introduction to Partially Stabilized Zirconia

Partially stabilized zirconia (PSZ) is widely used because of its enhanced fracture toughness and nonlinear stress-strain behavior. These favorable mechanical properties of PSZ result from a solid state phase transformation at regions of high stress concentration (e.g. crack tips). This effect, known as transformation toughening, was first reported by Garvie et al. [2] and was extensively investigated by [3–5]. Generally, some conditions have to be fulfilled for transformation toughening. The existence of a metastable phase in the material is required, which can be achieved either by microstructural parameters such as grain size or by changing the chemical composition. The martensitic (instantaneous) transformation from the metastable parent phase to the stable resultant phase has to be stress-induced.

The PSZ ceramic material under consideration is stabilized by MgO, resulting in finely dispersed lenticular precipitates of tetragonal (t-phase) embedded coherently in the grains of a polycrystalline cubic matrix material (see Fig. 21.2). These precipitates can transform into the monoclinic (m-phase) [7] triggered either by temperature or stress, resulting in the formation of multiple, partially self-accommodating variants. The $t \rightarrow m$ phase transformation, if unconstrained, is accompanied by a volume dilatation of about 4% and a shear strain of about 8%. The increase in volume induces (residual) compressive stresses in the cubic (c-phase) matrix leading to a shielding effect at stress concentrations, which contributes to the toughness of the material.

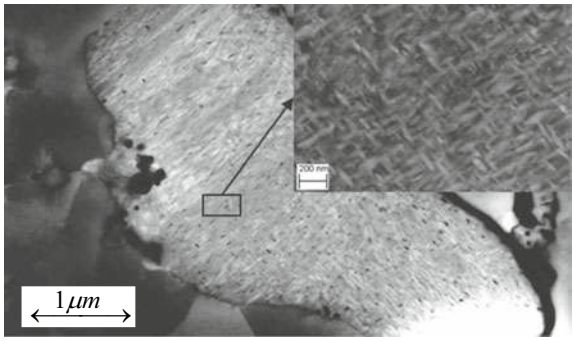

Fig. 21.2 Typical microstructure of a TRIP-PSZ composite produced in the CRC 799 by spark plasma sintering. The image shows a PSZ particle surrounded by TRIP steel together with a zoom into the particle showing the typical PSZ microstructure (reprinted from [6])

21.2 Micromechanical Phase-Field Approach

Phase-field is considered to be a powerful mathematical computational tool in simulations involving interface kinetics. In the past decades PF approach has been successfully established in various fields for materials science understanding such as: solidification, solid-state phase transformation, precipitate evolution and coarsening kinetics, grain growth, martensitic phase transformation (MPT) and also in damage and crack growth phenomena.

For past few decades there has been active research towards the direction of modelling partially stabilized zirconia (PSZ) materials. Wang et al. [8] was one of the early study on PSZ for $c \rightarrow t$ phase transformation involving Ginzburg-Landau (GL) phenomenological theory based PF model. Later in [9] the authors simulated alternating band structure formed by self-organized orientation variants of t-phase particles. In [10] the first three-dimensional model for generic $c \rightarrow t$ MPT was presented. Mamivand et al. [11] reported the first work on anisotropic and inhomogeneous PF modeling for $t \rightarrow m$ phase transformation in zirconia ceramics. The work discussed the simulation results based on different initial and boundary conditions in comparison to experimental observations. Further the authors [12] incorporated the effect of stress and temperature to capture the forward $t \rightarrow m$ and reverse $m \rightarrow t$ transformation to model pseudo-elastic behavior in polycrystalline zirconia.

A comprehensive work on non-conserved type GL-based phase-field models for generic martensitic phase transformation was developed in a series of three papers from Levitas et al. [13–15]. Levitas et al. used a $2-3-4$ or higher order polynomial for approximating the Gibbs energy and effective strain transition from austenite to any martensitic variant. This work principally relies on the phenomenological GL phase-field model developed by Levitas et al. with $2-4-6$ type Landau potential.

21.2.1 Phase-Field Method

The temporal and spatial evolution of non-conserved phase-field variables is described by the phenomenological Ginzburg-Landau kinetic equation

$$\frac{\partial \phi}{\partial t} = -L\left(-\beta \nabla^2 \phi + \frac{\partial \psi_{\mathrm{gl}}}{\partial \phi}\right). \tag{21.1}$$

Here L is the positive kinetic coefficient, and β is a positive gradient energy coefficient. The interface energy contribution provided by Levitas and Preston [13] was used.

Here the total enthalpy ψ_{gl} is described by additive contributions from an elastic ψ_{el} and a stress-independent chemical part of free enthalpy ψ_{ch}. The individual contributions are based on the work of Levitas and Preston [13, 14].

$$\psi_{\mathrm{gl}} = \psi_{\mathrm{el}}(\boldsymbol{\epsilon}, \boldsymbol{\epsilon}_{\mathrm{tr}}, \phi) + \psi_{\mathrm{ch}}(\theta, \phi). \tag{21.2}$$

The order parameter considered here ranges from $-1 \leqslant \phi \leqslant 1$, where $\phi = \pm 1$ are the two possible product variants of m-phase and $\phi = 0$ represents the parent t-phase in two dimensions, see Fig. 21.3b. The values ± 1 correspond to the variants having opposite shear (self accommodating variants) in order to form twins during $t \rightarrow m$ transformation. So, a single order parameter ϕ represents a group of phases consisting of variant m_+, its counter self accommodating variant m_- and the parent phase t in $t \rightarrow m$ transformation. As discussed in the work of Levitas et al. [15] the most opted $2-4-6$ polynomial for such a crystal set is used further to describe

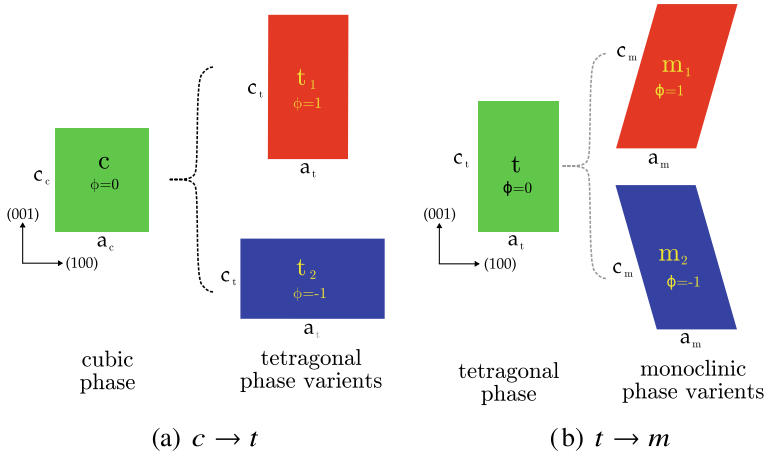

Fig. 21.3 Order parameter and lattice transformation representation of parent and product phases during martensitic phase transformation in zirconia ceramics. **a** $c \rightarrow t$ lattice transformation, **b** $t \rightarrow m$ lattice transformation schematic in two dimensions

the potential in this work and to model the phase transformation. A similar method is considered in representing parent c-phase and product variants of t-phase during $c \rightarrow t$ transformation.

In mechanics total strain tensor is decomposed into an elastic and an inelastic/transformation term, such as,

$$\boldsymbol{\epsilon} = \boldsymbol{\epsilon}_{\mathrm{el}} + \boldsymbol{\epsilon}_{\mathrm{tr}}(\tilde{\phi}). \tag{21.3}$$

Here $\boldsymbol{\epsilon}_{\mathrm{tr}}(\tilde{\phi})$ provides resultant transformation strain weighted with fraction of product phase $\varphi(\tilde{\phi})$. The modified order parameter $\tilde{\phi}$ is used instead of ϕ to avoid any unbounded solution which may lead to unphysical mechanical properties. This implies $\epsilon_{\mathrm{tr}}(0) = 0$ and $\epsilon_{\mathrm{tr}}(\pm 1) = \boldsymbol{\epsilon}_{\mathrm{tr}}^{m\pm}$ respectively. In same way fourth-rank effective elastic constants $\boldsymbol{E}_{\mathrm{eff}}$ can be written as fraction weighted with respect to product phase. The transformation/Bain strains and elastic constants are listed in Tables 21.1 and 21.2. For more detailed explanation on the PF method applied especially to simulation of zirconia material we refer to our previous work [16].

The Ginzburg-Landau equations are coupled to the basic equations of continuum mechanics by applying the week form of equilibrium of momentum in a FEM framework.

$$\nabla \cdot \boldsymbol{\sigma} = 0. \tag{21.4}$$

The resulting second order partial differential equations for phase-field variable ϕ and displacement vector u_i are solved concurrently using the finite element method framework implemented in COMSOL multiphysics.

21.2.2 Model Setup

Since both the transformations $c \rightarrow t$ and $t \rightarrow m$ are martensitic, the aforementioned PF approach is used to describe both phase transformation scenarios in zirconia ceramics. It is known that, t-phase and m-phase crystal during $t \rightarrow m$ transformation share same crystal lattice points in a symmetrical manner leading to 12 possible orientation relations of parent lattice to product lattice in three dimensions (3 correspondences based on choice of lattice axis direction, two variants for each correspondence and two orientations for each variant). This is also similar to the case of c-phase and t-phase crystal during $c \rightarrow t$ transformation. In two dimensions the problem reduces to a simple set of two product crystal variants (see Fig. 21.3). The other cases of crystal transformation belong on the third dimension, so for simplification, they could be neglected from modeling. In $t \rightarrow m$ transformation this simple crystal lattice transformation set (see Fig. 21.3b) is enough to describe twin formation during transformation in two dimensions and thus could reproduce the effect of self accommodation in order to reduce the total strain energy of the system.

Since the specific domain setup differs in some cases of our simulations provided in the following subsections, they are discussed in detail in the corresponding

Table 21.1 Variant transformation strains involved in $c \rightarrow t$ and $t \rightarrow m$ transformation [8, 17, 18]

Lattice transformation	Transformation strain ϵ_{ij}
$c \rightarrow t_1$	$\epsilon_{\text{tr}}^{t1} = \begin{bmatrix} -0.0007 & 0 \\ 0 & 0.0197 \end{bmatrix}$
$c \rightarrow t_2$	$\epsilon_{\text{tr}}^{t2} = \begin{bmatrix} 0.0197 & 0 \\ 0 & -0.0007 \end{bmatrix}$
$t \rightarrow m_+$	$\epsilon_{\text{tr}}^{m+} = \begin{bmatrix} 0.012479 & 0.079614 \\ 0.079614 & 0.019139 \end{bmatrix}$
$t \rightarrow m_-$	$\epsilon_{\text{tr}}^{m-} = \begin{bmatrix} 0.012479 & -0.079614 \\ -0.079614 & 0.019139 \end{bmatrix}$

Table 21.2 Elastic stiffness (in GPa) of c-phase , t-phase and m-phase [19]

Phases	$\mathbf{E}_{11}$	$\mathbf{E}_{22}$	$\mathbf{E}_{33}$	$\mathbf{E}_{44}$	$\mathbf{E}_{55}$	$\mathbf{E}_{66}$	$\mathbf{E}_{12}$	$\mathbf{E}_{13}$	$\mathbf{E}_{16}$	$\mathbf{E}_{23}$	$\mathbf{E}_{26}$	$\mathbf{E}_{36}$	$\mathbf{E}_{45}$
c-phase	390	390	390	60	60	60	162	162	0	162	0	0	0
t-phase	327	327	264	59	59	59	100	62	0	62	0	0	0
m-phase	361	408	258	100	81	126	142	55	−21	196	31	−18	−23

subsections of selected results. Overall in common, we assume anisotropic elastic behaviour in both elastic and phase transformation domain in our simulations. The effective transformation strain and elastic constants at a material point inside the phase transformation domain are evaluated as a function of ϕ [16]. The description of anisotropy is necessary to capture variant orientation relationship and the effects of various external loading directions on MPT. The material parameters used in the model are listed in Tables 21.1 and 21.2.

21.2.3 Selected Results and Discussion

21.2.3.1 Phase Stability and Energy Barriers

Using CALPHAD [20] method an unambiguous representation of the temperature dependent Gibbs free energy values of individual phases from the thermodynamical aspect could be evaluated [21]. But the form of energy landscape for intermediate phase transition from parent to product phase is still ambiguous and is a missing piece of puzzle. Most of the phase-field methods rely on these energy landscape to reproduce a more relevant and accurate material behavior. There are two major methods used by phase-field to approximate the transformation path a common tangent

method [20] which expresses a linear behavior between parent and product phase minima. On other hand potential function methods [13, 22] utilize an non-linear analytical representation of path between parent and product phase minima. Both of these methods confide in phenomenological modeling of free energy based on the phase stability conditions. In this work a generic model for martensitic phase transformation developed by Levitas and Preston [14] is used and adapted for simulating zirconia ceramics material. We use $2-4-6$ potential function [16] method which is utilized to represent a non-linear behavior and exhibit a transition barrier based on thermo-mechanical conditions.

On the thermodynamic perspective of zirconia at ambient temperature, it is clear that the global minimum is at m-phase and the global maximum is at t-phase . So theoretically the metastable t-phase always tends to transform to stable m-phase . But in almost all commercial PSZ ceramics (refer MgO-ZrO_2micrographs from the book of Hannink et al. [18]) the t-phase is observed to be stable at ambient temperature. Multiple factors may cause such a stabilization, which include: stabilizer doping such as MgO, presence of residual stresses from prior $c \rightarrow t$ transformation, but also defects like dislocations and grain boundaries. Later in this work, the effect of residual stress is investigated. Here in this section we compare the potential functions from Mamivand et al. [11] and Levitas and Preston [14] commonly used in literature for modelling $t \rightarrow m$ transformations. We investigate the capabilities of these functions for such a stabilization.

The $2-4-6$ potential used by Mamivand et al. [11] for approximating the Gibbs energy contribution defines energy barrier just by the analytical function. The barrier is then levered by the enthalpy difference between the parent and product phase irrespective of temperature, see Fig. 21.4a. Even at ambient temperature the approximated Gibbs energy landscape provides an energy barrier considering only thermodynamic contribution by pure zirconia, which is in contradiction to true physical behaviour. In the case of Levitas and Preston [14] based formulation for temperatures below M_s the function doesn't exhibit any barrier for transformation.

At high temperature just above M_s (see Fig. 21.4d) the energy landscape calculated based on Mamivand's potential formulation shows local minima at the parent and product phase. For the same, a global maximum or energy barrier is visible at order parameter $\phi \approx 0.1$ (see $T < M_s$). But as the temperature increases this decreases the barrier, and after crossing the T_0 there remains an intermediate local minimum which is neither parent nor product phase, the local minimum is close to order parameter $\phi \approx 0.1$, see Fig. 21.4b, c. In contrast, Levitas type potential used in this work has no intermediate minimum rather provides a barrier between the parent and product phase for temperatures above M_s.

Based on Levitas et al. formulation, utilized in this work for zirconia ceramics at any temperature, a global/local minima is retained at the product phase. And for $T > M_s$ a local minimum is also retained in parent phase, see Fig. 21.4b, d. Thus the potential function used in this work results in a proper representation of zirconia ceramics material behaviour from a pure thermodynamic stand point.

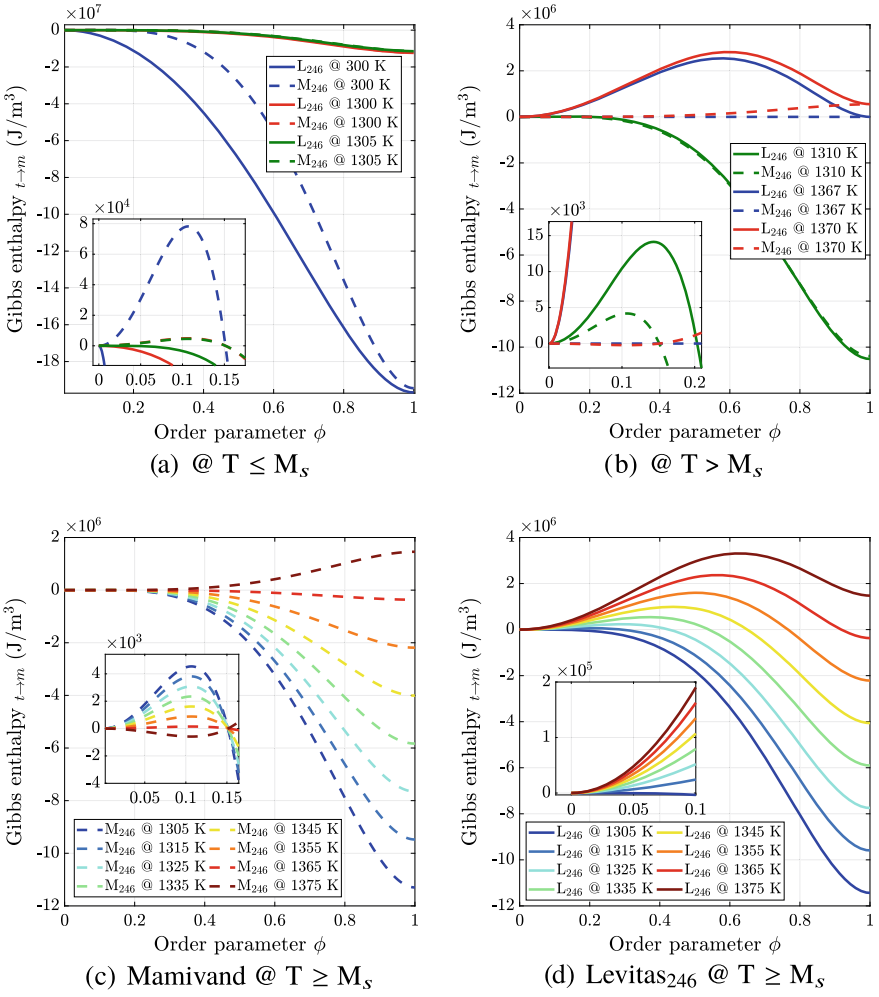

(a) @ T ≤ M$_s$ (b) @ T > M$_s$

(c) Mamivand @ T ≥ M$_s$ (d) Levitas$_{246}$ @ T ≥ M$_s$

Fig. 21.4 Comparison of estimated $2-4-6$ potential based thermodynamic Gibbs enthalpy $\psi_{\text{ch}}(\theta, \phi)$ as a function of order parameter during $t \to m$ transformation at various temperatures for Levitas and Preston [14] based model used for zirconia ceramics [16] to Mamivand et al. [11] model

21.2.3.2 Variant Selection by Energy Barriers

In this section we would like present distinctive differences in microstructure and evolution path between cooling induced and stress induced $t \to m$ transformations. We show that the different behaviour can be explained by the presence of an energy barrier in the Gibbs free enthalpy. In the latter case, sequential growth of monoclinic lamellae is observed because of possible variant selection based on energy barriers,

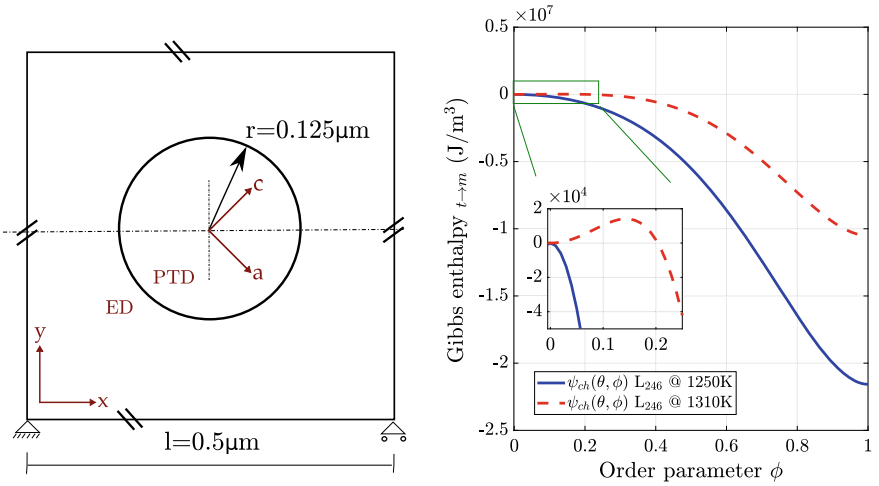

(a) Simulation domain setup (b) $\psi_{\mathrm{ch}}(\theta, \phi)$ @ 1250 K and 1310 K

Fig. 21.5 **a** Representation of simulation domain with boundary conditions. Material coordinate system (abc) and geometrical coordinate system (xyz). Axis c and z are outward normal to the paper. **b** Comparison of stress-independent chemical free enthalpy

whereas cooling induced microstructure evolution is characterized by an almost homogeneous nucleation of the monoclinic phase.

For simulating different microstructure evolution, such a domain setup is chosen, where the t-phase lentils are stabilized in the cubic matrix after annealing. A single crystal setup with a square c-phase elastic domain (ED) of 0.5 μm × 0.5 μm with an embedded circular phase transformation domain (PTD) of radius 0.125 μm (see Fig. 21.5a) is created. As initial condition in PTD the tetragonal phase is superimposed with random noise on order parameter ϕ within a given range. The elastic domain here represents a cubic matrix surrounding a single t-phase particle. A circular form of embedded phase transformation domain is chosen in order to avoid any geometrical influence on the microstructure formation. The initial displacement is set zero in the whole domain. Additionally, a displacement periodic boundary condition is imposed at the boundaries. In order to mimic a rotated crystal around the b-axis (normal to the paper) (see Fig. 21.5a) the material parameters, transformation strain and elastic constants are transformed accordingly. Other common simulation and material parameters used are already discussed above and listed in Table 21.3.

For simulating stress induced transformation, we choose homogeneous isothermal conditions at 1310 K, above $M_s = 1305$ K. On the other hand, for cooling induced transformation we choose homogeneous isothermal condition at 1250 K below M_s. The Gibbs enthalpy landscapes based on pure thermodynamic contribution for both temperatures are compared in Fig. 21.5b.

Figure 21.6a–c show a cooling induced martensitic transformation in a single crystal, rotated by 45° around 'b'-axis (see Fig. 21.5a) with isothermal condition

Table 21.3 Input parameters used in $t \rightarrow m$ simulation

Description	Symbol	Value	Unit
m-phase start temperature	$M_s^{t\rightarrow m}$	1305	K
m-phase equilibrium temperature	$T_0^{t\rightarrow m}$	1367	K
Gradient energy coefficient	β	5×10^{-11}	J/m
Kinetic coefficient	L	2	m^3/Js
Material parameter	a	6	–

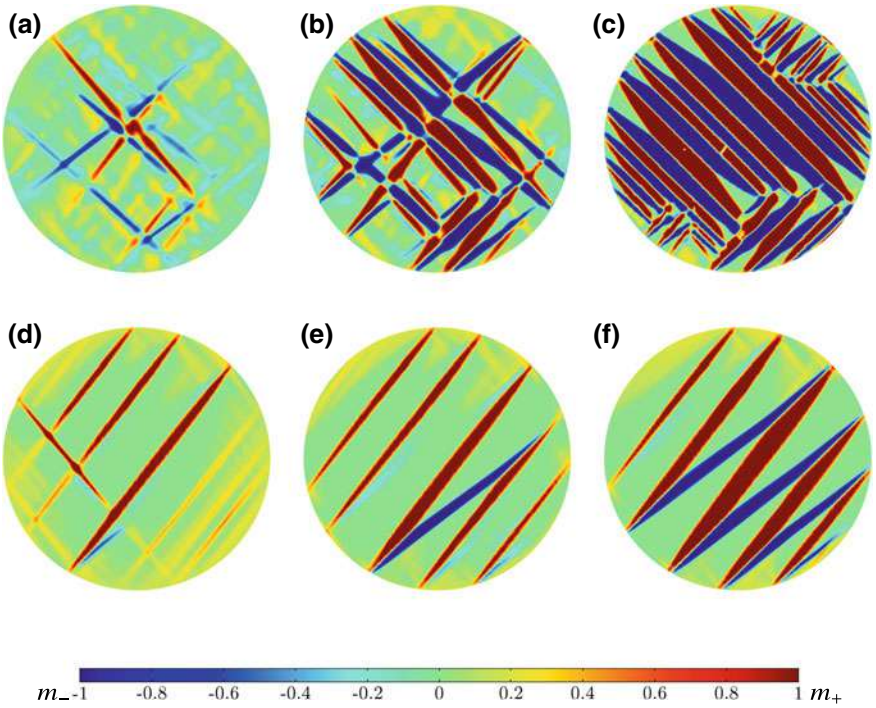

Fig. 21.6 A comparison between cooling induced case (top row (**a**–**c**)) and stress induced case (bottom row (**d**–**f**)). The color legend represents the order parameter ϕ. A sequential growth of lamella, observed during stress induced case due to variant selection based on external loading. Microstructure evolution snapshots at various stages of pseudo-time

below M_s at 1250 K. A surface plot inside the PTD shows the evolution of order parameter ϕ where the color legend represents, red being m^+, blue as m^- and green as t.

In cooling induced case there is no intermediate energy barrier between parent and product phase for transformation (see Fig. 21.5b) since the temperature is below M_s and here product m-phase is stable. So after initialization an almost homogeneous nucleation process takes place where all possible nucleation sites

of all possible variants are preferred to grow because of the adequate thermodynamic driving force (see Fig. 21.6a–d). In the numerical simulation, such condition will lead to different microstructure arrangements for different initialization. The evolved microstructures would be of mixed patterns where junction planes are parallel or orthogonal to 'c'-axis, which could be observed within a single grain (both orientation scenarios specified by Hannink et al. [18]). In Fig. 21.6c a large quantity of junction plane between two m-phase variants are orthogonal to 'c'-axis direction and there are small amount of junction planes (upper right, lower left and lower right) oriented parallel to 'c'-axis. Figures of both such lamella directions of twin formation have already been presented in the work of Hannink et al. [18] within a single t-phase lentil.

Simulation parameters here remain the same as cooling induced microstructure formation case, except the operating temperature being 1310 K above M_s and with $\sigma_{\text{app}} = 1$ GPa compression along 'b'-axis (see Fig. 21.5a). An initial superimposed noise with a range confined within the barrier of the Gibbs enthalpy landscape (see Fig. 21.5b) is applied.

Since the pure thermodynamic driving force is not adequate to trigger the transformation, there would not be martensitic evolution at all. As the compressive stress is superimposed additionally to the thermodynamic contribution, depending on the orientation of crystal relative to the applied stress some variants are preferred to grow by decreasing the energy barrier and some are obstructed by increasing the barrier. In other words, the energy landscape is skewed such that some variants have energy barrier and others don't, see Fig. 21.9a. This becomes clear by comparison between solid blue curve where no external stress is applied, and dashed red curve after application of external stress. Here in dashed red curve one variant experiences a barrier and the other doesn't. In this example (Fig. 21.6d–f) the m^+—red nucleation sites are preferred. At the initial stage, m^+ red variant nucleates and grows and meanwhile m^- blue variant vanishes because of the energy barrier. Additionally, by superimposing normal stress σ_{app} the driving force exceeds the minimum driving force required for transformation above M_s and triggers the transformation. Initially only m^+ variant lamellae grow such that they increase the strain energy. As the lamellae reach the grain boundary or imperfections, this piles up stress and triggers the m^- blue self accommodating variant thus reducing a part of the strain energy gained.

According to the investigation on MgO-$ZrO_2$by Kelly and Ball [17] the potential twinning plane/junction plane for twin related variants is either $[100]_m$/'a'-axis or $[001]_m$/'c'-axis, based on our model base axis orientation in Fig. 21.3. The resulting junction plane $[001]_m$/'c'-axis (see Fig. 21.6) is consistent with the experimental observations of [17, 18, 23, 24]. It is clear that among the two possible orientation scenarios specified by Hannink et al. [18] between m-phase and t-phase , junction plane parallel to 'c'-axis, twin-related variants retain some untransformed t-phase , which is also consistent with our observations. But the reason for possible conditions under which such oriented structure could be reproduced has not been discussed yet before.

21.2.3.3 Origin and Effect of Residual Stresses

The probable initial existence of residual stresses [25, 26] in the t-phase matrix as a result of the $c \rightarrow t$ transformation and their effect on $t \rightarrow m$ transformation is also not well understood yet. Such a residual stress is not yet considered in modeling for $t \rightarrow m$. In almost all commercial ceramics t-phase is stable at ambient temperature. Multiple factors may cause such a stabilization, here we look into the possibility and the effects of residual stress present prior to $t \rightarrow m$ transformation. In order to evaluate the peak residual stress which could be expected during $c \rightarrow t$ transformation, we simulate $c \rightarrow t$ transformation inside a c-phase matrix. The evolution of average pressure inside the t-phase lentil during transformation is tracked. This pressure is later used as an initial condition to mimic presence of residual stress during $t \rightarrow m$ transformation.

A simple model for single lentil setup within a square phase transformation domain is chosen with a size such that an average size of tetragonal lentil could be accommodated. This phase transformation domain is placed within an large elastic domain with c-phase . The transformation domain is initialized with c-phase and a circular seed of t-phase is placed at the centre of the phase transformation domain. The initialization and boundary conditions are set similar to those of model for $t \rightarrow m$. The domain is allowed to transform from cubic to tetragonal ($c \rightarrow t$) by undercooling at 1300 K without any external mechanical loading. The thermodynamic functions for evaluating Gibbs enthalpy values are taken from [11, 21]. We assume anisotropic elastic behavior for the whole domain. The elastic constants of respective phases are provided in Table 21.2. Based on the lattice constants from [8] one can evaluate the transformation strain (see Table 21.1), the critical temperature $M_s^{c\rightarrow t} = 1423$ K and equilibrium temperature $T_0^{c\rightarrow t} = 584$ K acquired from [27]. All other parameters are similar to those of previously explained model setup and listed in Tables 21.2 and 21.3.

Figure 21.7 shows single and multi-variant t-phase lentils evolving inside a c-phase matrix. As the initial tetragonal inclusion grows to lentil shape, its interior is under compression. On left half, the mean in-plane pressure $\sigma_{\bar{p}} = -(\sigma_{xx} + \sigma_{yy})/2$ is plotted. The legend red represents material under compression and blue represents material under tension. On the right half, the surface plot of order parameter ϕ is presented. Therein, green color represents c-phase and red color represents t-phase . In commercial ceramics, stable tetragonal lentils are observed at ambient temperature. So the peak mean in-plane pressure experienced by these t-phase lentils during their formation is considered to be the initial condition for $t \rightarrow m$ transformation. Figure 21.8 shows an evolution of the mean in-plane pressure versus the area fraction of a single t-phase lentil in an infinite domain. The numerical fluctuations during the initial stages are of no interest, but a strong saturation trend in the later stages is considerd resulting in a 0.21GPa mean in-plane pressure inside a lentil. Although a single lentil is considered here, in reality the cubic matrix is populated with multiple lentils so a superimposed stress state of multiple lentils will lead to higher value than the one estimated here.

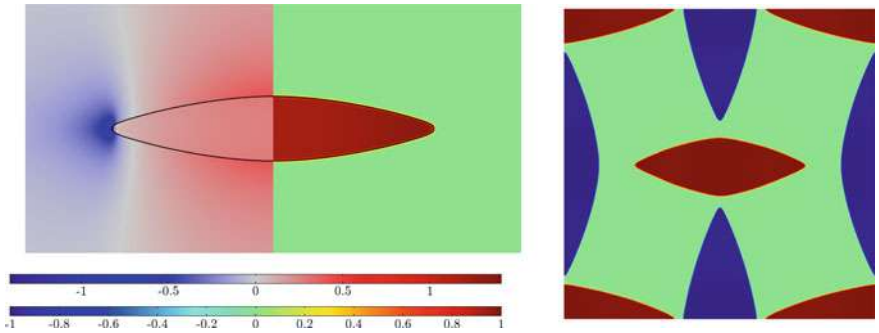

(a) Single lentil simulation (b) Multi lentil simulation

Fig. 21.7 Evolution of single-variant and multi-variant lentils during $c \rightarrow t$ transformation

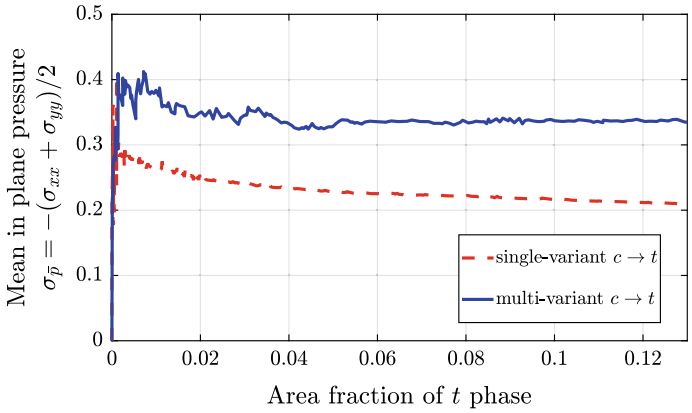

Fig. 21.8 Evolution of mean inplane pressure $\sigma_{\bar{p}}$ inside t-phase lentil versus fraction of t-phase

In order to evaluate the mean in-plane pressure on a multi lentil setup, a similar setup like a single lentil setup is choose. This setup represents a periodically placed RVE. The placement of the initial seeds are arranged such that they represent a proper microstructure. The seed at the center is replaced with a noise where an equal possibility is given to both variants to nucleate and grow. Because of the stress state of the neighboring t-phase lentils a selective nucleation of red variant takes place which is more favorable. The peak average pressure experienced by these t-phase lentils are tracked and plotted in Fig. 21.8. In this multi lentil setup the resulting mean in-plane pressure inside the lentils is 0.35 GPa which is larger than that of the single lentil simulation case. This gives a clear evidence of residual stress from prior $c \rightarrow t$ transformation.

As consequence of result from single and multi lentil simulations we choose $\approx$0.3 GPa as the initial pressure inside the lentil which is also consistent with the FEM based investigation on tetragonal inclusion in a cubic matrix by [26].

By applying a hydrostatic residual stress to the system an energy barrier is introduced thus allowing t-phase stability below M_s. This is visible in Fig. 21.9a on the solid blue line showing a local maximum near to the t-phase . The dotted green line shows the pure stress free chemical contribution of Gibbs enthalpy where the m-phase is stable and there is no energy barrier for $t \rightarrow m$ transformation. By superimposing an externally applied compressive stress one could skew the energy landscape, thus favouring a single variant so that stress induced transformation is possible below M_s temperature. A similar simulation setup for $t \rightarrow m$ transformation as described in the previous section is used. Additionally, for introducing a residual stress an equibiaxial type loading of $\sigma_{\bar{p}} = -0.3$ GPa is applied. The temperature is $T = 1250\,\text{K} < M_s$. Figure 21.9b shows the microstructure formed by stress induced transformation at 1250 K. It is clear that the residual stress from the $c \rightarrow t$ transformation contributed to the stability of t-phase . As the operating temperature decreases the residual stress required to introduce a barrier for transformation increases (see Fig. 21.10). By this it becomes clear that residual stress is not the only contribution involved in the t-phase stability.

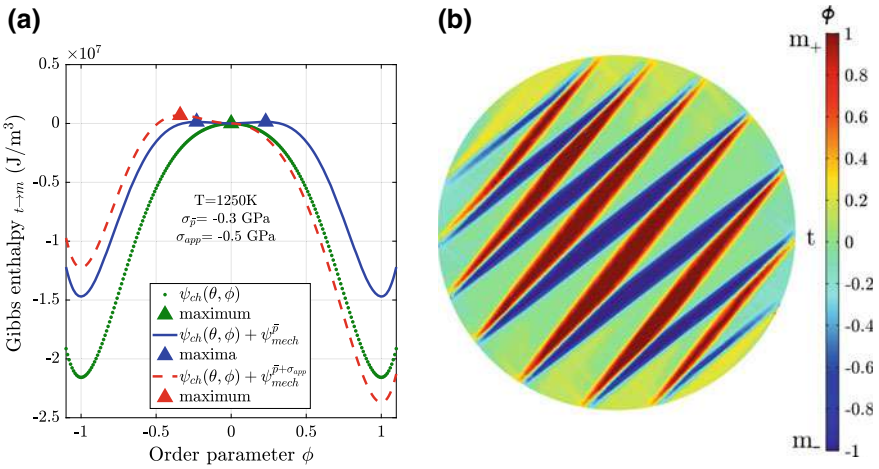

Fig. 21.9 Possibility of t-phase stability and stress induced transformation below M_s temperature at 1250 K, influence of residual stress and asymmetry in energy barrier by superimposing externally applied compression. On left, effect of residual stress and applied uniaxial compression on Gibbs enthalpy landscape below M_s at 1250 K. On right, surface plot of order parameter ϕ inside PTD. **a** Enthalpy landscape with various energy contributions, **b** surface plot of ϕ

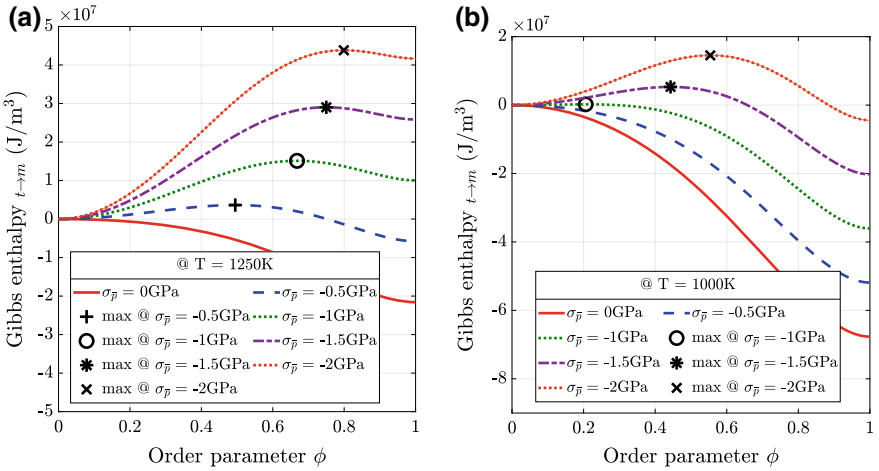

Fig. 21.10 Impact of residual stress on energy barrier at various temperatures. The intermediate local maxima showing presence of a energy barrier are represented with unique marker. A trend of increasing energy barrier with increasing residual stress is visible. **a** $T = 1250$ K, **b** $T = 100$ K

21.3 Mesomechanical Model

The understanding of how the microstructure influences the mechanical response is an essential pre-requisite for materials tailored to match specific requirements. The aim of the present work is to develop a transformation criterion for lenticular inclusions embedded into an elastic matrix based on the work of Hensl et al. [6] that accounts for the experimentally observed tension-compression asymmetry. This criterion is then used in order to investigate the influence of the microstructural features, such as size and shape of the inclusions, on the mechanical response. A homogenization approach, schematically depicted in Fig. 21.11, provides first insights into the response of a grain.

21.3.1 Transformation Criterion for a Single Precipitate Embedded in an Infinite Matrix

In this section we extend the transformation criterion developed in [6] in order to account for the pressure sensitivity of the material. This is done in a plane-strain setting based on a number of assumptions.

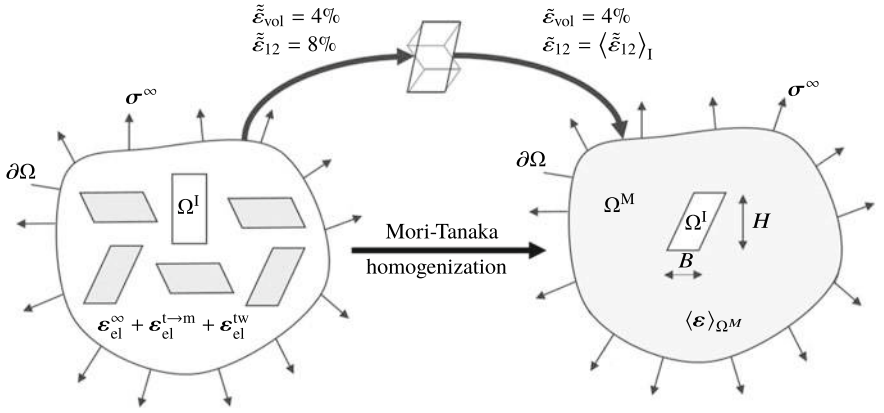

Fig. 21.11 Illustration of homogenization techniques used to model the effective material behavior of a polycrystal, influenced by the microstructure of each grain

21.3.1.1 Working Hypotheses

1. The elastic tensors of the cubic matrix and tetragonal precipitate (inclusion) are assumed to be isotropic and identical.
2. The inclusion is modeled as having a rectangular cross-section with width B, height H and aspect ratio $\alpha = H/B$ in its untransformed state.
3. The pseudo-twin structure after $t \to m$ transformation is modeled as a stack of equal-thickness lamellae, each of which carries a strain of $\tilde{\tilde{\varepsilon}}_{11} = \tilde{\tilde{\varepsilon}}_{22} = 2\%$ resulting in a relative volume change of $\tilde{\tilde{\varepsilon}}_{\mathrm{vol}} = 4\%$ and shear transformation strain $\tilde{\tilde{\varepsilon}}_{12} = \pm 8\%$ (specified in the crystallographic coordinate system[1]). Note that, while all lamellae are assumed to have the same thickness, the actual value of this thickness as well as the number of lamellae $2k$ are part of the solution and the corresponding effective shear strain of the inclusion is denoted by $\tilde{\boldsymbol{\varepsilon}}^{(k)} := \left\langle \tilde{\tilde{\varepsilon}} \right\rangle_{\mathrm{I}}$, where $\langle \cdot \rangle_{\mathrm{I}}$ is the averaging operator over the domain of the inclusion. Specifically, $\tilde{\varepsilon}_{11}^{(k)} = \tilde{\tilde{\varepsilon}}_{11}$, $\tilde{\varepsilon}_{22}^{(k)} = \tilde{\tilde{\varepsilon}}_{22}$ resulting in $\tilde{\varepsilon}_{\mathrm{vol}}^{(k)} = \tilde{\tilde{\varepsilon}}_{\mathrm{vol}} =: \tilde{\varepsilon}_{\mathrm{vol}}$ and $\tilde{\varepsilon}_{12}^{(k)} = \left\langle \tilde{\tilde{\varepsilon}}_{12} \right\rangle_{\mathrm{I}}$.
4. As the specific lamellae arrangement is not part of the solution, we estimate the elastic energy contribution resulting from the "zig-zag" at the inclusion boundary by assuming strictly alternating configuration (see Fig. 21.12).
5. We assume that phase transformation occurs when the Gibbs-enthalpy is equal in the transformed (G^{m}) and untransformed $\left(G^{\mathrm{t}}\right)$ states, i.e.,

$$\Delta G = G^{\mathrm{m}} - G^{\mathrm{t}} = \Delta E_{\mathrm{el}} + \Delta E_{\mathrm{ch}} + \Delta E_{\mathrm{sur}} \stackrel{!}{=} 0, \tag{21.5}$$

[1] If nothing else is specified, all tensor components in this work are referred to a coordinate system with orthonormal basis $(O, \{\boldsymbol{e}_1, \boldsymbol{e}_2\})$, where $\boldsymbol{e}_1$ is aligned along the tetragonal c-axis.

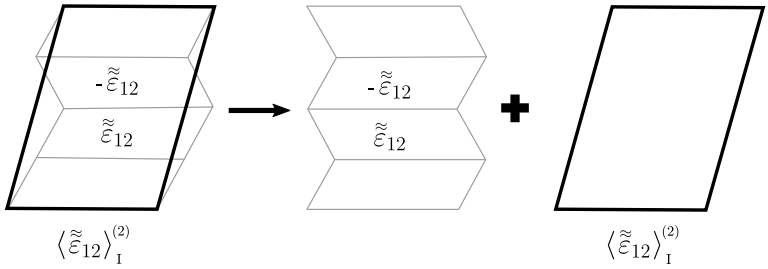

Fig. 21.12 Schematic illustration of the superposition scheme used to estimate the elastic energy of a "twinned" inclusion

where ΔE_{el} is the difference in the elastic strain energy, ΔE_{ch} is the difference in the chemical part of the bulk enthalpy and ΔE_{sur} is the difference in surface energy.

21.3.1.2 Energetic Contributions

The difference in surface energies is readily obtained as

$$\Delta E_{\mathrm{sur}} = 2(B+H)\Delta\beta_{\mathrm{I/M}} + (2k-1)B\,\beta_{\mathrm{I/I}}, \tag{21.6}$$

where the first term is the contribution of the interface between inclusion and matrix and the second term corresponds to the newly formed interfaces between different monoclinic variants. Here $\beta_{\mathrm{I/M}}$ is the difference in surface energies between a tetragonal-cubic and a monoclinic-cubic interface and $\beta_{\mathrm{I/I}}$ is the surface energy for an interface between two different monoclinic variants. The difference in the chemical bulk enthalpy is given by

$$\Delta E_{\mathrm{ch}} = -BH\Delta H^{t\to m}\frac{T_0 - T}{T_0}, \tag{21.7}$$

where $\Delta H^{t\to m}$ is the specific transformation heat and T_0 is the equilibrium temperature between the tetragonal and monoclinic phases.

In general, the elastic strain energy is given by

$$E_{\mathrm{el}} = \frac{1}{2}\int_{\Omega} \boldsymbol{\sigma} : \boldsymbol{\varepsilon}_{\mathrm{el}}\,\mathrm{d}A. \tag{21.8}$$

In the untransformed case only the homogeneous far-field stress $\boldsymbol{\sigma}^{\infty}$ and the corresponding elastic strain $\boldsymbol{\varepsilon}_{\mathrm{el}}^{\infty} = \mathbb{C}^{-1} : \boldsymbol{\sigma}^{\infty}$ with elastic stiffness tensor $\mathbb{C}$ are present, i.e.,

$$E_{\mathrm{el}}^{\mathrm{t}} = \frac{1}{2}\int_{\Omega} \boldsymbol{\sigma}^{\infty} : \boldsymbol{\varepsilon}_{\mathrm{el}}^{\infty}\,\mathrm{d}A = \frac{1}{2}\boldsymbol{\sigma}^{\infty} : \boldsymbol{\varepsilon}_{\mathrm{el}}^{\infty}\int_{\Omega} \mathrm{d}A. \tag{21.9}$$

This energy is unbounded if the domain Ω is infinite. After $t \to m$ transformation and self-accommodation, additional elastic strains due to transformation $\boldsymbol{\varepsilon}_{\mathrm{el}}^{t\to m}$ and the formation of the lamellar structure $\boldsymbol{\varepsilon}_{\mathrm{el}}^{\mathrm{tw}}$ are introduced, i.e.,

$$\boldsymbol{\varepsilon}_{\mathrm{el}} = \boldsymbol{\varepsilon}_{\mathrm{el}}^{\infty} + \boldsymbol{\varepsilon}_{\mathrm{el}}^{t\to m} + \boldsymbol{\varepsilon}_{\mathrm{el}}^{\mathrm{tw}}. \tag{21.10}$$

The corresponding stress is

$$\boldsymbol{\sigma} = \boldsymbol{\sigma}^{\infty} + \boldsymbol{\sigma}^{t\to m} + \boldsymbol{\sigma}^{\mathrm{tw}} \tag{21.11}$$

and the energy difference between the transformed and untransformed states is immediately found to be

$$\Delta E_{\mathrm{el}} = E_{\mathrm{el}}^{\mathrm{m}} - E_{\mathrm{el}}^{\mathrm{t}} = \frac{1}{2}\int_{\Omega} \left[\left(\boldsymbol{\sigma}^{\infty} + \boldsymbol{\sigma}^{t\to m} + \boldsymbol{\sigma}^{\mathrm{tw}}\right) : \left(\boldsymbol{\varepsilon}_{\mathrm{el}}^{\infty} + \boldsymbol{\varepsilon}_{\mathrm{el}}^{t\to m} + \boldsymbol{\varepsilon}_{\mathrm{el}}^{\mathrm{tw}}\right) - \boldsymbol{\sigma}^{\infty} : \boldsymbol{\varepsilon}_{\mathrm{el}}^{\infty}\right] \mathrm{d}A. \tag{21.12}$$

Note that this difference is bounded, since the contribution of the homogeneous far-field stress cancels out and we find

$$\Delta E_{\mathrm{el}} = \underbrace{\boldsymbol{\sigma}^{\infty} : \int_{\Omega} \boldsymbol{\varepsilon}_{\mathrm{el}}^{t\to m}\,\mathrm{d}A}_{\Delta E_{\mathrm{el}}^{\mathrm{t}\to\mathrm{m},1}} + \underbrace{\boldsymbol{\sigma}^{\infty} : \int_{\Omega} \boldsymbol{\varepsilon}_{\mathrm{el}}^{\mathrm{tw}}\,\mathrm{d}A}_{\Delta E_{\mathrm{el}}^{\mathrm{tw},1}} + \underbrace{\frac{1}{2}\int_{\Omega} \boldsymbol{\sigma}^{t\to m} : \boldsymbol{\varepsilon}_{\mathrm{el}}^{t\to m}\,\mathrm{d}A}_{\Delta E_{\mathrm{el}}^{\mathrm{t}\to\mathrm{m},2}} + \underbrace{\int_{\Omega} \boldsymbol{\sigma}^{t\to m} : \boldsymbol{\varepsilon}_{\mathrm{el}}^{\mathrm{tw}}\,\mathrm{d}A}_{\Delta E_{\mathrm{el}}^{\mathrm{t}\to\mathrm{tw}}} + \underbrace{\frac{1}{2}\int_{\Omega} \boldsymbol{\sigma}^{\mathrm{tw}} : \boldsymbol{\varepsilon}_{\mathrm{el}}^{\mathrm{tw}}\,\mathrm{d}A}_{\Delta E_{\mathrm{el}}^{\mathrm{tw},2}}. \tag{21.13}$$

The evalution of the individual integrals is closely related to the procedure presented in [6], which in turn is based on the closed form solution for rectangular inclusions with eigenstrains [28].

It can be shown [6] that as a particular result of assuming equal-size monoclinic lamellae, $\Delta E_{\mathrm{el}}^{\mathrm{tw},1} = \Delta E_{\mathrm{el}}^{\mathrm{t}\to\mathrm{tw}} = 0$, while $\Delta E_{\mathrm{el}}^{\mathrm{tw},2}$ can be obtained in the form

$$\Delta E_{\mathrm{el}}^{\mathrm{tw},2} = -B^2 \frac{E\tilde{\tilde{\varepsilon}}_{12}^2}{4\pi k^2(1-\nu^2)} \underbrace{\sum_{\zeta=1}^{k}\sum_{\eta=1}^{k}\sum_{i=1}^{11} g_i\,(\zeta,\eta,\alpha,k)}_{F(\alpha,k)}, \tag{21.14}$$

where the $g_i\,(\zeta,\eta)$ are functions of the geometry of the inclusion and number of lamellae, which are listed in the appendix of [6]. In order to evaluate $\Delta E_{\mathrm{el}}^{\mathrm{t}\to\mathrm{m},1}$ we make use of the fact that in the domain of the inclusion Ω^{I} the elastic strain due to phase transformation can be computed as

$$\boldsymbol{\varepsilon}_{\mathrm{el}}^{t\to m} = \boldsymbol{\varepsilon}^{t\to m} - \tilde{\boldsymbol{\varepsilon}}^{(k)} \tag{21.15}$$

and can write

$$\Delta E_{\mathrm{el}}^{t\to m,1} = \boldsymbol{\sigma}^{\infty} : \int_{\Omega} \boldsymbol{\varepsilon}^{t\to m}\,\mathrm{d}A - \boldsymbol{\sigma}^{\infty} : \tilde{\boldsymbol{\varepsilon}}^{(k)} \int_{\Omega^{\mathrm{I}}} \mathrm{d}A \tag{21.16}$$

$$= \boldsymbol{\sigma}^{\infty} : \int_{\Omega} \boldsymbol{\varepsilon}^{t\to m}\,\mathrm{d}A - \boldsymbol{\sigma}^{\infty} : \tilde{\boldsymbol{\varepsilon}}^{(k)}\, BH. \tag{21.17}$$

Introducing the usual split into volumetric and deviatoric parts

$$\boldsymbol{\sigma}^{\infty} = \boldsymbol{s}^{\infty} - p^{\infty}\boldsymbol{I}, \quad \boldsymbol{\varepsilon}^{t\to m} = \boldsymbol{e}^{t\to m} + \frac{1}{3}\varepsilon_{\mathrm{vol}}^{t\to m}\boldsymbol{I}, \quad \tilde{\boldsymbol{\varepsilon}}^{(k)} = \tilde{\boldsymbol{e}}^{(k)} + \frac{1}{3}\tilde{\varepsilon}_{\mathrm{vol}}^{(k)}\boldsymbol{I}, \tag{21.18}$$

where $\boldsymbol{I}$ is the unit-tensor, and making use of working Assumption 3 we find

$$\Delta E_{\mathrm{el}}^{t\to m,1} = \boldsymbol{s}^{\infty} : \int_{\Omega} \boldsymbol{e}^{t\to m}\,\mathrm{d}A - p^{\infty} : \int_{\Omega} \varepsilon_{\mathrm{vol}}^{t\to m}\,\mathrm{d}A + \left(p^{\infty}\,\tilde{\varepsilon}_{\mathrm{vol}}^{(k)} - \boldsymbol{s}^{\infty} : \tilde{\boldsymbol{e}}^{(k)}\right) BH \tag{21.19}$$

$$= \boldsymbol{s}^{\infty} : \int_{\Omega} \boldsymbol{e}^{t\to m}\,\mathrm{d}A - p^{\infty} : \int_{\Omega} \varepsilon_{\mathrm{vol}}^{t\to m}\,\mathrm{d}A + \left(p^{\infty}\,\tilde{\varepsilon}_{\mathrm{vol}}^{(k)} - 2\sigma_{12}^{\infty}\,\tilde{\varepsilon}_{12}^{(k)}\right) BH. \tag{21.20}$$

The evaluation of the above integrals is more involved than may appear at the first glance, since the integrands are singular at every kink at the boundary of the inclusion, therefore integration is carried out using the same procedure that was applied in [6] by a transformation into equivalent line integrals

$$\Delta E_{\mathrm{el}}^{t\to m,1} = \sigma_{12}^{\infty} \lim_{r\to\infty} \int_0^{2\pi} [u_1 r\sin(\varphi) + u_2 r\cos(\varphi)]\,\mathrm{d}\varphi$$

$$- p^{\infty} \lim_{r\to\infty} \int_0^{2\pi} [u_1 r\cos(\varphi) + u_2 r\sin(\varphi)]\,\mathrm{d}\varphi + \left(p^{\infty}\,\tilde{\varepsilon}_{\mathrm{vol}}^{(k)} - 2\sigma_{12}^{\infty}\,\tilde{\varepsilon}_{12}^{(k)}\right) BH, \tag{21.21}$$

resulting in the relatively simple expression

$$\Delta E_{\mathrm{el}}^{t\to m,1} = \frac{BH}{2\,(1-\nu)}\left[(1-2\nu)\,p^{\infty}\tilde{\varepsilon}_{\mathrm{vol}}^{(k)} - \sigma_{12}^{\infty}\,\tilde{\varepsilon}_{12}^{(k)}\right], \tag{21.22}$$

where ν is POISSON's ratio. For further details on the integration procedure, cf. [6]. The remaining energy difference $\Delta E_{\mathrm{el}}^{t\to m,2}$ is calculated using a very similar procedure, resulting in

$$\Delta E_{\mathrm{el}}^{t\to m,2} = \frac{\mu}{1-\nu}BH\left[P_1\left(\tilde{\varepsilon}_{12}^{(k)}\right)^2 + \frac{2}{9}\frac{1-\nu+P_2}{1-2\nu}\left(\tilde{\varepsilon}_{\mathrm{vol}}^{(k)}\right)^2\right], \tag{21.23}$$

with

$$P_1 = \frac{1}{\pi}\left[\frac{1}{\alpha}\ln\left(1+\alpha^2\right) + \alpha\ln\left(1+\frac{1}{\alpha^2}\right)\right], \tag{21.24a}$$

$$P_2 = \frac{1}{\pi}\left[\arctan\left(\frac{1}{\alpha}\right) - \arctan(\alpha)\right]. \tag{21.24b}$$

Using a basis-free representation of the stress tensor we finally find

$$\begin{aligned}\Delta E_{\mathrm{el}} = {} & \frac{BH}{2\,(1-\nu)}\left[(1-2\nu)\,p^{\infty}\tilde{\varepsilon}_{\mathrm{vol}}^{(k)} - \left(\boldsymbol{e}_1\cdot\boldsymbol{\sigma}^{\infty}\cdot\boldsymbol{e}_2\right)\,\tilde{\varepsilon}_{12}^{(k)}\right] + \\ & + \frac{\mu}{1-\nu}BH\left[P_1\left(\tilde{\varepsilon}_{12}^{(k)}\right)^2 + \frac{2}{9}\frac{1-\nu+P_2}{1-2\nu}\left(\tilde{\varepsilon}_{\mathrm{vol}}^{(k)}\right)^2\right].\end{aligned} \tag{21.25}$$

21.3.1.3 The Transformation Criterion

Substituting the energy differences computed in the previous section into the transformation criterion (21.5) we find

$$\begin{aligned}\frac{1-\nu}{\alpha B^2\mu}\Delta G\left(\boldsymbol{\sigma}^{\infty}, T, k\right) = {} & \frac{1}{2\mu}\left[(1-2\nu)\,p^{\infty}\tilde{\varepsilon}_{\mathrm{vol}} - \left(\boldsymbol{e}_1\cdot\boldsymbol{\sigma}^{\infty}\cdot\boldsymbol{e}_2\right)\,\tilde{\varepsilon}_{12}^{(k)}\right] + \\ & + P_1\left(\tilde{\varepsilon}_{12}^{(k)}\right)^2 + \frac{2}{9}\frac{1-\nu+P_2}{1-2\nu}\tilde{\varepsilon}_{\mathrm{vol}}^2 - \frac{1}{2\pi k^2\alpha}\tilde{\varepsilon}_{12}^2 F(\alpha,k) \\ & - \Delta H^{\mathrm{t}\to\mathrm{m}}\frac{T_0-T}{T_0} \\ & + \frac{1-\nu}{\mu\alpha}\left[\frac{2}{B}\,(\alpha+1)\,\Delta\beta_{\mathrm{I/M}} + \frac{1}{B}\,(2k-1)\,\beta_{\mathrm{I/I}}\right] \stackrel{!}{=} 0,\end{aligned} \tag{21.26}$$

Note that (21.26) is not an equation that can be solved directly for the stress (at fixed temperature) or temperature (at fixed stress level) required to initiate the phase

transformation, since nearly all terms depend on the number of lamellae $2k$. This ambiguity is resolved by choosing the number of lamellae such that it minimizes the Gibbs free enthalpy in the transformed state, i.e.,

$$\hat{k} = \arg\min_{k \in \mathbb{N}^+} \Delta G\left(\boldsymbol{\sigma}^\infty, T, k\right). \tag{21.27}$$

Having thus determined a value for k, (21.26) can be rewritten e.g. as a criterion for the applied far-field stress at fixed temperature,

$$\left|\boldsymbol{e}_1 \cdot \boldsymbol{\sigma}^\infty \cdot \boldsymbol{e}_2\right| - (1-2\nu)\frac{\tilde{\varepsilon}_{\mathrm{vol}}}{\left|\tilde{\varepsilon}_{12}^{\left(\hat{k}\right)}\right|} p^\infty \stackrel{!}{=} C_1, \tag{21.28}$$

with

$$C_1 := \frac{1}{\left|\tilde{\varepsilon}_{12}^{\left(\hat{k}\right)}\right|}\left(2\mu P_1\left(\tilde{\varepsilon}_{12}^{(k)}\right)^2 + \frac{4\mu}{9}\frac{1-\nu+P_2}{1-2\nu}\tilde{\varepsilon}_{\mathrm{vol}}^2 - \frac{\mu}{\pi k^2 \alpha}\tilde{\varepsilon}_{12}^2 F(\alpha, k)\right.$$
$$\left. -2\mu\Delta H^{t\to m}\frac{T_0 - T}{T_0} + \frac{2(1-\nu)}{\alpha B}\left[2(\alpha+1)\Delta\beta_{\mathrm{I/M}} + (2k-1)\beta_{\mathrm{I/I}}\right]\right). \tag{21.29}$$

For future reference we note that in the present scenario the far-field stress is at the same time the average stress over the whole domain $\langle\boldsymbol{\sigma}\rangle$ and the average matrix stress $\langle\boldsymbol{\sigma}\rangle_{\Omega^{\mathrm{M}}}$. Since in a general setting the inclusion will transform depending on the stress in the surrounding matrix, we can reinterpret the criterion (21.28) and write

$$\left|\boldsymbol{e}_1 \cdot \langle\boldsymbol{\sigma}\rangle_{\Omega^{\mathrm{M}}} \cdot \boldsymbol{e}_2\right| - (1-2\nu)\frac{\tilde{\varepsilon}_{\mathrm{vol}}}{\left|\tilde{\varepsilon}_{12}^{\left(\hat{k}\right)}\right|}\langle p\rangle_{\Omega^{\mathrm{M}}} \stackrel{!}{=} C_1. \tag{21.30}$$

21.3.2 Uniaxial Loading

In this section we apply the transformation criterion to uniaxial loading conditions in order to investigate the tension-compression asymmetry predicted by the model as well as geometric effects.

21.3.2.1 Orientation Dependence of the Transformation Stress

In the case of uniaxial loading, i.e., $\boldsymbol{\sigma}^{\infty} = \bar{\sigma}_{11}^{\infty}\, \bar{\boldsymbol{e}}_1 \otimes \bar{\boldsymbol{e}}_1$, we find

$$\boldsymbol{e}_1 \cdot \boldsymbol{\sigma}^{\infty} \cdot \boldsymbol{e}_2 = \bar{\sigma}_{11}^{\infty}\, (\boldsymbol{e}_1 \cdot \bar{\boldsymbol{e}}_1)(\bar{\boldsymbol{e}}_1 \cdot \boldsymbol{e}_2) = \frac{1}{2}\bar{\sigma}_{11} \sin(2\varphi) \quad \text{and} \quad p^{\infty} = -\frac{1}{3}\bar{\sigma}_{11}, \tag{21.31}$$

where φ is the angle enclosed between the crystallographic a-axis and the direction of loading. The transformation criterion (21.28) reduces to

$$\left|\bar{\sigma}_{11}^{\infty}\right| = \frac{C_1}{\underbrace{\frac{1}{2}\sin(2\varphi) \pm \frac{1}{3}(1-2\nu)\dfrac{\tilde{\varepsilon}_{\mathrm{vol}}}{\left|\tilde{\varepsilon}_{12}^{(\hat{k})}\right|}}_{=:C_2}} =: \sigma_{\mathrm{tr}}, \tag{21.32}$$

where the positive sign holds for tensile and the negative for compressive loading. Es expected, the stress required to initiate phase transformation strongly depends on the orientation of the inclusion relative to the applied load and is minimal if the tetragonal c-axis is aligned along the direction of maximum shear (see Fig. 21.13). Due to the increase in volume during the phase transition an asymmetry between tensile and compressive loading is observed. Further, it is clear from Fig. 21.13 that, while under sufficiently large tensile loading all inclusions will transform, this is not true in compression. In that case no transformation will occur if the misalignment between the tetragonal a-axis and the loading direction is less than $\varphi_{\mathrm{lim}} \approx 8°$. As a consequence, the maximal achievable transformation strain in a texture-free polycrystal is larger under tensile loading.

21.3.2.2 Sensitivity with Respect to the Inclusion Size, Aspect Ratio and Interfacial Energy

Is is clear that the critical stress to initiate phase transformation depends not only on the orientation of the inclusion relative to the applied load as discussed above, but among other parameters also on its geometry and assumptions concerning the interface energy between monoclinic lamellae. The effect of these parameters is investigated here under unaxial compression for a fixed orientation $\varphi = 45°$ by varying the values given in Table 21.4 in the range of $\pm 10\%$. The results are shown in Figs. 21.14, 21.15 and 21.16 and concur to the expectations: The transformation stress decreases with increasing size B and aspect ratio α of the inclusions and increases with increasing surface energy $\beta_{\mathrm{I/I}}$.

The sensitivity to the inclusion size and shape is particularly pronounced; for $\alpha = 5$ a change in B from 29 to 24 nm results in a change in transformation stress

of 250% in relative terms (see Fig. 21.14). A similar effect is achieved by changing the aspect ratio from 6 to 4 (see Fig. 21.15). Further, it should be noted that the transformation stress abruptly changes at certain values of B. This effect is due to

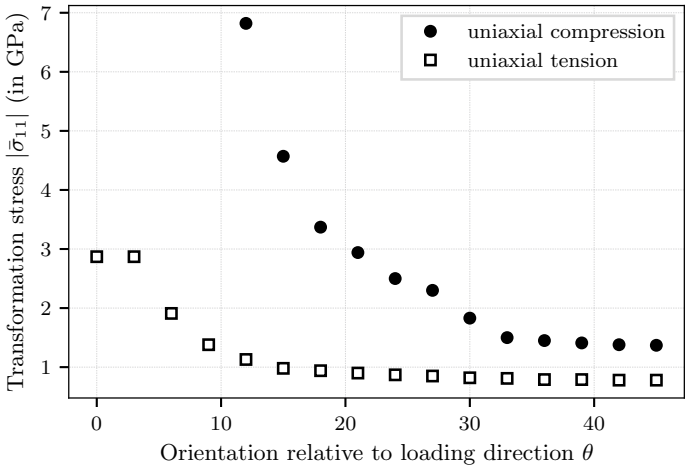

Fig. 21.13 Absolute value of the uniaxial stress necessary to induce phase transformation in dependence on the grain orientation φ with respect to the direction of external loading

Table 21.4 Baseline for the material parameters

B	α	E	ν	$\beta_{\mathrm{I/I}}$	$\Delta\beta_{\mathrm{I/M}}$	$\Delta H^{t\to m}$	T_0	T
36 nm	5.0	181 GPa	0.3	0.39 J/m^2 [25]	0.79 J/m^2 [25]	282 J/m^3 [29]	1150 K [30, 31]	22 K

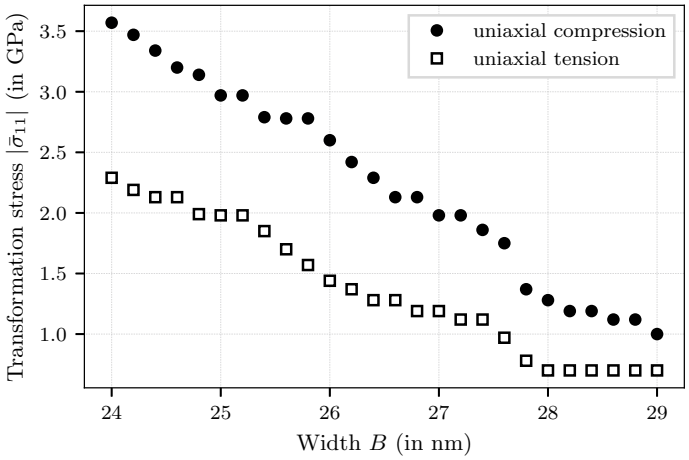

Fig. 21.14 Influence of the inclusion size B on the transformation stress under uniaxial compression for inclusions oriented under $\theta = 45°$ with respect to the direction of external loading

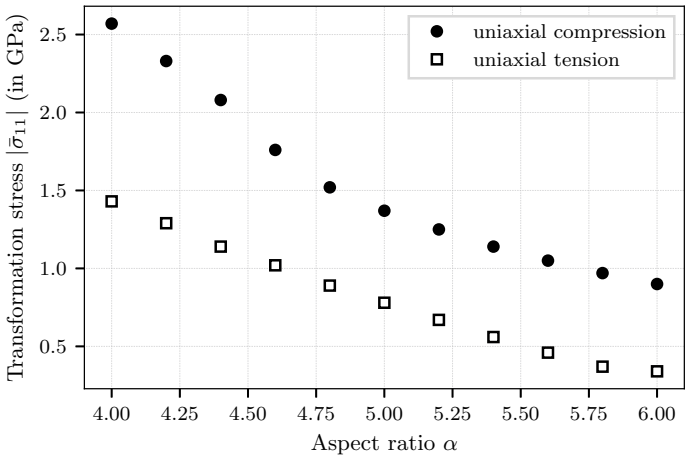

Fig. 21.15 Influence of the inclusion aspect ratio α on the transformation stress under uniaxial tension and compression for inclusions oriented under $\theta = 45°$ with respect to the direction of external loading

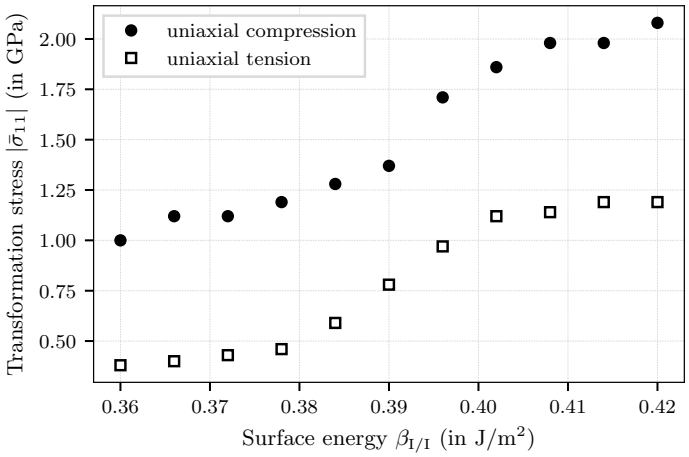

Fig. 21.16 Influence of the surface energy $\beta_{\mathrm{I/I}}$ between different monoclinic variants on the transformation stress under uniaxial tension and compression for inclusions oriented under $\theta = 45°$ with respect to the direction of external loading

the discrete nature of the optimization problem (21.27) and a direct consequence of our assumptions concerning the post-transformation microstructure; every jump of the transformation stress corresponds to a change in number of lamellae k and therefore to a change in microstructure.

21.4 Homogenization Within an Infinite Grain

The transformation criterion developed in the previous section can be used to describe the effective mechanical response of a PSZ grain with a volume fraction f_t of tetragonal inclusions, i.e. to relate the average stress $\langle\boldsymbol{\sigma}\rangle = \boldsymbol{\sigma}^{\infty}$ and the average strain $\langle\boldsymbol{\varepsilon}\rangle$ via an effective elastic stiffness tensor $\langle\mathbb{C}\rangle\left(\langle\boldsymbol{\sigma}\rangle_{\mathcal{B}_M}, T\right)$ in the form

$$\langle\dot{\boldsymbol{\sigma}}\rangle = \langle\mathbb{C}\rangle\left(\langle\boldsymbol{\sigma}\rangle_{\mathcal{B}_M}, T\right) : \langle\dot{\boldsymbol{\varepsilon}}\rangle, \tag{21.33}$$

where $\langle\boldsymbol{\sigma}\rangle_{\mathcal{B}_M}$ is the average matrix stress, which accounts for the interaction between the inclusions in accordance with Mori-Tanaka's method. In the case of monodispersed inclusions of size $\hat{B}$ the average matrix stress is given directly by [32]

$$\langle\boldsymbol{\sigma}\rangle_{\mathcal{B}_M} = \boldsymbol{\sigma}^{\infty} - f_m\left(\langle\boldsymbol{\sigma}\rangle_{\mathcal{B}_M}, T\right)\mathbb{C}^M : (\mathbb{S} - \mathbb{I}) : \tilde{\boldsymbol{\varepsilon}}^{(k)}\left(\langle\boldsymbol{\sigma}\rangle_{\mathcal{B}_M}, T, \hat{B}\right), \tag{21.34}$$

with monoclinic volume fraction $f_m\left(\langle\boldsymbol{\sigma}\rangle_{\mathcal{B}_M}, T\right)$, elastic stiffness of the matrix $\mathbb{C}^M = \mathbb{C}$ and ESHELBY tensor $\mathbb{S}$. Together with the transformation criterion (21.30) this equation can be used to determine the transformation strain in the inclusions, the average matrix stress and the monoclinic phase content. As the volume expansion during $t \to m$ transformation increases the tensile stresses in the matrix, which in turn facilitate the transformation, $f_m\left(\langle\boldsymbol{\sigma}\rangle_{\mathcal{B}_M}, T\right) = f_t$ immediately after the onset of the transformation and the process is autocatalytic. The corresponding effective elastic stiffness tensor is [33]

$$\begin{aligned}\langle\mathbb{C}\rangle\left(\langle\boldsymbol{\sigma}\rangle_{\mathcal{B}_M}, T, \hat{B}\right) = \mathbb{C}^M + f_m\left(\langle\boldsymbol{\sigma}\rangle_{\mathcal{B}_M}, T\right)\left[\mathbb{C}^I\left(\tilde{\boldsymbol{\varepsilon}}^{(k)}\left(\langle\boldsymbol{\sigma}\rangle_{\mathcal{B}_M}, T, \hat{B}\right)\right) - \mathbb{C}^M\right] : \\ : \{\mathbb{T}\} : \left[\left(1 - f_m\left(\langle\boldsymbol{\sigma}\rangle_{\mathcal{B}_M}, T\right)\right)\mathbb{I} + f_m\left(\langle\boldsymbol{\sigma}\rangle_{\mathcal{B}_M}, T\right)\{\mathbb{T}\}\right]^{-1},\end{aligned} \tag{21.35}$$

where $\mathbb{I}$ is the 4th-order identity, $\mathbb{C}^I\left(\tilde{\boldsymbol{\varepsilon}}^{(k)}\left(\langle\boldsymbol{\sigma}\rangle_{\mathcal{B}_M}, T, \hat{B}\right)\right)$ the elastic (tangent) stiffness of the inclusions,

$$\begin{aligned}\mathbb{T}\left(\tilde{\boldsymbol{\varepsilon}}^{(k)}\left(\langle\boldsymbol{\sigma}\rangle_{\mathcal{B}_M}, T, B\right)\right) := \Big[\mathbb{I} + \mathbb{S} : \left(\mathbb{C}^M\right)^{-1} \\ : \left[\mathbb{C}^I\left(\tilde{\boldsymbol{\varepsilon}}^{(k)}\left(\langle\boldsymbol{\sigma}\rangle_{\mathcal{B}_M}, T, B\right)\right) - \mathbb{C}^M\right]\Big]^{-1}\end{aligned} \tag{21.36}$$

and $\{\cdot\}$ denotes the orientation average. It is well known [18] that there exists an orientation relationship between the tetragonal inclusions and the cubic parent lattice such that the principal directions of the unit cells coincide, i.e., in a two dimensional scenario two families of inclusions (denoted by subscripts $\rightarrow$ and $\uparrow$) with mutually orthogonal c-axes exist in each grain. As a consequence, we find

$$\{\mathbb{T}\} = \frac{1}{2}\left(\mathbb{T}^{\rightarrow} + \mathbb{T}^{\uparrow}\right). \tag{21.37}$$

Choosing an orthonormal basis such that $\boldsymbol{e}_1$ is aligned along the c-axis of inclusion family $\rightarrow$, we find the following non-vanishing components of the ESHELBY tensors $\mathbb{S}^{\rightarrow}$ and $\mathbb{S}^{\uparrow}$

$$S^{\rightarrow}_{1111} = \frac{1}{2}\left[P_1 - (2P_2 + P_3)\right], \qquad S^{\rightarrow}_{1122} = -\frac{1}{2}\left[P_1 + (2P_2 + P_3)\right], \tag{21.38a}$$

$$S^{\rightarrow}_{2211} = -\frac{1}{2}\left[P_1 - (2P_2 + P_3)\right], \quad S^{\rightarrow}_{2222} = \frac{1}{2}\left[P_1 + (2P_2 + P_3)\right], \tag{21.38b}$$

$$S^{\rightarrow}_{1212} = \frac{1}{2}P_1, \qquad S^{\uparrow}_{1111} = \frac{1}{2}\left[P_1 + (2P_2 + P_3)\right], \tag{21.38c}$$

$$S^{\uparrow}_{1122} = -\frac{1}{2}\left[P_1 - (2P_2 + P_3)\right], \quad S^{\uparrow}_{2211} = -\frac{1}{2}\left[P_1 + (2P_2 + P_3)\right], \tag{21.38d}$$

$$S^{\uparrow}_{2222} = \frac{1}{2}\left[P_1 - (2P_2 + P_3)\right], \quad S^{\uparrow}_{1212} = \frac{1}{2}P_1, \tag{21.38e}$$

with P_1, P_2 defined in (21.24) and

$$P_3 = \frac{1}{\pi}\left[\frac{1}{\alpha}\ln\left(1+\alpha^2\right) - \alpha\ln\left(1+\frac{1}{\alpha^2}\right)\right]. \tag{21.39}$$

Prior to the $t \rightarrow m$ transformation $\mathbb{C}^{\mathrm{I}} = \mathbb{C}$ with bulk modulus K and shear modulus μ. To complete the formulation, assumptions concerning post-transformation behavior of $\mathbb{C}^{\mathrm{I}}$ are required, specifically

1. the elastic properties of the monoclinic and tetragonal phase are identical,
2. as long as $\left|\tilde{\varepsilon}^{(k)}_{12}\right| < \tilde{\tilde{\varepsilon}}_{12}$, the inclusions have no resistance to shear parallel to the c-axis, i.e. in the $\boldsymbol{e}_1 \otimes \boldsymbol{e}_2$-direction.

As a consequence we can write the (tangent) elastic stiffness of the inclusion in Voigt notation referring to the usual crystallographic coordinate system as

$$\mathbb{C}^{\mathrm{I}} = \begin{bmatrix} C^{\mathrm{I}}_{1111} & C^{\mathrm{I}}_{1122} & 0 \\ C^{\mathrm{I}}_{1122} & C^{\mathrm{I}}_{1111} & 0 \\ 0 & 0 & C^{\mathrm{I}}_{1212}\left(\tilde{\boldsymbol{\varepsilon}}^{(k)}\left(\langle\boldsymbol{\sigma}\rangle_{\mathcal{B}_M}, T, B\right)\right) \end{bmatrix}_{\boldsymbol{e}_i\otimes\boldsymbol{e}_j\otimes\boldsymbol{e}_k\otimes\boldsymbol{e}_l} \tag{21.40}$$

with

$$C^{\mathrm{I}}_{1111} = K + \frac{4}{3}\mu, \qquad C^{\mathrm{I}}_{1122} = K - \frac{2}{3}\mu,$$

and

$$C^{\mathrm{I}}_{1212}\left(\tilde{\boldsymbol{\varepsilon}}^{(k)}\left(\langle\boldsymbol{\sigma}\rangle_{\mathcal{B}_M}, T, B\right)\right) = \begin{cases}\mu & \left|\tilde{\varepsilon}^{(k)}_{12}\left(\langle\boldsymbol{\sigma}\rangle_{\mathcal{B}_M}, T, B\right)\right| = \tilde{\tilde{\varepsilon}}_{12},\\ 0 & \text{else.}\end{cases} \tag{21.41}$$

Under these assumptions we obtain from (21.35)

1. before the onset of transformation ($f_{\mathrm{m}}\left(\langle\boldsymbol{\sigma}\rangle_{\mathcal{B}_M}, T\right) = 0$)

$$\langle\mathbb{C}\rangle\left(\langle\boldsymbol{\sigma}\rangle_{\mathcal{B}_M}, T, \hat{B}\right) = \mathbb{C}, \tag{21.42}$$

2. after the onset of transformation ($f_{\mathrm{m}}\left(\langle\boldsymbol{\sigma}\rangle_{\mathcal{B}_M}, T\right) = f_{\mathrm{t}}$)

$$\langle\mathbb{C}\rangle\left(\langle\boldsymbol{\sigma}\rangle_{\mathcal{B}_M}, T, \hat{B}\right) = \begin{bmatrix} K + \left[\frac{4}{3} - Z_1(\varphi, f_{\mathrm{t}})\right]\mu & K - \left[\frac{2}{3} - Z_1(\varphi, f_{\mathrm{t}})\right]\mu & 0 \\ K - \left[\frac{2}{3} - Z_1(\varphi, f_{\mathrm{t}})\right]\mu & K + \left[\frac{4}{3} - Z_1(\varphi, f_{\mathrm{t}})\right]\mu & 0 \\ 0 & 0 & \left[1 - Z_2(\varphi, f_{\mathrm{t}})\right]\mu \end{bmatrix}, \tag{21.43}$$

where

$$Z_1(\varphi, f_{\mathrm{t}}) := Z(f_{\mathrm{t}})\sin^2(2\varphi), \qquad Z(f_{\mathrm{t}})\cos^2(2\varphi), \tag{21.44}$$

$$Z_2(\varphi, f_{\mathrm{t}}) := Z(f_{\mathrm{t}}) = \frac{f_{\mathrm{t}}}{1 - [1 - f_{\mathrm{t}}]P_1}, \qquad \cos\varphi = \boldsymbol{e}_1 \cdot \bar{\boldsymbol{e}}_1 \tag{21.45}$$

3. after the transformation shear reaches its maximum value $\tilde{\tilde{\varepsilon}}_{12}$,

$$\langle\mathbb{C}\rangle\left(\langle\boldsymbol{\sigma}\rangle_{\mathcal{B}_M}, T, \hat{B}\right) = \mathbb{C}. \tag{21.46}$$

21.5 Continuum Mechanics Approach

A pragmatic engineering approach to phase transition is a phenomenological modeling based on non-linear constitutive laws in the framework of continuum mechanics. The fundamentals are outlined e.g. in [34]. In particular for partially stabilized zirconia (PSZ), such a model was developed by Sun et al. [29]. Based on the concept of representative volume element (RVE) and the Hill-Rice internal variable theory [35], this model provides a set of constitutive equations for the inelastic deformations caused by tetragonal-monoclinic $t \rightarrow m$ phase transformation as function of monoclinic volume fraction. The model is restricted to a material point only. The authors of [29] did not realize an implementation of their model into a numerical tool to solve a boundary value problem for applications to real structures of PSZ. Therefore, in the present work, the Sun model was implemented into the finite ele-

ment code ABAQUS [36] to allow simulations of the TRIP-matrix composite as will be reported in Chap. 22.

Due to missing quantitative data for the model parameters Sun et al. [29] introduced instead of this an additional hardening term in the transformation condition, which is limited to the special case of proportional mechanical loading under isothermal conditions. Another weakness of this model is the assumption and averaging of homogeneously distributed microscopic quantities over the RVE. Therefore, in Mehlhorn et al. [37] the basic concept of the Sun model has been extended to capture not only the mechanical but as well the thermally induced phase transformation and thermal expansion to simulate thermomechanical processes. Moreover, the influence of the size of transformable tetragonal particles in the cubic matrix has been incorporated. The basic assumptions and the specific formulation of the model within a thermodynamic framework will be presented in the following.

21.5.1 Constitutive Model for Phase Transformation in PSZ

21.5.1.1 Homogenization of PSZ Material

To find the effective material behavior, a RVE is considered with two spatially discrete components, see Fig. 21.17. The first component, called *matrix*, contains two crystallographic phases: the untransformable cubic zirconia and transformable, tetragonal particles embedded in the cubic phase. The second component, denoted as *inclusions*, contains monoclinic zirconia particles, which are generated by phase transformation from their metastable tetragonal parents when the RVE is sufficiently high loaded.

The micro-scale field quantities inside the RVE are denoted with lower case letters, such as the stress $\boldsymbol{\sigma}$ and the strain $\boldsymbol{\epsilon}$. By calculating the volume average of these microscopic quantities (denoted by the operator $\langle \cdot \rangle$), the respective macroscopic quantities are found, which are referred to with upper case letters $\boldsymbol{\Sigma}$ and $\boldsymbol{E}$. The

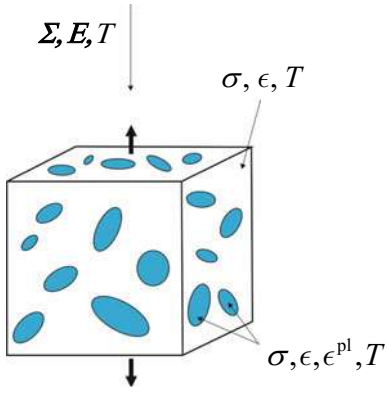

Fig. 21.17 Representative volume element of PSZ: matrix of cubic and tetragonal phase, inclusions of monoclinic particles

temperature T is assumed to be homogeneously distributed in the RVE. We denote the RVE domain with $\mathcal{B}_R$, the matrix and inclusion subdomains with $\mathcal{B}_M$ and $\mathcal{B}_I$, and their volumes with V_R, V_M and V_I, respectively. Thus, the relative volume fraction of transformed material is the basic internal variable calculated by

$$f_{\mathrm{m}} = V_I / V_R. \tag{21.47}$$

The macroscopic stress tensor is obtained by volume averaging as

$$\boldsymbol{\Sigma} = \langle \boldsymbol{\sigma} \rangle_{\mathcal{B}_R} = \frac{1}{V_R} \int_{\mathcal{B}_R} \boldsymbol{\sigma} \, \mathrm{d}V = f_{\mathrm{m}} \, \langle \boldsymbol{\sigma} \rangle_{\mathcal{B}_I} + (1 - f_{\mathrm{m}}) \, \langle \boldsymbol{\sigma} \rangle_{\mathcal{B}_M} . \tag{21.48}$$

The strain tensors can be decomposed into an elastic and plastic part $\boldsymbol{E} = \boldsymbol{E}^{\mathrm{el}} + \boldsymbol{E}^{\mathrm{pl}}$ and $\boldsymbol{\epsilon} = \boldsymbol{\epsilon}^{\mathrm{el}} + \boldsymbol{\epsilon}^{\mathrm{pl}}$, respectively. Using Hooke's law, the stress-strain relation for the RVE is determined by the elastic stiffness tensor $\mathbb{C}$

$$\boldsymbol{E}^{\mathrm{el}} = \mathbb{C}^{-1} : \boldsymbol{\Sigma} = \mathbb{C}^{-1} : \langle \boldsymbol{\sigma} \rangle_{\mathcal{B}_R} = \left\langle \mathbb{C}^{-1} : \boldsymbol{\sigma} \right\rangle_{\mathcal{B}_R} = \langle \boldsymbol{\epsilon} \rangle_{\mathcal{B}_R} . \tag{21.49}$$

The transformation strains exist only in the monoclinic inclusions and consist of a volumetric (dilatational) and a shear (deviatoric) component. This results in a macroscopic strain tensor

$$\boldsymbol{E}^{\mathrm{pl}} = \boldsymbol{E}^{\mathrm{pd}} + \boldsymbol{E}^{\mathrm{ps}} = f_{\mathrm{m}} \left\langle \boldsymbol{\epsilon}^{\mathrm{pd}} \right\rangle_{\mathcal{B}_I} + f_{\mathrm{m}} \left\langle \boldsymbol{\epsilon}^{\mathrm{ps}} \right\rangle_{\mathcal{B}_I} . \tag{21.50}$$

The microscopic volume dilatation $\boldsymbol{\epsilon}^{\mathrm{pd}}$ is assumed to be stress independent and constant ($\boldsymbol{I}$ denotes the rank-two unit tensor).

$$\boldsymbol{\epsilon}^{\mathrm{pd}} = \left\langle \boldsymbol{\epsilon}^{\mathrm{pd}} \right\rangle_{\mathcal{B}_I} = \frac{1}{3} \mathrm{tr}(\boldsymbol{\epsilon}^{\mathrm{pl}}) \boldsymbol{I}, \tag{21.51}$$

The shear component of the transformation strain $\boldsymbol{\epsilon}^{\mathrm{ps}}$, when averaged over a monoclinic volume element $d\mathcal{B}_I$, is proportionally related to the deviatoric stress $\boldsymbol{s}^M$ acting in the matrix material as follows

$$\boldsymbol{\epsilon}^{\mathrm{ps}} = \left\langle \boldsymbol{\epsilon}^{\mathrm{ps}} \right\rangle_{d\mathcal{B}_I} = A \frac{\boldsymbol{s}^M}{\sigma^M_{\mathrm{eq}}} \tag{21.52}$$

with the equivalent v.-Mises matrix stress σ^M_{eq}. The constant material parameter A describes the strength of the constraint imposed on the transformed monoclinic inclusions by the surrounding elastic matrix. The matrix stress $\boldsymbol{\sigma}^M$ is related to the macroscopic stress $\boldsymbol{\Sigma}$ acting on the RVE, via the elastic stiffness $\mathbb{C}$ and the amount f_{m} of transformed phase, and can be calculated by an Eshelby approach (see e.g. [38]) and the Mori-Tanaka homogenization scheme.

In addition, we consider a thermal expansion strain $\boldsymbol{E}^{\mathrm{th}}$ of the RVE, whereby $\Delta T = T - T_0$ denotes the difference between the temperature T at a specific process time and the initial or reference temperature T_0. The thermal expansion tensor $\boldsymbol{\alpha}$ is taken as constant.

$$\boldsymbol{E}^{\mathrm{th}} = \boldsymbol{\alpha}\Delta T. \tag{21.53}$$

21.5.1.2 Thermodynamic State Potentials

According to the thermodynamical framework of material modeling (see e.g. [39]), the constitutive equations of an elastic-plastic material can be derived from energy potential functions. The thermodynamical state of the RVE can be defined by the specific Helmholtz free energy φ_R, which is a function of the strain $\boldsymbol{E}$, the temperature T and the actual state of inelastic deformation represented by the monoclinic volume fraction f_{m} and the transformation strain $\langle \boldsymbol{\epsilon}^{\mathrm{ps}} \rangle_{\mathcal{B}_I}$.

$$\varphi_R = \varphi_R \left(\boldsymbol{E},\, T,\, f_{\mathrm{m}},\, \left\langle \boldsymbol{\epsilon}^{\mathrm{ps}} \right\rangle_{\mathcal{B}_I} \right). \tag{21.54}$$

The Helmholtz free energy φ_R of PSZ consists of three components: the stored elastic energy φ_R^{el}, the change in chemical free energy $\Delta\varphi_R^{\mathrm{ch}}$ and the surface free energy $\Delta\varphi_R^{\mathrm{sur}}$

$$\varphi_R = \varphi_R^{\mathrm{el}} + \Delta\varphi_R^{\mathrm{ch}} + \Delta\varphi_R^{\mathrm{sur}}. \tag{21.55}$$

The stored elastic energy φ_R^{el} is composed of two contributions: (i) the energy stored due to the elastic deformation, which is the total strain minus transformation and thermal strain terms $\boldsymbol{E}^{\mathrm{el}} = \boldsymbol{E} - \boldsymbol{E}^{\mathrm{pl}} - \boldsymbol{E}^{\mathrm{th}}$, and (ii) the elastic energy stored due to the internal stresses which are induced by the transformational eigenstrains $\boldsymbol{\epsilon}^{pl}$. Substituting the according expressions from (21.50) and (21.53), we get

$$\begin{aligned} \varphi_R^{\mathrm{el}} \left(\boldsymbol{E},\, T,\, f_{\mathrm{m}},\, \left\langle \boldsymbol{\epsilon}^{\mathrm{pl}} \right\rangle_{\mathcal{B}_I} \right) = \frac{1}{2} \left(\boldsymbol{E} - f_{\mathrm{m}} \left\langle \boldsymbol{\epsilon}^{\mathrm{pl}} \right\rangle_{\mathcal{B}_I} - \boldsymbol{\alpha}\Delta T \right) : \mathbb{C} : \left(\boldsymbol{E} - f_{\mathrm{m}} \left\langle \boldsymbol{\epsilon}^{\mathrm{pl}} \right\rangle_{\mathcal{B}_I} - \boldsymbol{\alpha}\Delta T \right) \\ - \frac{f_{\mathrm{m}}}{2V_R} \int_{\mathcal{B}_R} \boldsymbol{\sigma} : \boldsymbol{\epsilon}^{pl}\, \mathrm{d}V. \end{aligned} \tag{21.56}$$

A detailed derivation of the last term in the above equation is given in [40].

Given the difference of volume specific chemical free energy $\Delta\varphi^{\mathrm{ch}(t\to m)}$ between tetragonal and monoclinic phases of zirconia, the chemical free energy of the RVE $\Delta\varphi_R^{\mathrm{ch}}$ is changed during phase transformation by

$$\Delta\varphi_R^{\mathrm{ch}}\,(T,\, f_{\mathrm{m}}) = f_{\mathrm{m}}\, \Delta\varphi^{\mathrm{ch}}\,(T) = f_{\mathrm{m}}\, q \left(\frac{T}{T^*} - 1 \right). \tag{21.57}$$

In the present extension of the Sun model a temperature dependence of the phase transformation is incorporated by specifying $\Delta\varphi^{\mathrm{ch}}(T)$ as a function of the temperature, where q is the volume specific heat of transformation of zirconia and T^* is the tetragonal-monoclinic equilibrium temperature of zirconia.

Due to phase transformation the interface between particles and matrix exhibits a surface free energy $\Delta\varphi_R^{\mathrm{sur}}$. This energy term per volume of the RVE is calculated from the change of specific surface free energy $\Delta\varphi^{\mathrm{sur}(t\to m)}$ of zirconia and the monoclinic volume fraction f_{m} as follows

$$\Delta\varphi_R^{\mathrm{sur}}\left(f_{\mathrm{m}}\right) = \frac{3\,f_{\mathrm{m}}}{r(f_{\mathrm{m}})}\Delta\varphi^{\mathrm{sur}(t\to m)}. \tag{21.58}$$

In the original work [29] all transformable inclusions are assumed as spheres of equal size of radius $r(f_{\mathrm{m}}) = \text{const}$. However, the phase stability of a particle depends on its size as shown by Garvie [25], i.e. that smaller crystallites require a higher thermodynamical driving force to transform than larger particles. Therefore, Mehlhorn et al. [37] introduced a more realistic approach by assuming a continuous size distribution of transformable particles in the model. As a first approximation, this distribution function $h(r)$ may be chosen as constant in the

$$h(r) = \begin{cases} \frac{1}{r_{\max}-r_{\min}} & \text{for} \quad r_{\min} \le r \le r_{\max} \\ 0 & \text{for} \quad r < r_{\min} \text{ or } r > r_{\max}. \end{cases} \tag{21.59}$$

During loading, the phase transformation starts at largest particles with radius $r_{\max}$. A further increase in loading will trigger smaller particles to transform until all particles down to the radius $r_{\min}$ have become monoclinic. In the intermediate stage, the volume of all transformed particles, whose size is in the interval $[r, r_{\max}]$, is

$$V(r) = \frac{4}{3}\pi \int_r^{r_{\max}} h(\bar{r})\bar{r}^3\,\mathrm{d}\bar{r}, \quad f_{\mathrm{m}}(r) = \frac{V(r)}{V_R}. \tag{21.60}$$

constituting a corresponding volume fraction $f_{\mathrm{m}}(r)$ in the RVE. The maximum volume fraction is attained when all particles are monoclinic $f_{\mathrm{m}}^{\max} = f_{\mathrm{m}}(r_{\min})$. Inserting (21.59) in (21.60) leads to

$$f_{\mathrm{m}}(r) = \frac{1-(r/r_{\max})^4}{1-(r_{\min}/r_{\max})^4} f_{\mathrm{m}}^{\max}. \tag{21.61}$$

The inverse $f_{\mathrm{m}}^{-1}(r) = r(f_{\mathrm{m}})$ can be calculated analytically as follows

$$r\left(f_{\mathrm{m}}\right) = r_{\max}\left[1-\left(1-(r_{\min}/r_{\max})^4\right)\frac{f_{\mathrm{m}}}{f_{\mathrm{m}}^{\max}}\right]^{\frac{1}{4}}, \tag{21.62}$$

which marks the particle size dependent change in surface energy in (21.58).

By introducing a second thermodynamic dissipation function, an energetic transformation criterion was derived [29], which represents a combination of an isotropic expanding and kinematic shifting limit surface in the macroscopic stress space

$$F\left(\boldsymbol{\Sigma}, f_{\mathrm{m}}, \left\langle \boldsymbol{\epsilon}^{\mathrm{pl}} \right\rangle_{\mathcal{B}_I}\right) = \left(\boldsymbol{\Sigma} - f_{\mathrm{m}}\, \mathbb{C} : (\boldsymbol{\Lambda} - \mathbb{I}) : \left\langle \boldsymbol{\epsilon}^{\mathrm{pl}} \right\rangle_{\mathcal{B}_I}\right) : \left\langle \boldsymbol{\epsilon}^{\mathrm{pl}} \right\rangle_{d\mathcal{B}_I} - C(f_{\mathrm{m}}) = 0. \tag{21.63}$$

Hereby, the average matrix eigenstress $-f_{\mathrm{m}}\, \mathbb{C} : (\boldsymbol{\Lambda} - \mathbb{I}) : \left\langle \boldsymbol{\epsilon}^{\mathrm{pl}} \right\rangle_{\mathcal{B}_I}$ acts as backstress. ($\boldsymbol{\Lambda}$ is the so-called Eshelby tensor and $\mathbb{I}$ denotes the rank-four unity tensor.) The term $C(f_{\mathrm{m}})$ represents the energetic barrier, which must be overcome for phase transformation. It contains energy constants as well as a phenomenological hardening function depending linearly on f_{m}. Finally, the macroscopic constitutive law is obtained as relationship between the rates of strain and stress

$$\dot{\boldsymbol{E}} = \mathbb{C}^{-1} : \dot{\boldsymbol{\Sigma}} + \dot{f}_{\mathrm{m}} \left(\epsilon^{\mathrm{pd}} \boldsymbol{I} + A \frac{\boldsymbol{s}^M}{\sigma^M_{eq}} \right), \tag{21.64}$$

wherein the first term represents the elastic behavior and the second the inelastic deformation due to phase transformation. The general form resembles to a rate-independent associated flow. The rate of phase change $\dot{f}_{\mathrm{m}}$ is obtained from the consistency condition $\dot{F} = 0$.

This constitutive relationship is conformal with the second law of thermodynamics, demanding that the dissipation rate $\mathcal{D}$ is always positive. Obviously, the dissipation rate is proportional to the change in volume fraction of the monoclinic phase

$$\mathcal{D} = \begin{cases} D_0 \dot{f}_{\mathrm{m}} & \dot{f}_{\mathrm{m}} > 0 \text{ (tetragonal-to-monoclinic)} \\ -D_0 \dot{f}_{\mathrm{m}} & \dot{f}_{\mathrm{m}} < 0 \text{ (monoclinic-to-tetragonal)} \end{cases} \tag{21.65}$$

The proportionality factor D_0 is a phenomenological model parameter. The model accounts for both forward and reverse phase transformation by distinguishing between positive and negative rates of change. Also, the expression of C differs depending on whether forward or reverse transformation occurs.

21.5.2 Numerical Results

21.5.2.1 Particle Size Dependent Surface Energy Change

In order to understand, how the radius r of the currently active transforming particles varies with the monoclinic volume fraction f_{m} during the process of phase transformation, (21.62) is studied for three different size distribution functions $h_i(r_{\min}, i, r_{\max})$ with $i = 1, 2, 3$. For the upper limit of the particle size range a typical PSZ particle

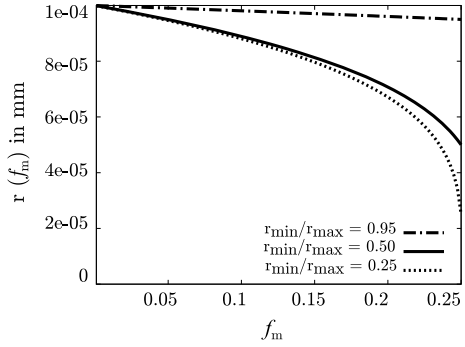

Fig. 21.18 Graphical representation of the function $r(f_m)$ in (21.62) for different particle size ratios and $f_m^{max} = 0.25$ [37]

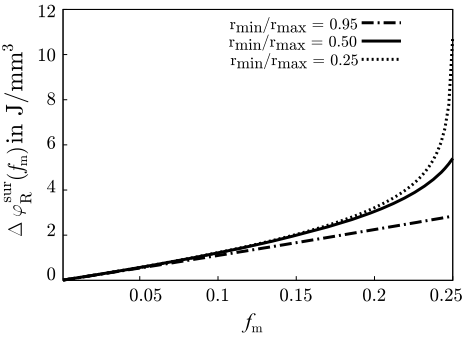

Fig. 21.19 Graphical representation of surface energy $\Delta\varphi_R^{sur}$ in (21.58) for different particle size ratios [37]

radius of $r_{max} = 1 \cdot 10^{-7}$ m is chosen. The values of r_{min} are taken as following fractions: $r_{min,1}/r_{max} = 0.95$, $r_{min,2}/r_{max} = 0.5$, and $r_{min,3}/r_{max} = 0.25$. Figure 21.18 gives a graphical representation of (21.62), using these values. It is obvious that a narrow size distribution (as $r_{min}/r_{max} = 0.95$) is very close to a constant particle size of the original Sun model, resulting in a slight dependence of the radius r on the transformed volume fraction f_m. The wider the distribution function $h(f_m)$ is (i.e. with smaller particle size ratios r_{min}/r_{max}), the stronger is the nonlinear dependence of r on f_m.

The influence of $r(f)$ on the volume specific surface energy change $\Delta\varphi_R^{sur}$ (21.58) is illustrated in Fig. 21.19. For a narrow particle size distribution with ratio $r_{min}/r_{max} = 0.95$, the surface energy change $\Delta\varphi_R^{sur}$ grows almost linear with f_m similar as in the original Sun model. For smaller ratios r_{min}/r_{max}, the extended material model shows a strong nonlinear increase of $\Delta\varphi_R^{sur}$, especially if $f_m \to f_m^{max}$, as it can be seen for $r_{min}/r_{max} = 0.25$ in Fig. 21.19. This means, $\Delta\varphi_R^{sur}$ acts as a transformation barrier, preventing very small particles from transforming even under high thermal or mechanical loading.

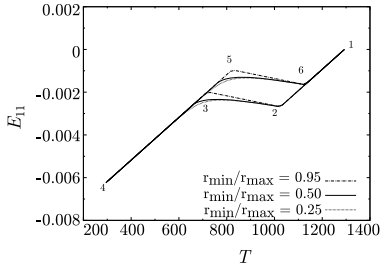

(a) Strain-temperature curves ($D_0 = 10$ MPa, $f_m^{max} = 0.25$)

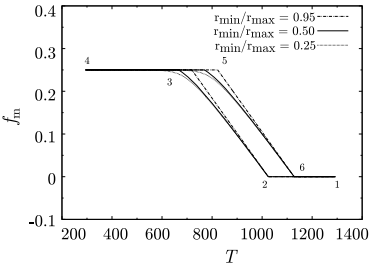

(b) Phase fraction-temperature curves ($D_0 = 10$ MPa, $f_m^{max} = 0.25$)

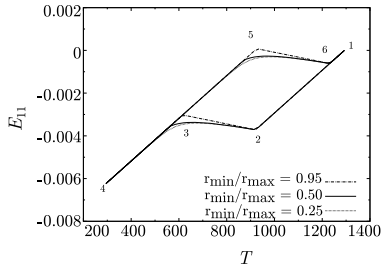

(c) Strain-temperature curves ($D_0 = 30$ MPa, $f_m^{max} = 0.25$)

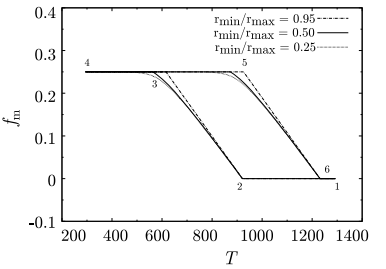

(d) Phase fraction-temperature curves ($D_0 = 30$ MPa, $f_m^{max} = 0.25$)

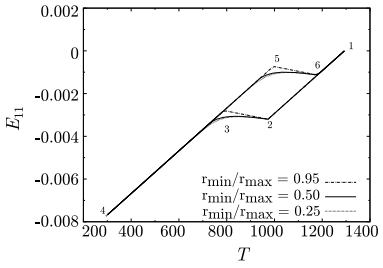

(e) Strain-temperature curves ($D_0 = 20$ MPa, $f_m^{max} = 0.15$)

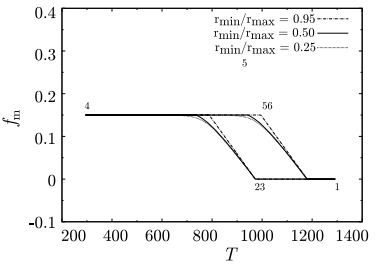

(f) Phase fraction-temperature curves ($D_0 = 20$ MPa, $f_m^{max} = 0.15$)

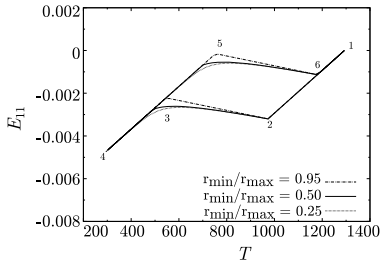

(g) Strain-temperature curves ($D_0 = 20$ MPa, $f_m^{max} = 0.35$)

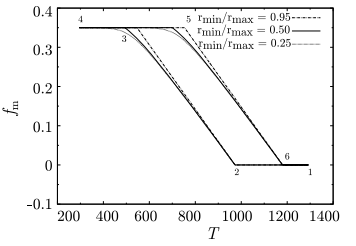

(h) Phase fraction-temperature curves ($D_0 = 20$ MPa, $f_m^{max} = 0.35$)

Fig. 21.20 Calculated strain-temperature curves and corresponding phase development for different particle size ratios. The sequence of the cooling-heating cycle is visualized by the numbers 1, …, 6 [37]

21.5.2.2 Temperature-Induced Phase Transformation

In order to demonstrate the ability of the extended material model to reproduce the hysteresis strain-temperature behavior of PSZ ceramics, a cooling-heating cycle 1373 K – 293 K – 1373 K is numerically simulated. The required model parameters associated with the changes in chemical energy (q and T^*, see (21.57)), are taken from literature: heat of transformation $q = 2.82\,\mathrm{J/m^3}$ and the phase equilibrium temperature $T^* = 1447\,\mathrm{K}$. The difference in specific surface energies between the tetragonal and monoclinic phase was set to $\Delta\varphi^{\mathrm{sur}(t\to m)} = 0.36\,\mathrm{J/m^2}$, see [37]. Since no values for the dissipation parameter D_0 and the amount of transformable tetragonal material $f_{\mathrm{m}}^{\max}$ were available, they were estimated in order to obtain physically meaningful results. Moreover, a variation of these parameters is performed to study their influence on the material model behavior. D_0 was specified to the values 10, 20, and 30 MPa. $f_{\mathrm{m}}^{\max}$ was set to 0.15, 0.25 and 0.35, respectively. For all remaining model parameters the values published by Sun et al. [29] are used.

Figure 21.20 shows the numerically obtained strain-temperature curves $E_{11} - T$ and the corresponding phase evolution f_{m}–T during the cooling-heating cycle for different sets of model parameters. As it can be seen, the typical strain hysteresis loops of PSZ ceramics are predicted by the material model, caused by a tetragonal-to-monoclinic transformation on cooling and a reverse transformation on heating. In each diagram, the influence of particle size distribution is included by varying the ratio ($r_{\mathrm{min,i}}$, $r_{\max}$). It can be seen in all diagrams, that smaller size ratios lead to a considerably nonlinear strain-temperature behavior and rounded transition curves. The influence of D_0 on the strain-temperature curves can be observed in Fig. 21.20a–d. D_0 governs the size of the strain hysteresis between cooling and heating. In contrast, $f_{\mathrm{m}}^{\max}$ influences the total transformation strain and hence the length of the temperature interval in which transformation occurs, see Fig. 21.20e–h.

These results demonstrate the feasibility of the extended material model, which forms a solid basis for simulations of structures and composites made of PSZ. Unfortunately, it was not possible to identify the required parameters for the type of MgO-stabilized ZrO_2 manufactured in the CRC799.

21.6 Simulations of ZrO_2-Particle Reinforced TRIP-Steel Composite

In order to assist the development of particle reinforced composites manufactured by a powder metallurgical process route from TRIP-steel and partially stabilized ZrO_2 ceramics particles, accompanying numerical simulations have been carried out. The mechanical properties of such a composite material are quite complex as they arise from the properties of its individual components, their volume content, and the properties of the interface between them. As explained in the previous sections, PSZ can undergo a stress-triggered phase transformation. This can lead to an additional

toughening effect compared to non-transformable ceramics as observed in [41]. The TRIP-steel exhibits a deformation induced phase transformation from the austenitic parent phase to martensite. By combining the two materials using TRIP steel as matrix and PSZ as strengthening particles, an elasto-viscoplastic particle-reinforced composite is created with the capability of phase transformation in each component.

21.6.1 Unit Cell Model of the Composite

A well established method to investigate the mechanical response of composites is a parameter study using a suitable mechanical cell model of the composite, which is simulated by means of the finite element method, see for example Mishnaevsky [42].

In this work, this approach has been applied to study the effective stress-strain behavior of this particulate TRIP steel-ZrO_2 composite. Details can be found in the publications of Mehlhorn, Prüger et al. [43–45]. The influence of the volume content of ZrO_2 particles and the interface properties on the overall response of the composite is investigated. Three different interface types are considered: (i) perfectly bonded, (ii) not bonded, and (iii) cohesive law, respectively, The calculations of the material responses are performed using a finite element analysis of unit cells of the composites under tensile, compressive and biaxial loading. Here, selected results will be reported.

Numerical simulations of composites require proper constitutive equations for both constituents. Here, the Sun model [29] as explained above is employed for the PSZ ceramics. For modeling the viscoplastic deformation and martensitic phase transformation of the TRIP steel, the constitutive law developed by Prüger [46] is applied. It describes the strain-induced transformation from a fully austenitic microstructure (γ) to martensite (α') under thermal and/or mechanical loading. Both material models were available as Fortran routines implemented via UMAT interface into the finite element software ABAQUS [47]. More information about the used material parameters for the PSZ and the specific TRIP-steel can be found in [43–45], and in Chap. 22.

In case of the particular composite, sintered together from steel and ceramic particles, one can assume a representative unit cell consisting of a large number of approximately equally sized and uniformly distributed ceramic particles in a TRIP steel matrix. For simplicity, the embedded ceramic particles are assumed to be spheres. This leads to the unit cell model shown in Fig. 21.21, which is a cube of edge length $2a$ with a single spherical ZrO_2 particle placed in its center.

The mechanical model exhibits a triple symmetry with respect to geometry and loading. Therefore the use of one-eighth of the RVE is admissible, and a corresponding FEM discretization is elaborated. Although the unit cell was numerically simulated under various stress triaxialities, only the results for uniaxial loading are reported here. Regarding the interface between the components, two limiting cases are discussed here: the perfectly bonded connection and the non-bonded, frictionless movable contact. An optimal composite possesses a high energy absorption capacity

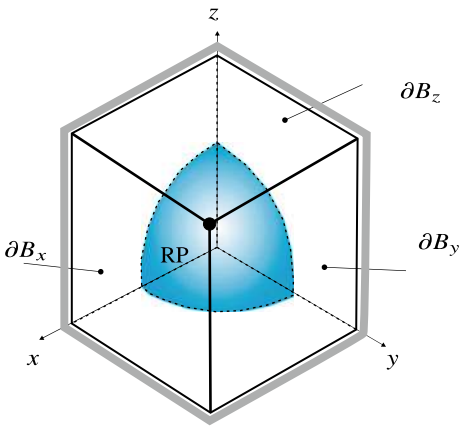

Fig. 21.21 Sketch of unit cell (one-eighth volume) for the TRIP-ZrO_2 composite. Symmetry boundary conditions are set on the coordinate planes $x = 0$, $y = 0$ and $z = 0$. Appropriate displacement and stress boundary conditions are prescribed on opposite planes ∂B_x, ∂B_y and ∂B_z for the different load cases.
The radius r of the particle is adjusted to the volume fraction f of zirconia content by $f(r) = \frac{V_{\text{sphere}}}{V_{\text{cube}}} = \frac{\pi r^3}{6a^3}$

and exhibits pronounced phase transformation in the ZrO_2 ceramic and the TRIP steel. The macroscopic true stress and true strain tensors Σ and $\mathbf{E}$ are used in order to evaluate the mechanical work according to $W = \int_0^{\bar{\mathbf{E}}} \Sigma : \mathrm{d}\mathbf{E}$, where $\bar{\mathbf{E}}$ denotes the considered deformation stage. Because the elastic strains are small, W equals approximately the energy absorption for sufficiently large total strains. In order to quantify the relative change in energy absorption capacity, this energy is related to those values W_{hom} obtained for a unit cell made only of TRIP steel.

During deformation an inhomogeneous distribution of the volume fractions of the monoclinic zirconia and the martensite develop in the ceramic and the TRIP steel, respectively. Therefore the averages of $f_{\alpha'}$ and f_{m} over the corresponding volumes are used. The simulation is stopped, when the maximum principle stress in the PSZ reaches its ultimate tensile strength $\sigma_{\text{cr}}^{\text{t}} = 1600\,\text{MPa}$.

21.6.2 Results and Discussion

The macroscopic true stress and true strain curves are calculated for different variants. The following diagrams show the second invariants Σ^{eq} and E^{eq} of both variables (to allow comparison with different stress states). The macroscopic strain invariant acts as a loading parameter, whereas the stress and the phase transformation in both components of the composite represent the material response. Table 21.5 summarizes the relative change in energy absorption capability for uniaxial tension.

Table 21.5 Energy absorption capacity for the composite with perfectly bonded and non-cohesive interface in uniaxial loading

f	0.05	0.05	0.10	0.10	0.20	0.20
Interface	Bonded	Non-cohesive	Bonded	Non-cohesive	Bonded	Non-cohesive
W/W_{hom}	1.06	0.92	1.16	0.85	1.37	0.72

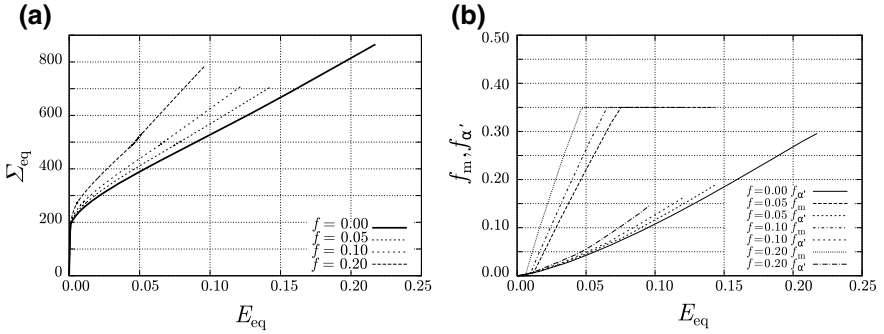

Fig. 21.22 Numerical results for the RVE with perfectly bonded interface in uniaxial loading: **a** stress-strain diagram and **b** phase development curves [43]

In case of the **perfectly bonded interface**, the stress-strain curves show a distinct dependence on the volume fraction of ZrO_2 ceramic f, as depicted in Fig. 21.22a. It can be observed that an increasing f leads to higher yield stresses and strain hardening rates compared to the unreinforced TRIP steel ($f = 0$). As consequence, a pronounced increase in the energy absorption W of the composite is obtained. Comparing the values given in Table 21.5, the ratio W/W^{hom} increases up to more than 35% (for same macroscopic equivalent strain). Due to the strong interface, load is transferred from the matrix to the reinforcement during deformation of the composite. Therefore high stresses occur in the ceramic, which reduces the maximal attainable strain with increasing zirconia content f. Regarding the phase transformation behavior, a higher volume fraction of zirconia f enhances the tendency to phase transformation in zirconia as well as in TRIP steel (Fig. 21.22b). The phase transformation capacity in the PSZ component is saturated to the maximum of 35% in a smaller strain interval. The tendency to phase transformation in the TRIP steel f'_α increases at higher zirconia content, but is limited due to failure of the ceramic.

In case of a **non-cohesive interface**, both the initial yield stress and the strain hardening rate tend to decrease with higher zirconia content f, see Fig. 21.23a. Figure 21.23b shows that the development of martensite is considerably higher than in the case of the perfectly bonded interface. At the end of deformation nearly 30% of martensite has evolved. Because of the non-cohesive interface, no tensile stresses are transferred from the TRIP steel matrix to the zirconia inclusion. Thus, no phase transformation is seen in zirconia. Moreover, the area of the load bearing cross-section consists of TRIP steel only and is the smaller the higher the zirconia content

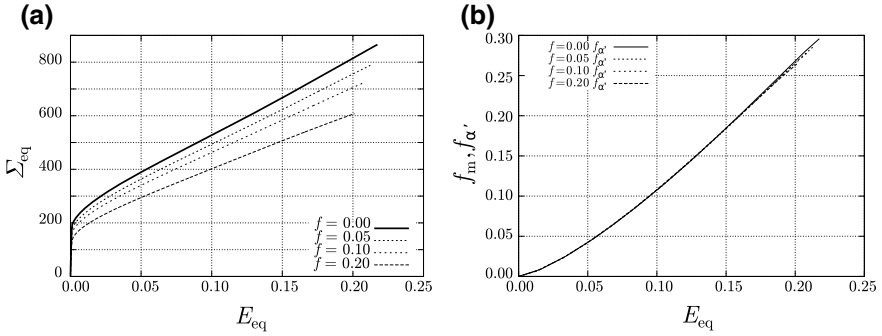

Fig. 21.23 Numerical results for the RVE with non-cohesive interface in uniaxial loading: **a** stress-strain diagram and **b** phase development curves [43]

becomes, which reduces macroscopic yield stress. After debonding, the particle acts partially like a void. However, no softening is observed in the macroscopic stress-strain response because of the hardening behavior of the TRIP steel and the locking effect caused by the particle.

One can conclude that the behavior of the real composite material lies between the two extreme cases considered here, since the interface between ceramic and steel has a finite strength. Moreover, the impact of particle reinforcement is stronger under compressive loading [45].

21.7 Conclusions

Based on the work of Levitas and Preston [13] for generic martensitic transformation, a phase-field model for MgO-ZrO_2 material was implemented [16]. The potential function used in this work results in a proper representation of transformation behavior of zirconia ceramics from a pure thermodynamic stand point. In the simulations different patterns of microstructures were found for cooling induced and stress induced transformation. These patterns are consistent with experimental observations by Hannink et al. [18]. It is evident that the presence of an energy barrier plays a key role in variant selection and the transformation path taken. By which, in stress induced case a sequential growth of lamellae was visible. In contrast, the cooling induced case is categorized with an almost homogeneous nucleation where all variants are preferred to evolve. Additionally on a single crystal level the simulations showed that, in the stress induced case, microstructure with junction planes parallel to the 'c'-axis is formed because of variant selection. It was shown that residual stresses inside t-phase lentils from $c \rightarrow t$ transformation have a magnitude of $\approx$0.3 GPa and contribute to the stability of the t-phase. Also the magnitude of stress required for introducing energy barrier increases with decreasing temperature below M_s.

A mesomechanical, two-dimensional model for Mg-PSZ with an energetic transformation criterion based on the analytical solution for a rectangular inclusion in an infinite matrix has been successfully developed. Using this model the influence of individual parameters such as size, geometry and surface energies on the transformation initiation and resulting microstructure can be efficiently studied. It predicts that the stability of the tetragonal inclusions deteriorates as the inclusions grow in size and aspect-ratio. Further, the tension-compression asymmetry of the transformation behavior known from experiments is captured correctly. A homogenization approach based on the Mori-Tanaka method predicts the transformation to be auto-catalytic within a grain.

A continuum material model for transformation plasticity in partially stabilized zirconia ceramics has been further developed to account for (i) particle size dependent phase transformation behavior, (ii) temperature dependent phase transformation, and (iii) thermoelastic deformation. These more physically based features lead to a nonlinear hardening behavior and smoothly rounded hysteresis curves for the strain and the generated monoclinic phase fraction during a temperature cycle. The influence of the tetragonal particle size distribution on phase transformation could be predicted qualitatively quite well.

Finally, the mechanical properties of a TRIP steel matrix reinforced by ZrO_2 particles are analyzed, taking the phase transformation in both constituents into account. The influence of the volume content and the interface properties of ZrO_2 particles on the overall response of the composite is investigated. Material variants with three different zirconia contents and two different interface types, perfectly bonded and non-cohesive, respectively, are considered. The calculations of the material responses are performed using a finite element analysis of representative volume elements of the composites under tensile, compressive and biaxial loading. The results indicate that the enrichment of the TRIP steel with zirconia particles leads to a significant strengthening effect provided the interface has cohesive properties.

Acknowledgements The authors gratefully acknowledge the the German Research Foundation or Deutsche Forschungsgemeinschaft (DFG) for supporting this work in subproject C4, and was created as part of the Collaborative Research Center TRIP-Matrix-Composites (Project number 54473466—CRC 799). We appreciate the contributions of former colleagues Dr.-Ing. Uwe Mühlich, Dr.-Ing. Stefan Prüger, and Lars Mehlhorn to the achievements.

References

1. S. Decker, L. Krüger, S. Richter, S. Martin, U. Martin, Steel Res. Int. **83**(6), 521 (2012)
2. R.C. Garvie, R.H.J. Hannink, R.T. Pascoe, Nature **258**(5537), 703 (1975)
3. A.G. Evans, A.H. Heuer, J. Am. Ceram. Soc. **63**(5–6), 241 (1980)
4. A.G. Evans, N. Burlingame, M. Drory, W.M. Kriven, Acta Metall. **29**(2), 447 (1981)
5. F.F. Lange, J. Mater. Sci. **17**(1), 240 (1982)
6. T. Hensl, U. Mühlich, M. Budnitzki, M. Kuna, Acta Mater. **86**, 361 (2014)
7. R.C. Garvie, J. Phys. Chem. **69**(4), 1238 (1965)
8. Y. Wang, H. Wang, L.Q.Q. Chen, A.G. Khachaturyan, J. Am. Ceram. Soc. **76**(12), 3029 (1993)

9. Y. Wang, H.Y.Y. Wang, L.Q.Q. Chen, A.G. Khachaturyan, J. Am. Ceram. Soc. **78**(3), 657 (1995)
10. Y. Wang, A.G. Khachaturyan, Acta Mater. **45**(2), 759 (1997)
11. M. Mamivand, M.A. Zaeem, H.E. Kadiri, L.Q. Chen, Acta Mater. **61**(14), 5223 (2013)
12. M. Mamivand, M. Asle Zaeem, H. El Kadiri, Int. J. Plast. **60**, 71 (2014)
13. V. Levitas, D. Preston, Three-dimensional Landau theory for multivariant stress-induced martensitic phase transformations I Austenite <–> martensite. Phys. Rev. B **66**(13), 1–9 (2002). https://doi.org/10.1103/PhysRevB.66.134206
14. V. Levitas, D. Preston, Three-dimensional Landau theory for multivariant stress-induced martensitic phase transformations. II. Multivariant phase transformations and stress space analysis. Phy. Rev. B **66**(13), 1–15. https://doi.org/10.1103/PhysRevB.66.134207
15. V. Levitas, D.L. Preston, D.W. Lee, Phys. Rev. B **68**(13), 1 (2003)
16. M.K. Rajendran, M. Kuna, M. Budnitzki, Undercooling versus stress induced martensitic phase transformation: the case of MgO—partially stabilized zirconia. Comput. Mater. Sci. **174**, 109460 (2019). https://doi.org/10.1016/j.commatsci.2019.109460
17. P.M. Kelly, C.J. Ball, J. Am. Ceram. Soc. **69**(3), 259 (1986)
18. R.H.J. Hannink, P.M. Kelly, B.C. Muddle, J. Am. Ceram. Soc. **83**(3), 461 (2000)
19. X.S. Zhao, S.L. Shang, Z.K. Liu, J.Y. Shen, J. Nucl. Mater. **415**(1), 13 (2011)
20. H. Lukas, S. Fries, B. Sundman, *Computational Thermodynamics—The CALPHAD Method* (Cambridge University Press, 2007)
21. D. Pavlyuchkov, G. Savinykh, O. Fabrichnaya, J. Eur. Ceram. Soc. **34**(5), 1397 (2014)
22. L.Q. Chen, W. Yang, Phys. Rev. B **50**(21), 15752 (1994)
23. G.K. Bansal, A.H. Heuer, Acta Metall. **20**(11), 1281 (1972)
24. G.K. Bansal, A.H. Heuer, Acta Metall. **22**(4), 409 (1974)
25. R.C. Garvie, J. Phys. Chem. **82**(2), 218 (1978)
26. C.R. Chen, S.X. Li, Q. Zhang, Mater. Sci. Eng. A **272**(2), 398 (1999)
27. W.E. Lee, M. Rainforth, *Ceramic Microstructures Property Control by Processing* (Chapman & Hall, 1994)
28. R. Garvie, M. Swain, J. Mater. Sci. **20**, 1193 (1985)
29. Q.P. Sun, K.C. Hwang, S.W. Yu, J. Mech. Phys. Solids **39**(4), 507 (1991)
30. C. Wang, M. Zinkevich, F. Aldinger, J. Am. Ceram. Soc. **89**(12), 3751 (2006)
31. I.W. Chen, Y.H. Chiao, Acta Metall. **31**(10), 1627 (1983)
32. T. Mori, K. Tanaka, Acta Metall. **21**(5), 571 (1973)
33. Y. Benvensite, Mech. Mater. **6**(2), 147 (1987)
34. F.D. Fischer, Q.P. Sun, K. Tanaka, Appl. Mech. Rev. **49**(6), 317 (1996)
35. J.R. Rice, J. Mech. Phys. Solids **19**(6), 433 (1971)
36. Abaqus, *Abaqus, Online documentation*, 6th edn. (Dassault Systems, 2014)
37. L. Mehlhorn, U. Mühlich, M. Kuna, Adv. Eng. Mater. **15**(7), 638 (2013)
38. D. Gross, T. Seelig, *Bruchmechanik—Mit einer Einführung in die Mikromechanik*, 4th edn. (Springer, Berlin Heidelberg, 2007)
39. A. Puzrin, G. Houlsby, Int. J. Plast. **16**(9), 1017 (2000)
40. T. Mura, Mechanics of elastic and inelastic solids, in *Micromechanics of Defects in Solids* (Springer, 1991)
41. D.B. Marshall, J. Am. Ceram. Soc. **69**(3), 173 (1986)
42. L.L. Mishnaevsky, Acta Mater. **52**(14), 4177 (2004)
43. L. Mehlhorn, S. Prüger, S. Soltysiak, U. Mühlich, M. Kuna, Steel Res. Int. **82**(9), 1022 (2011)
44. S. Prüger, L. Mehlhorn, S. Soltysiak, M. Kuna, Comput. Mater. Sci. **64**, 273 (2012)
45. S. Prüger, L. Mehlhorn, U. Mühlich, M. Kuna, Adv. Eng. Mater. **15**(7), 542 (2013)
46. S. Prüger, Thermomechanische Modellierung der dehnungsinduzierten Phasenumwandlung und der asymmetrischen Verfestigung in einem TRIP-Stahlguss. Ph.D. thesis, TU Bergakademie Freiberg, 2016
47. Hibbitt, Karlsson, Sorenson, *ABAQUS: Version 6.7 Documentation* (HKS, 2009)

Chapter 22
Modeling of the Thermomechanical Behavior, Damage, and Fracture of High Alloy TRIP-Steel

Andreas Seupel, Andreas Burgold, Stefan Prüger, Michael Budnitzki and Meinhard Kuna

Abstract The aim of this chapter is to give insight into the continuum mechanics based modeling of high alloy TRIP-steels. A powerful thermomechanical framework is presented, which incorporates finite viscoplasticity, the TRIP-effect, complete thermomechanical coupling, and non-local damage. Based on this, different variants of material models are developed. Thereby, selected topics concerning the material behavior of TRIP-steels are examined: Firstly, the mechanical behavior at different temperatures and strain rates is modeled including tension-compression-asymmetry and curve crossing effects. Secondly, the influence of phase transformation on fracture is investigated. Because of the TRIP-effect, higher stresses occur during crack tip blunting. Furthermore, a transformation induced shielding effect is revealed by the evaluation of material forces. Thirdly, damage evolution and crack extension are simulated with a cohesive zone model and with the non-local damage model, respectively. The damage related parameters of these models are determined using available experimental data. The developed numerical models enable quantitative assessments of failure in components made of TRIP-steels.

22.1 Introduction

In order to optimize design and functionality of components and structures made of TRIP-steels, appropriate macroscopic models for simulation purposes are required. Furthermore, micromechanically informed models can be used in numerical studies to improve the material design itself, e.g., the constitution of composite materials like the particle-reinforced TRIP-matrix composites considered in CRC 799 [1–5].

The particular challenges of modeling the deformation behavior of high alloy TRIP-steels are manifold: Firstly, a considerable variation of mechanical response with changing temperature is observed due to the high influence of temperature on the underlying deformation mechanisms (TRIP-effect: transformation induced plas-

A. Seupel (✉) · A. Burgold · S. Prüger · M. Budnitzki · M. Kuna
Institute of Mechanics and Fluid Dynamics, Lampadiusstraße 4, 09596 Freiberg, Germany
e-mail: Andreas.Seupel@imfd.tu-freiberg.de

H. Biermann and C. G. Aneziris (eds.), *Austenitic TRIP/TWIP Steels and Steel-Zirconia Composites*, Springer Series in Materials Science 298,
https://doi.org/10.1007/978-3-030-42603-3_22

ticity, TWIP-effect: twinning induced plasticity, dislocation glide, [6–8]). A thermomechanical coupling has to be taken into account in order to explain and model loading rate effects basically caused by the temperature dependency, e.g., the curve crossing effect [9, 10]. Another modeling aspect is given by the observed loading state dependent strain hardening of TWIP and TRIP-steels often recognized as tension-compression asymmetry or strength differential effect [11–14]. Moreover, the question arises, how the TRIP-effect influences the damage and fracture behavior of austenitic steels. This becomes of interest in safety applications, metal forming, and lightweight design. Taking damage and material degradation into account, conceptional problems arise: So-called local damage models imply an ill-posed boundary value problem in the classical continuum mechanics framework. A regularization method is necessary to circumvent pathological effects during numerical treatment, e.g., the mesh dependency well known from numerical analyses utilizing the Finite-Element-Method (FEM).

In this paper, two types of material models for high alloy TRIP-steels are presented – each developed to meet different requirements according to the CRC's state-of-the-art: Firstly, a micromechanically motivated model is considered and enhanced which is based on an advanced homogenization scheme [15]. Thereby, information on the state and micromechanical features of both phases, austenite and martensite, can be included. In addition, the model exhibits a higher predictive character than purely phenomenological approaches. For example, the model is successfully applied in micromechanical simulations conducted to assess and to improve the properties of particle reinforced TRIP-matrix-composites [16–18]. Furthermore, the model is used in fundamental investigations on fracture mechanics aspects of high alloy TRIP-steel, which reveal the role of martensitic phase transformation on ductility and fracture resistance [19–21]. Moreover, essential enhancements of the micromechanical model are proposed elsewhere, especially to incorporate thermomechanical coupling and stress state dependent hardening behavior of high alloy TRIP-steels [9, 22].

However, due to the high complexity and sophisticated numerical treatment of the micromechanical model, a robust phenomenological alternative is developed as basis for advanced damage modeling. The main aim is to set up a regularized damage model, which does not suffer from pathological localization effects. Simultaneously, a thermomechanically coupled variant of the model is proposed, which includes asymmetric strain hardening.

The paper is organized as follows: In the next section, a thermomechanical-micromorphic framework for finite deformations is briefly introduced, which is especially used as basis for the regularized damage model and to discuss thermodynamical aspects.

In the third section, the distinct material models are presented. As common starting point, a multiplicative viscoplasticity and martensite kinetics models for the strain induced regime are used.

In the fourth section, modeling results on thermomechanical material response, damage, and fracture are presented. The thermomechanically enhanced phenomenological model is calibrated to experimental results of a cast X3CrMnNi 16-6-6 TRIP-steel developed within the CRC 799. Afterwards, the model is assessed by

comparing the model predictions of thermomechanical loading and inhomogeneous deformation scenarios to available experiments. Using the micromechanical material model, numerical investigations on influence of the TRIP-effect on crack tip fields and fracture mechanics properties are discussed. Fracture of high alloy TRIP-steels is modeled by a cohesive zone approach, and finally by the micromorphic model of ductile damage.

22.2 Thermomechanical Framework

The thermomechanically coupled modeling as well as the regularized damage formulation are set up within the micromorphic framework proposed by Forest [23]. The thermomechanical DOF are the displacement vector $\vec{u}$ and the absolute temperature ϑ. The degrees of freedom (DOF) are enriched by a scalar valued micromorphic variable $\varepsilon_{\mathrm{nl}}$:

$$\mathrm{DOF} = \{\vec{u}, \vartheta, \varepsilon_{\mathrm{nl}}\}\,. \tag{22.1}$$

The micromorphic variable has a local counterpart, which should be enhanced by gradient effects.

The local material behavior depends on the evolution of state variables (SV). Inelastic, loading history dependent processes are treated by the thermodynamics of internal variables principle. The chosen state variables read

$$\mathrm{SV} = \left\{\boldsymbol{\varepsilon}^{\mathrm{el}}_{\log}, \vartheta, \kappa_\alpha, \varepsilon_{\mathrm{nl}}, \mathrm{grad}_{\mathrm{x}}\varepsilon_{\mathrm{nl}}\right\}, \tag{22.2}$$

where $\boldsymbol{\varepsilon}^{\mathrm{el}}_{\log}$ and κ_α denote the elastic logarithmic strain and an arbitrary set of scalar internal variables, respectively. Additionally, the material's state is influenced by the micromorphic variable $\varepsilon_{\mathrm{nl}}$ and its spatial gradient.

22.2.1 Balance Equations

The necessary mechanical and micromorphic balance equations can be deduced with help of the *principle of virtual power* [23, 24]. The continuity equation (conservation of mass, mass density ρ) is assumed:

$$\dot{\rho} + \rho\,\mathrm{div}_{\mathrm{x}}\vec{v} = 0, \tag{22.3}$$

where $\vec{v}$ denotes the substantial velocity. In what follows, virtual quantities are highlighted by an asterisk $()^*$. The internal virtual power P_{i}^* yields

$$P_{\mathrm{i}}^{*} = -\int_{\mathfrak{B}} p_{\mathrm{i}} \,\mathrm{d}v, \quad p_{\mathrm{i}}^{*} = \boldsymbol{\sigma} : \boldsymbol{D}^{*} + m_{\mathrm{nl}} \dot{\varepsilon}_{\mathrm{nl}}^{*} + \vec{M}_{\mathrm{nl}} \cdot \mathrm{grad}_{\mathrm{x}} \dot{\varepsilon}_{\mathrm{nl}}^{*}, \tag{22.4}$$

with the prescribed virtual power density p_{i}^{*}. The spatial domain currently occupied by the material body is given by $\mathfrak{B}$. The boundary of the material body and the infinitesimal volume element are denoted as $\partial\mathfrak{B}$ and dv, respectively. The symmetric CAUCHY-stress tensor and the rate of deformation tensor are denoted as $\boldsymbol{\sigma}$ and $\boldsymbol{D}$, respectively. The virtual power is enriched by the micromorphic variable and its gradient as well as by their conjugated generalized stresses m_{nl} and $\vec{M}_{\mathrm{nl}}$.

The external virtual power is formulated by volume specific and contact terms

$$P_{\mathrm{e}}^{*} = \int_{\mathfrak{B}} \rho \vec{f} \cdot \vec{v}^{*} \,\mathrm{d}v + \int_{\partial\mathfrak{B}_{\mathrm{t}}} \vec{t} \cdot \vec{v}^{*} \,\mathrm{d}a + \int_{\partial\mathfrak{B}_{\mathrm{m}}} m_{\mathrm{c}} \dot{\varepsilon}_{\mathrm{nl}}^{*} \,\mathrm{d}a, \tag{22.5}$$

where $\vec{f}$ is a mass specific force and $\vec{t}$ as well as m_{c} denote tractions acting on the infinitesimal surface element $\mathrm{d}a$.

Furthermore, a classical D'ALEMBERT inertia term is considered

$$P_{\mathrm{a}}^{*} = -\int_{\mathfrak{B}} \rho \dot{\vec{v}} \cdot \vec{v}^{*} \,\mathrm{d}v. \tag{22.6}$$

Evaluating the principle of virtual power,

$$P_{\mathrm{i}}^{*} + P_{\mathrm{e}}^{*} + P_{\mathrm{a}}^{*} = 0, \tag{22.7}$$

yields the following balance equations: Firstly, the balance of linear momentum is obtained, which is complemented by boundary and initial conditions:

$$\mathrm{div}_{\mathrm{x}} \boldsymbol{\sigma} + \rho \vec{f} = \rho \dot{\vec{v}} \qquad \forall \vec{x} \in \mathfrak{B}, \tag{22.8}$$

$$\vec{t} = \boldsymbol{\sigma} \cdot \vec{n} \qquad \forall \vec{x} \in \partial\mathfrak{B}_{\mathrm{t}} \tag{22.9}$$

$$\vec{u} = \bar{\vec{u}} \qquad \forall \vec{x} \in \partial\mathfrak{B}_{\mathrm{u}}, \tag{22.10}$$

$$\vec{v}\,(\vec{x}, t_0) = \vec{v}_0 \qquad \forall \vec{x} \in \mathfrak{B}. \tag{22.11}$$

The outward unit normal is introduced as $\vec{n}$.

Secondly, the micromorphic balance and related boundary conditions are obtained

$$\mathrm{div}_{\mathrm{x}} \vec{M}_{\mathrm{nl}} = m_{\mathrm{nl}} \qquad \forall \vec{x} \in \mathfrak{B}, \tag{22.12}$$

$$m_{\mathrm{c}} = \vec{M}_{\mathrm{nl}} \cdot \vec{n} \qquad \forall \vec{x} \in \partial\mathfrak{B}_{\mathrm{m}}, \tag{22.13}$$

$$\varepsilon_{\mathrm{nl}} = \bar{\varepsilon}_{\mathrm{nl}} \qquad \forall \vec{x} \in \partial\mathfrak{B}_{\mathrm{e}}. \tag{22.14}$$

Furthermore, the local forms of the thermodynamical principles read

$$\rho\dot{\psi} + \vartheta\dot{s} + s\dot{\vartheta} = p_{\mathrm{i}} - \mathrm{div}_{\mathrm{x}}\vec{q}_{\mathrm{th}} + \rho\, p_{\mathrm{th}} \qquad \text{(energy balance)}. \tag{22.15}$$

and

$$-\rho s\dot{\vartheta} - \rho\dot{\psi} + p_{\mathrm{i}} - \frac{1}{\vartheta}\vec{q}_{\mathrm{th}} \cdot \mathrm{grad}_{\mathrm{x}}\vartheta \geq 0. \qquad \text{(dissipation inequality)}. \tag{22.16}$$

Herein, the HELMHOLTZ free energy ψ is chosen as state potential. The specific entropy, the heat flux, and the mass specific heat source are denoted as s, $\vec{q}_{\mathrm{th}}$, and p_{th}, respectively. The term p_{i} denotes the physical counterpart of the virtual power given in (22.4).

22.2.2 Constitutive Assumptions and Equations

The high formability and ductile damage mechanisms of TRIP-steels imply a finite deformation framework as basis of constitutive modeling. As constitutive assumption, an additive split of the rate of deformation tensor $\boldsymbol{D}$ into an elastic, viscoplastic, and transformation induced part is considered:

$$\boldsymbol{D} = \boldsymbol{D}_{\mathrm{el}} + \boldsymbol{D}_{\mathrm{vpl}} + \boldsymbol{D}_{\mathrm{trip}}. \tag{22.17}$$

A state potential based on the logarithmic strain is proposed:

$$\psi = \psi\left(\boldsymbol{\varepsilon}^{\mathrm{el}}_{\mathrm{log}}, \vartheta, \kappa_\alpha, \varepsilon_{\mathrm{nl}}, \mathrm{grad}_{\mathrm{x}}\varepsilon_{\mathrm{nl}}\right). \tag{22.18}$$

The constitutive-dependent quantities $\left\{\boldsymbol{\sigma}, s, K_\alpha, m_{\mathrm{nl}}, \vec{M}_{\mathrm{nl}}\right\}$ have the same dependencies as ψ (principle of equi-presence). Utilizing the COLEMAN-NOLL-procedure [25], constitutive relations can be deduced from the dissipation inequality (22.16) plugging in the state potential (22.18):

$$\boldsymbol{\sigma} = \rho\frac{\partial\psi}{\partial\boldsymbol{\varepsilon}^{\mathrm{el}}_{\mathrm{log}}},\; s = -\frac{\partial\psi}{\partial\vartheta},\; \vec{M}_{\mathrm{nl}} = \rho\frac{\partial\psi}{\partial\mathrm{grad}_{\mathrm{x}}\varepsilon_{\mathrm{nl}}},\; m_{\mathrm{nl}} = \rho\frac{\partial\psi}{\partial\varepsilon_{\mathrm{nl}}}. \tag{22.19}$$

The conjugated thermodynamic forces to the internal variables are defined as

$$K_\alpha = \rho\frac{\partial\psi}{\partial\kappa_\alpha}. \tag{22.20}$$

Furthermore, expressions for the thermal and mechanical dissipation remain, which have to be fulfilled independently:

$$\gamma_{\mathrm{th}} = -\frac{1}{\vartheta}\vec{q}_{\mathrm{th}} \cdot \mathrm{grad}_{\mathrm{x}}\vartheta \geq 0, \tag{22.21}$$

$$\gamma_{\mathrm{m}} = \boldsymbol{\sigma} : \left(\boldsymbol{D}_{\mathrm{vpl}} + \boldsymbol{D}_{\mathrm{trip}}\right) - K_{\alpha}\dot{\kappa}_{\alpha} \geq 0. \tag{22.22}$$

The thermal and mechanical dissipation inequalities set restrictions on the definitions of the heat flux vector $\vec{q}_{\mathrm{th}}$, the evolution equations of the inelastic deformation rates $\left\{\boldsymbol{D}_{\mathrm{vpl}}, \boldsymbol{D}_{\mathrm{trip}}\right\}$, and the internal variables κ_{α} to be proposed.

22.2.2.1 State Potential

To specify the state potential (22.18), the set of state variables is complimented by the choice of scalar internal variables $\kappa_{\alpha} = \{r, f_{\mathrm{sb}}, z, D\}$:

- r: strain hardening variable (isotropic)
- f_{sb}: volume fraction of shear bands
- z: volume fraction of α'-martensite
- D: damage variable (isotropic)

Subsequently, a multiplicative viscoplasticity approach is introduced, as classified by Lemaître and Chaboche [26, Sect. 6.4.2]. Therefore, the state potential must not contain the hardening variable r to ensure non negative mechanical dissipation, see [26, Sect. 6.4.2]. Moreover, the stored energy in shear bands is neglected. Thus, the HELMHOLTZ free energy is given as $\psi\left(\boldsymbol{\varepsilon}^{\mathrm{el}}_{\mathrm{log}}, \vartheta, z, D, \varepsilon_{\mathrm{nl}}, \mathrm{grad}_{\mathrm{x}}\varepsilon_{\mathrm{nl}}\right)$:

$$\rho\psi = \rho\psi_{\mathrm{el}}\left(\boldsymbol{\varepsilon}^{\mathrm{el}}_{\mathrm{log}}, \vartheta, D\right) + \rho\psi_{\mathrm{chem}}\left(\vartheta, z\right) + \rho\psi_{\vartheta}\left(\vartheta\right) + \rho\psi_{\mathrm{nl}}\left(\varepsilon_{\mathrm{nl}}, \mathrm{grad}_{\mathrm{x}}\varepsilon_{\mathrm{nl}}\right). \tag{22.23}$$

The thermoelastic part reads

$$\psi_{\mathrm{el}} = (1 - D)\,\frac{1}{\rho}\frac{1}{2}\left(\boldsymbol{\varepsilon}^{\mathrm{el}}_{\mathrm{log}} - \alpha_{\mathrm{th}}\left(\vartheta - \vartheta_0\right)\boldsymbol{\delta}\right) : \boldsymbol{\mathcal{C}} : \left(\boldsymbol{\varepsilon}^{\mathrm{el}}_{\mathrm{log}} - \alpha_{\mathrm{th}}\left(\vartheta - \vartheta_0\right)\boldsymbol{\delta}\right). \tag{22.24}$$

Isotropic thermoelastic properties are assumed for the cast TRIP-steel, defined by the fourth order tensor of elastic stiffness $\boldsymbol{\mathcal{C}}$ and the thermal expansion coefficient α_{th}. Moreover, the elastic and thermal expansion properties are assumed to be similar for the austenitic and martensitic phase [27]. Damage D degrades the elastic energy leading to material softening.

The chemical part describes the difference in GIBBS-energy of the two phases given by a rule of mixture:

$$\psi_{\mathrm{chem}} = (1 - z)\,\psi_{\mathrm{a}}\left(\vartheta\right) + z\psi_{\mathrm{m}}\left(\vartheta\right). \tag{22.25}$$

The purely temperature dependent term

$$\psi_\vartheta = c_\epsilon^0 \left(\vartheta - \vartheta \ln \left(\frac{\vartheta}{\vartheta_*} \right) \right), \tag{22.26}$$

defines a constant part c_ϵ^0 of the specific heat similar for both phases with a reference temperature ϑ_*.

The last term in (22.23) comprises the micromorphic contributions. A conventional quadratic structure is prescribed, see [23]:

$$\begin{aligned} \rho \psi_{\mathrm{nl}} = & \frac{1}{2} H_{\mathrm{nl}} \left(\int_{t_0}^{t} \dot{\varepsilon}_{\mathrm{l}} \left(\boldsymbol{D}_{\mathrm{vpl}} \right) \, \mathrm{d}\tau - \varepsilon_{\mathrm{nl}} \right)^2 \\ & + \frac{1}{2} A_{\mathrm{nl}} \, \mathrm{grad}_{\mathrm{x}} \varepsilon_{\mathrm{nl}} \cdot \mathrm{grad}_{\mathrm{x}} \varepsilon_{\mathrm{nl}}. \end{aligned} \tag{22.27}$$

The first part penalizes the difference of the local strain like value, defined by the integral, and the micromorphic variable $\varepsilon_{\mathrm{nl}}$. The penalty stiffness is prescribed by the parameter H_{nl}. The integral defines a scalar value, which is extracted from the viscoplastic deformation rate $\boldsymbol{D}_{\mathrm{vpl}}$ serving as driving force for damage. The second term states the micromorphic gradient contribution weighted by the parameter A_{nl}.

22.2.2.2 Consistent Rate Formulation

The CAUCHY-stress defined in (22.19) can be evaluated using (22.23) and (22.24):

$$\boldsymbol{\sigma} = \rho \frac{\partial \psi}{\partial \boldsymbol{\varepsilon}_{\log}^{\mathrm{el}}} = (1 - D) \, \boldsymbol{\mathcal{C}} : \left(\boldsymbol{\varepsilon}_{\log}^{\mathrm{el}} - \alpha_{\mathrm{th}} \left(\vartheta - \vartheta_0 \right) \boldsymbol{\delta} \right). \tag{22.28}$$

Applying the effective stress concept [28], the constitutive equation reads

$$\hat{\boldsymbol{\sigma}} = \frac{\boldsymbol{\sigma}}{1 - D} = \boldsymbol{\mathcal{C}} : \left(\boldsymbol{\varepsilon}_{\log}^{\mathrm{el}} - \alpha_{\mathrm{th}} \left(\vartheta - \vartheta_0 \right) \boldsymbol{\delta} \right), \tag{22.29}$$

where $\hat{\boldsymbol{\sigma}}$ designates the effective stress acting on an undamaged cross section of the material; $\boldsymbol{\sigma}$ is then interpreted as the net stress. In what follows, a hat $\hat{(\cdot)}$ highlights quantities which are computed from the effective stress tensor $\hat{\boldsymbol{\sigma}}$.

The stress-strain relation has to be given in an objective rate form in order to implement the model into the user subroutine UMAT of the FEM-software ABAQUS. As objective time derivative, the logarithmic rate $\overset{\diamond}{(\cdot)}$ introduced by Xiao et al. [29, 30] is applied to both sides of (22.29). Hence, the rate formulation

$$\overset{\diamond}{\hat{\boldsymbol{\sigma}}} = \boldsymbol{\mathcal{C}} : \left(\boldsymbol{D}_{\mathrm{el}} - \alpha_{\mathrm{inst}} \boldsymbol{\delta} \dot{\vartheta} \right), \tag{22.30}$$

is consistent with the notion of elasticity [31], where α_{inst} denotes the instantaneous coefficient of thermal expansion. The logarithmic rate of the logarithmic strain tensor $\boldsymbol{\varepsilon}^{\mathrm{el}}_{\log}$ yields the rate of deformation tensor $\boldsymbol{D}_{\mathrm{el}}$ as shown in [30]. The logarithmic rate of the effective CAUCHY-stress reads

$$\overset{\diamond}{\hat{\boldsymbol{\sigma}}} = \frac{\mathrm{d}\hat{\boldsymbol{\sigma}}}{\mathrm{d}t} - \boldsymbol{\Omega}_{\log} \cdot \hat{\boldsymbol{\sigma}} - \hat{\boldsymbol{\sigma}} \cdot \boldsymbol{\Omega}^{\mathrm{T}}_{\log}. \tag{22.31}$$

The skew logarithmic spin $\boldsymbol{\Omega}_{\log}$ can be found in [29].

22.2.2.3 Generalized Stresses

The COLEMAN-relations for generalized stresses in (22.19) are specified as

$$\vec{M}_{\mathrm{nl}} = A_{\mathrm{nl}} \operatorname{grad}_{\mathrm{x}} \varepsilon_{\mathrm{nl}}, \tag{22.32}$$

$$m_{\mathrm{nl}} = H_{\mathrm{nl}} \left(\varepsilon_{\mathrm{nl}} - \int_{t_0}^{t} \dot{\varepsilon}_{\mathrm{l}} \left(\boldsymbol{D}_{\mathrm{vpl}} \right) \, \mathrm{d}\tau \right) = H_{\mathrm{nl}} \left(\varepsilon_{\mathrm{nl}} - \varepsilon_{\mathrm{l}} \right), \tag{22.33}$$

where the integral is substituted for reasons of clarity by ε_{l}. With (22.32) and (22.33) at hand, the micromorphic balance (22.12) can be rewritten in the established manner [23, 32]

$$L^2_{\mathrm{nl}} \Delta_{\mathrm{x}} \varepsilon_{\mathrm{nl}} = \varepsilon_{\mathrm{nl}} - \varepsilon_{\mathrm{l}} \qquad \forall \vec{x} \in \mathfrak{B}, \tag{22.34}$$

where the internal length L_{nl} is defined as

$$L^2_{\mathrm{nl}} = \frac{A_{\mathrm{nl}}}{H_{\mathrm{nl}}} \geq 0. \tag{22.35}$$

The spatial Laplacian is denoted as Δ_{x}. Thereby, the micromorphic balance (22.34) is identical to the partial differential equation of implicit gradient enhancement proposed by Peerlings et al. [33], which has been used in own preliminary studies [34, 35]. Following the suggestion in [33], trivial natural boundary conditions are prescribed on all free boundaries

$$\operatorname{grad}_{\mathrm{x}} \varepsilon_{\mathrm{nl}} \cdot \vec{n} = 0 \qquad \forall \vec{x} \in \partial \mathfrak{B}_{\mathrm{m}} = \partial \mathfrak{B}. \tag{22.36}$$

As result of this choice, the overall mean values of the micromorphic variable and its local counterpart are equal [34].

22.2.2.4 Thermodynamic Forces

The conjugated thermodynamic forces $K_\alpha = \{R, F_{\mathrm{sb}}, Z, Y\}$ associated with the set of internal variables are specified by (22.20) as

$$R = \rho \frac{\partial \psi}{\partial r} = 0, \tag{22.37}$$

$$F_{\mathrm{sb}} = \rho \frac{\partial \psi}{\partial f_{\mathrm{sb}}} = 0, \tag{22.38}$$

$$Z = \rho \frac{\partial \psi}{\partial z} = \rho \psi_{\mathrm{m}}(\vartheta) - \rho \psi_{\mathrm{a}}(\vartheta) = \triangle g_{\mathrm{chem}}^{\mathrm{a} \to \mathrm{m}}(\vartheta), \tag{22.39}$$

$$Y = \rho \frac{\partial \psi}{\partial D} = -\frac{1}{2} \left(\boldsymbol{\varepsilon}_{\log}^{\mathrm{el}} - \alpha_{\mathrm{th}} (\vartheta - \vartheta_0) \boldsymbol{\delta} \right) : \boldsymbol{\mathcal{C}} : \left(\boldsymbol{\varepsilon}_{\log}^{\mathrm{el}} - \alpha_{\mathrm{th}} (\vartheta - \vartheta_0) \boldsymbol{\delta} \right). \tag{22.40}$$

The driving force for martensitic phase transition Z consists of the energy difference $\triangle g_{\mathrm{chem}}^{\mathrm{a} \to \mathrm{m}}(\vartheta)$, which is negative once the temperature is below the thermodynamic equilibrium temperature [36], i.e., in the region of interest. The energy release rate Y is always negative or zero, $Y \leq 0$.

22.2.3 Dissipation and Heat Equation

The mechanical dissipation (22.22) can be intermediately specified as

$$\gamma_{\mathrm{m}} = \boldsymbol{\sigma} : \left(\boldsymbol{D}_{\mathrm{vpl}} + \boldsymbol{D}_{\mathrm{trip}} \right) - Z \dot{z} - Y \dot{D}. \tag{22.41}$$

The requirement $\gamma_{\mathrm{m}} \geq 0$ is discussed in detail after introducing the evolution laws for the martensite volume fraction $\dot{z}$ and the damage variable $\dot{D}$ for the different modeling approaches.

The heat equation can be obtained from the energy balance (22.15), see [9]. Neglecting coupling terms and assuming FOURIERs law, a rudimentary format can be obtained typically used for computation purposes [9]:

$$\rho c_\epsilon^0 \dot{\vartheta} = \lambda_{\mathrm{th}} \Delta_{\mathrm{x}} \vartheta + \tilde{p} \qquad \forall \vec{x} \in \mathfrak{B} \tag{22.42}$$

with the heat source

$$\tilde{p} = \gamma_{\mathrm{m}} + \rho \, p_{\mathrm{th}}. \tag{22.43}$$

The specific heat c_ϵ^0 and the conductivity λ_{th} are assumed as constants.

22.3 Material Models

22.3.1 Preliminaries for both Models

Both considered material models are based on the previously introduced thermomechanical framework and a multiplicative viscoplasticity formulation discussed within the next subsection. In order to describe the α'-martensite formation, two modifications of the OLSON-COHEN model [37] (OC-model) for strain induced martensite evolution are developed for thermomechanical loading conditions: A micromechanically extended approach and a simplified empirical model allowing for a fast parameter calibration. The macroscopic TRIP-kinematics are introduced to conclude the section.

22.3.1.1 Multiplicative Viscoplasticity

In order to take characteristic strain rate effects of high alloy TRIP-steels into account, a multiplicative viscoplasticity framework is utilized. A dissipation potential of NORTON-type is proposed:

$$\phi\left(\boldsymbol{\sigma}\right) = \frac{\left(1-D\right)\dot{\varepsilon}_0\sigma_\mathrm{y}}{m+1}\left(\frac{\hat{\sigma}_\mathrm{eq}}{\sigma_\mathrm{y}}\right)^{(m+1)}. \tag{22.44}$$

The model parameters m and $\dot{\varepsilon}_0$ control the strain rate sensitivity. Isotropic strain hardening can be taken into account by the yield stress $\sigma_\mathrm{y}\left(r,z\right)$. Within the next sections, the potential (22.44) is extended by contributions of all invariants of the effective stress tensor:

$$\hat{I}_1 = \mathrm{tr}\left(\hat{\boldsymbol{\sigma}}\right), \qquad \hat{J}_2 = \frac{1}{2}\hat{\boldsymbol{S}}:\hat{\boldsymbol{S}}, \qquad \hat{J}_3 = \frac{1}{3}\mathrm{tr}\left(\hat{\boldsymbol{S}}\cdot\hat{\boldsymbol{S}}\cdot\hat{\boldsymbol{S}}\right), \tag{22.45}$$

where the stress deviator is introduced as

$$\hat{\boldsymbol{S}} = \hat{\boldsymbol{\sigma}} - \frac{1}{3}\hat{I}_1\boldsymbol{\delta}. \tag{22.46}$$

The unit tensor of second order is denoted as $\boldsymbol{\delta}$. The original NORTON-potential (22.44) is only influenced by the VON MISES equivalent stress

$$\hat{\sigma}_\mathrm{eq} = \sqrt{3\hat{J}_2}. \tag{22.47}$$

22.3.1.2 Strain Induced Martensite

The well established OC-model [37] is based on the observation that nuclei of α'-martensite are predominantly formed at intersections of shear bands. The evolution of shear band volume fraction f_{sb} is modeled as

$$\dot{f}_{\mathrm{sb}} = \alpha_{\mathrm{oc}} \left(1 - f_{\mathrm{sb}}\right) \dot{\varepsilon}_{\mathrm{eq}}, \tag{22.48}$$

where the parameter α_{oc} is a function of temperature and stress state [38–40]. As scalar measure of plastic deformation, the rate of equivalent (visco-)plastic deformation $\dot{\varepsilon}_{\mathrm{eq}}$ is utilized. The original evolution equation of α'-martensite volume fraction z proposed by Olson and Cohen [37] reads

$$\dot{z} = (1 - z)\, \beta_{\mathrm{oc}}\, n_{\mathrm{oc}}\, f_{\mathrm{sb}}^{(n_{\mathrm{oc}}-1)}\, \dot{f}_{\mathrm{sb}}. \tag{22.49}$$

The probability to form a martensite embryo at a shear band intersection is cast into the parameter β_{oc}. The specific geometric setting of the shear bands is taken into account by the parameter n_{oc}. Modifications of (22.48) and (22.49) are discussed in the separate section of the different material models.

22.3.1.3 TRIP Kinematics

During martensitic phase transformation, inelastic strains occur which become visible on the macroscopic scale of polycrystalline material [41, 42]. These so-called TRIP-strains comprise a volumetric part and a deviatoric part. Two effects lead to these inelastic strains: A formation of favorable oriented martensite variants according to the applied stress state (MAGEE-effect) and additional plastic deformation of the austentite during accommodation of newly formed martensite (GREENWOOD-JOHNSON-effect), see [43] and [44, p. 69ff]. An empirical evolution law of the TRIP-deformation rate reads

$$\boldsymbol{D}_{\mathrm{trip}} = \left(k_{\mathrm{gj}}\, \hat{\sigma}_{\mathrm{eq}} \frac{\mathrm{d}\varphi\,(z)}{\mathrm{d}z} + k_{\mathrm{s}} \right) \boldsymbol{N} \dot{z} + \frac{1}{3} \triangle_{\mathrm{v}} \boldsymbol{\delta} \dot{z} \tag{22.50}$$

with the flow normal

$$\boldsymbol{N} = \frac{3}{2\hat{\sigma}_{\mathrm{eq}}} \hat{\boldsymbol{S}}. \tag{22.51}$$

From (22.50), many modifications proposed in literature can be deduced [9, 12, 38, 39, 41, 45–50]. The first part shows that the magnitude of the TRIP-strain depends on the applied stress level as measured by Nagayama et al. [42]; the parameter k_{gj} is called GREENWOOD- JOHNSON-constant. The additional constant contribution k_{s} is used by Stringfellow et al. [38].

The volumetric strain is prescribed by the parameter $\triangle_{\mathrm{v}}$, which typically ranges from 2 to 4% depending on the carbon content of the considered alloy.

Nagayama et al. [42] and Ahrens [41] conducted experiments on temperature induced martensitic transformation and simultaneously applied external stresses. From these experiments, a magnitude for the stress dependent, deviatoric uni-axial TRIP-strain of about 1.5–2.0 % can be found. This is in accordance to the statement of Martin [51, Sect. 2.1.6] that the TRIP-contribution to the whole inelastic deformation is comparatively small. The high ductility of high alloy TRIP-steels is attributed to the excellent strain hardening, which postpones localization effects.

22.3.2 Micromechanically Motivated Model

Starting with the assumption that formed α'-martensite nuclei and domains act as inclusions, homogenization schemes can be developed to predict the effective macroscopic material response. Thereby, the modeling gains a microstructural well-founded character. The utilized analytic homogenization approach is well documented in literature. Therefore, only a brief summary is given, which is needed to understand the results on crack tip loading in Sect. 22.4.3. For details, the reader is referred to the numerous available publications devoted to the model development within CRC 799 [9, 22, 47, 52, 53]. Damage effects are neglected for this approach, i.e., $D = 0$ and $\hat{\boldsymbol{\sigma}} = \boldsymbol{\sigma}$.

22.3.2.1 Homogenization Method

It is assumed that the viscoplastic properties of austenite and martensite differ widely. Therefore, independent dissipation potentials according to (22.44) are introduced for each phase. The rate of viscoplastic equivalent strain follows for each phase l as

$$\dot{\varepsilon}_{\mathrm{eq}}^{(l)} = \frac{\partial \phi^{(l)}\left(\sigma_{\mathrm{eq}}^{(l)}\right)}{\partial \sigma_{\mathrm{eq}}^{(l)}} = \dot{\varepsilon}_0 \left(\frac{\sigma_{\mathrm{eq}}^{(l)}}{\sigma_{\mathrm{y}}^{(l)}}\right), \tag{22.52}$$

where $l = \mathrm{a}$ and $l = \mathrm{m}$ denote austenite and martensite, respectively. The macroscopically effective properties are determined as described in [15, 22]. A variational principle is utilized, which is established by Ponte Castañeda and Suquet [54]. The necessary condition for an optimally chosen linear comparison composite is deduced in the case of statistically isotropic and uniformly distributed phases with isotropic behavior as

$$\sigma_{\mathrm{eq}}^{(l)} = \sigma_{\mathrm{eq}} \sqrt{\frac{1}{\nu^{(l)}} \frac{\partial \Theta^{\mathrm{hom}}}{\partial \Theta^{(l)}}}, \tag{22.53}$$

where the effective compliance Θ^{hom} is computed using a lower Hashin-Shtrikman bound

$$\Theta^{\mathrm{hom}} = \frac{v^{\mathrm{m}}\left(\frac{2}{\Theta^{\mathrm{a}}}+\frac{3}{\Theta}\right)+v^{\mathrm{a}}\left(\frac{2}{\Theta^{\mathrm{m}}}+\frac{3}{\Theta}\right)}{\frac{v^{\mathrm{m}}}{\Theta^{\mathrm{m}}}\left(\frac{2}{\Theta^{\mathrm{a}}}+\frac{3}{\Theta}\right)+\frac{v^{\mathrm{a}}}{\Theta^{\mathrm{a}}}\left(\frac{2}{\Theta^{\mathrm{m}}}+\frac{3}{\Theta}\right)}. \tag{22.54}$$

Therein, $v^{(l)}$ denotes the volume fraction of phase l, i.e., $v^{\mathrm{m}} = z$ and $v^{\mathrm{a}} = 1 - z$. The value of Θ is chosen as $\Theta = \max\left(\Theta^{\mathrm{a}}, \Theta^{\mathrm{m}}\right)$, where the compliance of a single phase is defined as

$$\Theta^{(l)} = \frac{3}{\sigma_{\mathrm{eq}}^{(l)}}\dot{\varepsilon}_{\mathrm{eq}}^{(l)}. \tag{22.55}$$

The strain hardening functions of each phase $\sigma_{\mathrm{y}}^{(l)}$ are chosen as power laws.

A stress state dependent yielding and strain hardening can be introduced by taking the third invariant of stress deviator J_3 into account. This leads to major modifications of the homogenization scheme. The reader is referred to the work of Prüger [22] dealing with this topic.

22.3.2.2 Martensite Kinetics and TRIP-kinematics: Stringfellow-Model

An established modification of the OC-model has been proposed by Stringfellow et al. [38]. Further enhancements have been incorporated, e.g., in [9, 39, 40]. Due to the homogenizations approach, plastic deformations of the single phases are accessible. Thus, the dependencies of the martensite kinetics on equivalent plastic strain are substituted as functions of the viscoplastic strain in austenite $\dot{\varepsilon}_{\mathrm{eq}}^{\mathrm{a}}$. The modified OC-kinetics of strain induced martensite, following [9], read as

$$\dot{z} = (1-z)\left(A\dot{f}_{\mathrm{sb}} + B\left(\dot{g} - \dot{\bar{g}}\right)\right) \tag{22.56}$$

with prefactors

$$A = \beta_{\mathrm{oc}}\, n_{\mathrm{oc}}\, f_{\mathrm{sb}}^{(n_{\mathrm{oc}}-1)}\, P, \tag{22.57}$$

$$B = \beta_{\mathrm{oc}}\, f_{\mathrm{sb}}^{n_{\mathrm{oc}}} \frac{\mathrm{d}P}{\mathrm{d}g} H\left(\dot{P}\right), \tag{22.58}$$

and the normal distribution

$$P = \frac{1}{\sqrt{2\pi}\, s_{\mathrm{g}}} \int_{-\infty}^{g} \exp\left[-\frac{1}{2}\left(\frac{g^* - \bar{g}}{s_{\mathrm{g}}}\right)^2\right] \mathrm{d}g^*. \tag{22.59}$$

Therein, g denotes the driving force for martensite formation and $\bar{g}$ a barrier function [55]:

$$\bar{g} = \bar{g}_0 + \bar{g}_1 \varepsilon_{\mathrm{eq}}^{\mathrm{a}}. \tag{22.60}$$

The driving force g is formulated as the sum of the chemical contribution $Z(\vartheta)$ and a mechanical part motivated from the energy term $\boldsymbol{\sigma} : \boldsymbol{D}_{\mathrm{trip}}$ [22, Sect. 5.4]:

$$g = -Z + \left(\left(k_{\mathrm{gj}} \, \sigma_{\mathrm{eq}} \frac{\mathrm{d}\varphi(z)}{\mathrm{d}z} + k_{\mathrm{s}} \right) \sigma_{\mathrm{eq}} + \triangle_{\mathrm{v}} \sigma_{\mathrm{h}} \right). \tag{22.61}$$

The chemical driving force Z is typically determined by thermodynamical calculations, see [47]. Moreover, s_{g} is a fitting parameter of the model.

As mentioned above, the parameter of shear band formation α_{oc} is a function of temperature and stress state. Prüger [22] proposes the approach

$$\alpha_{\mathrm{oc}}(h, \vartheta) = \left\langle \alpha_1 + \alpha_2 \vartheta + \alpha_3 \vartheta^2 - \alpha_4 \arctan(h) \right\rangle, \tag{22.62}$$

where the stress triaxiality is introduced as

$$h = \frac{\sigma_{\mathrm{h}}}{\sigma_{\mathrm{eq}}} \tag{22.63}$$

with the hydrostatic stress

$$\sigma_{\mathrm{h}} = \frac{1}{3} I_1. \tag{22.64}$$

The MACAULY-brackets

$$\langle x \rangle = \begin{cases} 0 & x < 0 \\ x & x \geq 0 \end{cases} \tag{22.65}$$

in (22.62) ensure a monotonically increasing shear band volume fraction.

For the micromechanical approach, the generally introduced TRIP-deformation rate $\boldsymbol{D}_{\mathrm{trip}}$ defined in (22.50) is utilized.

22.3.3 Phenomenological Model

The phenomenological modeling strategy is developed as a robust engineering tool comprising characteristic aspects of the thermomechanical, stress state dependent and damage behavior of high alloy TRIP-steel. Finally, two variants of the model are implemented into a FE-code: The first variant contains all thermomechanical

features, the second includes ductile damage within the micromorphic framework at isothermal conditions. A combination of both is subject of current work.

22.3.3.1 Viscoplastic Flow Rules

As already introduced in the state potential (22.24), damage degrades the elastic properties and thus the bearable stress, see (22.28). Ductile damage is microscopically caused by the nucleation, growth, and coalescence of microvoids. At high stress triaxialities, growth of voids is the dominant damage mechanism, which influences the plastic yielding and flow behavior [56, 57]. In this regime, the impact of hydrostatic stresses on plastic flow needs to be taken into account. A heuristic modification of the NORTON-potential (22.44) through a contribution of the hydrostatic stress is proposed

$$\phi\left(\boldsymbol{\sigma}\right) = \frac{\left(1-D\right)\dot{\varepsilon}_0\sigma_\mathrm{y}}{m+1}\left(\frac{\hat{\sigma}_\mathrm{eq}^2 + q_1 D\left\langle\hat{\sigma}_\mathrm{h}\right\rangle^2}{\sigma_\mathrm{y}^2}\right)^{\left(\frac{m+1}{2}\right)}. \tag{22.66}$$

A similar elliptic yield function in the rate independent framework is utilized in the gradient-enhanced damage model of Seupel and Kuna [35]. Dissipation potentials of similar structure are likewise proposed in creep damage mechanics [58].

An associated viscoplastic flow is assumed

$$\boldsymbol{D}_\mathrm{vpl} = \frac{\partial\phi}{\partial\boldsymbol{\sigma}} = \dot{\varepsilon}_\mathrm{eq}\boldsymbol{N} + \dot{\varepsilon}_\mathrm{h}\boldsymbol{\delta}, \tag{22.67}$$

which leads to deviatoric and volumetric viscoplastic strains. The prefactors in (22.67) are identified as equivalent and volumetric viscoplastic strain rates

$$\dot{\varepsilon}_\mathrm{eq} = \dot{\varepsilon}_0\frac{\hat{\sigma}_\mathrm{eq}}{\sigma_\mathrm{y}}\left(\frac{\hat{\sigma}_\mathrm{eq}^2 + q_1 D\left\langle\hat{\sigma}_\mathrm{h}\right\rangle^2}{\sigma_\mathrm{y}^2}\right)^{\left(\frac{m-1}{2}\right)}, \tag{22.68}$$

$$\dot{\varepsilon}_\mathrm{h} = \dot{\varepsilon}_0\frac{\left\langle\hat{\sigma}_\mathrm{h}\right\rangle q_1 D}{3\sigma_\mathrm{y}}\left(\frac{\hat{\sigma}_\mathrm{eq}^2 + q_1 D\left\langle\hat{\sigma}_\mathrm{h}\right\rangle^2}{\sigma_\mathrm{y}^2}\right)^{\left(\frac{m-1}{2}\right)}, \tag{22.69}$$

respectively. The model parameter q_1 controls the hydrostatic stress dependency. As long as q_1 is set to zero or no damage occurs $D = 0$, the original volume preserving NORTON-type flow is obtained. A relation between (22.68) and (22.69) can be found [59]:

$$\dot{\varepsilon}_\mathrm{h} = \frac{q_1 D\left\langle h\right\rangle}{3}\dot{\varepsilon}_\mathrm{eq}. \tag{22.70}$$

In presence of damage, the hydrostatic plastic flow linearly depends on stress triaxiality h. This is in accordance to micromechanical findings within creep damage mechanics [60], but contrary to the known exponential influence deduced in [56, 57], cf. [61]. In contrast to the GURSON-model, the volumetric plastic strain of the present model can just increase, because a volumetric flow occurs only for positive hydrostatic stresses.

An additional influence of the third stress invariant $\hat{J}_3$ on plastic flow is neglected, which is in accordance with investigations on initial yielding of the considered TRIP-steel conducted by Kulawinski et al. [62]. The asymmetric strain hardening is fully captured by the definition of the evolution equation for the hardening variable r.

22.3.3.2 Isotropic Strain Hardening

An empirical mixture rule is adopted in order to take the influence of formed α'-martensite on strain hardening into account, which has been successfully applied in other studies [12, 27, 50]. Thus, the yield stress reads

$$\sigma_{\mathrm{y}}\left(r, z, \vartheta\right) = \sigma_0\left(\vartheta\right) + Z_1 m_{\mathrm{z}}\left(z\right) + H\left(r\right). \tag{22.71}$$

Furthermore, only the initial yield stress σ_0 is considered as function of temperature as employed for an AISI 304 steel elsewhere [27]. The additional hardening contribution of martensite is captured by the second term, where $m_{\mathrm{z}}\left(z\right)$ is introduced to modify the shape of the flow curve during martensite evolution. The choice of the hardening function ensures that no strain softening can occur during martensite formation for $\vartheta = \text{const}$. Material degradation arises only due to the evolution of the damage variable D.

Because of the direct influence of the stress state dependent martensitic phase transition, asymmetric strain hardening in uni-axial tension and compression is naturally predicted by the model. Hence, a higher strain hardening would be predicted in tension than in compression due to the enhanced phase transformation in tension, whereas the inverse trend is experimentally observed [12], [63, Sect. 5.3.2]. To take the realistic asymmetric strain hardening into account, Seupel and Kuna [12] propose an evolution of the hardening variable r depending on the orientation in stress space, which is described by the LODE-angle

$$\cos 3\phi = \frac{3\sqrt{3}}{2} \frac{\hat{J}_3}{\hat{J}_2^{\frac{3}{2}}}. \tag{22.72}$$

The evolution of the hardening variable reads

$$\dot{r} = \left(1 + \frac{b}{2}\left(1 - \cos 3\phi\right)\right) \dot{\varepsilon}_{\mathrm{eq}} \geq 0, \tag{22.73}$$

where the parameter $b > -1$ controls the influence of stress state. For $b = 0$, the hardening variable coincides with the equivalent viscoplastic strain. For $b > 0$, the hardening rate is increased in case of uni-axial compression ($\cos 3\phi = -1$) compared to uni-axial tension ($\cos 3\phi = 1$), which is in accordance with the experimentally revealed behavior.

The same tendencies in strain hardening are observed, if the TWIP-mechanism is active [11, 63]. The tension-compression asymmetry vanishes, if planar dislocation glide is the dominant deformation mechanism, see [63, Sect. 5.3.2]. For the considered steel, the transition of deformation mechanisms is explained as function of temperature [6, 51]. Accordingly, the hardening asymmetry should depend on deformation mechanism and/or temperature, respectively. Therefore, the parameter b is assumed as function of martensite volume fraction and temperature in the following manner:

$$b\left(z,\vartheta\right) = \begin{cases} b_0 \exp\left(-\left(\frac{\vartheta - T_0}{T_1}\right)^2\right) \exp\left(-\left(\frac{z - z_0}{z_1}\right)^2\right) & \vartheta \geq T_0 \\ b_0 \exp\left(-\left(\frac{z - z_0}{z_1}\right)^2\right) & \vartheta < T_0 \end{cases} \tag{22.74}$$

Thereby, the asymmetric hardening asymptotically vanishes for temperatures above T_0. When martensite transformation is active, the asymmetry can additionally vary during loading at constant temperature due to the second exponential function, which contains the fitting parameters z_0 and z_1.

22.3.3.3 Martensite Kinetics and TRIP-Kinematics: Empirical Model

Motivated by the sound investigations on stress state dependency of strain induced martensite formation and the suggested empirical kinetics approach of Beese and Mohr [64], a less sophisticated, empirical extension of the OC-kinetics can be proposed. The original evolution equation introduced by Olson and Cohen [37] is considered, see (22.49). In β_{oc}, the probability that a shear band intersection becomes a martensite embryo is included. As shown in [37], the parameters α_{oc} and β_{oc} are functions of temperature. Similar to the proposal in (22.62) for the parameter of shear band formation, Seupel and Kuna [12] use

$$\alpha_{\mathrm{oc}}\left(h,\vartheta\right) = \alpha_{\mathrm{t}}\left(\vartheta\right)\left[\alpha_0 + \alpha_1\left(\frac{2}{\pi}\arctan\left(\alpha_2 h\right) + 1\right)\right]. \tag{22.75}$$

As discussed in [9], the non-linear function of stress triaxiality should saturate to a certain level. As long as $\alpha_1 \geq 0$, no negative shear band rate can be caused by the stress state. Regarding $\alpha_1 < 0$, a non-negative rate of shear bands is obtained, if the parameters fulfill $\alpha_0 \geq 0$ and $\alpha_1 \geq -\frac{\alpha_0}{2}$. As temperature influence, probability functions are chosen [37]:

$$\alpha_{\mathrm{t}}\left(\vartheta\right) = \begin{cases} \exp\left(-\left(\frac{\vartheta-\alpha_3}{\alpha_4}\right)^2\right) & \vartheta \geq \alpha_3 \\ 1 & \vartheta < \alpha_3. \end{cases} \tag{22.76}$$

For β_{oc}, a similar structure given by (22.75) and (22.76) is assumed with parameters $\beta_0 - \beta_4$. Despite the empirical character of the extended kinetics law, less parameters are needed compared to the enhanced STRINGFELLOW-approach (Sect. 22.3.2.2).

The generally introduced TRIP-deformation rate (22.50) is utilized with the following parameters:

$$k_{\mathrm{gj}} = 8.1 \times 10^{-5}\,\mathrm{MPa}^{-1}, \quad \varphi\left(z\right) = \left(2 - z\right) z, \quad k_{\mathrm{s}} = 0, \quad \triangle_{\mathrm{v}} = 0.02. \tag{22.77}$$

This set of parameters leads to a comparatively small contribution of transformation induced plasticity to the whole deformation.

22.3.3.4 Ductile Damage

Damage models devoted to high alloy TRIP-steels have been mainly developed for applications at cryogenic temperatures employing concepts of continuum damage mechanics [65–67]. A ductile damage mechanism is assumed as common feature of the mentioned approaches. Regularized damage models for TRIP-steels are less investigated, except first studies [12].

The evolution of ductile damage is known to be dependent on plastic deformation and stress state. Seupel and Kuna [35] propose an empirical, regularized model for ductile damage, which is able to predict failure due to void based mechanisms at high stress triaxialities and shear dominated failure. The mentioned model is a gradient-enhanced version of local engineering approaches, e.g., [68]. In the present section, the approach of Seupel and Kuna [35] is adopted for the micromorphic-viscoplastic framework.

The empirical approach to ductile failure is based on the hypothesis, that damage can be neglected in a certain deformation range, but evolves rather fast after initiation [68]. The initiation of damage is captured by a loading history dependent indicator function $\omega\left(\varepsilon_{\mathrm{eq}}, \boldsymbol{\sigma}\right)$, which is not directly coupled to the constitutive equations similar to well known failure criteria. Exceeding a critical value $\omega \geq \omega_{\mathrm{c}}$ determines the initiation of damage, i.e., the onset of evolution of the local damage driving force $\dot{\varepsilon}_{\mathrm{l}}\left(\boldsymbol{D}_{\mathrm{vpl}}\right)$. Its evolution is proposed as

$$\dot{\varepsilon}_{\mathrm{l}} = \begin{cases} 0, & \omega\left(\boldsymbol{\sigma}, \varepsilon_{\mathrm{eq}}, z\right) < \omega_{\mathrm{c}} \\ q_2 \dot{\varepsilon}_{\mathrm{eq}} + q_3 \dot{\varepsilon}_{\mathrm{h}} \overset{(22.70)}{=} \left(q_2 + \frac{q_1 q_3 D\langle h\rangle}{3}\right) \dot{\varepsilon}_{\mathrm{eq}}, & \omega\left(\boldsymbol{\sigma}, \varepsilon_{\mathrm{eq}}, z\right) \geq \omega_{\mathrm{c}}. \end{cases} \tag{22.78}$$

The model parameters q_2 and q_3 can be adjusted to weight between shear ($\dot{\varepsilon}_{\mathrm{eq}}$) and void growth dominated damage ($\dot{\varepsilon}_{\mathrm{h}}$), respectively. It should be mentioned, that the local damage driving strain ε_{l} is associated to the dissipation potential and viscoplas-

tic flow. Mediavilla et al. [69] propose a non-local damage model using a comparable driving strain, but therein the plastic yielding stays purely deviatoric.

The micromorphic counterpart $\varepsilon_{\mathrm{nl}}$ of the damage driving strain is given by solving the micromorphic balance (22.34). To reach at a regularized damage model, the damage evolution is formulated with help of the micromorphic (non-local) variable $\varepsilon_{\mathrm{nl}}$. Following [69], an auxiliary variable κ is defined to avoid pathological healing effects, cf. [34, 35],

$$\dot{\kappa} \geq 0, \qquad \dot{\kappa}\,(\varepsilon_{\mathrm{nl}} - \kappa) = 0, \qquad \varepsilon_{\mathrm{nl}} - \kappa \leq 0. \tag{22.79}$$

An exponential dependency of damage evolution on κ is assumed:

$$\dot{D} = \begin{cases} 3\,(1-D)\,\frac{\dot{\kappa}}{\varepsilon_{\mathrm{c}}} & D < D_{\mathrm{c}} \\ D_{\max} a^{*} \exp\left(-a^{*}\,(\kappa - \kappa^{*})\right)\dot{\kappa} & D \geq D_{\mathrm{c}} \end{cases} \tag{22.80}$$

or in integrated form

$$D = \begin{cases} 1 - (1-D_0)\exp\left(-3\frac{\kappa}{\varepsilon_{\mathrm{c}}}\right) & D < D_{\mathrm{c}} \\ D_{\max}\left(1 - \exp\left(-a^{*}\,(\kappa - \kappa^{*})\right)\right) & D \geq D_{\mathrm{c}} \end{cases} \tag{22.81}$$

with

$$a^{*} = \frac{3}{\varepsilon_{\mathrm{c}}}\frac{(1-D_{\mathrm{c}})}{(D_{\max} - D_{\mathrm{c}})}, \tag{22.82}$$

$$\kappa^{*} = -\frac{\varepsilon_{\mathrm{c}}}{3}\ln\left(\frac{1-D_{\mathrm{c}}}{1-D_0}\right) + \frac{1}{a^{*}}\ln\left(1 - \frac{D_{\mathrm{c}}}{D_{\max}}\right). \tag{22.83}$$

Because κ is a monotonically increasing variable without upper limit, a totally damaged state ($D \approx 1$) can be reached asymptotically. In order to ensure the robustness of the model near to total failure, the numerical value of damage is limited by a prescribed saturation of D towards $D_{\max} < 1$ as proposed by Seupel and Kuna [35] (second case in (22.80) and (22.81), respectively).

The exponential damage law is motivated by the evolution of porosity assuming a nearly volume preserving matrix material, c.f. [57]. The purely void growth based damage mechanism is included in the current formulation by imposing $\varepsilon_{\mathrm{c}} = 1, q_2 = 0$ and $q_3 = 1$ with $D_0 > 0$. The additional parameter ε_{c} can be used to adjust the slope of the damage law. The saturation value of damage is prescribed as $D_{\max} = 0.999 \approx 1$ and the transition value is set to $D_{\mathrm{c}} = 0.995$, i.e., near the state of total material failure.

To avoid a spurious widening of the total damaged zone, Seupel and Kuna [35] suggest to fix the local contribution $\dot{\varepsilon}_{\mathrm{l}} = 0$ in case the totally damaged state $D \geq D_{\mathrm{c}}$ is reached. This patch solution damps the widening of the totally damaged domain, but other sophisticated methods, cf. [70], should be taken into account in ongoing

works. The zone of totally damaged integration points or finite elements mimics the actually discontinuous crack.

22.3.3.5 Thermodynamic Consistency

The mechanical dissipation introduced in (22.41) can be specified for the phenomenological model as

$$\gamma_{\mathrm{m}} = \sigma_{\mathrm{eq}} \left(\dot{\varepsilon}_{\mathrm{eq}} + \hat{\sigma}_{\mathrm{eq}} k_{\mathrm{gj}} \frac{\mathrm{d}\varphi\,(z)}{\mathrm{d}z} \dot{z} \right) + \sigma_{\mathrm{h}}\ (\dot{\varepsilon}_{\mathrm{h}} + \triangle_{\mathrm{v}} \dot{z}) - \triangle g_{\mathrm{chem}}^{\mathrm{a} \rightarrow \mathrm{m}} \dot{z} - Y \dot{D}. \quad (22.84)$$

The rates of the introduced internal variables are constructed to yield $\dot{\kappa}_{\alpha} \geq 0$. The first part of γ_{m} (σ_{eq} (...)) is always larger or equal to zero. The damage contribution is likewise non-negative, because $Y \leq 0$. The chemical contribution is positive as long as the temperature is below the thermodynamic equilibrium temperature. For temperatures above, this restriction is not fulfilled automatically and this part has to be controlled. For experimentally calibrated models, $\dot{z}$ should vanish in this temperature region, i.e., the chemical part is typically thermodynamically consistent. The dissipation contribution of volumetric plastic strain is always non-negative, see (22.69), whereas the volumetric TRIP-strains can cause a negative dissipation in compression states [9], i.e., if $\sigma_{\mathrm{h}} < 0$. To ensure positive dissipation, the hydrostatic TRIP-part is neglected in the mechanical dissipation as proposed by Mahnken and Schneidt [46]. Nonetheless, it should be mentioned that the damage model without martensite evolution is thermodynamically consistent in a strict sense.

22.3.4 Numerical Implementation

In order to analyze complex boundary value problems numerically, the material models are implemented into the FE-code ABAQUS via the user-defined subroutine UMAT. Implementation aspects of the micromechanically motivated and phenomenological model within the thermomechanical framework are discussed in literature [22, 34, 35]. One particular aspect should be emphasized: The implementation of the micromorphic damage model is simplified due to the similarity of the HELMHOLTZ-type equation (22.34) and the steady state case of the heat equation (22.42) as pointed out in [34]. A simple renaming of variables ($\varepsilon_{\mathrm{nl}} \leftrightarrow \vartheta$), a modification of the heat source ($\tilde{p} \leftrightarrow -\varepsilon_{\mathrm{nl}} + \varepsilon_{\mathrm{l}}$), and the interpretation of the conductivity $\lambda_{\mathrm{th}} \leftrightarrow L_{\mathrm{nl}}^2$ allow a fast implementation into the commercial FE-code. A major advantage is the usage of the available thermomechanical finite element library and post-processing tools, which becomes interesting for engineering applications.

22.4 Results

In this section the introduced models are applied. A detailed study on the phenomenological modeling approach from Sect. 22.3.3 is conducted to demonstrate its ability to comprise the influence of stress state and temperature on martensite kinetics as well as strain hardening behavior. Furthermore, the micromechanically motivated model from Sect. 22.3.2 is used in order to study the stress field in front of a crack. Additionally, the crack driving force is formulated in consideration of plastic deformation and phase transformation. Finally, a cohesive zone approach and the micromorphic damage model (Sect. 22.3.3) are utilized to simulate ductile fracture in a particular TRIP-steel.

22.4.1 Material

Consistent experimental investigations on a cast TRIP-steel X3CrMnNi 16-6-6 (see [53, 63]) are used as reference for calibration and validation purposes. The exact chemical composition is given in Table 22.1. A detailed characterization of the material can be found in [63]. The material used to manufacture the CT-specimen for fracture mechanics test exhibits a slightly deviating composition, see Table 22.1.

22.4.2 Deformation and Phase Transition Behavior

For the phenomenological model from Sect. 22.3.3, a step-by-step calibration strategy is pursued: Firstly, the model parameters of the martensite kinetics law are estimated with help of experimental data. Afterwards, the temperature and stress state dependent isotropic strain hardening law is fitted to a characteristic subset of tests. Following Prüger et al. [9], a simultaneous calibration to uni-axial tests at quasi-static loading, but different temperatures can be used as starting point. Damage effects are neglected at this stage of modeling. The validity of the model is assessed by predictions of the material behavior at other temperature conditions, strain rates, and inhomogeneous loading states. A comparable assessment for the micromechanically motivated model discussed in Sect. 22.3.2 can be found in recent literature [9, 22].

Table 22.1 Chemical composition of considered cast TRIP-steels in mass %

Alloy	Fe	C	N	Cr	Mn	Ni	Si
X2CrMnNi 15-5-7	Bal.	0.03	0.03	15.5	6.1	6.1	0.9
X2CrNiMn 15-7-5	Bal.	0.023	0.086	14.5	5.36	6.85	0.88

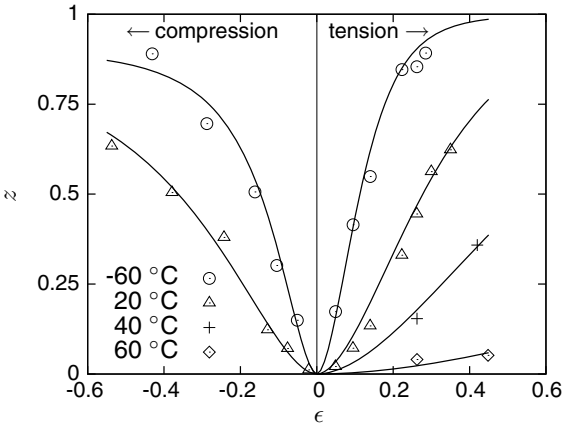

Fig. 22.1 Martensite volume fraction z versus true strain ϵ curves for uni-axial tension-compression loadings at different temperatures and constant strain rate $\dot{\epsilon}_t = 4 \times 10^{-4}\ \mathrm{s}^{-1}$: symbols correspond to experimental data of cast X3CrMnNi 16-6-6, solid lines correspond to the fitted empirical model (Sect. 22.3.3.3)

22.4.2.1 Martensite Kinetics

The empirical model of strain induced martensite kinetics (Sect. 22.3.3.3) is calibrated using experimental data from uni-axial, quasi-static tensile and compression tests at different temperatures ranging from −60 to 60 °C [6, 10, 63, 71]. The calibration result is shown in Fig. 22.1 in terms of evolving martensite volume fraction during straining. A good match of the martensite evolutions is obtained with the *a priori* estimation of the model parameters given in Table 22.2 and the exponent $n_{oc} = 1.868$. For calibration purposes, the approximate coincidence of true strain ϵ and the equivalent plastic strain ε_{eq} is assumed. Due to the occurrence of additional TRIP-strains depending on stress, a small deviation is to be expected finally.

22.4.2.2 Asymmetric Strain Hardening

The isotropic strain hardening contributions in (22.71) are chosen as functions of the hardening variable r, the temperature ϑ, and the martensite volume fraction z in the following manner [34]:

Table 22.2 Model parameters of empirical martensite kinetics (22.76)

α_0	α_1	α_2	α_3	α_4	β_0	β_1	β_2	β_3	β_4
–	–	–	K	K	–	–	–	K	K
2.77	1.14	−100	233.15	63.26	2.27	2.88	100	313.15	27.36

Table 22.3 Model parameters of isotropic strain hardening (22.85)–(22.87)

σ_0	H_0	q	H_{inf}	r_c	Z_1	Z_2	c_1	c_2
MPa	MPa	–	MPa	–	MPa	–	–	K
174.2	1305.6	0.927	269.0	0.277	510.1	1.193	-0.0014	373.15

Table 22.4 Model parameters of asymmetric strain hardening (22.74)

b_0	T_0	T_1	z_0	z_1
–	K	K	–	–
2.259	228.431	90.441	0.276	0.314

$$H(r) = \begin{cases} H_0 r^q & r \le r_c \\ H_0 r_c^q + H_{\text{inf}} \left(1 - \exp\left(-\frac{H_0 q r_c^{q-1}}{H_{\text{inf}}} (r - r_c)\right)\right) & \text{else} \end{cases}, \tag{22.85}$$

$$\sigma_0(\vartheta) = \exp(c_1(\vartheta - c_2))\,\sigma_0, \tag{22.86}$$

$$m_z(z) = 1 - \exp(-Z_2 z). \tag{22.87}$$

Thermoelastic properties for the considered steel are taken from literature [9]. Appropriate values for the parameters of strain rate sensitivity m and $\dot{\varepsilon}_0$ are also proposed in literature [9, 48]: $m = 40$ and $\dot{\varepsilon}_0 = 4 \times 10^{-4}\ \text{s}^{-1}$. Nine model parameters for isotropic strain hardening are to be identified and calibrated (22.85)–(22.87). Additionally, five parameters for stress state dependent evolution of the hardening variable have to be estimated, see (22.74). The final sets of estimated parameters are summarized in Tables 22.3 and 22.4.

As reference test data, force versus elongation curves of uni-axial, quasi-static tension and compression tests at −60, 20 and 100 °C [6, 10, 63, 71] are chosen. At these temperatures, different amounts of martensite are reached, from nearly 100% down to 0%, see Fig. 22.1. The reasonable calibration results are illustrated in Fig. 22.2.

The stress state dependent strain hardening becomes clearly visible in terms of the true stress versus strain curves, see Fig. 22.3. In addition to the calibrated temperatures, predictions are made for 60 and 200 °C. The corresponding experimental data is published in [6, 10, 63, 71]. From −60 to 60 °C, substantial higher stress levels are attained in uni-axial compression compared to tension. The asymmetry vanishes at about 200 °C, because neither martensite nor shear bands are formed, which is predicted by the model. Moreover, the qualitative change in strain hardening with temperature is reflected. The prediction at 60 °C in the compression regime deviates slightly. This indicates that other effects, especially the TWIP-effect, and their influence on strain hardening have to be considered in ongoing works.

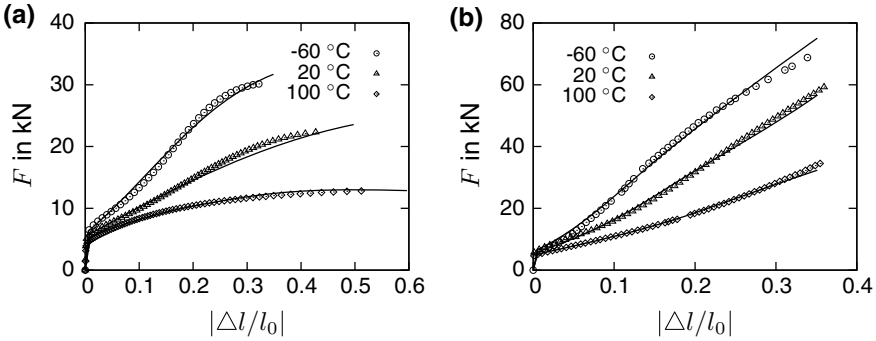

Fig. 22.2 Force F versus elongation $\Delta l/l_0$ curves at different temperatures and constant engineering strain rate $\dot{\epsilon}_t = 4 \times 10^{-4}\ s^{-1}$, symbols correspond to experimental data of cast X3CrMnNi 16-6-6, solid lines correspond to the fitted phenomenological model, **a** Uni-axial tension, **b** Uni-axial compression

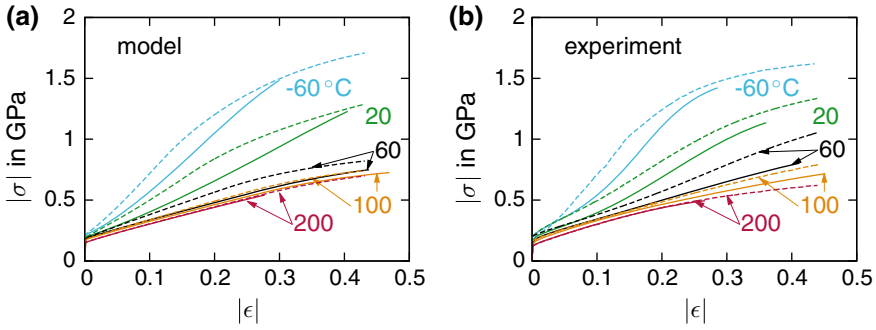

Fig. 22.3 True stress σ versus true strain ϵ curves for different temperatures and stress states at $\dot{\epsilon}_t = 4 \times 10^{-4}\ s^{-1}$, solid lines correspond to tensile and dashed lines to compressive loadings, respectively; **a** Model predictions, **b** Experimental data of cast X3CrMnNi 16-6-6

22.4.2.3 Strain Rate Dependency

A characteristic strain rate effect of high alloy TRIP-steels is the so-called curve crossing observed in tensile tests [9]: The temperature increase during plastic deformation inhibits the formation of α'-martensite and thereby restricts the strain hardening capability. The temperature increases with increasing strain rates, because adiabatic conditions are asymptotically reached. The typical experimental observation based on data from [10, 63, 71, 72] is shown in Fig. 22.4: After a higher stress level at low strains, the curves of higher strain rates drop below the quasi-static reference curve. In order to reproduce this behavior, a thermomechanical coupling is mandatory [9].

For the numerical simulations via FEM, a FE-implementation of the whole experimental setup becomes necessary in order to consider the heat transfer from the specimen to clamps and environment. A detailed description of the utilized

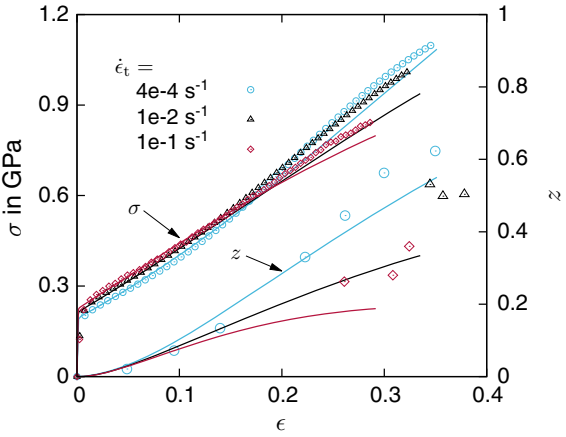

Fig. 22.4 Stress σ and martensite volume fraction z versus true strain ϵ curves at different technical strain rates $\dot{\epsilon}_t$ during uni-axial tension test: symbols correspond to experimental data of cast X3CrMnNi 16-6-6, solid lines denote the model prediction

FE-model is given in [9]. For the micromechanically motivated model introduced in Sect. 22.3.2, the ability to cover the curve crossing effect is shown in [9]. The same analysis is conducted for the phenomenological model with the results summarized in Fig. 22.4: Qualitatively, the curve crossing in strain hardening and the lower α'-martensite content at higher strain rates can be reproduced. A good match of the experimental stress versus strain curves is visible for strains $\epsilon < 0.18$ for all considered strain rates. The predictions cannot fit for higher strain rates exactly, because there is an initial deviation of the quasi-static case at strains larger than 0.18. Additionally, due to the full dissipative formulation of the model, a temperature increase ($\Delta\vartheta \approx 70$ K) is predicted which is considerably higher than measured in experiments ($\Delta\vartheta \approx 45$ K, [63]). As result, the strain hardening and martensite formation are weakened too much. This can be adjusted by introducing an empirical TAYLOR-QUINNEY-coefficient controlling the amount of dissipated power, see [73]. Despite the discussed need of improvements, the predictions of the models are physically reasonable.

22.4.2.4 Inhomogeneous Loading States

In addition to the uni-axial tests from [63], a series of round notched tensile tests has been conducted [53]. As test conditions, room temperature (20 °C) and quasi-static loading has been applied. A detailed description of the test setup and the evaluation procedure are given in [53]. The predictions of the calibrated material model are assessed by a comparison with the experimental results in Fig. 22.5. Good predictions of the force response are nearly made up to the onset of failure indicated by a rather sudden load drop for all differently notched specimens. Due to neglected damage, clear overestimations in the post-failure regime are visible. The indicated softening within the simulated curves is purely due to necking. Material softening caused by damage is taken into account in Sect. 22.4.4.2.

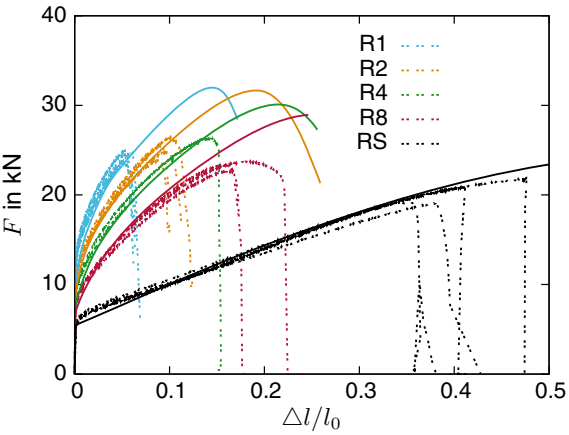

Fig. 22.5 Force F versus elongation $\Delta l/l_0$ curves for differently notched tensile tests, numbers highlight the notch radius in mm (RS—smooth test); solid lines correspond to the model prediction, dashed lines denote experiments of cast X3CrMnNi 16-6-6

22.4.3 Stress Analysis and Material Forces for Cracks in TRIP-steels

In this section, the micromechanically motivated material model from Sect. 22.3.2 is applied for fracture mechanics investigations. The material parameters are based on experimental data of cast steel X3CrMnNi 16-6-6, see Table 22.1 and references [20, 21, 53].

22.4.3.1 Crack Tip Fields in Front of a Blunting Crack Tip

In ductile materials, cracks tend to blunt during opening. Thereby, finite strains occur in front of the tip leading to characteristic shapes of the stress and strain fields. The phase transformation influences these crack tip fields and leads to some new characteristics, which are shown within this section.

From linear elastic fracture mechanics it is known, that the stresses become singular at the crack tip. The same holds for elastic-plastic fracture mechanics at small strains, compare the well established HRR-field [74, 75]. If plasticity and finite strains are considered, the situation is different. In this case crack tip blunting is incorporated, which means that an initially sharp crack deforms to a notch like shape. The stress fields are not singular any more. The stress component perpendicular to the surface of the blunted notch vanishes (σ_{11} in the ligament), because of the free surface. The crack opening stress (σ_{22}) reaches a maximum value at a distance in front of the crack and a finite value at the surface of the notch, see McMeeking [76]. If the considered material has a very high work hardening capacity, it is possible that the distinctive σ_{22} maximum does not occur. Instead the stress monotonically increases towards the crack tip and reaches high values there. This is reported by Yuan et al. [77] for an austenitic steel with pronounced strain hardening.

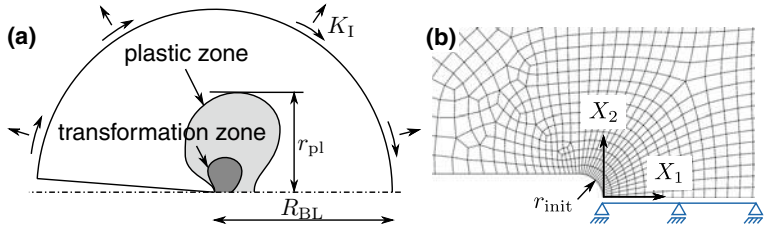

Fig. 22.6 **a** Sketch of the boundary-layer approach, **b** Detailed view of the initial crack tip and the finite element mesh together with the utilized coordinate system, reprinted from [20], with permission from Elsevier

In order to study the fields at a blunting crack without influence of a specific specimen geometry, small scale yielding under plain strain conditions is assumed. This is realized by a boundary-layer model, which is a circular region surrounding the crack tip, compare Fig. 22.6. Displacements known from the linear elastic K-field are prescribed on the boundary. In order to ensure small scale yielding, zones of inelastic deformation have to be small compared to the radius R_{BL}. In the case of strain induced phase transformation the transformation zone is always embedded inside the plastic zone, and thus $r_{pl} \ll R_{BL}$ is sufficient.

The boundary value problem is solved numerically employing finite elements. The boundary-layer model is discretized by quadrilateral elements with quadratic shape functions and reduced integration (ABAQUS: CPE8R). A zoomed view of the mesh near the crack is given in Fig. 22.6. It is typical to use a small initial radius at the crack tip in blunting studies, which is also shown in the figure. If the radius blunts to several times of its initial size, the resulting stress fields will be the same as for an initially sharp crack. The advantage of this initial radius is that distorted elements will show up later compared to the sharp crack tip. Further information can be found in [20].

The simulations yield steady state solutions for the mechanical fields. Thus, for example the distributions of stresses at different load levels K_I are self similar. They coincide in a single curve, if the distance to the initial crack tip in the reference configuration X_1 (Fig. 22.6) is normalized by J/σ_0, which is proportional to the crack tip opening displacement. Hereby, J is the J-integral and σ_0 is the initial yield stress of the material. Under small scale yielding and plane strain J is related to the prescribed K-factor and the elastic constants via

$$J = \frac{K_I^2(1-\nu^2)}{E}. \tag{22.88}$$

In order to point out the effect of the transformation hardening and the transformation strains, different model materials are considered, see Table 22.5. Figure 22.7 shows the corresponding true stress-strain curves and the evolution of martensite volume fraction. The variants are realized by an appropriate choice of the material

Table 22.5 Investigated model materials—Overview

Variant	Description, *influence*
TRIP	TRIP-steel
$\Uparrow$	*Volumetric transformation strain*
$\triangle_{\mathrm{v}} = 0$	TRIP-steel without volumetric transformation strain
$\Uparrow$	*Deviatoric transformation strain*
$\boldsymbol{\epsilon}_{\mathrm{trip}} = \mathbf{0}$	TRIP-steel without any transformation strain,
$\Uparrow$	*Transformation induced hardening*
Aust.	Austenite (without phase transformation)

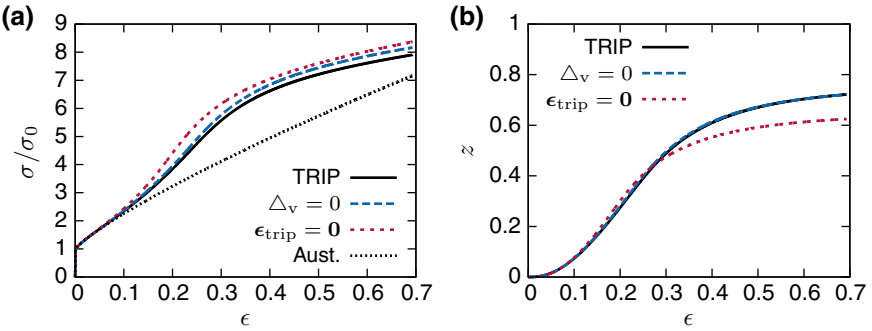

Fig. 22.7 Uniaxial behavior of the different model materials, **a** True stress-strain curves (σ vs. ϵ), **b** Evolution of martensite volume fraction z versus true strain ϵ

parameters, compare [20]. On the one hand, there is the TRIP-steel showing the full phase transformation with corresponding hardening and straining. On the other hand, there is a non-transforming austenite as reference. In between, there are two variants of TRIP-steel to study the role of deviatoric and volumetric transformation strain: one without volumetric transformation strain ($\triangle_{\mathrm{v}} = 0$), and the other one without any transformation strain ($\boldsymbol{\epsilon}_{\mathrm{trip}} = \mathbf{0}$).

At first, results for the TRIP-steel are discussed. The course of the stress components in the ligament is depicted in Fig. 22.8. Towards the crack tip (from right to left) an increase of the stress components is visible. The component σ_{11} reaches a maximum at $X_1 = 0.23J/\sigma_0$ and goes down to zero with smaller distance X_1. The stress component σ_{22} increases continuously towards the tip and does not show a maximum at some distance in front of the tip. This is consistent with [77] for material exhibiting high strain hardening. Furthermore, the crack opening stress σ_{22} shows a characteristic curvature, which is highlighted by the inflection points in Fig. 22.8. These characteristics are triggered by phase transformation. They occur in or near to the region with considerable martensite volume fraction, see Fig. 22.9. The stress triaxiality h, which is also depicted in Fig. 22.9, has a maximum in front of the tip and goes down to a finite non-zero value towards the crack.

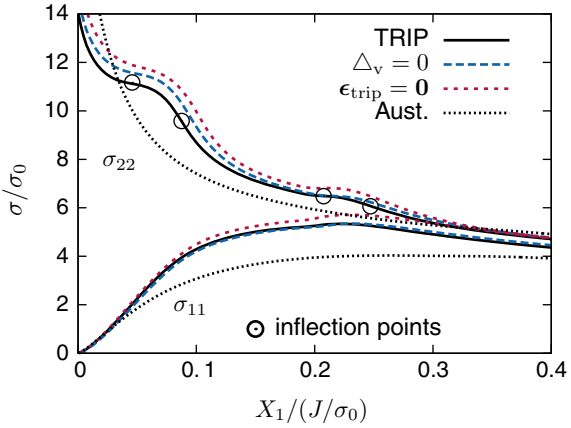

Fig. 22.8 Distribution of the stress components σ_{11} and σ_{22} in front of the blunting crack in the ligament for the different model materials, $X_1/(J/\sigma_0)$ is the normalized distance to the crack tip in the undeformed configuration

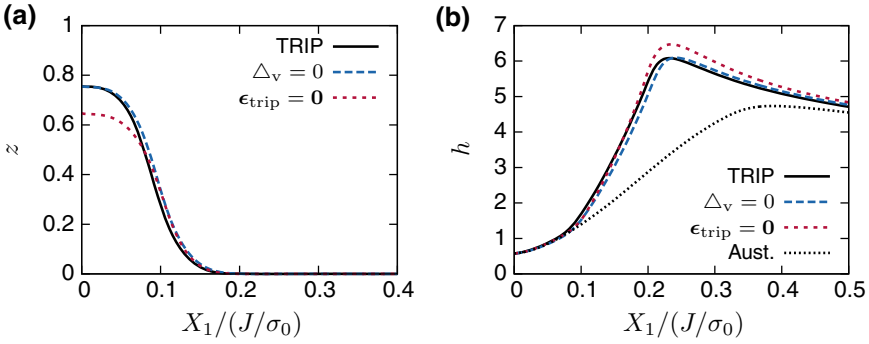

Fig. 22.9 Distribution of the martensite volume fraction z (**a**) and stress triaxiality h (**b**) in the ligament for the model materials, $X_1/(J/\sigma_0)$ is the normalized distance to the crack tip

In the next step the different model materials are taken into account. Comparing austenite to TRIP-steel, it becomes clear that phase transformation leads to higher stresses and stress triaxiality in the region near to the transformation zone. This is consistent with findings of Stringfellow [78]: By comparing TRIP-steel to non-transforming austenite, an increase of equivalent stress due to phase transformation was found. Considering the other two TRIP-variants one can conclude that the main effect comes from transformation induced hardening. The TRIP-steel without transformation strain already shows all the characteristic features (inflection points, increased stresses). The transformation strains reduce the stress components because of strain softening and affect the stress fields considerably near the tip, where the highest martensite volume fraction is present.

Interestingly, there is a region very near to the crack tip, where the stresses are highest in the austenite. This is explained with the different hardening behavior of the model materials. It can already be seen in Fig. 22.7, that the TRIP-steel variants reach higher stresses, but the austenite has the higher hardening modulus at strains larger than 0.3. Asymptotically, the stress-strain curve of pure austenite leads to the highest stresses, which is observed in the crack tip fields.

The implications of these observations on fracture in TRIP-steels were discussed in detail by Burgold et al. [20]. In the case of cleavage, phase transformation could have a negative effect, because of the higher principal stresses. But there is an open question, how martensite affects the critical fracture strength. In the case of ductile fracture, the transformation has a positive impact on toughness, because the transformation induced hardening hinders the growth of micro voids. This is supported by the work of Hütter et al. [79], who studied the effect of hardening on the ductile fracture mechanism by micromechanical simulations. In both cases (ductile fracture and cleavage) a shielding effect due to phase transformation can occur, because martensite evolution dissipates mechanical work, which is not available for crack growth anymore.

22.4.3.2 Material Forces in Consideration of Phase Transformation

In this section the influence of phase transformation on the crack driving force in TRIP-steels and a possible shielding effect are investigated. Therefore, the theory of material forces (also called configurational forces) is applied, which are generalized thermodynamic forces acting on defects, see e.g. [80–82]. A great advantage of the approach is that it distinguishes between the material force acting on the crack tip and those occuring in zones of inelastic deformation, see e.g. [83–86]. Generally, a material force $\vec{G}_\mathrm{D}$ acting on defects in a domain surrounded by the contour Γ reads

$$\vec{G}_\mathrm{D} = \int_\Gamma \boldsymbol{Q} \cdot \vec{n} \; \mathrm{d}S \tag{22.89}$$

with the unit normal vector $\vec{n}$ and the energy-momentum tensor of elasto-statics $\boldsymbol{Q}$ according to Eshelby, see [81]. The tensor $\boldsymbol{Q}$ is calculated by

$$\boldsymbol{Q} = \psi \boldsymbol{\delta} - (\operatorname{grad} \vec{u})^\mathrm{T} \cdot \boldsymbol{\sigma} \tag{22.90}$$

with the unit tensor of second order $\boldsymbol{\delta}$.

In this section we assume small strains, isothermal and static conditions, and the absence of body forces. The small strain tensor can be additively decomposed into elastic and inelastic strains.

$$\boldsymbol{\varepsilon} = \boldsymbol{\varepsilon}_\mathrm{el} + \boldsymbol{\varepsilon}_\mathrm{trip} + \boldsymbol{\varepsilon}_\mathrm{vpl} \tag{22.91}$$

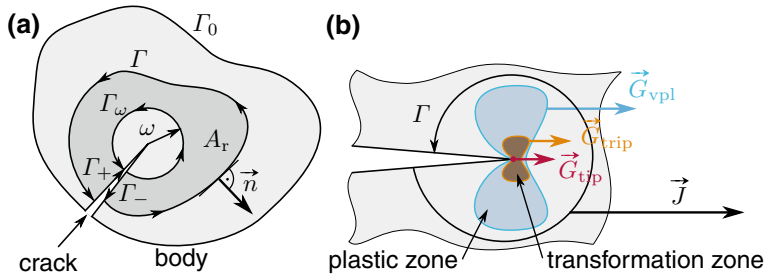

Fig. 22.10 **a** Cracked body with different contours and regular subpart A_r, **b** Different material forces near a crack tip in TRIP-steel acting on different defects

The application of material forces to TRIP-steel has been discussed in detail by Kuna et al. [21]. Thereafter, a local balance of material forces is established by taking the divergence of $\boldsymbol{Q}$, which after some rearrangements leads to

$$\operatorname{div} \boldsymbol{Q} + \boldsymbol{\sigma} : \operatorname{grad} \boldsymbol{\varepsilon}_{\mathrm{vpl}} + \boldsymbol{\sigma} : \operatorname{grad} \boldsymbol{\varepsilon}_{\mathrm{trip}} + \left| \triangle g_{\mathrm{chem}}^{\mathrm{a}\to\mathrm{m}} \right| \operatorname{grad} z = \vec{0}. \tag{22.92}$$

The term $\triangle g_{\mathrm{chem}}^{\mathrm{a}\to\mathrm{m}}$ describes the difference in the chemical energy of austenite and martensite and is known from Sect. 22.2.2.4. Following (22.92) the divergence of $\boldsymbol{Q}$ is balanced by material body forces resulting from gradients of the internal variables $\boldsymbol{\varepsilon}_{\mathrm{trip}}$, $\boldsymbol{\varepsilon}_{\mathrm{vpl}}$ and z. The gradient terms enter the derivation, because the gradient of the HELMHOLTZ potential ψ is evaluated, see [21].

Furthermore, the global balance of material forces is achieved by integrating the local balance (22.92) over a regular subpart A_r of the body. Figure 22.10 depicts the case of a cracked body with its regular subpart (domain A_r) and an enclosing contour $C = \Gamma + \Gamma_+ + \Gamma_- - \Gamma_\omega$. Applying the divergence theorem to the integrated local balance and some rearrangements enable the formulation of the material force acting on the crack tip:

$$\vec{G}_{\mathrm{tip}} = \lim_{\omega\to 0} \int_{\Gamma_\omega} \boldsymbol{Q} \cdot \vec{n} \, \mathrm{d}S = \vec{J} - \vec{G}_{\mathrm{trip}} - \vec{G}_{\mathrm{vpl}} \tag{22.93}$$

$$\vec{J} = \int_{\Gamma} \boldsymbol{Q} \cdot \vec{n} \, \mathrm{d}S \tag{22.94}$$

$$\vec{G}_{\mathrm{trip}} = \lim_{\omega\to 0} \int_{A_r} -\left(\boldsymbol{\sigma} : \operatorname{grad} \boldsymbol{\varepsilon}_{\mathrm{trip}} + \left| \triangle g_{\mathrm{chem}}^{\mathrm{a}\to\mathrm{m}} \right| \operatorname{grad} z \right) \, \mathrm{d}A \tag{22.95}$$

$$\vec{G}_{\mathrm{vpl}} = \lim_{\omega\to 0} \int_{A_r} -\boldsymbol{\sigma} : \operatorname{grad} \boldsymbol{\varepsilon}_{\mathrm{vpl}} \, \mathrm{d}A \tag{22.96}$$

The crack driving force $\vec{G}_{\text{tip}}$ is a J-integral evaluated over a vanishingly small contour Γ_ω surrounding the crack tip. It is computed by subtracting material forces $\vec{G}_{\text{trip}}$ and $\vec{G}_{\text{vpl}}$, which result from inelastic processes in the domain A_{r}, from the usual J-integral vector $\vec{J}$. $\vec{G}_{\text{tip}}$ turns out to be a modified J-integral, which is path independent in the case of plastic deformations and phase transformations.

The different material forces relevant for the considered TRIP-steel are illustrated in Fig. 22.10. There is the usual J-integral describing the sum of material forces for all defects inside the contour Γ. The crack driving force $\vec{G}_{\text{tip}}$ acts directly on the tip. The material forces due to inelastic processes $\vec{G}_{\text{trip}}$ and $\vec{G}_{\text{vpl}}$ act on the transformation zone and the plastic zone, respectively. In the case, that Γ only includes a part of these zones, the terms $\vec{G}_{\text{trip}}$ and $\vec{G}_{\text{vpl}}$ are material forces acting on this part of the zones. As long as the inelastic material forces are positive, they decrease the available crack driving force, see (22.93), which indicates a shielding effect.

The material forces are computed numerically by finite elements within the software package ABAQUS. Therefore, postprocessing of the FE results is performed. With the help of the equivalent domain integral method, nodal material forces are formulated, compare [19, 21, 83]. The global material forces (22.93)–(22.96) are then achieved by a weighted summation of the nodal material forces.

In the following, material forces are evaluated for the example of small scale yielding under plain strain conditions. Again the boundary-layer model, Fig. 22.6, is used, this time without an initial radius at the tip. Material parameters and additional information concerning the numerical model can be found in [21].

A cohesive zone (ABAQUS built-in) is placed at the ligament in order to incorporate crack initiation and propagation. One reason is that the path independence of the crack driving force can be elaborated under non-proportional loading. The other reason is that the cohesive zone model (CZM) contains a parameter G_0 called work of separation, which is exactly the dissipated work per area of crack extension. It is therefore the critical value of the crack driving force during crack extension, which has to be calculated correctly by the proposed material force method.

A bilinear traction separation relation is applied, which includes reversible opening of the cohesive zone until the cohesive strength t_0 is reached. The corresponding value of the separation is s_0. Loading beyond this point is connected to damage evolution and a descending load carrying capacity of the cohesive zone. At the separation s_{t} the cohesive zone is totally damaged and cannot carry tractions anymore. During the complete separation process until s_{t}, the work of separation G_0 is consumed.

The mesh consists of fully integrated quadrilateral elements with quadratic shape functions (ABAQUS: CPE8). The mesh design in the region of crack extension can be seen in the following figures.

A detailed view of different nodal material forces (notation: node (K)) is shown in Fig. 22.11. The upper crack face is depicted with the initial crack tip approximately in the center. A close scrutiny of these figures reveals, that there are substantial material forces at the nodes connected to the cohesive zone (nodes on the crack face right to the initial tip). Since the CZM incorporates the fracture process, these are nodal material forces acting on the smeared crack tip. Furthermore, there are

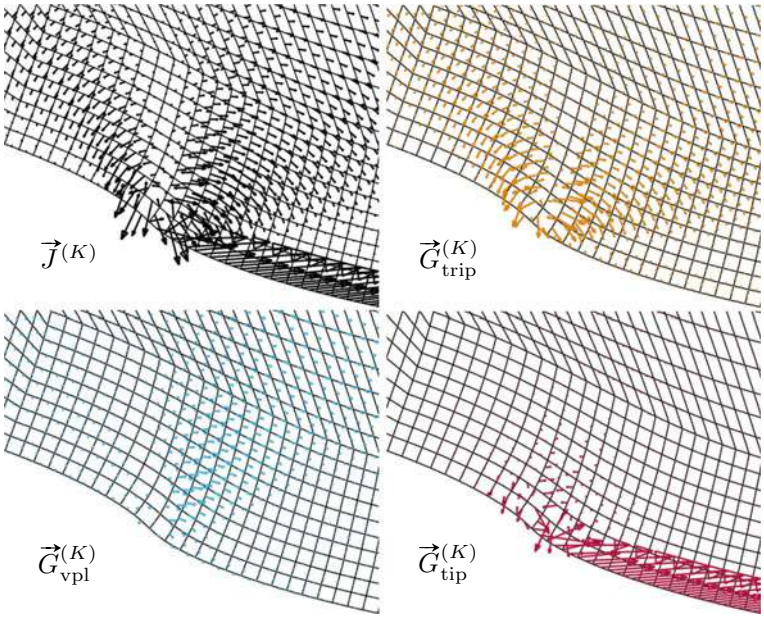

Fig. 22.11 Distribution of the different nodal material forces (node (K)), which are nodal contributions to the material forces of (22.93)–(22.96), the region near the initial crack tip (center of the crack flank) is shown during fracture initiation, cohesive elements are not shown here, reprinted from [21], with permission from Springer Nature

considerable nodal material forces in the bulk resulting from viscoplastic deformation and phase transformation. In contrast to the nodal contributions to the usual J-integral $\vec{J}^{(K)}$, the nodal contributions to the material force acting on the tip $\vec{G}^{(K)}_{\mathrm{tip}}$ nearly vanish in the volume, because of the subtraction of the inelastic nodal material forces $\vec{G}^{(K)}_{\mathrm{trip}}$ and $\vec{G}^{(K)}_{\mathrm{vpl}}$. Small remaining vectors can be explained with numerical errors in the computation of the gradients of the internal variables. They have actually no influence on the material forces after summation of the nodal contributions, see the next paragraph.

The nodal material forces are summed up to get material forces acting on the crack, the plastic zone and the transformation zone. In the case of crack propagation under mode I only the x_1-components are non-zero. These components of the different material forces are plotted in Fig. 22.12. Firstly, plausibility is checked: The regular J-integral J_1 equals the J-integral J_1^{SSY}, which is prescribed at the boundary layer, see again (22.88). Furthermore, once the cohesive zone is fully initiated, the crack driving force G_1^{tip} equals the work of separation G_0 of the CZM. The symbols in the diagram mark start and end of the fracture initiation process. At $s^{\mathrm{tip}} = s_0$, the first cohesive element reaches the cohesive strength and starts to damage. At $s^{\mathrm{tip}} = s_{\mathrm{t}}$, the first cohesive element reaches total damage and for the first time $G_1^{\mathrm{tip}} = G_0$ is

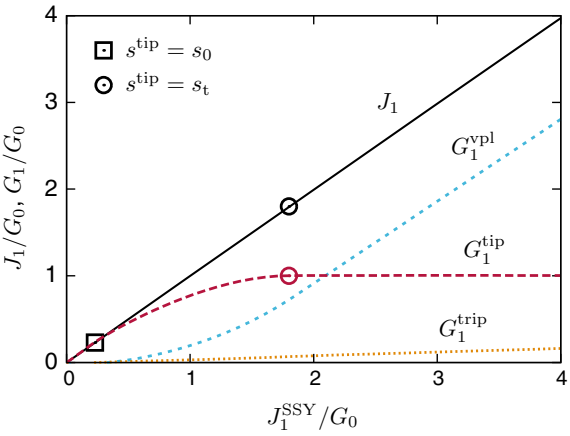

Fig. 22.12 Evolution of the nonzero component of the material forces for the boundary-layer model, J_1^{SSY} is the prescribed J-integral (external loading), G_0 is the work of separation of the CZM, start and end of fracture initiation is marked by symbols, reprinted from [21], with permission from Springer Nature

fulfilled. Thus, the proposed material force method is verified to give reasonable results.

Secondly, the contributions of the inelastic processes can be viewed in detail, Fig. 22.12. In contrast to the local distribution of the nodal material forces, the plasticity induced material force G_1^{vpl} is dominant compared to the transformation induced G_1^{trip}. This is because the plastic zone is much larger than the transformation zone in the example. Both contributions are positive, which underlines the shielding effect of viscoplasticity and martensitic phase transformation.

In Fig. 22.13, the path independence of the formulated crack driving force is demonstrated by evaluating G_1^{tip} for different domains and comparing it to the usual J-integral J_1. Until the start of fracture initiation in the CZM, both values are equal. For the case of monotonically and proportionally loaded cracks, the classical J-integral is known to be approximately path independent even if inelastic material behavior is present. This changes during crack initiation: J_1 becomes path dependent whereas the material force acting directly on the crack tip G_1^{tip} remains path independent.

22.4.4 Damage and Fracture of High Alloy TRIP-steel

Now, the simulation of damage and crack extension in high alloy TRIP-steel is elaborated in more detail. On the one hand, a cohesive zone model (CZM) is applied and appropriate cohesive parameters are estimated. On the other hand, damage evolution and crack growth is modeled by the phenomenological model, Sect. 22.3.3, including the developed non-local ductile damage formulation.

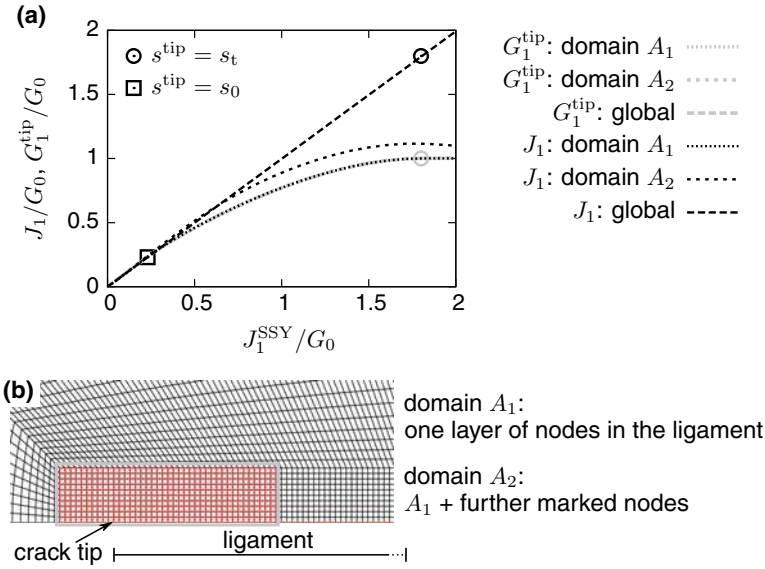

Fig. 22.13 Demonstration of the path independence of the crack driving force G_1^{tip}, **a** Evaluation of the J-integral J_1 and G_1^{tip} for different domains, J_1^{SSY} is the prescribed J-integral, G_0 is the work of separation of the CZM, **b** Definition of the different domains used in the diagram, adapted from [21], with permission from Springer Nature

22.4.4.1 Simulation of Crack Growth Using a Cohesive Zone Model

In the last section, the versatility of the cohesive zone model for the simulation of crack extension was shown. In particular, the material parameter G_0 (work of separation) is the critical value of the material force acting on the crack tip. To apply this fracture criterion, it is important to identify G_0 for the given material.

In this section, the cohesive zone parameters are identified for the cast TRIP-steel X2CrNiMn 15-7-5. The chemical composition of the investigated steel is given in Table 22.1. The corresponding experiments are carried out on CT-specimens with chevron notch, see Fig. 22.14 and the paper by Burgold et al. [87] for further details. Fracture mechanical experiments on austenitic steels are a difficult task, because of the high work hardening capability and ductility. Excessive large scale yielding, which is shown in Fig. 22.14, impose challenges to the experiments and standard methods for measuring the crack length since compliance method or potential drop method do not work [87]. Therefore, special optical techniques (see Henkel et al. [88]) are used in order to measure crack extension Δa and crack tip opening displacement CTOD δ at the surface of the specimen. From the experiments, force-displacement curves and crack growth resistance curves in terms of CTOD versus crack extension are obtained.

Because of large necking and thickness reduction during the tests three dimensional finite element calculations at finite strains are carried out, see [87, 89],

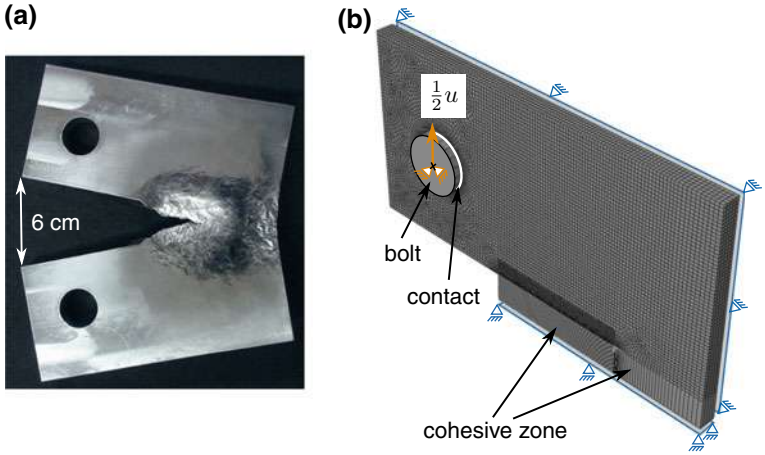

Fig. 22.14 **a** Deformed CT-specimen made of austenitic cast steel, **b** Finite element model with boundary conditions, displacement u is prescribed on the bolt, reprinted from [87], with permission from Carl Hanser Verlag GmbH & Co. KG, München

employing the commercial FE software ABAQUS. A quarter of the CT-specimen is modeled, compare Fig. 22.14. A vertical displacement u is prescribed on the bolt, that is connected to the deformable body by a contact algorithm.

The utilized CZM was developed by Roth et al. [90, 91]. Hereby, a smooth exponential traction separation relation is applied, which has an adjustable shape due to two shape parameters $\hat{\varepsilon}$ and $\hat{\omega}$. One finding of the study is, that the choice $\hat{\varepsilon} = \hat{\omega} = 1$ facilitates a good fit of the experimental data. Therewith, the well known traction separation relation from Xu and Needleman [92] is obtained.

The body is discretized by fully integrated continuum elements with linear shape functions (ABAQUS: C3D8). One layer of cohesive elements, which are user defined elements (UEL) [90, 91], is placed in the ligament. In contrast to ABAQUS built-in cohesive elements, the user elements work correctly on symmetry planes under large deformations.

It turned out to be sufficient to model the material behavior of the applied steel by a simplified constitutive law, in which transformation strains are not considered. The yield function of the rate independent model for isothermal conditions is given by

$$y_{\mathrm{pl}}(\boldsymbol{\sigma}, \sigma_{\mathrm{y}}) = \sigma_{\mathrm{eq}}(\boldsymbol{\sigma}) - \sigma_{\mathrm{y}} \leq 0 \tag{22.97}$$

with the VON MISES equivalent stress σ_{eq} and the yield stress σ_{y}. An associated flow rule is considered and the evolution equation for the plastic rate of deformation takes the form

$$\boldsymbol{D}_{\mathrm{pl}} = \dot{\Lambda}_{\mathrm{pl}} \frac{\partial y_{\mathrm{pl}}}{\partial \boldsymbol{\sigma}} = \dot{\varepsilon}_{\mathrm{eq}} \boldsymbol{N}. \tag{22.98}$$

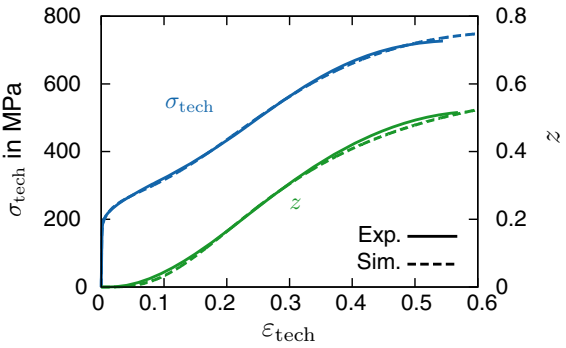

Fig. 22.15 Engineering stress-strain curves and evolution of martensite volume fraction z under uniaxial tension, comparison between experimental data and simulation with the material model

Hereby, the plastic multiplier $\dot{\Lambda}_{\text{pl}}$ is equal to the rate of equivalent plastic strain $\dot{\varepsilon}_{\text{eq}}$. The tensor $\boldsymbol{N}$ is the flow normal known from (22.51).

The evolution of the yield stress σ_{y} is defined by the hardening law (22.71). This relation is simplified because the isothermal case is considered and LODE-angle dependence is not taken into account ($r = \varepsilon_{\text{eq}}$ because $b = 0$ in (22.73))

$$\sigma_{\text{y}}\left(\varepsilon_{\text{eq}}, z\right) = \sigma_0 + Z_1 m_z\left(z\right) + H\left(\varepsilon_{\text{eq}}\right). \tag{22.99}$$

Thus, in addition to Z_1 the initial yield stress σ_0 becomes a material parameter. The work hardening term $H\left(\varepsilon_{\text{eq}}\right)$, see (22.85), is modified by $r_{\text{c}} \to \infty$ and reads

$$H\left(\varepsilon_{\text{eq}}\right) = H_0\, \varepsilon_{\text{eq}}^{q} \tag{22.100}$$

with the parameters H_0 and q. The martensite influence term $m_z\left(z\right)$ is given by (22.87) with the parameter Z_2.

The martensite kinetics is based on the empirical approach of Sect. 22.3.3.3. Therefore, the volume fraction of shear bands evolves as described by (22.48), in which α_{oc} is directly taken as material parameter. The rate of martensite volume fraction is computed by (22.49) with β_{oc} and n_{oc} as additional material parameters.

The parameters of the material model are adequately calibrated to data from tensile tests of the cast TRIP-steel X2CrNiMn 15-7-5, see Fig. 22.15. In addition to the mechanical data, the martensite volume fraction z is measured in situ by a novel magnetic device developed by Hauser et al. [93] and is applied in the calibration procedure. The identified parameters are given in Table 22.6.

Table 22.6 Parameters of the rate independent TRIP-steel model

σ_0	H_0	q	Z_1	Z_2	α_{oc}	β_{oc}	n_{oc}
MPa	MPa	–	MPa	–	–	–	–
153.8	434.2	0.401	370.9	2.06	5.66	0.988	3.805

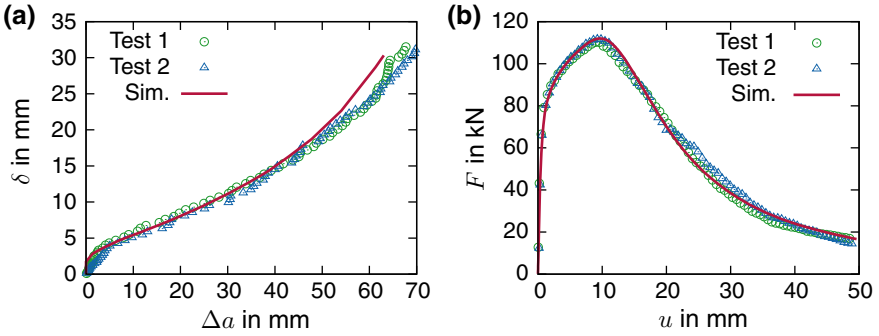

Fig. 22.16 Comparison of experiments and simulation, **a** Crack growth resistance curves in terms of CTOD δ and crack extension Δa, **b** Force-displacement curves (F vs. u)

Table 22.7 Identified set of cohesive zone parameters

t_0	G_0	$\hat{\varepsilon}$	$\hat{\omega}$
MPa	kJ/m^2	–	–
700	425	1	1

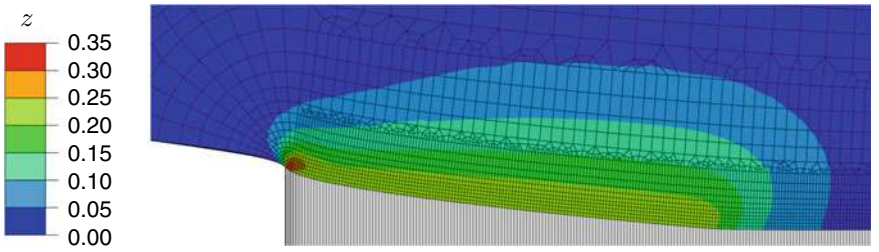

Fig. 22.17 Plot of the distribution of martensite volume fraction z during crack extension, note the cohesive elements (white) in the ligament

Ultimately, the remaining independent cohesive parameters G_0 and t_0 have been chosen in a way, that the simulated force-displacement curve and crack growth resistance curve fit the experimental ones. The results are depicted in Fig. 22.16. Data from two realizations of the experiment are compared to the simulation with the final parameter set, which is given in Table 22.7. The two tests show only small differences and the simulation fits both tests very well. This supports the identified set of parameters and the whole modeling approach. Thus, the fracture process in the investigated CT-specimens is characterized by the given cohesive parameters. This concept was also successfully applied to a non-transforming austenitic steel in [87].

Finally, the martensite distribution around the crack is illustrated in Fig. 22.17. The highest amount (0.3–0.35) of martensite is formed during crack tip blunting near the

initial crack tip. During crack extension a zone of martensite volume fraction between 0.2 and 0.25 is moved through the ligament.

22.4.4.2 Simulations Using the Micromorphic Model of Ductile Damage

Here, the micromorphic damage extensions of the phenomenological model from Sect. 22.3.3 will be used for simulation of ductile crack growth at isothermal conditions. Test results of the cast TRIP-steel X3CrMnNi 16-6-6 are utilized for calibration and validation. As described in [35], the calibration strategy for the considered class of damage models consists of three steps:

1. Choosing and fitting an isotropic strain hardening law to data of smooth and slightly notched tensile tests
2. Estimating an appropriate damage indicator function using FE-analysis and experimental results, e.g., of notched tensile tests
3. Fitting the damage parameters (q_1–q_3, ε_c and L_{nl}) to match results of a fracture mechanics test

For the first calibration step, the parameters of the strain hardening model for cast X3CrMnNi 16-6-6 (Sect. 22.4.2) are slightly modified. This is done in order to improve the fit to the notched tensile tests discussed in Sect. 22.4.2.4.

For the second calibration step, undamaged FE-simulations of the notched tensile tests are performed to extract the loading history which leads to initiation of damage in critical regions, see [35]. As critical region, the center of the specimen at the symmetry plane is defined, since here the highest stress triaxiality occurs. The history until the rather sudden deviation of simulated and experimental force versus elongation curves is taken into account. The equivalent strain to damage initiation is plotted versus the stress triaxiality in Fig. 22.18. For all considered notch radii, a drop of triaxiality during deformation is observed, which is in contrast to recent results of a pressure vessel steel [35]. This behavior can be attributed to the strain hardening of the TRIP-steel: The high hardening capability delays a localization of deformation and the blunting of the notch decreases the triaxiality of the loading state. As indicator of damage initiation, the integral formulation

$$\omega\left(h, \varepsilon_{eq}\right) = \int_0^{\varepsilon_{eq}(t)} \Omega\left(h\right)\, \mathrm{d}\varepsilon_{eq}, \tag{22.101}$$

$$\Omega\left(h\right) = \Omega_1 + \Omega_2 \exp\left(\Omega_3 h\right) \tag{22.102}$$

is used, which constitutes a modified Rice-Tracey-approach, see illustration in Fig. 22.18. The identified parameters read $\Omega_1 = 0.094$, $\Omega_2 = 0.666$, and $\Omega_3 = 2.721$.

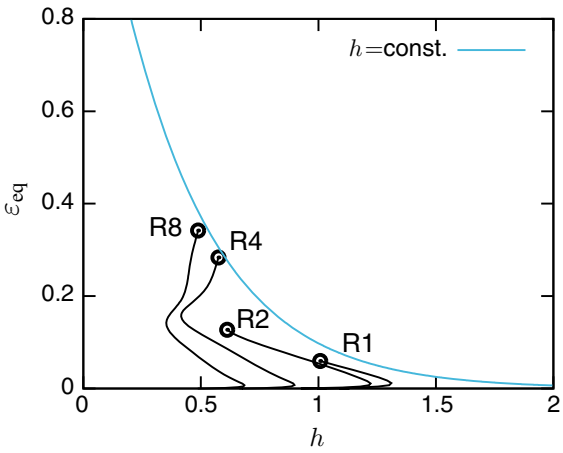

Fig. 22.18 Damage initiation locus (equivalent plastic strain ε_{eq} vs. stress triaxiality h): Loading history at the critical locations for the differently notched tensile tests, circles mark damage initiation; the damage initiation locus for constant triaxiality during loading is added as solid blue line

In addition to the notched tensile tests, fracture mechanics experiments are necessary in order to perform the third step of the proposed parameter calibration. Due to missing experimental results on fracture parameters of cast X3CrMnNi 16-6-6, a numerical prediction serves as fracture mechanics reference. Appropriate parameters of a cohesive zone model are available for a similar steel in Sect. 22.4.4.1. These results are utilized to make a realistic guess for the fracture behavior of X3CrMnNi 16-6-6. A simulation of the 3D-CT-specimen is performed using the calibrated cohesive zone model from Sect. 22.4.4.1 and the calibrated material model for X3CrMnNi 16-6-6. Because fracture is completely described by the cohesive zone, damage of the bulk material is neglected. The obtained reference force versus displacement curve and the crack growth resistance curve in terms of CTOD versus crack length are shown in Figs. 22.19 and 22.21. The crack extension Δa is evaluated using the maximum stress criterion with respect to the undeformed configuration at the surface of the specimen as explained in [94]. This criterion can be similarly evaluated for the cohesive zone model and the ductile damage approach.

The CT-specimen, see Fig. 22.14 and reference [87], is implemented as FE-model in ABAQUS. To avoid highly distorted elements, a small radius $r_t = 0.05$ mm is applied at the crack tip as suggested in literature (see Fig. 22.20, [35, 76, 94]), which is permissible for the expected blunting prior to crack propagation. A 3D-finite element formulation employing reduced integration with quadratic shape functions for the displacement and linear shape functions for the micromorphic DOF are used (ABAQUS: C3D20RT). Along the ligament, a mesh size of $b_e/L_{nl} = 0.25$ is prescribed, where b_e is the edge length of the element, see Fig. 22.20. This recommendation can be found in literature to obtain converged results [34, 35, 95]. The axi-symmetric models of notched tensile tests are also meshed with the mentioned restrictions in regions of interest (ABAQUS elements: CAX8RT).

During the calibration process, the parameters q_1 and q_3 are fixed to the value 3. Only the internal length L_{nl}, the influence of equivalent strain q_2 (void nucle-

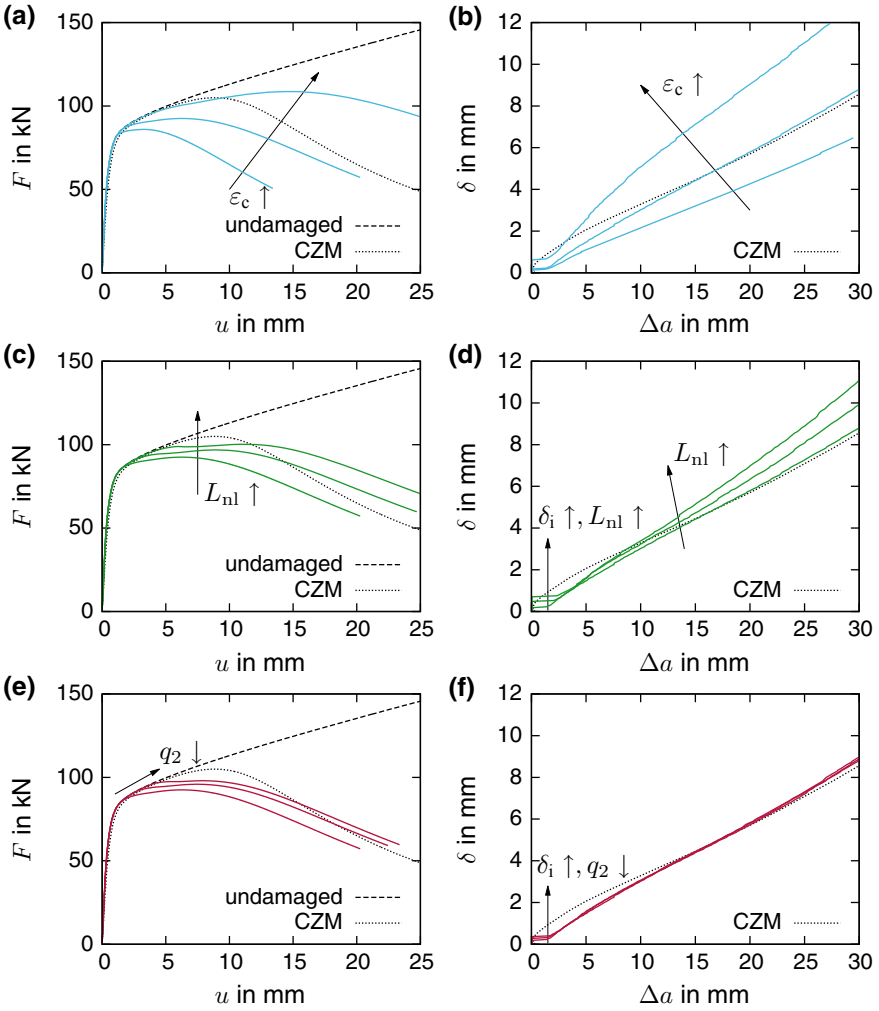

Fig. 22.19 Influence of different parameters of the damage evolution law on structural response of the CT-specimen (force F vs. displacement u curves, crack growth resistance CTOD δ vs. Δa), Top row (**a**, **b**): $\varepsilon_c = \{0.2, 0.3, 0.5\}$, Middle row (**c**, **d**): $L_{nl} = \{0.5, 0.75, 1\}$ mm, Bottom row (**e**, **f**): $q_2 = \{0.01, 0.025, 0.1\}$

ation), and the acceleration parameter ε_c are varied. Considerable small values are prescribed for q_2, because void growth is assumed as the main damage mechanism in the considered domain of moderate to high stress triaxialities.

In order to assess the influence of the free parameters, a sensitivity study is performed. The reference set of parameters is prescribed as: $\varepsilon_c = 0.3$, $L_{nl} = 0.5$ mm, and $q_2 = 0.1$. The results are summarized in Fig. 22.19 and compared to the reference cohesive zone simulation as well as the pure blunting solution: With varying ε_c,

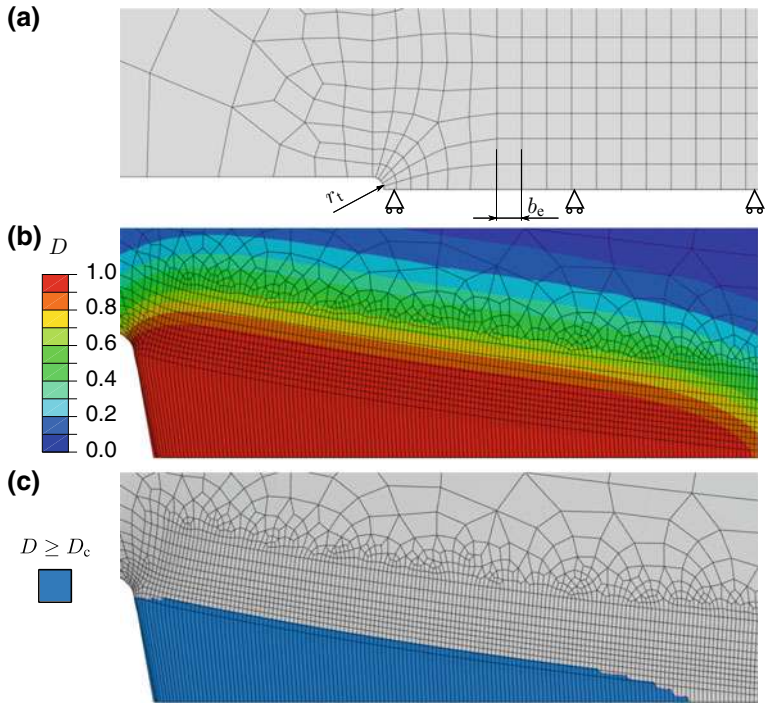

Fig. 22.20 Simulation of the CT-specimen, **a** Initial FE-mesh with crack tip rounding, **b** Deformed structure with damage distribution D at a crack extension of $\approx$15 mm, **c** Highlighted elements undergoing total damage

the slope of the crack growth resistance curve and the decreasing branch can be controlled. Simultaneously, the force level is changed. The internal length L_{nl} can be used to calibrate the maximum force and the crack initiation value, here the critical crack tip opening δ_{i}. Changing q_2 determines the deviation of the force response from the undamaged solution.

Motivated by the sensitivity study, a rough accordance is obtained with the manual calibration of the damage parameters: $\varepsilon_{\mathrm{c}} = 0.2$, $L_{\mathrm{nl}} = 1.0$ mm, and $q_2 = 0.01$. The response of the calibrated model is illustrated in Fig. 22.21. The location and amount of the maximum force need further improvement and the crack tip opening is underestimated. But the softening branch of the force versus displacement curve and the slope of the crack growth resistance curve are in acceptable accordance. It should be mentioned that a considerably large crack propagation can be modeled in a robust manner ($\Delta a = 30$ mm); the simulations are interrupted externally after reaching the prescribed crack length. The contour plots in Fig. 22.20 show that damage is distributed over some layers of elements indicating the regularized character of the proposed damage model. The crack is represented by a layer of total

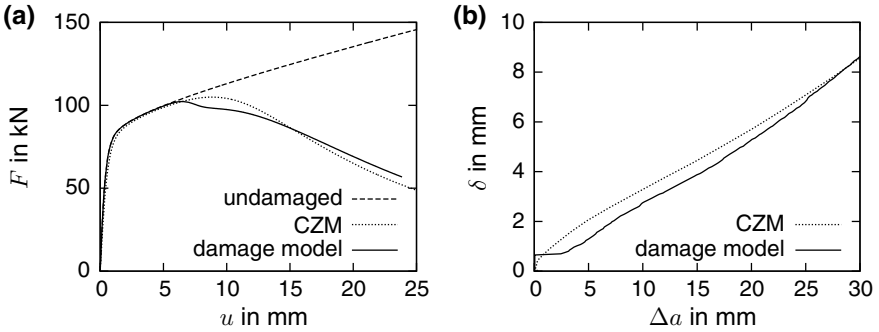

Fig. 22.21 Calibration results of micromorphic damage model with cohesive zone simulation (CZM) as reference, simulation without damage is added, **a** Force F versus displacement u, **b** CTOD δ versus crack extension Δa

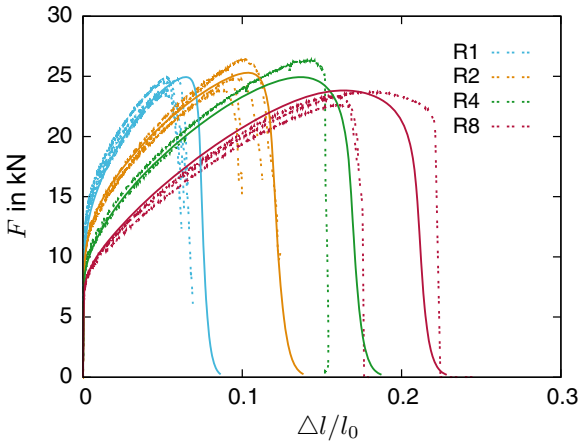

Fig. 22.22 Force F versus elongation $\Delta l/l_0$ curves for notched tensile tests; solid lines correspond to the damage model prediction, dashed lines denote experiments

damaged, highly distorted elements. Hence, the applied patch solution for damping pathological widening of the damage zone works well in this special case.

With the estimated damage initiation and evolution parameters at hand, the notched tensile tests are simulated until failure. A comparison of predicted and experimental force versus elongation response reveals a reasonable agreement, see Fig. 22.22. The elongation at failure is slightly overestimated by the simulation for the small notch radii, but the load carrying capability is fully captured.

In conclusion, the proposed and calibrated micromorphic approach of ductile damage for high alloy TRIP-steel is able to reproduce the deformation, damage, and failure behavior including stable crack propagation.

22.5 Conclusions

Based on a profound thermomechanical framework, a micromechanically based material model and a phenomenological approach are developed, which account for typical phenomena attributed to high alloy TRIP-steel: stress state dependent strain hardening, loading rate sensitivity and temperature dependency. In addition, a regularized ductile damage model, which is formulated with help of the micromorphic approach, is included.

For the phenomenological modeling approach, the applicability is demonstrated by calibration and validation with experiments of a cast X3CrMnNi 16-6-6 steel exhibiting strain induced α'-martensite formation. After calibrating the model to a subset of experiments (quasi-static loaded, uni-axial tension and compression tests at different temperatures), some predictive simulations are conducted. Firstly, predictions of stress-strain response at temperatures, which are not considered during calibration, are of reasonable quality. Especially, the disappearance of the tensions-compression asymmetry of strain hardening with increasing temperature is correctly reflected. Secondly, acceptable results are obtained for tensile tests at increased strain rates, where the thermomechanical coupling becomes important: The characteristic curve crossing of strain hardening curves is clearly captured by the model. Finally, simulations of notched tensile tests yield good agreement to available experiments. Hence, the model is also validated for inhomogeneous deformation.

With the help of the micromechanically motivated model, the effect of martensitic phase transformation on the loading situation at crack tips is investigated. The course of the stresses in front of a blunting crack shows characteristic curvature attributed to phase transformation. The most important influence is an increase in the stress components due to transformation induced hardening. Additional hardening affects ductile fracture in a positive manner, because the growth of microvoids is postponed. Another study examined the crack driving force for TRIP-steels under consideration of plastic deformation and phase transformation. By applying the theory of material forces a modified J-integral was formulated, which is path independent under these circumstances. Resulting from this, a shielding effect due to both inelastic strains was observed for small scale yielding.

Taking fracture process into account, a pragmatic cohesive zone model is successfully calibrated to reproduce crack propagation during loading of a CT-specimen. In combination with the cohesive zone, a simplified material model for isothermal and quasi-static conditions turned out to be sufficient to enable a good fit of the CT-tests. Finally, the micromorphic ductile damage model is applied to predict damage, crack propagation and failure of different structures made of a cast X3CrMnNi 16-6-6 steel (CT-specimen, notched tensile tests). A reasonable agreement to experimental and numerical reference data is obtained after performing a developed calibration strategy.

Hence, versatile modeling tools for TRIP-steels are available, which are ready to be applied in simulations of future engineering applications.

Acknowledgements The authors gratefully acknowledge the Deutsche Forschungsgemeinschaft (DFG, German Research Foundation) for funding the research in the framework of the Collaborative Research Center "TRIP-Matrix-Composite", (project number 54473466—SFB 799, subproject C5). In addition the authors thank the involved staff from SFB 799 and from the Institute of Mechanics and Fluid Dynamics (TU Freiberg) as well as Dr. Uwe Mühlich for their collaboration and numerous fruitful discussions.

References

1. H. Biermann, U. Martin, C.G. Aneziris, A. Kolbe, A. Müller, W. Schärfl, M. Hermann, Adv. Eng. Mater. **11**, 1000 (2009)
2. D. Ehinger, L. Krüger, U. Martin, C. Weigelt, C.G. Aneziris, Steel Res. Int. **82**, 1048 (2011)
3. D. Ehinger, L. Krüger, U. Martin, C. Weigelt, C.G. Aneziris, Int. J. Solids Struct. **66**, 207 (2015)
4. C. Weigelt, C.G. Aneziris, H. Berek, D. Ehinger, U. Martin, Adv. Eng. Mater. **14**(1–2), 53 (2012)
5. A. Jahn, A. Kovalev, A. Weiß, S. Wolf, L. Krüger, P.R. Scheller, Steel Res. Int. **82**, 39 (2011)
6. S. Martin, S. Wolf, U. Martin, L. Krüger, Solid State Phenomen. **172–174**, 172 (2011)
7. M. Linderov, C. Segel, A. Weidner, H. Biermann, A. Vinogradov, Mat. Sci. Eng. A **597**, 183 (2014)
8. C. Ullrich, S. Martin, C. Schimpf, A. Stark, N. Schell, D. Rafaja, Adv. Eng. Mater. **21**(5), 1801101 (2019)
9. S. Prüger, A. Seupel, M. Kuna, Int. J. Plast. **55**, 182 (2014)
10. S. Wolf, S. Martin, L. Krüger, U. Martin, Mat. Sci. Eng. A **594**, 72 (2014)
11. A. Seupel, R. Eckner, A. Burgold, M. Kuna, L. Krüger, Mat. Sci. Eng. A **662**, 342 (2016)
12. A. Seupel, M. Kuna, in *Proceedings of the 14th International Conference on Computational Plasticity - Fundamentals and Applications, COMPLAS 2017* (2017), pp. 576–587
13. M.P. Miller, D.L. McDowell, Int. J. Plast. **12**(9), 875 (1996)
14. J. Serri, M. Martiny, G. Ferron, Int. J. Mech. Sci. **47**(6), 884 (2005)
15. I. Papatriantafillou, M. Agoras, M. Aravas, G. Haidemenopoulos, Comput. Method. Appl. M. **195**, 5094 (2006)
16. L. Mehlhorn, S. Prüger, S. Soltysiak, U. Mühlich, M. Kuna, Steel Res. Int. **82**(9), 1022 (2011)
17. S. Prüger, L. Mehlhorn, S. Soltysiak, M. Kuna, Comp. Mater. Sci. **64**, 273 (2012)
18. S. Prüger, L. Mehlhorn, U. Mühlich, M. Kuna, Adv. Eng. Mater. **15**(7), 542 (2013)
19. A. Burgold, M. Kuna, S. Prüger, Procedia Mater. Sci. **3**(0), 461 (2014). 20th European Conference on Fracture
20. A. Burgold, M. Kuna, S. Prüger, Eng. Fract. Mech. **138**, 169 (2015)
21. M. Kuna, A. Burgold, S. Prüger, Int. J. Fract. **193**, 171 (2015)
22. S. Prüger, Thermomechanische Modellierung der dehnungsinduzierten Phasenumwandlung und der asymmetrischen Verfestigung in einem TRIP-Stahlguss. Ph.D. thesis, TU Bergakademie Freiberg (2016). (in German)
23. S. Forest, J. Eng. Mech. **135**(3), 117 (2009)
24. P. Germain, SIAM J. Appl. Mech. **25**(3), 556 (1973)
25. B.D. Coleman, W. Noll, Arch. Ration. Mech. An. **13**(1), 167 (1963)
26. J. Lemaitre, J.L. Chaboche, *Mechanics of solid materials* (Cambridge University Press, 1998)
27. H. Hallberg, P. Håkansson, M. Ristinmaa, Int. J. Plasticity **23**, 1213 (2007)
28. J. Lemaitre, Nucl. Eng. Des. **80**, 233 (1984)
29. H. Xiao, O.T. Bruhns, A. Meyers, Acta Mech. **124**, 89 (1997)
30. H. Xiao, O.T. Bruhns, A. Meyers, Acta Mech. **138**, 31 (1999)
31. A. Eshraghi, K.D. Papoulia, H. Jahed, J. Appl. Mech. **80**(2), 021027 1 (2013)
32. E. Diamantopoulou, W. Liu, C. Labergere, H. Badreddine, K. Saanouni, P. Hu, Int. J. Damage Mech. **26**(2), 314 (2017)

33. R.H.J. Peerlings, R. de Borst, W.A.M. Brekelmans, J.H.P. de Vree, Int. J. Numer. Meth. Eng. **39**, 3391 (1996)
34. A. Seupel, G. Hütter, M. Kuna, Eng. Fract. Mech. **199**, 41 (2018)
35. A. Seupel, M. Kuna, Int. J. Damage Mech. **28**(8), 1261 (2019)
36. I. Tamura, Met. Sci. **16**, 245 (1982)
37. G.B. Olson, M. Cohen, Metall. Trans. A **6A**, 791 (1975)
38. R.G. Stringfellow, D.M. Parks, G.B. Olson, Acta Metall. Mater. **40**(7), 1703 (1992)
39. Y. Tomita, T. Iwamoto, Int. J. Mech. Sci. **37**(12), 1295 (1995)
40. T. Iwamoto, T. Tsuta, Y. Tomita, Int. J. Mech. Sci. **40**, 173 (1998)
41. U. Ahrens, Beanspruchungsabhängiges Umwandlungsverhalten und Umwandlungsplastizität niedrig legierter Stähle mit unterschiedlich hohen Kohlenstoffgehalten. Ph.D. thesis, TU Paderborn (2003). (in German)
42. K. Nagayama, T. Terasaki, K. Tanaka, F.D. Fischer, T. Antretter, G. Cailletaud, F. Azzouz, Mat. Sci. Eng. A **308**, 25 (2001)
43. F.D. Fischer, G. Reisner, E. Werner, K. Tanaka, G. Cailletaud, T. Antretter, Int. J. Plast. **16**, 723 (2000)
44. M. Berveiller, F.D. Fischer (eds.), *Mechanics of Solids with Phase Changes* (Springer, 1997)
45. R. Mahnken, A. Schneidt, T. Antretter, Int. J. Plast. **25**, 183 (2009)
46. R. Mahnken, A. Schneidt, Arch. Appl. Mech. **80**, 229 (2010)
47. S. Prüger, M. Kuna, S. Wolf, L. Krüger, Steel Res. Int. **82**(9), 1070 (2011)
48. R. Zaera, J.A. Rodríguez-Martínez, A. Casado, J. Fernández-Sáez, A. Rusinek, R. Pesci, Int. J. Plast. **29**, 77 (2012)
49. H. Hallberg, P. Håkansson, M. Ristinmaa, Int. J. Solids Struct. **47**(11–12), 1580 (2010)
50. A. Seupel, M. Kuna, Appl. Mech. Mater. **784**, 484 (2015)
51. S. Martin, Deformationsmechanismen bei verschiedenen Verformungstemperaturen in austenitischem TRIP/TWIP-Stahl. Ph.D. thesis, TU Bergakademie Freiberg (2013). (in German)
52. S. Prüger, M. Kuna, Proc. Appl. Math. Mech. **11**, 425 (2011)
53. S. Prüger, M. Kuna, K. Nagel, H. Biermann, Computational Plasticity XI Fundamentals and Applications 869–881 (2011)
54. P.P. Castañeda, P. Suquet, Adv. Appl. Mech. **34**, 172 (1997)
55. F. Lani, Q. Furnémont, T.V. Rompaey, F. Delanney, P.J. Jaques, T. Pardoen, Acta Mater. **55**, 3695–3705 (2007)
56. J.R. Rice, D.M. Tracey, J. Mech. Phys. Solids **17**, 201 (1969)
57. A.L. Gurson, J. Eng. Mater. Technol. **44**, 2 (1977)
58. M. Kuna, S. Wippler, Eng. Fract. Mech. **77**, 3635 (2010)
59. N. Aravas, Int. J. Numer. Meth. Eng. **24**, 1395 (1987)
60. A.C.F. Cocks, J. Mech. Phys. Solids **37**(6), 693 (1989)
61. J. Besson, Int. J. Damage Mech. **19**, 3 (2010)
62. D. Kulawinski, S. Ackermann, A. Seupel, T. Lippmann, S. Henkel, M. Kuna, A. Weidner, H. Biermann, Mat. Sci. Eng. A **642**, 317 (2015)
63. S. Wolf, Temperatur- und dehnratenabhängiges Werkstoffverhalten einer hochlegierten CrMnNi-TRIP/TWIP-Stahlgusslegierung unter einsinniger Zug- und Druckbeanspruchung. Ph.D. thesis, TU Bergakademie Freiberg (2012). (in German)
64. A.M. Beese, D. Mohr, Acta Mater. **59**, 2589 (2011)
65. C. Garion, B. Skoczen, Int. J. Damage Mech. **12**, 313 (2003)
66. S.W. Yoo, C.S. Lee, W.S. Park, M.H. Kim, J.M. Lee, Comp. Mater. Sci. **50**, 2014 (2011)
67. C.S. Lee, B.M. Yoo, M.H. Kim, J.M. Lee, Int. J. Damage Mech. **22**(1), 95 (2012)
68. J. Lian, M. Sharaf, F. Archie, S. Münstermann, Int. J. Damage Mech. **22**(2), 188 (2013)
69. J. Mediavilla, R.H.J. Peerlings, M.G.D. Geers, Comput. Method. Appl. M. **195**, 4617 (2006)
70. B. Vandoren, A. Simone, Comput. Method. Appl. M. **332**, 644 (2018)
71. L. Krüger, S. Wolf, U. Martin, P. Scheller, A. Jahn, A. Weiß, DYMAT 1069–1074 (2009)
72. L. Krüger, S. Wolf, S. Martin, U. Martin, A. Jahn, A. Weiß, P.R. Scheller, Steel Res. Int. **32**(8), 1087 (2011)
73. R. Zaera, J.A. Rodríguez-Martínez, D. Rittel, Int. J. Plast. **40**, 185 (2013)

74. J. Hutchinson, J. Mech. Phys. Solids **16**(1), 13 (1968)
75. J.R. Rice, G.F. Rosengren, J. Mech. Phys. Solids **16**, 1 (1968)
76. R. McMeeking, J. Mech. Phys. Solids **25**(5), 357 (1977)
77. H. Yuan, G. Lin, A. Cornec, Int. J. Fract. **71**(3), 273 (1995)
78. R.G. Stringfellow, Mechanics of Strain-Induced Transformation Toughening in Metastable Austenitic Steels. Ph.D. thesis, Massachusetts Institute of Technology (1990)
79. G. Hütter, L. Zybell, U. Mühlich, M. Kuna, Comp. Mater. Sci. **80**, 61 (2013)
80. M.E. Gurtin, *Configurational Forces as Basic Concepts of Continuum Physics* (Springer, New York, 2000)
81. R. Kienzler, G. Herrmann, *Mechanics in Material Space* (Springer, Berlin Heidelberg, 2000)
82. G.A. Maugin, *Configurational forces: thermomechanics, physics, mathematics, and numerics* (CRC Press, 2011)
83. T. Nguyen, S. Govindjee, P. Klein, H. Gao, J. Mech. Phys. Solids **53**(1), 91 (2005)
84. B. Näser, M. Kaliske, R. Müller, Comput. Mech. **40**(6), 1005 (2007)
85. N. Simha, F. Fischer, G. Shan, C. Chen, O. Kolednik, J. Mech. Phys. Solids **56**(9), 2876 (2008)
86. O. Kolednik, R. Schöngrundner, F. Fischer, Int. J. Fract. **187**(1), 77 (2014)
87. A. Burgold, S. Henkel, S. Roth, M. Kuna, H. Biermann, Mater. Test. **60**(4), 341 (2018)
88. S. Henkel, D. Holländer, M. Wünsche, H. Theilig, P. Hübner, H. Biermann, S. Mehringer, Eng. Fract. Mech. **77**(11), 2077 (2010)
89. A. Burgold, S. Roth, M. Kuna, Advances in Fracture and Damage Mechanics XVII 167–172 (2018)
90. S. Roth, G. Hütter, M. Kuna, Int. J. Fract. **188**(1), 23 (2014)
91. S. Roth, Entwicklung und Implementierung zyklischer Kohäsivzonenmodelle zur Simulation von Werkstoffermüdung. Ph.D. thesis, TU Bergakademie Freiberg (2015). URL http://nbn-resolving.de/urn:nbn:de:bsz:105-qucosa-209735. (in German)
92. X.P. Xu, A. Needleman, Modell. Simul. Mater. Sci. Eng. **1**(2), 111 (1993)
93. M. Hauser, M. Wendler, S.G. Chowdhury, A. Weiß, J. Mola, Mater. Sci. Tech. **31**(12), 1473 (2015)
94. G. Hütter, T. Linse., U. Mühlich, M. Kuna, Int. J. Solids Struct. **50**, 662 (2013)
95. T. Linse, G. Hütter, M. Kuna, Eng. Fract. Mech. **95**, 13 (2012)

Chapter 23
Properties of Phase Microstructures and Their Interaction with Dislocations in the Context of TRIP Steel Systems

Rachel Strobl, Michael Budnitzki and Stefan Sandfeld

Abstract Transformation Induced Plasticity (TRIP) steels undergo a diffusionless phase transformation from austenite to martensite, resulting in a material exhibiting desireable material properties such as exceptional balance of strength and ductility as well as good fatigue behavior. Computational modeling at the mesoscale is potentially a suitable tool for studying how plastic deformation interacts with phase transformations and ultimately affects the bulk properties of these steels. We introduce models that represent the phase microstructure in a continuum approach and couple a time-dependent Ginzburg-Landau equation with discrete dislocation via their elastic strain energy densities. With this, the influence of several dislocation configurations are examined, namely a single dislocation, a "penny-shaped crack", and a "dislocation cascade". It is shown that the strain due to the presence of dislocations has a significant influence on the resultant martensitic microstructure. Furthermore, the importance of using a non-local elasticity approach for the dislocation stress fields is demonstrated.

23.1 Introduction

The solid-solid phase transformation in transformation induced plasticity (TRIP) steels leads to desirable properties for engineering applications. In the case of a Cr-Mn-Ni steel matrix, a high fault austinite phase is converted to α-martensite, and a high number of dislocations are active during the process of phase transformation, as also seen via in situ experiments, e.g., as in [1].

R. Strobl · M. Budnitzki · S. Sandfeld (✉)
Institute of Mechanics and Fluid Dynamics, Lampadiusstraße 4, Freiberg, Germany
e-mail: stefan.sandfeld@imfd.tu-freiberg.de

R. Strobl
e-mail: rachel.strobl@imfd.tu-freiberg.de

M. Budnitzki
e-mail: michael.budnitzki@imfd.tu-freiberg.de

H. Biermann and C. G. Aneziris (eds.), *Austenitic TRIP/TWIP Steels and Steel-Zirconia Composites*, Springer Series in Materials Science 298,
https://doi.org/10.1007/978-3-030-42603-3_23

Computer simulations and numerical modeling of TRIP-steels can be very beneficial for understanding the interaction of different microstructural phenomena, such as planar defects (e.g., phase transformations) and linear defects (dislocations), all of which may have significant influence on the mechanical properties of the bulk material. Dislocations are responsible for plastic deformation of metals; they may interact among themselves and can also be nucleated, e.g., during martensitic phase transformations. The combination of martensitic phase transformations and dislocation activity results in lattice distortions and may ultimately lead to increased work hardening.

Predictive modeling requires to spatially resolve the relevant physical phenomena and to describe their evolution in time. E.g., molecular dynamics (MD) simulations are inherently able to model both phase transformations and dislocations [2–4]. However, the computational cost for solving Newton's equation of motion together with the interaction of *all* atoms for volumes and strain rates that are comparable to experimentally used ones is very high. As a consequence, typical MD simulations operate with strain rates that are several orders of magnitudes higher than the experimentally used strain rates and, at the same time, are also restricted to relatively small systems with typical sizes ranging from several nanometers to a few hundreds of nanometers.

Phenomenological continuum models of plasticity can reach relevant timescales and length scales, however, details regarding phase transformations or dislocations can only be incorporated indirectly and are generally not directly based on the underlying mechanisms. A macroscopic continuum model also cannot resolve the interface of two phases properly due to a highly coarsened resolution. Phase field models (PFMs) are based on the minimization of total energy and are "mesoscopic" methods in which individual atoms or their interactions are not explicitly represented, but in which microscopic effects are still able to be considered. However, this requires either input from lower scale methods or parameterization with experimental data.

The general phase field approach is based on a set of order parameters, $\phi_1, \ldots, \phi_n$, continuous functions in space, which represent the different phases in the system. The time evolution of the order parameters is governed by the minimization of total energy. Based on this, the relevant physical properties are described as functions of the order parameters. The governing PFM equation is the time dependent Ginsburg-Landau (TDGL) evolution equation [5], first implemented for martensitic phase transformations by Khachaturyan [6].

In the following we will introduce a coupled phase field—dislocation framework that shows how dislocations or idealized cracks interact with phase boundaries between a martensitic and an austenitic phase. A second focus is then on a general approach in the context of non-local elasticity for representing the stress field of discrete dislocations.

The following nomenclature is employed throughout this chapter: We denote vectors by bold lower case latin $\mathbf{a}$ and greek $\boldsymbol{\alpha}$ letters, and the dot operator "$\cdot$" denotes the scalar product $\mathbf{a} \cdot \mathbf{b} \in \mathcal{R}$. We will, however, abuse this notation and use the dot "$\cdot$" as well for inner products, whenever appropriate.

Second order tensors are denoted by bold uppercase latin letters $\mathbf{A}$. We introduce a scalar product between second order tensors denoted by ":" as $\mathbf{A} : \mathbf{B} := \mathrm{tr}\mathbf{A} \cdot \mathbf{B}^\top$,

where $\mathbf{B}^\top$ is the transpose of $\mathbf{B}$ and $\mathrm{tr}(\cdot)$ denotes the trace operator. In an inner product space this product implies the norm $\|\mathbf{A}\| := \sqrt{\mathbf{A} : \mathbf{A}}$. Given an orthogonal tensor $\mathbf{R}$ and an arbitrary order tensor $\mathbf{\Phi}$, $\mathbf{R} * \mathbf{\Phi}$ denotes the RAYLEIGH product of $\mathbf{R}$ and $\mathbf{\Phi}$; for a second order tensor $\mathbf{A}$, we have $\mathbf{R} * \mathbf{A} = \mathbf{R} \cdot \mathbf{A} \cdot \mathbf{R}^\top$.

Third order tensors are denoted by bold calligraphic letters $\mathcal{A}$ and "$\vdots$" is the corresponding full contraction operator. Fourth order tensors are denoted by black board upper case letters $\mathbb{A}$.

23.2 Interaction Between Martensitic Phase Transformations and Dislocations

23.2.1 Phase Field Equations

The high strain induced via a phase transformation between face centered cubic (FCC) austenite and body centered cubic (BCC) martensite may trigger the nucleation of a large number of dislocations inside the material. Both dislocations and martensitic phase transformations affect the bulk properties of steels, and therefore, representing the interaction between dislocations and interfaces, and how this affects the phase transformation are essential for micromechanical modeling.

Thus, our computational model consists of two parts: the evolution of the phase microstructure is governed by the TDGL equation which minimizes the total energy in the system. The second part of the model considers discrete edge dislocations in a two-dimensional domain, for which an analytical solution of stress is available [7]. Such methods of coupling PFM and dislocations have been successfully applied for materials such as nickel-based superalloys [8, 9]. The modeling of the phase transformation will not consider any intermediate phases, and therefore only one order parameter, ϕ, is needed. It will also be assumed in the model that inside the martensitic phase, the dislocation mobility will approach zero, resulting in no movement of the dislocations inside the martensite phase. The TDGL requires the gradient energy at the phase boundary, the elastic strain energy, and a transformation potential. Here, contributions to the free energy arise from the elastic energy, W, the separation potential, f, and gradient energy. The time-dependent evolution of the order parameter is then given by

$$\frac{\partial \phi}{\partial t} = -M\left(\frac{\partial W}{\partial \phi} + G\left(\frac{\kappa_s}{L_{\mathrm{char}}}\frac{\partial f}{\partial \phi} + \kappa_g L_{\mathrm{char}} \Delta\phi\right)\right), \tag{23.1}$$

where ϕ is the order parameter describing the current phase at each point in space. The material specific parameters are mobility, M, interfacial energy density, G, characteristic length scale, L_{char}, and the calibration constants, κ_s and κ_g, which control the width of the interface between the two phases [10].

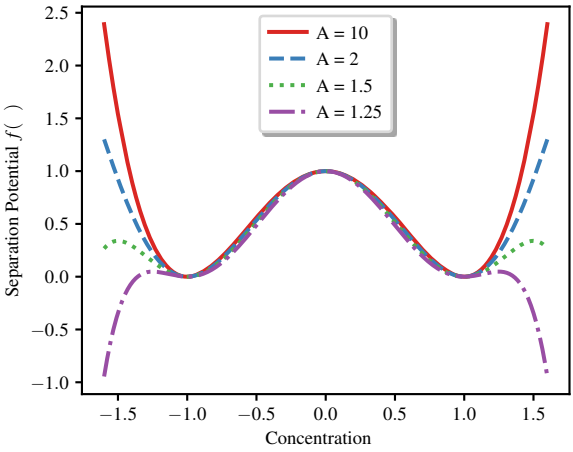

Fig. 23.1 Potential of phase transition. The two wells signify martensite variants 1 and 2. The local maximum signifies a metastable austenite phase

W is the elastic strain energy density which takes the form

$$W(\varepsilon, \phi) = \mathbf{E}_{\text{el}} : \mathbf{S} \tag{23.2}$$

where $\mathbf{E}_{\text{el}}$ is the elastic strain tensor and $\mathbf{S}$ is the stress tensor.

The second term describes the potential of phase transformation. In our model, we use a so-called "2-4-6 potential" (see Fig. 23.1), given as

$$f(\phi) = \frac{(3A^2 - 1 - 2\phi^2)(1 - \phi^2)^2}{(3A^2 - 1)}, \tag{23.3}$$

where A is a fit parameter which can be obtained from lower scale simulation methods. The final term accounts for the gradient of the interface between the two phases [11].

23.2.2 Dislocations and Mechanical Equilibrium Conditions

The stress field around a dislocation follows—outside the core region—linear elasticity. Any solid body in static equilibrium obeys the mechanical equilibrium equation, i.e., the divergence of the stress tensor, $\mathbf{S}$, must be zero,

$$\nabla \cdot \mathbf{S} = 0\,. \tag{23.4}$$

While this follows from the conservation of linear momentum, the conservation of angular momentum is responsible for the symmetry of the stress tensor, $\mathbf{S} = \mathbf{S}^{\mathrm{T}} \Leftrightarrow \mathrm{S}_{ij} = \mathrm{S}_{ji}$. Assuming linear elastic material, the stresses and strains are related by the

stiffness tensor, $\mathbb{C}$, as

$$\mathbf{S} = \mathbb{C} : \mathbf{E}_{\mathrm{e}}\left(\mathbf{E},\ \phi\right), \tag{23.5}$$

where, in a phase field ansatz, the elastic strain tensor, $\mathbf{E}_{\mathrm{e}}\left(\mathbf{E},\ \phi\right)$, is a function of the order parameter as well as of the total strain, $\mathbf{E}$. We assume a small strain context in our model, and therefore strains may be additively decomposed into their elastic and inelastic parts:

$$\mathbf{E}_{\mathrm{e}}\left(\mathbf{E},\ \phi\right) = \mathbf{E} - \mathbf{E}_{\mathrm{inel}}\,. \tag{23.6}$$

The tensor of inelastic strains, $\mathbf{E}_{\mathrm{inel}}$, consists of the transformation strain $\mathbf{E}_{\mathrm{tr}}$ and the dislocation eigenstrain $\mathbf{E}_{\mathrm{dis}}$. In the following we will only consider a horizontal slip system in a plane strain model. The plane components of the stress tensor for a single dislocation in an infinite, linear elastic medium then follow the following analytical solution [7]:

$$\mathrm{S}_{11} = \frac{-\mu\, b}{2\pi\,(1-\nu)}\,\frac{y\,(3x^2+y^2)}{(x^2+y^2)^2}, \tag{23.7}$$

$$\mathrm{S}_{22} = \frac{-\mu\, b}{2\pi\,(1-\nu)}\,\frac{y\,(x^2-y^2)}{(x^2+y^2)^2}, \tag{23.8}$$

$$\mathrm{S}_{12} = \frac{\mu\, b}{2\pi\,(1-\nu)}\,\frac{x\,(x^2-y^2)}{(x^2+y^2)^2}, \tag{23.9}$$

where b is the absolute value of the Burgers vector, μ is the shear modulus, and ν is Poisson's ratio. In order to avoid the unphysical diverging behavior close to the dislocation core, a numerical regularization approach as proposed in [12] is used; a physically more rigorous approach is presented in the subsequent section. The resulting stress components are shown in Fig. 23.2. The strain tensor, which governs the dislocation eigenstrain, can then be straightforwardly obtained from $\mathbf{E}_{\mathrm{dis}} = \mathbb{C}^{-1} : \mathbf{S}$. Equation (23.2) couples the phase field model and the dislocation model through the eigenstrain of dislocations and the eigenstrain contribution due to the phase transformation. While in this work we only consider stationary dislocation configurations, in general, the equation of motion for the dislocations would be a second equation where the two models are coupled.

23.2.3 Simulation Setup and Boundary Conditions

In order to observe the interaction between the dislocation and the phase field interface, a martensitic phase transformation needs to be triggered first. In our first simulation setup this is done via a martensitic "seed", which is an artificial inclusion of the martensite phase. The first simulation setup consists of a circular martensitic seed surrounded by an austenite matrix, as shown in Fig. 23.3a, with one dislocation placed inside the austenite phase. The entire domain measures 200 nm by 200 nm.

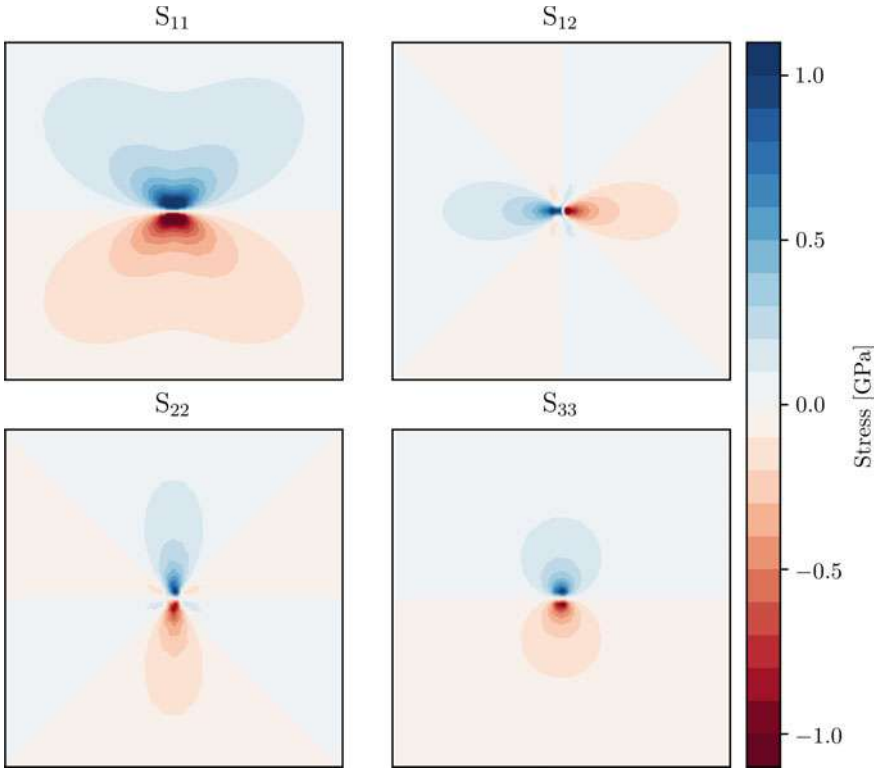

Fig. 23.2 Individual components to the stress tensor for a single dislocation, according to (23.7)–(23.9)

In our second simulation setup we use a penny-shaped crack, as shown in Fig. 23.3b, to initiate a phase transformation. The introduction of several stationary positive and negative dislocations on either ends of a crack mode II crack tip effectively mimics a small crack inside of a material. The equivalent dislocation distribution function of the crack is given by Weertman [13].

In both setups, free boundaries were considered. To avoid a rigid body motion, the domains were fixed in one corner, and in an adjacent corner, a zero displacement was prescribed in vertical direction only to avoid over-constraining the system. The two martensite variants are considered by one order parameter which is $\phi = 1$ for variant 1 and $\phi = -1$ for variant 2. The simulations progress by time integrating the TDGL, and we let them evolve until a quasi-static configuration is reached. The numerical implementation was done using the finite element method. We used quadratic shape functions and a rectangular mesh with 100 elements into each direction.

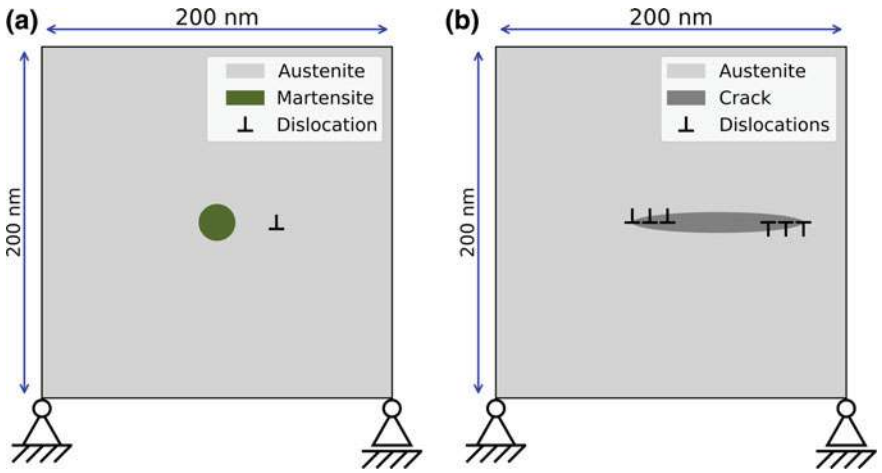

Fig. 23.3 Schematic of initial setups of the simulations showing **a** a martensitic seed surrounded by an austenite matrix, and **b** a penny-shaped crack in an austenite matrix

23.2.4 Simulation Results

23.2.4.1 Martensitic Seed and Edge Dislocation

Our first simulation set up considers the geometry and initial values shown in Fig. 23.3a. Figure 23.4 shows the order parameter, the S_{12} component of the stress tensor, and the elastic energy density at three distinct points in time. The initial configuration with the circular seed is an artificial and energetically highly unfavorable microstructural state. This is why immediately at the beginning of the simulation the horizontal and vertical martensitic bands originating from the location of the seed were created, as shown in the first snapshot. However, due to the spatially heterogeneous structure with changing transformation strains across the interfaces stresses and elastic strain energy are still high (Fig. 23.4 bottom and middle row) which show that equilibrium has not yet reached.

The TDGL minimizes total energy in the system, so as time progresses, the system will attempt to transform into a state where energy decreases. If there was no dislocation present, the system would be perfectly symmetric in the vertical and horizontal direction, and there would be no physical reason for one band to be preferred. The preferred band direction would only be decided based on numerical errors or other artifacts. However, the introduction of the dislocation breaks the symmetry (compare the right red region of the stress in Fig. 23.4 at $t = t_s$) and thereby determines the growth direction of the band. At the intermediate time step t_m, the horizontal band has already shrinked to nearly 50% of its original thickness, and the energy as well as the stress level have strongly decreased.

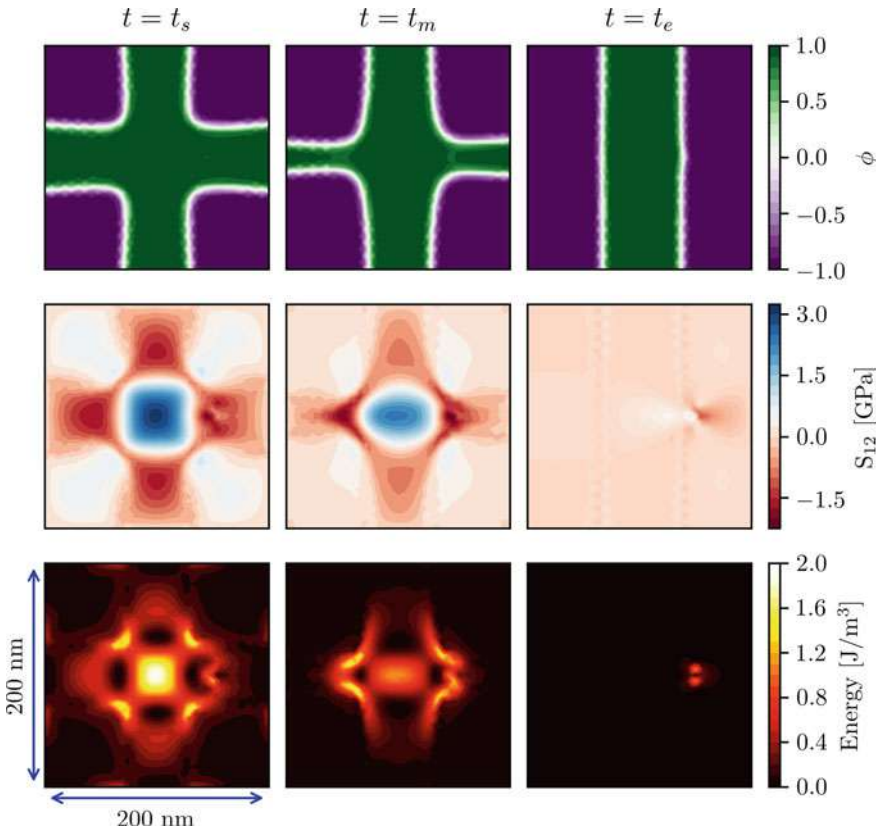

Fig. 23.4 Temporal evolution of order parameter, elastic energy density, and S_{12} with one dislocation. t_s is an early point in time, t_m is an intermediate time, and at t_e the quasi-static state is reached

At the quasi-stationary time, a fully formed, vertical martensitic band structure is observed, and a minimized energy and stress is reached. The band structure is at equilibrium because of the total strain is exactly the eigenstrain (except for the dislocation contribution), resulting in a deformed but stress-free state. However, the stress around the dislocation will not change because the dislocation is fixed in place. The "try" to relax this further causes a slight distortion from the original straight interface, as seen in Fig. 23.4. The shear stress at t_e still shows very slight remnants of the vertical phase microstructure; the reason is that the interface of the martensite band is not perfectly straight but has small fluctuations due to the used finite element approximation. Reducing the element size would remedy this effect.

23.2.4.2 Penny Shaped Crack in Austenitic Matrix

The introduction of a penny shaped crack induces enough eigenstrain in the system to trigger a phase transformation and is therefore an interesting way to get rid of the artificial initial seed. Similar as in the previous example, at the first snapshot in time, two perpendicular martensite bands can be observed (Fig. 23.5, left). Here, the stress field of the crack is responsible for the symmetry breaking. Again, the heterogenous microstructure causes a high stress and high strain energy density, which also decreases during the time integration of the TDGL equation. At the intermediate time step, one can additionally observe that the interfaces of the vertical band are pinned into place by the stress field of the crack, compare the slightly wavy structure of the band in Fig. 23.5. This "bump" is then progressing towards the top and the bottom such that at the stationary state the band stretches into vertical direction and has a thickness that is dictated by the crack length as shown in the right column in Fig. 23.5. At this point on time, a relaxed state with a minimum energy and a minimized stress is reached.

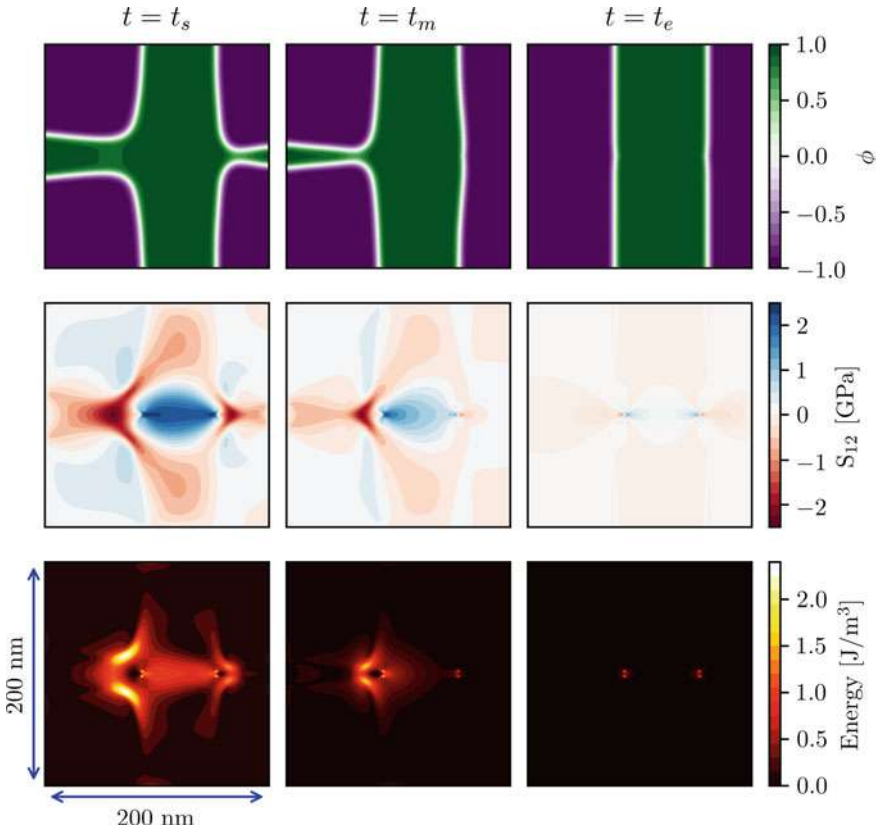

Fig. 23.5 Evolution in time of order parameter, elastic energy density, and S_{12} with a penny-shaped crack

23.3 On the Interaction of Planar Defects with Dislocations Within the Phase-Field Approach

23.3.1 Introduction

Phase field approaches have proven to be a very powerful tool for the investigation of the formation and evolution of microstructures due to solid-solid phase transformations and twinning. This appears to be the natural framework for the investigation of the interaction of planar crystal defects such as phase- or twin-boundaries with line defects (dislocations, disclinations). A typical phase field model for diffusionless (martensitic) transformations comprises of an evolution equations of ALLEN-CAHN-type for the order parameters ϕ_β

$$M_\beta \dot{\phi}_\beta = \alpha \Delta \phi_\beta - \rho \partial_{\phi_\beta} \psi, \tag{23.10}$$

where M_β and α are constants, ρ denotes the mass density, and ψ is a bulk free energy density. Assuming a small perturbation setting, the linear strain tensor $\mathbf{E}$ can be additively decomposed into elastic $\mathbf{E}_\mathrm{e}$ and inelastic (i.e., eigenstrain) $\mathbf{E}_\mathrm{tr}$ contributions, such that $\mathbf{E}_\mathrm{e}\big(\mathbf{E},\ \phi_\beta\big) = \mathbf{E} - \mathbf{E}_\mathrm{tr}\big(\phi_\beta\big)$. Assuming linear elasticity, the stress $\mathbf{S}$ is given by $\mathbf{S} = \mathbb{C} : \mathbf{E}_\mathrm{e}\big(\mathbf{E},\ \phi_\beta\big)$, and the free energy density takes the form

$$\psi\big(\mathbf{E},\ \phi_\beta,\ \theta\big) = \frac{1}{2}\mathbf{E}_\mathrm{e}\left(\mathbf{E},\ \phi\right) : \mathbb{C} : \mathbf{E}_\mathrm{e}\left(\mathbf{E},\ \phi\right) + \psi_\mathrm{b}\big(\phi_\beta,\ \theta\big)\,. \tag{23.11}$$

As a consequence, the evolution equation (23.10) can be rewritten as

$$M_\beta \dot{\phi}_\beta = \alpha \Delta \phi_\beta + \mathbf{S} : \partial_{\phi_\beta} \mathbf{E}_\mathrm{tr} - \rho \partial_{\phi_\beta} \psi_\mathrm{b}\,. \tag{23.12}$$

In classical elasticity theory the stresses diverge as the defect line is approached. In particular for dislocations the singularity is of $1/r$-type. As per (23.12), this results in singular driving forces for the evolution of the order parameters, effectively negating the concepts such as a nucleation barrier or a pile-up stress. Different approaches to regularize the stress in the core region exist in literature based either on the concept of a distributed BURGER's vector [12, 14–16] or generalized continuum theories [17–20]. However, the first strain gradient approach advocated by Po et al. [20] has the advantage that the obtained regularization is independent of the type of defect in question and therefore does not require any defect-specific information for the determination of model parameters. In principle, these parameters can directly be obtained from atomistic interaction potentials [21].

The purpose of this work is to follow a micromorphic approach and to derive a framework which consistently couples first strain gradient elasticity to ALLEN-CAHN-type microstructure evolution ensuring non-singular driving forces on the order parameters in the presence of line defects.

23.3.2 Balance Equations and Boundary Conditions

The principle of virtual power (PVP) provides a systematic way of deriving field equations and boundary conditions for arbitrary mechanical and coupled problems (cf. [22–24]). In the present work it is used in the following form: The virtual power of the inertia forces $\mathscr{P}^*_{\mathrm{a}}$ balances the virtual power $\mathscr{P}^*_{\mathrm{int}}$ of the internal and $\mathscr{P}^*_{\mathrm{ext}}$ of the external forces acting on any sub-domain $\mathscr{S}$ of the material body $\mathscr{B}$ for any admissible virtual velocity field $\mathbf{v}^*$ and virtual rate of order parameter field $\dot{\phi}^*$, i.e.,

$$\mathscr{P}^*_{\mathrm{a}} = \mathscr{P}^*_{\mathrm{int}} + \mathscr{P}^*_{\mathrm{ext}} \,. \tag{23.13}$$

For the sake of simplicity we disregard any higher order inertia terms [25] as well as inertial forces acting on the order parameter, resulting in

$$\mathscr{P}^*_{\mathrm{a}} = \int_{\mathscr{S}} \rho \dot{\mathbf{v}} \cdot \mathbf{v}^* \, \mathrm{d}V \,. \tag{23.14}$$

The power of internal forces is given by

$$\mathscr{P}^*_{\mathrm{int}} = -\int_{\mathscr{S}} \left(\mathbf{S}^\top : \mathbf{L}^* + \mathcal{T} \vdots \operatorname{grad} \mathbf{L}^* - \pi \, \dot{\phi}^* + \boldsymbol{\xi} \cdot \operatorname{grad} \dot{\phi}^* \right) \mathrm{d}V, \tag{23.15}$$

with $\mathbf{L}^* := \operatorname{grad} \mathbf{v}^*$. Here $\mathbf{S}$ and $\mathcal{T}$ are the CAUCHY and higher order stresses, respectively, while π and $\boldsymbol{\xi}$ are thermodynamic forces that directly correspond to the internal microforce and microstress introduced by Gurtin [26]. We note that the invariance requirement of $\mathscr{P}^*_{\mathrm{int}}$ with respect to superimposed rigid body motions results in $\mathbf{S} = \mathbf{S}^\top$. For the power of external forces we consider the very simple case of no body or contact forces acting on $\mathbf{L}^*$ and $\operatorname{grad} \dot{\phi}^*$, and only a contact (micro)force ζ acting $\dot{\phi}^*$

$$\mathscr{P}^*_{\mathrm{ext}} = \int_{\mathscr{S}} \mathbf{f} \cdot \mathbf{v}^* \rho \, \mathrm{d}V + \int_{\partial \mathscr{S}} \left(\mathbf{t} \cdot \mathbf{v}^* + \zeta \, \dot{\phi}^* \right) \mathrm{d}a \,. \tag{23.16}$$

In order to obtain the consequences of the PVP, the integrals in (23.15) are transformed using the following identities

$$\operatorname{div}(\mathbf{S} \cdot \mathbf{v}^*) = (\operatorname{div} \mathbf{S}) \cdot \mathbf{v}^* + \mathbf{S} : \mathbf{L}^*, \tag{23.17}$$

$$\operatorname{div}(\mathcal{T} : \mathbf{L}^*) = (\operatorname{div} \mathcal{T}) : \mathbf{L}^* + \mathcal{T} \vdots \operatorname{grad} \mathbf{L}^*, \tag{23.18}$$

$$\operatorname{div}\big((\operatorname{div} \mathcal{T}) \cdot \mathbf{v}^*\big) = (\operatorname{div} \operatorname{div} \mathcal{T}) \cdot \mathbf{v}^* + (\operatorname{div} \mathcal{T}) : \mathbf{L}^*, \tag{23.19}$$

$$\operatorname{div}(\boldsymbol{\xi} \, \dot{\phi}^*) = (\operatorname{div} \boldsymbol{\xi}) \, \dot{\phi}^* + \boldsymbol{\xi} \cdot \operatorname{grad} \dot{\phi}^*, \tag{23.20}$$

and the divergence theorem, resulting in

$$\mathscr{P}^*_{\text{int}} = \int_{\mathscr{S}} \big(\operatorname{div}\mathbf{S} - \operatorname{div}\operatorname{div}\mathcal{T}\big)\cdot\mathbf{v}^*\,\mathrm{d}V - \int_{\partial\mathscr{S}} \mathbf{n}\cdot\big(\mathbf{S}^\top - \operatorname{div}\mathcal{T}\big)\cdot\mathbf{v}^*\,\mathrm{d}a$$
$$- \int_{\partial\mathscr{S}} \mathbf{n}\cdot\mathcal{T} : \mathbf{L}^*\,\mathrm{d}a + \int_{\mathscr{S}} \big(\pi + \operatorname{div}\boldsymbol{\xi}\big)\,\dot{\phi}^*\,\mathrm{d}V - \int_{\partial\mathscr{S}} \mathbf{n}\cdot\boldsymbol{\xi}\,\dot{\phi}^*\,\mathrm{d}a\,. \tag{23.21}$$

Introducing the surface gradient operator

$$\operatorname{grad}_S(\cdot) = \operatorname{grad}(\cdot) - \partial_{\mathbf{n}}(\cdot)\otimes\mathbf{n}, \tag{23.22}$$

where $\partial_{\mathbf{n}}$ is the directional derivative in the direction of the outward normal $\mathbf{n}$, the third integral in expression (23.21) can be rewritten as

$$\int_{\partial\mathscr{S}} \mathbf{n}\cdot\mathcal{T} : \mathbf{L}^*\,\mathrm{d}a = \int_{\partial\mathscr{S}} \mathbf{n}\cdot\mathcal{T} : \operatorname{grad}_S\mathbf{v}^*\,\mathrm{d}a + \int_{\partial\mathscr{S}} \mathbf{n}\cdot\mathcal{T} : \partial_{\mathbf{n}}\mathbf{v}^*\otimes\mathbf{n}\,\mathrm{d}a \tag{23.23}$$
$$= \int_{\partial\mathscr{S}} \operatorname{div}_S\big(\mathbf{n}\cdot\mathcal{T}\cdot\mathbf{v}^*\big)\,\mathrm{d}a - \int_{\partial\mathscr{S}} \operatorname{div}_S\big(\mathbf{n}\cdot\mathcal{T}\big)\cdot\mathbf{v}\,\mathrm{d}a +$$
$$+ \int_{\partial\mathscr{S}} \mathbf{n}\cdot\mathcal{T} : \partial_{\mathbf{n}}\mathbf{v}^*\otimes\mathbf{n}\,\mathrm{d}a. \tag{23.24}$$

Finally, applying the surface divergence theorem and, for the sake of simplicity, neglecting any wedge line and corner contributions, we find

$$\int_{\partial\mathscr{S}} \operatorname{div}_S\big(\mathbf{n}\cdot\mathcal{T}\cdot\mathbf{v}^*\big)\,\mathrm{d}a = \int_{\partial\mathscr{S}} \big(\operatorname{div}_S\mathbf{n}\big)\mathbf{n}\otimes\mathbf{n} : \mathcal{T}\cdot\mathbf{v}^*\,\mathrm{d}a. \tag{23.25}$$

Enforcing (23.13) we arrive after a number of straightforward algebraic manipulations at the following field equations on $\mathscr{B}$

$$\rho\dot{\mathbf{v}} = \operatorname{div}(\mathbf{S} - \operatorname{div}\mathcal{T}) + \rho\mathbf{f}, \tag{23.26a}$$
$$0 = \operatorname{div}\boldsymbol{\xi} + \pi, \tag{23.26b}$$

and boundary conditions on $\partial\mathscr{B}$

$$\mathbf{t} = (\mathbf{S} - \operatorname{div}\mathcal{T})\cdot\mathbf{n} - \operatorname{div}_S(\mathbf{n}\cdot\mathcal{T}), \tag{23.26c}$$
$$\zeta = \boldsymbol{\xi}\cdot\mathbf{n}\,. \tag{23.26d}$$

We note that, introducing the total stress

$$\mathbf{S}_{\text{t}} := \mathbf{S} - \operatorname{div}\mathcal{T}, \tag{23.27}$$

the balance of linear momentum (23.26a) regains its standard form for simple materials

$$\rho\dot{\mathbf{v}} = \operatorname{div}\mathbf{S}_{\mathrm{t}} + \rho\mathbf{f}, \tag{23.28}$$

which is convenient for the numerical implementation.

23.3.3 Constitutive Equations

The following equations are formulated assuming the small perturbation hypothesis, i.e., both the displacement $\mathbf{u}$ as well as the displacement gradient can be considered small, $\mathbf{u} \ll L$ and $||\operatorname{grad}\mathbf{u}|| \ll 1$. In this case the deformation is characterized by the linear strain tensor $\mathbf{E} = \frac{1}{2}\left(\operatorname{grad}\mathbf{u} + (\operatorname{grad}\mathbf{u})^{\top}\right)$. Its gradient will be denoted $\mathcal{Y} := \operatorname{grad}\mathbf{E}$.

23.3.3.1 Laws of State

We choose the following ansatz for the free energy density and thermodynamic forces

$$\begin{aligned}
&\psi = \psi\left(\mathbf{E},\, \mathcal{Y},\, \phi,\, \operatorname{grad}\phi,\, \theta\right), && \boldsymbol{\xi} = \boldsymbol{\xi}\left(\mathbf{E},\, \mathcal{Y},\, \phi,\, \operatorname{grad}\phi,\, \theta\right),\\
&\mathbf{S} = \mathbf{S}\left(\mathbf{E},\, \mathcal{Y},\, \phi,\, \operatorname{grad}\phi,\, \theta\right), && \pi = \pi\left(\mathbf{E},\, \mathcal{Y},\, \phi,\, \operatorname{grad}\phi,\, \theta,\, \dot{\phi}\right).\\
&\mathcal{T} = \mathcal{T}\left(\mathbf{E},\, \mathcal{Y},\, \phi,\, \operatorname{grad}\phi,\, \theta\right),
\end{aligned}$$

The second law of thermodynamics in the form of the CLAUSIUS-DUHEM inequality is given for the isothermal case by

$$\begin{aligned}
\left(\mathbf{S} - \rho\partial_{\mathbf{E}}\psi\right) : \dot{\mathbf{E}} + \left(\mathcal{T} - \rho\partial_{\mathcal{Y}}\psi\right) \vdots \dot{\mathcal{Y}} - \left(\pi\ + \rho\partial_{\phi}\psi\right)\dot{\phi} +\\
+ \left(\boldsymbol{\xi} - \rho\partial_{\operatorname{grad}\phi}\psi\right)\cdot\operatorname{grad}\dot{\phi} \geqslant 0
\end{aligned} \tag{23.29}$$

an can be exploited using the classical COLEMAN-NOLL procedure to arrive at the laws of state

$$\mathbf{S} = \rho\partial_{\mathbf{E}}\psi, \qquad \mathcal{T} = \rho\partial_{\mathcal{Y}}\psi, \qquad \boldsymbol{\xi} = \rho\partial_{\operatorname{grad}\phi}\psi \tag{23.30}$$

and the residual dissipation inequality

$$-\pi_{\mathrm{d}}\,\dot{\phi} \geqslant 0, \quad \text{with} \quad \pi_{\mathrm{d}} := \pi + \rho\partial_{\phi}\psi\,. \tag{23.31}$$

23.3.3.2 Free Energy and Dissipation Potential

As customary in phase field models for solid-solid transformations, the free energy density can be split into an elastic-, a bulk chemical- and an interface-contribution

$$\psi = \psi_{\mathrm{e}}\left(\mathbf{E},\, \mathcal{Y},\, \phi,\, \theta\right) + \psi_{\mathrm{b}}\left(\phi,\, \theta\right) + \psi_{\mathrm{i}}\left(\phi,\, \operatorname{grad}\phi,\, \theta\right)\,. \tag{23.32}$$

In our formulation, the elastic free energy is of HELMHOLTZ-type, i.e.,

$$\begin{aligned}\rho\psi_{\mathrm{e}}\left(\mathbf{E},\, \mathcal{Y},\, \phi,\, \theta\right) = \frac{1}{2}\mathbf{E}_{\mathrm{e}}\left(\mathbf{E},\, \phi\right) : \mathbb{C}(\phi) : \mathbf{E}_{\mathrm{e}}\left(\mathbf{E},\, \phi\right) \\ + \frac{1}{2}\big(\mathbb{C}(\phi) : \mathcal{Y}\cdot\boldsymbol{\Lambda}(\phi)\big)\vdots\mathcal{Y},\end{aligned} \tag{23.33}$$

where $\mathbf{E}_{\mathrm{tr}}(\phi)$ is the inelastic strain, $\mathbf{E}_{\mathrm{e}}\left(\mathbf{E},\, \phi\right) := \mathbf{E} - \mathbf{E}_{\mathrm{tr}}(\phi)$ is the elastic strain, $\mathbb{C}$ the stiffness tensor and $\boldsymbol{\Lambda}(\phi)$ a gradient length scale tensor (cf. [20]). The specific choice of functional dependence of $\mathbf{E}_{\mathrm{tr}}(\phi)$, $\psi_{\mathrm{b}}\left(\phi,\, \theta\right)$ and $\psi_{\mathrm{i}}\left(\phi,\, \operatorname{grad}\phi,\, \theta\right)$ on the order parameter ϕ is of no relevance at this point, we will assume that the interface energy is of the form

$$\rho\psi_{\mathrm{i}}\left(\phi,\, \operatorname{grad}\phi,\, \theta\right) := \frac{\alpha}{2}\,||\operatorname{grad}\phi||^2 + g(\phi,\, \theta)\,. \tag{23.34}$$

Using the laws of state (23.30) we immediately find

$$\mathbf{S} = \mathbb{C}(\phi) : \mathbf{E}_{\mathrm{e}}\left(\mathbf{E},\, \phi\right) = \mathbb{C}(\phi) : \big(\mathbf{E} - \mathbf{E}_{\mathrm{tr}}(\phi)\big), \tag{23.35a}$$

$$\mathcal{T} = \mathbb{C}(\phi) : \mathcal{Y}\cdot\boldsymbol{\Lambda}(\phi), \tag{23.35b}$$

$$\boldsymbol{\xi} = \alpha\,\operatorname{grad}\phi, \tag{23.35c}$$

and combining the first two equations

$$\mathcal{T} = \mathbb{C}(\phi) : \operatorname{grad}\left(\mathbb{C}^{-1}(\phi) : \mathbf{S}\right)\cdot\boldsymbol{\Lambda}(\phi) + \mathbb{C}(\phi) : \operatorname{grad}\mathbf{E}_{\mathrm{tr}}(\phi)\cdot\boldsymbol{\Lambda}(\phi)\,. \tag{23.36}$$

Equation (23.27) can now be used in two ways: In conjunction with the laws of state (23.35a) and (23.35b) it is a constitutive equation for the total stress $\mathbf{S}_{\mathrm{t}}$, which enters the balance of linear momentum (23.28)

$$\mathbf{S}_{\mathrm{t}}\big(\mathbf{E},\, \mathcal{Y},\, \phi\big) = \mathbb{C}(\phi) : \mathbf{E}_{\mathrm{e}}\left(\mathbf{E},\, \phi\right) - \operatorname{div}\big[\mathbb{C}(\phi) : \mathcal{Y}\cdot\boldsymbol{\Lambda}(\phi)\big]\,. \tag{23.37}$$

When combined with (23.36), (23.27) can be used to determine the true stress $\mathbf{S}$ from the total stress $\mathbf{S}_{\mathrm{t}}$

$$\begin{aligned}\mathbf{S} - \operatorname{div}\big[\mathbb{C}(\phi) : \operatorname{grad}\big(\mathbb{C}^{-1}(\phi) : \mathbf{S}\big) \cdot \boldsymbol{\Lambda}(\phi)\big] \\ = \mathbf{S}_{\mathrm{t}} + \operatorname{div}\big(\mathbb{C}(\phi) : \operatorname{grad}\mathbf{E}_{\mathrm{tr}}(\phi) \cdot \boldsymbol{\Lambda}(\phi)\big)\,.\end{aligned} \tag{23.38}$$

In order to complete the phase field formulation we require a constitutive equation for π_{d}, which is obtained in the spirit of classical irreversible thermodynamics as

$$\dot{\phi} = -\partial_{\pi_{\mathrm{d}}}\Omega\,(\pi_{\mathrm{d}}) \tag{23.39}$$

from a dissipation potential $\Omega\,(\pi_{\mathrm{d}})$ that is homogeneous of degree two

$$\Omega\,(\pi_{\mathrm{d}}) := \frac{1}{2}M^{-1}\pi_{\mathrm{d}}^2, \tag{23.40}$$

where M is the so called mobility constant. Combining (23.26b), (23.31), (23.35c), (23.39) and (23.40) we find the classical ALLEN-CAHN equation

$$M\dot{\phi} = \alpha\,\Delta\phi - \rho\,\partial_{\phi}\psi, \tag{23.41}$$

or, specifically,

$$\begin{aligned}M\dot{\phi} = \alpha\,\Delta\phi + \mathbf{S} : \partial_{\phi}\mathbf{E}_{\mathrm{tr}} - \frac{1}{2}\mathbf{E}_{\mathrm{e}}\,(\mathbf{E},\,\phi) : \partial_{\phi}\mathbb{C}(\phi) : \mathbf{E}_{\mathrm{e}}\,(\mathbf{E},\,\phi) \\ - \frac{1}{2}\big(\mathbb{C}(\phi) : \mathcal{Y} \cdot \partial_{\phi}\boldsymbol{\Lambda}(\phi)\big) - \frac{1}{2}\big(\partial_{\phi}\mathbb{C}(\phi) : \mathcal{Y} \cdot \boldsymbol{\Lambda}(\phi)\big) \vdots \mathcal{Y} \\ - \rho\,\partial_{\phi}\psi_{\mathrm{b}}(\phi,\,\theta) - \partial_{\phi}g(\phi,\,\theta)\,.\end{aligned} \tag{23.42}$$

Note that all terms that appear in the driving force, and as per [17] the CAUCHY stress $\mathbf{S}$ in particular, are non-singular even in the presence of dislocations.

23.3.4 Special Cases

For phase transformations the crystal lattice on both sides of the interface will, in general, be different leading to different elastic properties and a different dislocation core structure. In this case the (23.28), (23.37), (23.38) and (23.42) retain their full complexity. In the following, we consider a number of scenarios for which this is not the case.

23.3.4.1 Homogeneous Bulk Material

In the bulk phase the order parameter does not vary in space, i.e., $\operatorname{grad}\phi = \mathbf{0}$, $\mathbb{C}(\phi) = \mathbb{C}$, $\boldsymbol{\Lambda}(\phi) = \boldsymbol{\Lambda}$, $\mathbf{E}_{\mathrm{tr}}(\phi) = \mathbf{0}$. The ALLEN-CAHN equation is fulfilled automatically and

(23.38), (23.37) recover the form derived by Po et al. [20]

$$\begin{aligned}&\mathbf{S} - \operatorname{div}\big((\operatorname{grad}\mathbf{S})\cdot\boldsymbol{\Lambda}\big) = \mathbf{S}_\mathrm{t}, \text{ with}\\ &\mathbf{S}_\mathrm{t}\big(\mathbf{E},\,\mathcal{Y}\big) = \mathbb{C} : \big[\mathbf{E} - \operatorname{div}\big(\mathcal{Y}\cdot\boldsymbol{\Lambda}\big)\big]\,.\end{aligned} \tag{23.43a}$$

For materials with cubic symmetry the gradient length scale tensor $\boldsymbol{\Lambda}$ is isotropic, i.e., $\boldsymbol{\Lambda} = \ell^2\mathbf{I}$, and the above expressions can be further simplified to the form derived by Lazar et al. [17]

$$\begin{aligned}&\mathbf{S} - \ell^2\Delta\mathbf{S} = \mathbf{S}_\mathrm{t}, \text{ with}\\ &\mathbf{S}_\mathrm{t}\big(\mathbf{E},\,\mathcal{Y}\big) = \mathbb{C} : \big(\mathbf{E} - \ell^2\operatorname{div}\mathcal{Y}\big) = \mathbb{C} : \big(\mathbf{E} - \ell^2\Delta\mathbf{E}\big)\,.\end{aligned} \tag{23.43b}$$

23.3.4.2 Grain Boundaries as Planar Defects

The crystal lattices on both sides of a grain boundary differ only by a rotation $\mathbf{Q}(\phi)$. Hence, we assume that the chemical bulk energy is independent of the order parameter, i.e., $\psi_\mathrm{b}(\phi,\,\theta) = \psi_\mathrm{b}(\theta)$. Then the elastic stiffness $\mathbb{C}(\phi)$ and the gradient length scale tensor $\boldsymbol{\Lambda}(\phi)$ can be expressed as $\mathbb{C}(\phi) = \mathbf{Q}(\phi) * \mathbb{C}$ and $\boldsymbol{\Lambda}(\phi) = \mathbf{Q}(\phi) * \boldsymbol{\Lambda}$, respectively. Furthermore, without loss of generality, $\mathbf{E}_\mathrm{tr}(\phi) = \mathbf{0}$. For this case (23.38), (23.37) and (23.42) take the form

$$\mathbf{S} - \operatorname{div}\Big[\big(\mathbf{Q}(\phi) * \mathbb{C}\big) : \operatorname{grad}\Big(\big(\mathbf{Q}(\phi) * \mathbb{C}^{-1}\big) : \mathbf{S}\Big)\cdot\big(\mathbf{Q}(\phi) * \boldsymbol{\Lambda}\big)\Big] = \mathbf{S}_\mathrm{t}, \tag{23.44a}$$

with

$$\mathbf{S}_\mathrm{t}\big(\mathbf{E},\,\mathcal{Y},\,\phi\big) = \mathbb{C}(\phi) : \mathbf{E} - \operatorname{div}\big[\big(\mathbf{Q}(\phi) * \mathbb{C}\big) : \mathcal{Y}\cdot\big(\mathbf{Q}(\phi) * \boldsymbol{\Lambda}\big)\big], \tag{23.44b}$$

and

$$\begin{aligned}M\dot{\phi} = \alpha\Delta\phi - \frac{1}{2}\mathbf{E} : \big(\partial_\phi\mathbf{Q}(\phi) * \mathbb{C}\big) : \mathbf{E} - \frac{1}{2}\big(\big(\mathbf{Q}(\phi) * \mathbb{C}\big) : \mathcal{Y}\cdot\big(\partial_\phi\mathbf{Q} * \boldsymbol{\Lambda}\big)\big) -\\ - \frac{1}{2}\big(\big(\partial_\phi\mathbf{Q}(\phi) * \mathbb{C}\big) : \mathcal{Y}\cdot\big(\mathbf{Q}(\phi) * \boldsymbol{\Lambda}\big)\big) \vdots \mathcal{Y} - \partial_\phi g(\phi,\,\theta)\,.\end{aligned} \tag{23.44c}$$

The isotropy of the gradient length scale tensor $\boldsymbol{\Lambda}$ for cubic crystals implies that $\mathbf{Q}(\phi) * \boldsymbol{\Lambda} = \boldsymbol{\Lambda} = \ell^2\mathbf{I}$, which simplifies (23.44) to the following form

$$\mathbf{S} - \ell^2\operatorname{div}\Big[\big(\mathbf{Q}(\phi) * \mathbb{C}\big) : \operatorname{grad}\Big(\big(\mathbf{Q}(\phi) * \mathbb{C}^{-1}\big) : \mathbf{S}\Big)\Big] = \mathbf{S}_\mathrm{t}, \tag{23.45a}$$

with

$$\mathbf{S}_\mathrm{t}\big(\mathbf{E},\,\mathcal{Y},\,\phi\big) = \mathbb{C}(\phi) : \mathbf{E} - \ell^2\operatorname{div}\big[\big(\mathbf{Q}(\phi) * \mathbb{C}\big) : \mathcal{Y}\big], \tag{23.45b}$$

and

$$M\dot{\phi} = \alpha\Delta\phi - \frac{1}{2}\mathbf{E} : \big(\partial_\phi \mathbf{Q}(\phi) * \mathbb{C}\big) : \mathbf{E} - \frac{1}{2}\ell^2 \big(\big(\partial_\phi \mathbf{Q}(\phi) * \mathbb{C}\big) : \mathcal{Y}\big) \vdots \mathcal{Y} - \partial_\phi g(\phi,\, \theta)\,. \tag{23.45c}$$

23.3.4.3 Twin Boundaries as Planar Defects

Since the twin variants on both sides of the boundary are related by mirror and/or rotational symmetry transformations between the unit cells, we can—as in the case of grain boundaries—assume that the bulk chemical energy remains unchanged, i.e., $\psi_\mathrm{b}(\phi,\, \theta) = \psi_\mathrm{b}(\theta)$, and the elastic stiffness $\mathbb{C}(\phi)$ and the gradient length scale tensor $\mathbf{\Lambda}(\phi)$ can be expressed using an orthogonal tensor $\mathbf{Q}(\phi)$ as $\mathbb{C}(\phi) = \mathbf{Q}(\phi) * \mathbb{C}$ and $\mathbf{\Lambda}(\phi) = \mathbf{Q}(\phi) * \mathbf{\Lambda}$, respectively. Under these assumptions we find

$$\begin{aligned}\mathbf{S} - \mathrm{div}\Big[\big(\mathbf{Q}(\phi) * \mathbb{C}\big) : \mathrm{grad}\,\Big(\big(\mathbf{Q}(\phi) * \mathbb{C}^{-1}\big) : \mathbf{S}\Big) \cdot \big(\mathbf{Q}(\phi) * \mathbf{\Lambda}\big)\Big] \\ = \mathbf{S}_\mathrm{t} + \mathrm{div}\big[\mathbb{C}(\phi) : \mathrm{grad}\,\big(\mathbf{E}_\mathrm{tr}(\phi)\big) \cdot \mathbf{\Lambda}(\phi)\big],\end{aligned} \tag{23.46a}$$

with

$$\mathbf{S}_\mathrm{t}\big(\mathbf{E},\, \mathcal{Y},\, \phi\big) = \mathbb{C}(\phi) : \mathbf{E}_\mathrm{e}(\mathbf{E}) - \mathrm{div}\big[\big(\mathbf{Q}(\phi) * \mathbb{C}\big) : \mathcal{Y} \cdot \big(\mathbf{Q}(\phi) * \mathbf{\Lambda}\big)\big], \tag{23.46b}$$

and

$$\begin{aligned}M\dot{\phi} = \alpha\Delta\phi + \mathbf{S} : \partial_\phi \mathbf{E}_\mathrm{tr} - \frac{1}{2}\mathbf{E}_\mathrm{e}(\mathbf{E},\, \phi) : \big(\partial_\phi \mathbf{Q}(\phi) * \mathbb{C}\big) : \mathbf{E}_\mathrm{e}(\mathbf{E},\, \phi) \\ - \frac{1}{2}\big(\big(\mathbf{Q}(\phi) * \mathbb{C}\big) : \mathcal{Y} \cdot \big(\partial_\phi \mathbf{Q} * \mathbf{\Lambda}\big)\big) \\ - \frac{1}{2}\big(\big(\partial_\phi \mathbf{Q}(\phi) * \mathbb{C}\big) : \mathcal{Y} \cdot \big(\mathbf{Q}(\phi) * \mathbf{\Lambda}\big)\big) \vdots \mathcal{Y} - \partial_\phi g(\phi,\, \theta)\,.\end{aligned} \tag{23.46c}$$

For cubic lattices these expressions simplify to

$$\mathbf{S} - \ell^2 \mathrm{div}\Big[\big(\mathbf{Q}(\phi) * \mathbb{C}\big) : \mathrm{grad}\,\Big(\big(\mathbf{Q}(\phi) * \mathbb{C}^{-1}\big) : \mathbf{S}\Big)\Big] \tag{23.47a}$$

$$= \mathbf{S}_\mathrm{t} + \ell^2 \mathrm{div}\big[\mathbb{C}(\phi) : \mathrm{grad}\,\mathbf{E}_\mathrm{tr}(\phi)\big], \tag{23.47b}$$

with

$$\mathbf{S}_\mathrm{t}\big(\mathbf{E},\, \mathcal{Y},\, \phi\big) = \mathbb{C}(\phi) : \mathbf{E}_\mathrm{e}(\mathbf{E},\, \phi) - \ell^2 \mathrm{div}\big[\big(\mathbf{Q}(\phi) * \mathbb{C}\big) : \mathcal{Y}\big], \tag{23.47c}$$

and

$$\begin{aligned}M\dot{\phi} = \alpha\Delta\phi + \mathbf{S} : \partial_\phi \mathbf{E}_\mathrm{tr} - \frac{1}{2}\mathbf{E}_\mathrm{e}(\mathbf{E},\, \phi) : \big(\partial_\phi \mathbf{Q}(\phi) * \mathbb{C}\big) : \mathbf{E}_\mathrm{e}(\mathbf{E},\, \phi) - \\ - \frac{1}{2}\ell^2 \big(\big(\partial_\phi \mathbf{Q}(\phi) * \mathbb{C}\big) : \mathcal{Y}\big) \vdots \mathcal{Y} - \partial_\phi g(\phi,\, \theta)\,.\end{aligned} \tag{23.47d}$$

23.3.4.4 Phase Boundaries Between Cubic Phases

In the case of phase boundaries between different cubic phases the gradient length scale tensor $\mathbf{\Lambda}$ is isotropic on both sides of the interface, even though not necessarily constant across the interface, i.e., $\mathbf{\Lambda} = \ell(\phi)^2\mathbf{I}$. This allows us to reduce (23.38), (23.37) and (23.42) to the following form

$$\begin{aligned}\mathbf{S} - \operatorname{div}\left[\ell(\phi)^2\,\mathbb{C}(\phi) : \operatorname{grad}\left(\mathbb{C}^{-1}(\phi) : \mathbf{S}\right)\right] \\ = \mathbf{S}_{\mathrm{t}} + \operatorname{div}\left(\ell(\phi)^2\,\mathbb{C}(\phi) : \operatorname{grad}\mathbf{E}_{\mathrm{tr}}(\phi)\right),\end{aligned} \tag{23.48a}$$

with

$$\mathbf{S}_{\mathrm{t}}\left(\mathbf{E},\, \mathcal{Y},\, \phi\right) = \mathbb{C}(\phi) : \mathbf{E}_{\mathrm{e}}\left(\mathbf{E},\, \phi\right) - \operatorname{div}\left(\ell(\phi)^2\,\mathbb{C}(\phi) : \mathcal{Y}\right), \tag{23.48b}$$

and

$$\begin{aligned}M\dot{\phi} = \alpha\Delta\phi + \mathbf{S} : \partial_\phi\mathbf{E}_{\mathrm{tr}} + \frac{1}{2}\mathbf{E}_{\mathrm{e}}\left(\mathbf{E},\, \phi\right) : \partial_\phi\mathbb{C}(\phi) : \mathbf{E}_{\mathrm{e}}\left(\mathbf{E},\, \phi\right) \\ - \ell(\phi)\partial_\phi\ell(\phi)\left(\mathbb{C}(\phi) : \mathcal{Y}\right) \vdots \mathcal{Y} - \frac{\ell(\phi)^2}{2}\left(\partial_\phi\mathbb{C}(\phi) : \mathcal{Y}\right) \vdots \mathcal{Y} \\ - \rho\partial_\phi\psi_{\mathrm{b}}(\phi,\, \theta) - \partial_\phi g(\phi,\, \theta)\,.\end{aligned} \tag{23.48c}$$

23.3.5 Examples

This section contains a number of examples that demonstrate basic properties of the proposed model.

23.3.5.1 Regularization in the Dislocation Core

As shown in Sect. 23.3.4.1, the present model reduces to the set of equations proposed by Po et al. [20] in the homogeneous bulk phase. Figure 23.6 shows the shear stress component S_{12} in the glide plane of a single edge dislocation with and without regularization ($\ell = 2$ nm). In the classical case, the stress in the dislocation core is singular, whereas it is well defined for the regularized solution.

23.3.5.2 Effect of the Regularization on the Interaction of Dislocations with a Phase Boundary

The following scenario considers a two-phase material with an initially flat interface between the austenite (A) and martensite (M) phases (see Fig. 23.7, left figure) and an immobile dislocation structure within the austenite. The material is cooled below the martensite start temperature, i.e., the interface will move to the right, interacting with the dislocation structure. This interaction significantly varies depending on the

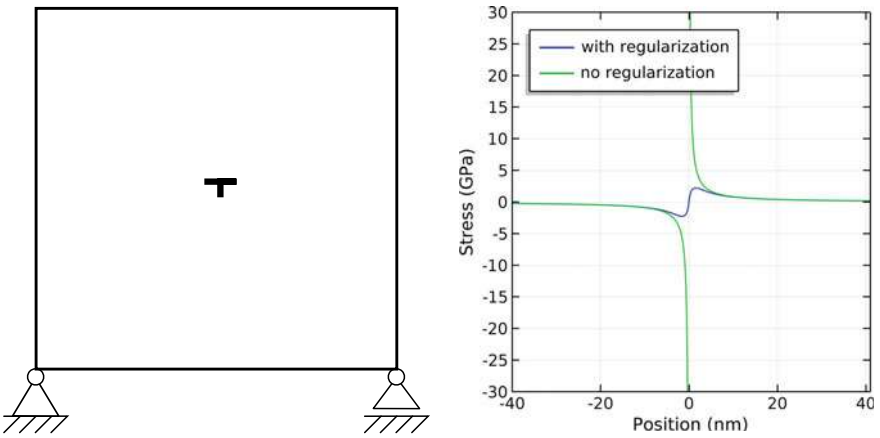

Fig. 23.6 Shear stress component S_{12} in the glide plane of a single edge dislocation

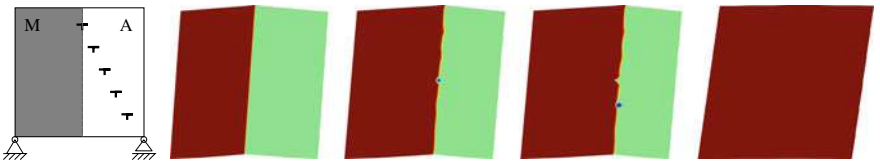

Fig. 23.7 Phase evolution for $\ell = 2$ nm

choice of the regularization. For a large regularization length ($\ell = 2$ nm) the stress in the dislocation core is relatively low, which enables the chemical driving force to pull the interface across the dislocation structure, resulting in a fully martensitic material (Fig. 23.7). With decreasing regularization length ($\ell = 1$ nm) the stress in the dislocation core increases, which leads to a stronger interaction with the interface, which, as a consequence, is arrested at the rightmost dislocation (Fig. 23.8). After the interface is immobile, the second martensitic variant is formed, which consumes the austenite. For an even smaller regularization length ($\ell = 0.5$ nm) the interface is arrested earlier in its progress (Fig. 23.9).

If, however, no regularization is present, this trend does not continue. The stress singularity in the dislocation core triggers the formation of martensite well ahead of the initial interface, enabling it to "overrun" the immobile dislocation structure

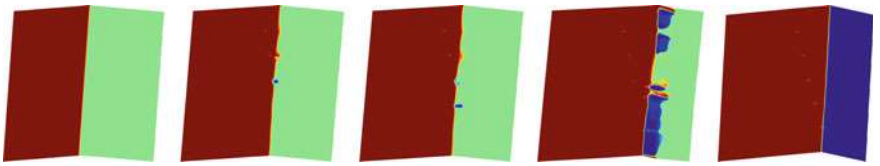

Fig. 23.8 Phase evolution for $\ell = 1$ nm

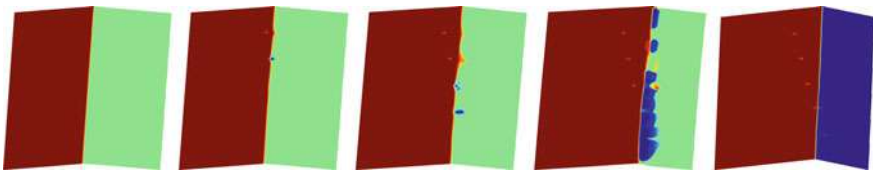

Fig. 23.9 Phase evolution for $\ell = 0.5$ nm

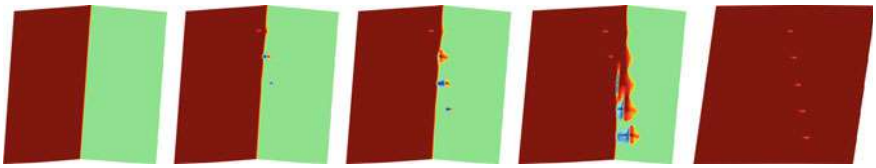

Fig. 23.10 Phase evolution without regularization

(Fig. 23.10). The result in this case is mesh sensitive, since the computed stress magnitude depends on the choice of discretization and therefore is unsuitable for quantitative investigations of the interaction of planar defects with dislocations.

23.4 Conclusions

In order to model the interaction of phase transformations and dislocations, we have coupled a time-dependent Ginzburg-Landau equation with the stress/strain fields of stationary configurations of discrete dislocations. This allowed us to study the effect that dislocations have on the resulting evolution of the microstructure. Coupling two simulation models for different deformation mechanisms is usually more involved than just the simulation of one phenomenon. However, the present work also showed that such a "multiphysical" approach might show a particular promise since, e.g., the artificial initial seed for the phase microstructure becomes superfluous, which makes our simulations more realistic.

However, only using stationary dislocation configurations is clearly not realistic: these dislocations would usually move and interact among themselves. Thus, future work will consider such behavior where the evolution of the phase microstructure is governed by the TDGL and the dislocation dynamics is governed by an equation of motion, both of which are coupled.

Acknowledgements The authors gratefully acknowledge the Deutsche Forschungsgemeinschaft (DFG) for supporting this work carried out within the framework of Collaborative Research Center SFB 799 (subproject C9).

References

1. A. Weidner, H. Biermann, J. Mech. **67**(8), 1729 (2015). https://doi.org/10.1007/s11837-015-1456-y
2. B. Li, X.M. Zhang, P.C. Clapp, J.A. Rifkin, J. Appl. Phys. **95**(4), 1698 (2004). https://doi.org/10.1063/1.1638609
3. J. Shim, Y. Cho, S. Kwon, W. Kim, B. Wirth, Appl. Phys. Lett. **90**(2), 021906 (2007). https://doi.org/10.1063/1.2429902
4. A. Ibarra, D. Caillard, J. San Juan, M.L. Nó, Appl. Phys. Lett. **90**(10), 101907 (2007). https://doi.org/10.1063/1.2710076
5. L.D. Landau, Zh. Eksp. Teor. Fiz. **7**, 19 (1937). [Ukr. J. Phys. 53, 25 (2008)]
6. A. Khachaturyan, *Theory of Structural Transformations in Solids* (Wiley, New York, 1983)
7. J.P. Hirth, J. Lothe, *Theory of Dislocations* (McGraw-Hill, New York, 1967)
8. R. Wu, S. Sandfeld, Scripta Mater. **123**, 42 (2016). https://doi.org/10.1016/j.scriptamat.2016.05.032
9. R. Wu, M. Zaiser, S. Sandfeld, Int. J. Plastic. **95**, 142 (2017). https://doi.org/10.1016/j.ijplas.2017.04.005
10. D. Schrade, B. Xu, R. Müller, D. Gross, *Proceedings of the ASME Conference on Smart Materials, Adaptive Structures and Intelligent Systems*, vol. 1 (2008), p. 299. https://doi.org/10.1115/SMASIS2008-411
11. R. Schmitt, C. Kuhn, R. Müller, K. Bhattacharya, Technische Mechanik **34**(1), 23 (2014). https://doi.org/10.24352/UM.OVGU-2017-051
12. W. Cai, A. Arsenlis, C.R. Weinberger, V.V. Bulatov, J. Mech. Phys. Solids **54**(3), 561 (2006). https://doi.org/10.1016/j.jmps.2005.09.005
13. J. Weertman, *Dislocation Based Fracture Mechanics* (World Scientific Pub Co Inc, 1996), pp. 2–5
14. R. Peierls, Proc. Phys. Soc. **52**(1), 34 (1940). https://doi.org/10.1088/0959-5309/52/1/305
15. F.R.N. Nabarro, Proc. Phys. Soc. **59**(2), 256 (1947). https://doi.org/10.1088/0959-5309/59/2/309
16. J. Lothe, *Elastic Strain Fields and Dislocation Mobility, Modern Problems in Condensed Matter Sciences*, vol. 31, ed. by V.L. Indenbom, J. Lothe (Elsevier, 1992), pp. 175–235. https://doi.org/10.1016/B978-0-444-88773-3.50008-X
17. M. Lazar, G.A. Maugin, E.C. Aifantis, Phys. Status Solidi B **242**(12), 2365 (2005). https://doi.org/10.1002/pssb.200540078
18. M. Lazar, G.A. Maugin, E.C. Aifantis, Int. J. Solids Struct. **43**(6), 1787 (2006). https://doi.org/10.1016/j.ijsolstr.2005.07.005
19. M. Lazar, G. Po, Phys. Lett. A **379**(24), 1538 (2015). https://doi.org/10.1016/j.physleta.2015.03.027
20. G. Po, M. Lazar, N.C. Admal, N. Ghoniem, Int. J. Plastic. **103**, 1 (2018). https://doi.org/10.1016/j.ijplas.2017.10.003
21. N.C. Admal, J. Marian, G. Po, J. Mech. Phys. Solids **99**, 93 (2017). https://doi.org/10.1016/j.jmps.2016.11.005
22. G. Maugin, Acta Mech. **35**(1–2), 1 (1980)
23. P. Germain, SIAM J. Appl. Math. **25**(3), 556 (1973). https://doi.org/10.1137/0125053
24. G. Del Piero, J. Mech. Mater. Struct. **4**(2), 281 (2009). https://doi.org/10.2140/jomms.2009.4.281
25. R. Mindlin, Arch. Ration. Mech. An. **16**(1), 51 (1964)
26. M. Gurtin, Physica D **92**(3–4), 178 (1996)

Chapter 24
Towards the Crystal Plasticity Based Modeling of TRIP-Steels—From Material Point to Structural Simulations

Stefan Prüger and Björn Kiefer

Abstract With the complex multi-scale behavior of high-alloyed TRIP steels in mind, this contribution aims to complement recently established continuum mechanical modeling approaches for such materials, by considering their anisotropic inelastic response at the single crystal level. This approach generally enables the consideration of initial textures and their deformation-induced evolutions. It also represents the key theoretical and algorithmic foundation for future extensions to include phase transformation and twinning effects. Several rate-independent and rate-dependent formulations are investigated. The former are naturally associated with Karush-Kuhn-Tucker type inequality constraints in the sense of a multi-surface plasticity problem, whereas in the latter, these constraints are handled by penalty-type approaches. More specifically, the primary octahedral slip systems of face-centered cubic crystal symmetry are explicitly taken into account in our model application of the general framework and hardening models of increasing complexity are incorporated. To test the efficiency and robustness of the different formulations, material point simulations are carried out under proportional and non-proportional deformation histories. A rate-independent augmented Lagrangian formulation is identified as most suitable in the considered context and its finite element implementation as a User-defined MATerial subroutine (UMAT) is consequently studied in depth. To this end, the loading orientation dependence of the deformation and localization behaviors are analyzed through simulation of a mildly notched tensile specimen as a representative inhomogeneous boundary value problem.

S. Prüger (✉) · B. Kiefer
Institute of Mechanics and Fluid Dynamics,
Technische Universität Bergakademie Freiberg, Lampadiusstrasse 4,
09596 Freiberg, Germany
e-mail: Stefan.Prueger@imfd.tu-freiberg.de

H. Biermann and C. G. Aneziris (eds.), *Austenitic TRIP/TWIP Steels and Steel-Zirconia Composites*, Springer Series in Materials Science 298,
https://doi.org/10.1007/978-3-030-42603-3_24

24.1 Introduction

During the past decades, new steel grades with improved mechanical properties, such as high strength and pronounced ductility, have been developed, mainly motivated by light-weight applications in the automotive industry, cf. [1–3]. The initially fully-austenitic steel, X3CrMnNi16-6-6, developed in the DFG Collaborative Research Center 799, clearly belongs to this group of advanced high-strength steels. Extensive mechanical and microstructural characterization, see [4–9] revealed that the mechanical properties can be attributed to the evolution of the microstructure during deformation, i.e. depending on temperature, stacking-fault energy and strain-rate, the face-centered cubic (fcc) austenite (γ) forms twins or stacking-faults with hexagonal close-packed structure (ε) or transforms to body-centered cubic (bcc) martensite (α'). In particular, the different deformation mechanisms can occur concurrently, as shown in Fig. 24.1, which renders the formulation of constitutive models at the macroscopic scale a challenging task, cf. [10–12]. Although such models are already quite complex, they rarely incorporate the effect of evolving anisotropy due to texture evolution, which is of great importance in forming simulations. Furthermore, the application of such models in structural simulations is naturally associated with a length scale, at which the characteristic sizes of the microstructure are small compared to other dimensions of the problem. Therefore, employing such models to predict the behavior of devices at the micrometer scale seems to be questionable. In contrast, crystal plasticity based modeling approaches can in principle account for these effects, however, an appropriate scale-transition law has to be incorporated to give reasonable predictions at macroscopic scale. Keeping in mind that the deformation behavior of the TRIP-steel under consideration is mainly influenced by interaction of the deformation mechanisms at multiple scales—ranging from interactions between grains to interactions of stacking-faults with martensitic inclusions within a single grain—a crystal plasticity based multi-scale modeling approach seems to be even more appropriate. Although the kinematic aspects of the different deformation mechanisms are reasonable well understood, their incorporation into conventional crystal plasticity models is a challenging subject of ongoing research, especially for TRIP-steels.

Aiming for a comprehensive description of the transformation behavior in low-alloyed TRIP-steels, a material model that incorporates the stress-assisted transformation from fcc austenite to body-centered tetragonal (bct) martensite under thermomechanical loading is proposed in [13], which also takes into account the twinned martensite microstructure. The influence of the initial crystal orientation on the mechanical and the transformation behavior under homogeneous deformation is studied in [14] for the two cases of a single austenitic grain and an austenitic grain embedded in a ferritic, elastic-plastic matrix, which is described by a phenomenological, isotropic J_2-plasticity model. In [15] the material model is extended to account for anisotropic plastic slip by means of a crystal plasticity model, which is employed both within the austenitic grains and in the ferritic matrix. A significant influence of the initial orientation of the austenitic grains—embedded in a single or oligocrystalline ferritic matrix—is found for macroscopically homogeneous deformation states.

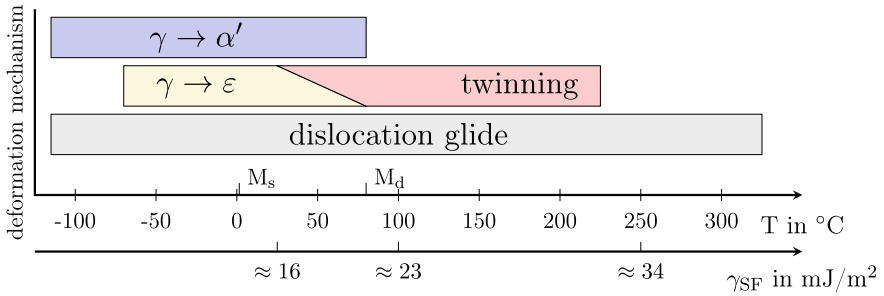

Fig. 24.1 Deformation mechanisms observed in the TRIP-steel X3CrMnNi16-6-6 as functions of temperature T or equivalently stacking-fault energy γ_{SF}. Data taken from [6]

Furthermore, in [16] this model is applied to the simulation of a representative volume element of a low-alloyed TRIP-steel with an idealized microstructure containing multiple austenite grains embedded in discretely resolved polycrystalline ferrite matrix under macroscopically homogeneous thermomechanical loading. Here the influence of the sequence of thermal and mechanical loading on the mechanical response and transformation behavior is investigated. The multi-scale character of the deformation and transformation behavior of low-alloyed TRIP-steels is accounted for in [17] by assuming an idealized lath martensite microstructure and combining the elastic-plastic material response of the two phases, austenite and martensite, with a criterion for the stress-assisted transformation and explicitly enforcing the compatibility and the stress equilibrium at their interfaces. In contrast to the models mentioned above, a single crystal material model for an initially fully-austenitic steel that shows a strain-induced transformation from fcc austenite to bcc martensite is considered in [18] and the transformation kinetics of Stringfellow [19] is applied at the single crystal scale and the evolution of deformation bands/bands of stacking-faults that act as nucleation sites for martensite is explicitly taken into account. Good agreement between numerical simulations and experimental results from uniaxial tensile tests for a wide range of strain rates is observed. A gradient extended crystal plasticity model that includes both stress-assisted and strain-induced austenite to martensite phase transformation is proposed in [20, 21] and is employed to study size effects in nanoindentation and in three-point bending tests and to investigate the influence of grain boundaries and twins in austenite grain on the transformation behavior. Consistent with thermodynamical considerations in [13, 14], a single crystal model that accounts for the stress-assisted austenite to martensite transformation is discussed in [22] and extended to include twinning [23]. Here again, the influence of the initial crystal orientation on the mechanical behavior under homogeneous deformations is considered. Increasing research activity in the field of high-manganese TWIP steels has led to the development of two single crystal material models [24, 25] that account for three different deformation mechanisms, namely slip, twinning and stacking-fault formation/ε-martensite formation. The latter model includes a dislocation density based hardening law, which is successfully calibrated based on quasi-static tensile

tests of a polycrystaline TWIP-steel together with the corresponding microstructure evolution in terms of ε-martensite and twin volume [26]. Rather recently, a single crystal plasticity model that incorporates the stress-assisted austenite to martensite transformation is applied to the prediction of polycrystalline response of two and three phase low-alloyed TRIP-steels and the corresponding forming limit diagrams [27]. Furthermore, the well-known transformation kinetics model of Olson-Cohen [28] is extended in [29] to account for the crystallographic nature of the formation of deformation bands/bands of stacking-faults. The kinetics law is then coupled to a crystal plasticity model to describe the strain-induced transformation from austenite to martensite. The comparison between numerical simulations and the results of polycrystalline experiments shows that the temperature and stress-state dependency of the mechanical response and the transformation behavior is well captured. For further information on the application of crystal plasticity models, the reader is referred to the comprehensive reviews [30–32].

Although the above literature review shows that numerous models have been proposed, which account for the coupling of two or three deformation mechanisms or the different nature of stress-assisted and strain-induced martensitic transformation, a material model that thoroughly captures all the deformation mechanisms mentioned in Fig. 24.1 and their transition over a wide range of temperatures still seems to be missing. In order to develop such a model—possessing a modular structure and being robust at the same time—a numerical framework has to be identified that allows for a robust and efficient implementation. While the above mentioned models are almost exclusively based on rate-dependent formulations, it is argued in [33] that such an approach may introduce an artificial rate-dependence into the model's response, if such a formulation is chosen only for numerical convenience and not due to experimental results. Hence, a systematic study regarding different numerical implementations has to be carried out to assess the efficiency and the robustness of the corresponding stress-update algorithms also considering different model complexity. The contribution at hand aims for such a study and will provide recommendations for appropriate algorithms both for rate-dependent and rate-independent formulations. Therefore, the choice of rate-dependence in the constitutive description of the different deformation mechanisms can solely be made based on experimental observations rather than numerics. The current study employs a single crystal plasticity model that is able to capture the deformation behavior of stable austenitic stainless steels as illustrated in [34]. Thus, an adequate description of the TRIP-steel X3CrMnNi16-6-6 at temperatures $T > 220$ °C is considered, where dislocation glide is the main deformation mechanism, see Fig. 24.1. This model will also form the basis for further model developments, eventually providing a modular constitutive description of the TRIP-steel under consideration. In order to enlighten the effect of rate-dependence on the constitutive response and the robustness of the corresponding stress update algorithms, the study comprises four different formulations and hardening laws of different complexity.

This contribution is structured as follows. The single crystal plasticity model is discussed in Sect. 24.2, while the comparison of the different formulations under homogeneous proportional and non-proportional loading histories is considered in

Sect. 24.3. In Sect. 24.4, a rate-independent formulation is employed to study the orientation dependence of the deformation and localization behavior of a mildly notched single crystal tensile specimen. Section 24.5 summarizes the main findings and outlines current and future research efforts on this topic.

24.2 Material Model

The constitutive behavior of face-centered cubic single crystals at finite deformations is described by a material model that builds on the approach proposed by Schmidt-Baldassari [35] in the rate-independent case and the formulation employed in [36–38] for the rate-dependent case. It is based on the multiplicative split of the deformation gradient into an elastic and a plastic part according to the proposal of Kröner [39] and Lee [40]

$$\mathbf{F} = \mathbf{F}^{\mathrm{e}} \cdot \mathbf{F}^{\mathrm{p}}. \tag{24.1}$$

In addition to this kinematic assumption, the intermediate configuration defined by such a split is taken as isoclinic as suggested in [41].

The elastic behavior, defined with respect to that intermediate configuration, is assumed to be governed by the isotropic, volumetric-isochorically decoupled free energy function of compressible Neo-Hooke type

$$\Psi^{\mathrm{e}} = \frac{1}{2}\kappa \left[\ln\left(J^{\mathrm{e}}\right)\right]^2 + \frac{1}{2}\mu \left[\overline{\mathbf{C}}^{\mathrm{e}} : \mathbf{I} - 3\right]. \tag{24.2}$$

Herein, J^{e} and $\overline{\mathbf{C}}^{\mathrm{e}}$ denote the determinant of the elastic part of the deformation gradient $\mathbf{F}^{\mathrm{e}}$ and the unimodular part of the elastic right Cauchy-Green tensor. The latter is obtained from the elastic Cauchy-Green tensor

$$\mathbf{C}^{\mathrm{e}} = \mathbf{F}^{\mathrm{eT}} \cdot \mathbf{F}^{\mathrm{e}} \tag{24.3}$$

via $\overline{\mathbf{C}}^{\mathrm{e}} = J^{\mathrm{e}-2/3}\mathbf{C}^{\mathrm{e}}$, while κ and μ are the bulk and shear moduli, respectively. The second Piola-Kirchhoff stress in the intermediate configuration $\widehat{\mathbf{S}}$ is defined as

$$\widehat{\mathbf{S}} = 2\,\frac{\partial \Psi^{\mathrm{e}}}{\partial \mathbf{C}^{\mathrm{e}}} \tag{24.4}$$

and specifically reads as

$$\widehat{\mathbf{S}} = J^{\mathrm{e}}\,\frac{\partial \Psi^{\mathrm{e}}_{\mathrm{vol}}}{\partial J^{\mathrm{e}}}\,\mathbf{C}^{\mathrm{e}-1} + 2\,\frac{\partial \Psi^{\mathrm{e}}_{\mathrm{iso}}}{\partial \mathbf{C}^{\mathrm{e}}} = \kappa \ln\left(J^{\mathrm{e}}\right)\mathbf{C}^{\mathrm{e}-1} + J^{\mathrm{e}-2/3}\mu\left[\mathbf{I} - \frac{1}{3}\,\mathrm{tr}\left(\mathbf{C}^{\mathrm{e}}\right)\mathbf{C}^{\mathrm{e}-1}\right] \tag{24.5}$$

for the elastic free energy density given in (24.2), cf. [42] for a detailed derivation. Furthermore, the Mandel stress tensor $\mathbf{M}$, which is also defined with respect to the

intermediate configuration, can be expressed as

$$\mathbf{M} = \mathbf{C}^{\mathrm{e}} \cdot \widehat{\mathbf{S}} = \left[\kappa \ln\left(J^{\mathrm{e}}\right) - \frac{1}{3}\mu \operatorname{tr}\left(\overline{\mathbf{C}}^{\mathrm{e}}\right) \right] \mathbf{I} + \mu\, \overline{\mathbf{C}}^{\mathrm{e}}. \tag{24.6}$$

The assumption of elastic isotropy is a reasonable approximation only for a few cubic metals, e.g. α-Tungsten, aluminum and vanadium [43], which are characterized by a Zener anisotropy index close to one [44]. This assumption is considered acceptable for the current contribution due to its simplicity. However, an extension of the material model to incorporate elastic anisotropy can be carried out by replacing the free energy density in (24.2) by the quadratic anisotropic free energy function discussed in [45], which is more suitable for moderately large elastic deformations. In contrast to the elastic behavior, the inelastic deformation of a single crystal is inherently anisotropic because it is governed by a finite number of distinct slip systems associated with the crystal lattice. For most face-centered cubic crystals it is reasonable to consider only the primary octahedral slip systems, consisting of $\{111\}$ slip planes and $\langle 110 \rangle$ slip directions, see Table 24.1. The inelastic slip on the different slip systems, γ_α, is linked to the plastic part of the deformation gradient and the plastic velocity gradient $\mathbf{L}^{\mathrm{p}}$ via the evolution equation

$$\mathbf{L}^{\mathrm{p}} = \dot{\mathbf{F}}^{\mathrm{p}} \cdot \mathbf{F}^{\mathrm{p}-1} = \sum_{\alpha=1}^{n} \dot{\gamma}_\alpha\, \mathbf{s}_\alpha \otimes \mathbf{n}_\alpha, \tag{24.7}$$

in which $\mathbf{s}_\alpha$ and $\mathbf{n}_\alpha$ denote the slip direction and the slip plane normal of the system α. In addition, these vectors are of unit length $|\mathbf{s}_\alpha| = |\mathbf{n}_\alpha| = 1$ and are mutually orthogonal $\mathbf{s}_\alpha \cdot \mathbf{n}_\alpha = 0$, where the latter property results in the inelastic part of the deformation gradient being isochoric. The onset of inelastic deformation on each slip system is described by limit surfaces of the form

$$\Phi_\alpha := \tau_\alpha - \left[\mathrm{Y}_0 + Y_\alpha(\varepsilon_\beta) \right]. \tag{24.8}$$

Herein, τ_α denotes the resolved shear stress on the slip system α and is computed as

$$\tau_\alpha = \mathbf{M} : [\, \mathbf{s}_\alpha \otimes \mathbf{n}_\alpha \,], \tag{24.9}$$

while Y_0 and Y_α respectively correspond to the initial yield stress and the driving force thermodynamically conjugate to the hardening variable ε_α. The driving force is consequently defined as

$$Y_\alpha := \frac{\partial \Psi^{\mathrm{p}}}{\partial \varepsilon_\alpha}, \tag{24.10}$$

where an additional split of the free energy due to elastic and inelastic effects has been assumed. In the current contribution, two different hardening functions are considered.

Table 24.1 Primary slip systems of a face-centered cubic single crystal

Miller indices	Schmid/Boas notation [46]	Slip plane normal	Slip direction
$(1,1,1)[1,\bar{1},0]$	B5	$\mathbf{n}_1 = \mathbf{n}_{13} = [1,1,1]/\sqrt{3}$	$\mathbf{s}_1 = -\mathbf{s}_{13} = [1,-1,0]/\sqrt{2}$
$(1,1,1)[1,0,\bar{1}]$	B4	$\mathbf{n}_2 = \mathbf{n}_{14} = [1,1,1]/\sqrt{3}$	$\mathbf{s}_2 = -\mathbf{s}_{14} = [1,0,-1]/\sqrt{2}$
$(1,1,1)[0,1,\bar{1}]$	B2	$\mathbf{n}_3 = \mathbf{n}_{15} = [1,1,1]/\sqrt{3}$	$\mathbf{s}_3 = -\mathbf{s}_{15} = [0,1,-1]/\sqrt{2}$
$(1,1,\bar{1})[1,\bar{1},0]$	C5	$\mathbf{n}_4 = \mathbf{n}_{16} = [1,1,-1]/\sqrt{3}$	$\mathbf{s}_4 = -\mathbf{s}_{16} = [1,-1,0]/\sqrt{2}$
$(1,1,\bar{1})[1,0,1]$	C3	$\mathbf{n}_5 = \mathbf{n}_{17} = [1,1,-1]/\sqrt{3}$	$\mathbf{s}_5 = -\mathbf{s}_{17} = [1,0,1]/\sqrt{2}$
$(1,1,\bar{1})[0,1,1]$	C1	$\mathbf{n}_6 = \mathbf{n}_{18} = [1,1,-1]/\sqrt{3}$	$\mathbf{s}_6 = -\mathbf{s}_{18} = [0,1,1]/\sqrt{2}$
$(1,\bar{1},1)[1,1,0]$	D6	$\mathbf{n}_7 = \mathbf{n}_{19} = [1,-1,1]/\sqrt{3}$	$\mathbf{s}_7 = -\mathbf{s}_{19} = [1,1,0]/\sqrt{2}$
$(1,\bar{1},1)[1,0,\bar{1}]$	D4	$\mathbf{n}_8 = \mathbf{n}_{20} = [1,-1,1]/\sqrt{3}$	$\mathbf{s}_8 = -\mathbf{s}_{20} = [1,0,-1]/\sqrt{2}$
$(1,\bar{1},1)[0,1,1]$	D1	$\mathbf{n}_9 = \mathbf{n}_{21} = [1,-1,1]/\sqrt{3}$	$\mathbf{s}_9 = -\mathbf{s}_{21} = [0,1,1]/\sqrt{2}$
$(\bar{1},1,1)[1,1,0]$	A6	$\mathbf{n}_{10} = \mathbf{n}_{22} = [-1,1,1]/\sqrt{3}$	$\mathbf{s}_{10} = -\mathbf{s}_{22} = [1,1,0]/\sqrt{2}$
$(\bar{1},1,1)[1,0,1]$	A3	$\mathbf{n}_{11} = \mathbf{n}_{23} = [-1,1,1]/\sqrt{3}$	$\mathbf{s}_{11} = -\mathbf{s}_{23} = [1,0,1]/\sqrt{2}$
$(\bar{1},1,1)[0,1,\bar{1}]$	A2	$\mathbf{n}_{12} = \mathbf{n}_{24} = [-1,1,1]/\sqrt{3}$	$\mathbf{s}_{12} = -\mathbf{s}_{24} = [0,1,-1]/\sqrt{2}$

Firstly, a purely phenomenological, Taylor-type hardening formulation of the form

$$Y_\alpha = \Delta \mathrm{Y}\left[1 - \exp\left(-\mathrm{h}A\right)\right] \tag{24.11}$$

is introduced, which incorporates the cumulative inelastic slip $A = \sum_\alpha \varepsilon_\alpha$ and is parameterized by the asymptotic increase in the yield stress ΔY as well as the dimensionless shape parameter h. It can be deduced from the inelastic part of the free energy function, i.e.

$$\Psi^{\mathrm{p,Taylor}} = \Delta \mathrm{Y}\left[A + \frac{1}{\mathrm{h}}\exp\left(-\mathrm{h}A\right)\right], \tag{24.12}$$

by means of (24.10). The application of the cumulative inelastic slip A in the hardening function (24.11) idealizes the interaction between different slip systems, but due to its simplicity, it has been extensively used to develop robust algorithmic frameworks for single crystal plasticity models [47–49].

Secondly, the alternative anisotropic hardening function

$$Y_\alpha = \Delta \mathrm{Y} \sum\nolimits_\beta \mathrm{h}^{\alpha\beta}\left[1 - \exp\left(-\mathrm{h}\varepsilon_\beta\right)\right], \tag{24.13}$$

proposed in [50], is considered, which introduces the symmetric interaction matrix $\mathrm{h}^{\alpha\beta}$ in a phenomenological manner. It allows for a more complex interaction of different slip systems and contains up to 6 material constants [46]. In the current contribution the structure of the interaction matrix is adopted from [51]. The energy corresponding to this type of hardening function is formulated as a quadratic form

$$\Psi^{\mathrm{p,GC}} = \frac{1}{2}\Delta \mathrm{Y}\mathrm{h} \sum\nolimits_\alpha s_\alpha \sum\nolimits_\beta \mathrm{h}^{\alpha\beta} s_\beta \tag{24.14}$$

in terms of the auxiliary variable s_α. The exponential type hardening is obtained from a non-associated evolution equation for s_α, which eventually leads to

$$s_\alpha = \frac{1}{\mathrm{h}} \left[1 - \exp\left(-\mathrm{h}\varepsilon_\alpha\right)\right]. \tag{24.15}$$

The driving force Y_α, introduced in (24.13), is obtained by taking the derivative of (24.14) with respect to s_α and the subsequent substitution of (24.15) to eliminate s_α from the resulting expression. Note that the hardening function (24.13) is exactly the one employed in the "GC model" in [36], which emanates from the small strain formulation presented in [50]. In order to close the system of equations evolution laws for the internal state variables have to be defined.

In the rate-independent formulation one obtains

$$\dot{\varepsilon}_\alpha = -\dot{\lambda}_\alpha \frac{\partial \Phi_\alpha}{\partial Y_\alpha} \tag{24.16}$$

for the hardening variables and for the inelastic velocity gradient

$$\mathbf{L}^{\mathrm{p}} = \sum_{\alpha=1}^{n} \dot{\lambda}_\alpha \frac{\partial \Phi_\alpha}{\partial \mathbf{M}} \tag{24.17}$$

from an associated formulation, which introduces the Lagrange multipliers $\dot{\lambda}_\alpha$, that are subject to the Karush-Kuhn-Tucker (KKT) conditions

$$\Phi_\alpha \leq 0 \quad \dot{\lambda}_\alpha \geq 0 \quad \dot{\lambda}_\alpha \Phi_\alpha = 0. \tag{24.18}$$

Considering the limit surface (24.8) and comparing the inelastic velocity gradient given in (24.17) with the evolution equation for the plastic part of the deformation gradient (24.7), one can readily identify

$$\dot{\gamma}_\alpha = \dot{\lambda}_\alpha \tag{24.19}$$

$$\dot{\varepsilon}_\alpha = \dot{\lambda}_\alpha \tag{24.20}$$

in the rate-independent case. In contrast to the commonly adopted, computational expensive active-set search algorithms to handle the inequalities in the KKT conditions, two different formulations of the rate-independent problem are considered here, which employ equality constraints only.

Firstly, the *augmented Lagrangian formulation*, initially proposed in connection with crystal plasticity in [35], is employed, which takes the principle of maximum plastic dissipation as starting point and reformulates the inequality constrained optimization problem into an equality constrained optimization problem by means of so-called slack variables [52, pp. 72, 158–164]. The Lagrange multipliers are then obtained from

$$\dot{\lambda}_\alpha = \max\left(0, \eta^* \Phi_\alpha\right), \tag{24.21}$$

in which the viscosity-like parameter η^* is introduced for purely numerical reasons, as it regularizes the problem, while the constraints are exactly enforced by means of the Lagrange multipliers.

Secondly, a formulation based on *nonlinear complementary functions* (NCP-functions) is considered. These functions have originally been proposed for constrained optimization problems, cf. [53]. A slightly more general form of NCP-functions is introduced by Kanzow and Kleinmichel in [54] and employed in the current contribution, which reads as

$$\sqrt{\left[\Phi_\alpha + \dot{\lambda}_\alpha\right]^2 - \Theta\, \Phi_\alpha \dot{\lambda}_\alpha} + \Phi_\alpha - \dot{\lambda}_\alpha = 0. \tag{24.22}$$

In particular, the parameter $\Theta = 0$ is chosen here and the Lagrange multipliers are obtained from (24.22) rather than from (24.18).

In the rate-dependent formulation, the KKT conditions in (24.18) are no longer applicable and the corresponding Lagrange multipliers are replaced by a potentially stress-dependent viscosity law v. This yields

$$\dot{\varepsilon}_\alpha = -v_\alpha(\tau_\alpha, Y_\alpha)\, \frac{\partial \Phi_\alpha}{\partial Y_\alpha} \tag{24.23}$$

and

$$\mathbf{L}^{\mathrm{vp}} = \sum_{\alpha=1}^{n} v_\alpha(\tau_\alpha, Y_\alpha)\, \frac{\partial \Phi_\alpha}{\partial \mathbf{M}}. \tag{24.24}$$

Assuming that an equation analogous to (24.7) holds for the viscoplastic part of the deformation gradient $\mathbf{F}^{\mathrm{vp}}$ in the context of a rate-dependent formulation, one may identify the general format for the evolution equations as

$$\dot{\gamma}_\alpha = v_\alpha(\tau_\alpha, Y_\alpha) \tag{24.25}$$

$$\dot{\varepsilon}_\alpha = v_\alpha(\tau_\alpha, Y_\alpha). \tag{24.26}$$

To study the influence of the type of viscosity law on the deformation behavior of single crystals — in particular in the rate-independent limit — this contribution considers two specific cases:

Firstly, the approach initially proposed by Perzyna [55] and extensively used in the groups of Cailletaud and Forest, cf. [36–38, 50, 51, 56–60], is considered, in which the viscosity law takes the form

$$v_\alpha^{\mathrm{PCF}} = \frac{1}{\eta} \left\langle \frac{\Phi_\alpha}{\mathrm{K}} \right\rangle^{\mathrm{n}}. \tag{24.27}$$

The positive material parameters K, n and η denote a stress-like scaling factor, the rate sensitivity exponent and a time-like parameter, respectively, where the inverse of the latter can be interpreted as a reference strain rate. The Macaulay brackets are defined as

$$\langle x \rangle = \begin{cases} x & \text{if } x > 0 \\ 0 & \text{else} \end{cases} \tag{24.28}$$

and are identical to the max-function, $m(x) = \max(0, x)$, and the ramp function, $r(x) = \frac{1}{2}(x + |x|)$.

Secondly, the viscosity law introduced by Cuitiño and Ortiz in [61] and employed for instance in Miehe's group, cf. [47–49], which specifically reads

$$v_\alpha^{\mathrm{OM}} = \frac{1}{\eta}\left[\left[\frac{\langle \Phi_\alpha \rangle}{\tau_\alpha^y(\varepsilon_\beta)} + 1\right]^{\mathrm{n}} - 1\right] \tag{24.29}$$

is also employed in the studies presented here. Note that the current slip resistance of the particular slip system α is denoted by τ_α^y and possesses the same functional dependency on the hardening variable ε_β as the quantity $\mathrm{Y}_0 + Y_\alpha(\varepsilon_\beta)$, but in (24.29) only Φ_α is explicitly dependent on both τ_α and Y_α. Therefore, the slip resistance τ_α^y is treated as history dependent normalization quantity, rather than an additional function of Y_α. This allows one to automatically guarantee thermodynamic consistency and enforce that the slip γ_α evolves identically to the hardening variables ε_α.

In order to carry out material point calculations and structural simulations, the different formulations of the rate-dependent and the rate-independent material models have been implemented into the scientific computing environment MATLAB and subsequently into the finite element program ABAQUS via the User-defined MATerial interface (UMAT). The evolution equations for the internal state variables are integrated by means of an implicit Euler backward scheme and a projection technique is employed to enforce the incompressibility constraint for the inelastic part of the deformation gradient. Details of the corresponding algorithms and the associated tangent operator can be found in [62].

24.3 Material Response Under Homogeneous Deformation

In this chapter, the material model described in Sect. 24.2 is employed in the simulation of a fully deformation-controlled simple shear test as well as a non-proportional tension/compression-shear cycle. The results obtained with the different formulations are illustrated in the subsequent sections.

24.3.1 Simple Shear Loading

Due to its simplicity, the fully deformation-controlled simple shear test is extensively used in the literature to assess the robustness of various stress-update algorithms for single crystal plastictiy, cf. [35, 47, 63–69]. For comparison, this test is also employed here, where the coefficients of the associated deformation gradient are prescribed as

$$[\mathbf{F}] = \begin{bmatrix} 1 & \gamma(t) & 0 \\ 0 & 1 & 0 \\ 0 & 0 & 1 \end{bmatrix}. \tag{24.30}$$

In particular, the simple shear motion, introduced in [63] is considered, in which the crystal lattice is misaligned with respect to the global coordinate axes and is characterized by the following orientation in terms of Euler angles $\{\varphi_1, \Phi, \varphi_2\} = \{0°, 18.4349°, 0°\}$ in Bunge notation [70], i.e. a sequential rotation about the z-, x- and z-axes is considered. The material parameters employed in the simulation correspond to an ideal plastic behavior at the scale of the slip system and are specified in Table 24.2. Therefore, any effective hardening or softening observed in the subsequently shown stress-strain diagrams is attributed to the reorientation of the crystal lattice, which approaches a stable orientation for large shear γ, asymptotically leading to a constant shear stress. Additionally, the rate-dependent material response is characterized by the rate exponent $\mathrm{n} = 20$ for the OM-viscosity function (24.29), while for the PCF-viscosity function (24.27) parameters are set to $\mathrm{n} = 10$ and $\mathrm{K} = 10^{-3}$ GPa, consistent with the experimentally observed range of rate-sensitivity exponents [71]. The influence of the chosen increment size $\Delta\gamma$ on the stress-strain curve is depicted in Fig. 24.2. In the rate-independent formulation, the augmented Lagrangian algorithm takes 15, 60 and 600 steps to reach the final shear amplitude $\gamma = 6$, while the Kanzow NCP-function respectively requires 100, 600, 1200 and 1800 steps. It can be seen that both formulations converge to the same material response for the smallest increment size. The augmented Lagrangian formulation reproduces the characteristic features of the stress-strain curve even for very large shear increments and the stress response converges monotonically as the shear increment is refined. In contrast, the formulation based on the Kanzow NCP-function requires significantly smaller shear increments to ensure the numerical convergence of the Newton-type algorithm. But even though the numerical convergence is achieved, the simulated stress-strain curve is very sensitive to the chosen increment size, in particular in the strain range $2 \leq \gamma \leq 6$. Herein, the constitutive response converges to the results of the augmented Lagrangian formulation with decreasing shear increment size in a non-monotonic manner. Although not shown in Fig. 24.2a, the same observations

Table 24.2 Material parameters for finite strain, simple shear loading

κ in GPa	μ in GPa	Y_0 in GPa	$\Delta\mathrm{Y}$ in GPa	h	η in s
49.98	21.1	0.06	0.0	0.0	50.0

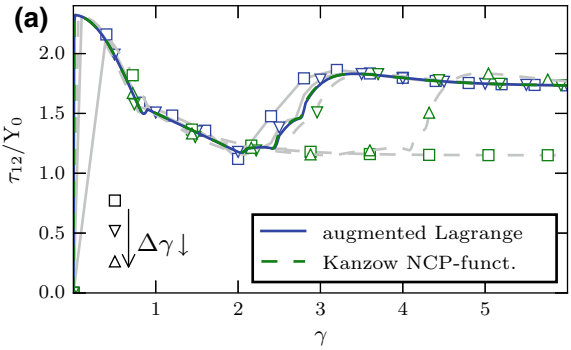

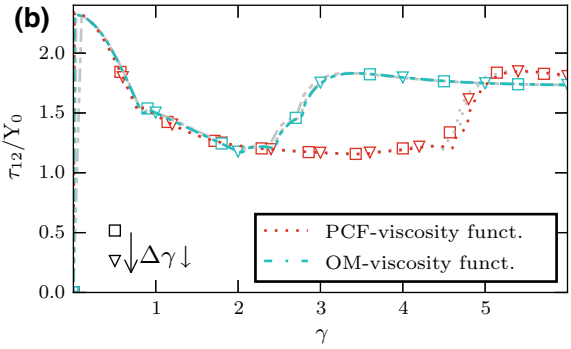

Fig. 24.2 Influence of the shear increment size $\Delta\gamma$ on simulated stress-strain curves for finite strain, simple shear loading, **a** rate-independent and **b** rate-dependent formulations. Gray lines with symbols indicate the stress response for different shear increment sizes, while colored lines correspond to the stress response obtained with the smallest shear increment size

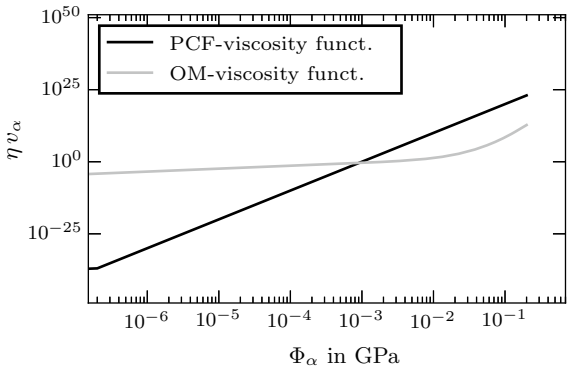

Fig. 24.3 Normalized viscosity functions for viscous parameters adopted in the simple shear test

have been made for the original Fischer-Burmeister NCP-function, which is recovered by the choice $\Theta = 2$ in (24.22).

In the rate-dependent formulation, the stress-strain curve under quasi-static loading condition, $\dot{\gamma} = 10^{-5}\mathrm{s}^{-1}$, is determined in 60, 180 and 600 steps for the OM-viscosity function and in 420, 600 and 1800 steps for the PCF-viscosity function. Figure 24.2b shows that apart from small deviations, which are due to the different viscosity functions and viscous parameters employed, the stress-strain curves feature the same behavior up to $\gamma \approx 2.3$. For larger shear strains however, a significant differ-

ence in the computed stress response is observed. While the OM-formulation leads to a stress-strain curve possessing the same characteristics as the rate-independent case, the PCF-formulation yields a stress response for which the transition to higher stress levels is significantly delayed. The working hypothesis explaining this observation is that small differences in the evolution of the plastic slip γ_α determined from the PCF- and OM-viscosity functions accumulate and that such an accumulation eventually leads to sudden deviation in the stress response at $\gamma \approx 2.3$. The presence of small differences between the different rate-dependent formulations is clearly visible from the comparison of the normalized viscosity functions (24.27) and (24.29), as illustrated in Fig. 24.3. In order to check the hypothesis, a sensitiv-

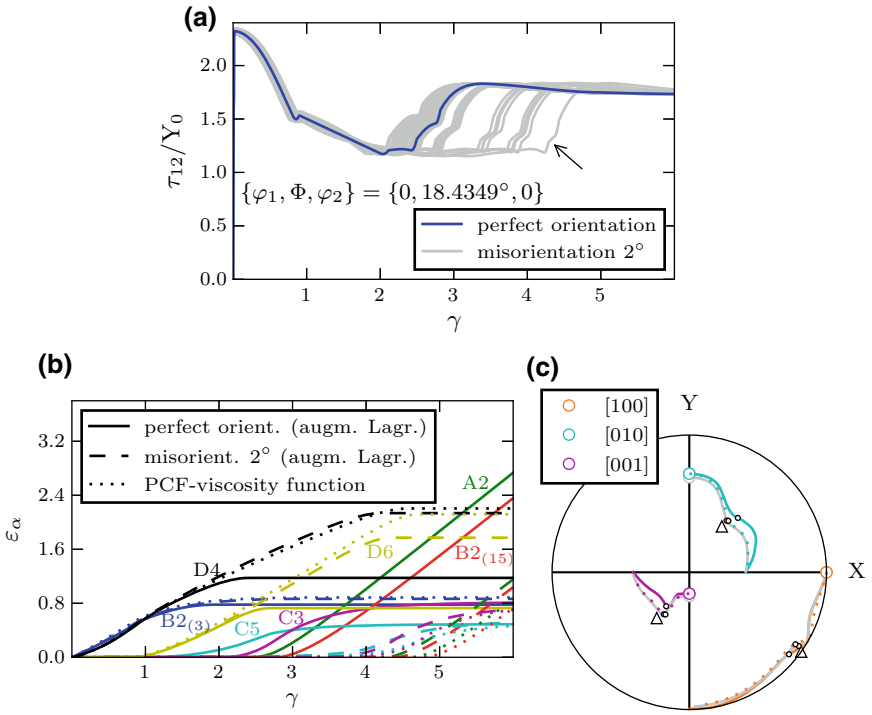

Fig. 24.4 Influence of an initial misorientation on: **a** the normalized stress-strain curve, **b** the evolution of the hardening variables and **c** the reorientation of the ⟨100⟩ directions in the pole figure employing a stereographic projection for finite strain, simple shear loading. The gray lines in **a** denote different realizations of perturbed initial orientations possessing a misorientation of 2°, while the arrow indicates the specific orientation for which the evolution of ε_α and the reorientation behavior are shown in (**b**) and (**c**), respectively.The labels of the different slip systems employed in **b** is consistent with Table 24.1. Note that, in **c** colored and gray solid lines represent the response of the augmented Lagrangian formulation for a perfectly oriented and a misaligned crystal, while the dotted lines correspond to the results of the rate-dependent PCF-formulation for a perfectly oriented crystal. Additionally, small black circles indicate the orientation at $\gamma = 2.0$, while the triangles denote a stable crystallographic orientation

ity analysis is performed, in which the influence of a small initial misorientation (2°) on the stress-strain curve is investigated. The simulations are carried out by means of the augmented Lagrangian formulation of the rate-independent material model and the shear component γ is incremented in 600 equidistant steps. The corresponding results are shown in Fig. 24.4a. It can be seen that the initial part of the stress-strain curve is rather nonsensitive to the perturbation of the initial orientation and that the initial misorientation strongly affects the stress-strain curve only in the range $2 \leq \gamma \leq 4.5$, which is consistent with the scatter observed in Fig. 24.2 for the different step sizes and formulations. Observing that small differences in the initial conditions lead to considerable deviations in the stress response indicates a stability problem, in particular a bifurcation. However, it is not caused by the Taylor ambiguity problem [72], where several combinations of plastic slip variables exist that lead to the same stress state. This is because, as shown in the literature, both the rate-independent augmented Lagrangian formulation as well as the rate-dependent formulations yield unique solutions for the slip system selection and the corresponding rates [67, 72] and thus the Taylor ambiguity problem is avoided. Conducting a systematic variation of the initial orientation according to $\phi_1 = \phi_2 = 0°$ and $\Phi \in [0°, 45°]$ reveals that the stability issue mentioned above is related to the discrete nature of the plastic flow of the single crystal. In fact choosing initial orientations in the range $\Phi \in [22.5°, 45°]$ asymptotically leads the reorientation of the crystal towards the stable orientation indicated by triangles in Fig. 24.4c. In the narrow range $\Phi \in [17°, 22°]$ the crystal approaches a different stable orientation, while for $\Phi \in [0°, 16°]$ a constant rotation of the crystal lattice is predicted by the material model. As the initial orientation $\{\varphi_1, \Phi, \varphi_2\} = \{0°, 18.4349°, 0°\}$ and the perturbed initial orientations considered are very close to the boundary of the two ranges of Φ, the sensitivity of the stress response to small perturbations is not surprising. It is therefore concluded that small initial misorientations or the accumulation of small differences in the evolution of the plastic slip variables in the rate-dependent case are responsible for selection of slip systems made by the corresponding algorithms. In addition to the stress-strain response, Fig. 24.4b illustrates the evolution of the hardening variables for three different cases. In particular, a rate-independent, perfectly oriented crystal as well as a rate-independent crystal with a specific misorientation of 2°, indicated by an arrow in Fig. 24.4a and a rate-dependent, perfectly oriented crystal based on the PCF-formulation is considered. Note that the slip systems, which are active only in the range $0 \leq \gamma \leq 1$ and overall show a low activity, i.e. $\varepsilon_\alpha < 0.35$, are not shown for the sake of clarity. Comparing the pattern of activation and deactivation of the slip systems of the perfectly oriented and the misaligned crystal, it is obvious that the initial misorientation delays the deactivation of the slip systems D4 and D6 as well as the activation of the systems C3, C5, A2 and $B2_{(15)}$, where the latter corresponds to slip system 15 in Table 24.1. This delay is responsible for the postponed transition to the orientation $\{\varphi_1, \Phi, \varphi_2\} = \{90°, 45°, 0°\}$, for which a constant yield stress and no rotation of the crystal is observed [63]. Furthermore, it is observed that the pattern of activation and deactivation of the slip systems computed for the perfectly oriented, rate-dependent crystal is similar to the pattern obtained for the misaligned, rate-independent crystal. This indicates that the slip γ_α deter-

mined via the rate-dependent formulation causes a small misalignment of the crystal compared to the results of the rate-independent response of the perfectly oriented crystal employing the augmented Lagrangian formulation, as shown in Fig. 24.4c. This leads to a different reorientation of the ⟨100⟩ directions and a delayed transition towards the orientation $\{\varphi_1, \Phi, \varphi_2\} = \{90°, 45°, 0°\}$. These observations therefore support the hypothesis introduced above and give an explanation for the differences in the stress response presented in Fig. 24.2.

Technically, the misorientation $\Delta\mathbf{R}$ is incorporated by means of the Euler-Rodrigues formula

$$\Delta\mathbf{R} = \mathbf{I} + [1 - \cos(\alpha)] + \sin(\alpha)\,\mathbf{A} \quad \text{with} \quad \mathbf{A} = -\boldsymbol{\epsilon} \cdot \mathbf{a}, \tag{24.31}$$

where $\boldsymbol{\epsilon}$ is the Levi-Civita tensor, while $\mathbf{a}$ denotes the rotation axis and α the corresponding angle. The misorientations employed in this section are generated by taking the rotation axis according to the 42 equally spaced points on the unit sphere [73] and the rotation angle $\alpha = 2°$. The initial orientation of the crystal with a predefined misorientation $\mathbf{R}^*$ is then obtained, according to [74, p. 68] from

$$\Delta\mathbf{R} = \mathbf{R}^* \cdot \mathbf{R}^{-1}, \tag{24.32}$$

in which $\mathbf{R}$ is the unperturbed initial orientation.

24.3.2 *Non-proportional Tension/compression-Shear Loading*

While the fully deformation-controlled simple shear test provided valuable insight into the robustness of the different formulations in the ideal plastic case, the capabilities of the different formulations in the hardening case are assessed now under complex loading conditions employing a non-proportional load cycle, similar to the one proposed in [38]. It corresponds to a uniaxial tension/compression loading combined with a simple shear loading and approximately mimics the deformation path observed in the dual actuator loading system described in [75] or a thin-walled tubular specimen in a tension-torsion testing device [76]. The temporal change of the coefficients of the deformation gradient tensor associated with this so-called *butterfly* test are prescribed according to

$$[\mathbf{F}] = \begin{bmatrix} * & F_{12}(t) & * \\ 0 & F_{22}(t) & * \\ * & * & * \end{bmatrix} \tag{24.33}$$

and are illustrated in Fig. 24.5a. The remaining coefficients, indicated by $*$, are determined by an iterative procedure, the *c*onstitutive driver, described in [77, 78] that enforces the associated components of the first Piola-Kirchhoff stress to vanish, see

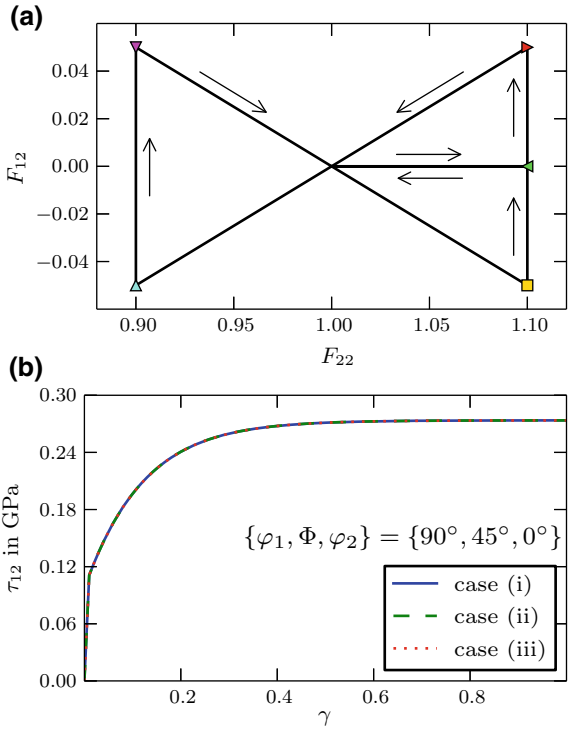

Fig. 24.5 **a** Biaxial, non-proportional deformation path in the butterfly test and **b** stress-strain curve for simple shear loading considering different interaction matrices, indicated by case (i),(ii) and (iii), see Table 24.3

also [79, p. 562f] for a spatial formulation. Furthermore, this procedure is enhanced by an adaptive time-stepping algorithm to allow for a step size adjustment of the prescribed components F_{12} and F_{22} based on the convergence behavior.

Recall that the degree of anisotropy in the hardening behavior of the single crystal material model depends on the choice of the interaction matrix in the hardening law, given in (24.13). Since its coefficients can be estimated from non-proportional tests involving strain path changes, cf. [80], it is interesting to study the influence of the interaction matrix on the performance of the different formulations in case of the butterfly test. Therefore, the initial orientation of the crystal is taken as $\{\varphi_1, \Phi, \varphi_2\} = \{0°, 0°, 0°\}$, i.e. the crystal axes are aligned with the axes of the global coordinate system and the hardening parameters are chosen according to Table 24.3, while the remaining parameters are taken from Table 24.2. The coefficients of the interaction matrix are adopted from the literature without modifications, while the hardening parameters ΔY are rescaled in the cases (ii) and (iii). This rescaling is necessary in order to solely study the effect of the deviation of the interaction matrix from the Taylor-type hardening case, because according to (24.13) keeping the parameter ΔY constant would result in considerably different hardening rates. Therefore, the hardening parameters ΔY are adjusted in such a manner that the stress-strain curves coincide under simple shear loading for the arbitrarily chosen orientation $\{\varphi_1, \Phi, \varphi_2\} = \{90°, 45°, 0°\}$, see Fig. 24.5b.

Table 24.3 Hardening parameters employed in the comparative study under finite deformation tension/compression-shear loading

case	Y_0 in GPa	ΔY in GPa	h	h_0	h_1	h_2	h_3	h_4	h_5	References
(i)	0.06	0.049	10	1.0	1.0	1.0	1.0	1.0	1.0	–
(ii)	0.06	0.04083	10	1.0	1.4	1.4	1.4	1.4	1.4	[58]
(iii)	0.06	0.01704	10	1.0	4.4	4.75	4.75	4.75	5.0	[37]

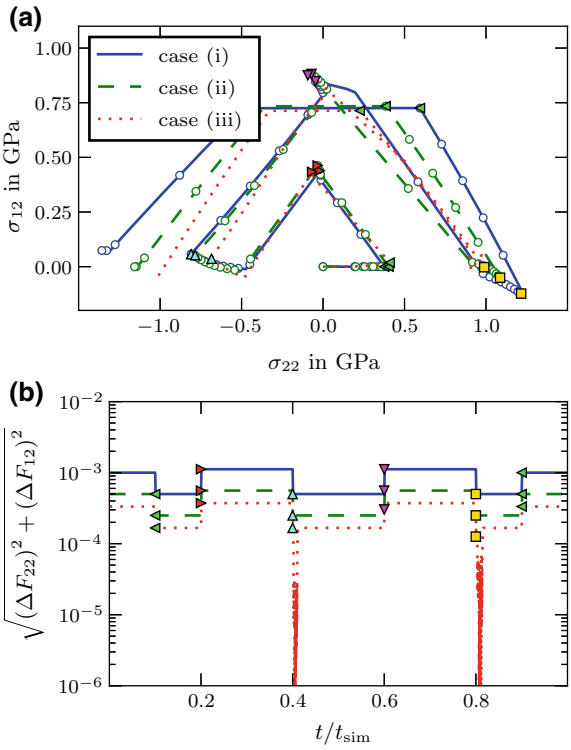

Fig. 24.6 Influence of the interaction matrix on: **a** the stress path in the butterfly test for different numbers of increments and **b** the norm of the prescribed deformation increment for the rate-independent, augmented Lagrangian formulation. The three different interaction matrices are indicated by case (i), (ii) and (iii), in agreement with Table 24.3. The filled symbols denote changes in the deformation path consistent with Fig. 24.5a

The calibrated material model is used to simulate the stress response to the non-proportional deformation path illustrated in Fig. 24.5a employing the rate-independent, augmented Lagrangian formulation and the rate-dependent formulation based on the OM-viscosity function, because both formulations proved robust and yielded consistent results in the fully deformation-controlled test conducted in Sect. 24.3.1. For the rate-independent formulation, the computed stress path is illustrated in Fig. 24.6a, in which the reference simulations, depicted with colored lines, required 1000, 2000 and 4500 increments for the different interaction matrices in cases (i), (ii) and (iii), respectively. Furthermore, white circles denote simulation results obtained with coarser increment sizes in the cases (i) and (ii), in which 50 and 1500 increments were employed, still yielding sufficiently accurate predictions of

the stress path. It is clearly visible from Fig. 24.6a that the interaction matrix significantly influences the stress response, especially at the latter stages of the deformation path, suggesting that the material parameters entering the interaction matrix could in principle be identified from such a non-proportional test.

Besides this observation, the choice of interaction matrix also significantly influences the performance of the augmented Lagrangian formulation in conjunction with the constitutive driver. In particular, while a rather coarse incrementation can be chosen in case (i), i.e. an interaction matrix corresponding to Taylor-type hardening is employed, the beneficial robustness of the formulation is diminished in case of the two-parameter interaction matrix (ii) and especially in case of the four-parameter interaction matrix (iii), at least if the same accuracy as in the reference simulation is sought. This aspect is also illustrated in Fig. 24.6b, which shows the evolution of the norm of prescribed deformation gradient components for the reference simulations. While no adaptive adjustment of the increment size is necessary in cases (i) and (ii), it is worth noting that at least one and a half times the number of increments are required in case (ii) compared to the reference simulation with Taylor-type hardening (i) to obtain a stress response independent of the chosen step size. In case (iii), an adaptive adjustment of the increment size is even necessary, particularly at the change in the deformation path from the combined tension/compression-shear loading to only shear loading in order to ensure convergence of the constitutive driver, yielding increment sizes below 10^{-6}. Thus, although the augmented Lagrangian formulation proved very robust in a fully deformation-controlled test in the absence of hardening, similar results cannot be obtained in situations where the hardening is anisotropic. This is due to the inclusion of interaction matrices other than the one corresponding to Taylor-type hardening and in particular in situations that involve iterative procedures to ensure stress-free conditions in certain directions. This is not surprising, because interaction matrices not associated with Taylor-type hardening allow for a change of the shape of the elastic domain and not only its size, which confronts the corresponding stress-update algorithm with a significantly more difficult task.

Furthermore, the rate-dependent formulation based on the OM-viscosity function is now employed in the simulation of the non-proportional tension/compression-shear cycle, where the deformation gradient coefficients are prescribed at $\dot{F}_{22} = 10^{-2}\,\mathrm{s}^{-1}$ and $\dot{F}_{12} = 5 \times 10^{-3}\,\mathrm{s}^{-1}$, respectively. The computed stress path is illustrated in Fig. 24.7a. Again, reference solutions are indicated by colored lines. Here, they were respectively obtained with 1000, 2000 and 3300 increments for the three different interaction matrices. In the cases (i) and (ii), additional simulations have been carried out with a coarser incrementation, employing 800 and 1000 increments. The corresponding results are again depicted with white circles. For these two cases, only minor differences are observed compared to the rate-independent results and the deviations can be attributed to the chosen viscosity parameters and the moderate loading rate. Note that the stress-update algorithm corresponding to the rate-dependent OM-formulation allows for a further reduction of the number of increments in case (i) and (ii), but this results in a significant loss of accuracy in the predicted stress path.

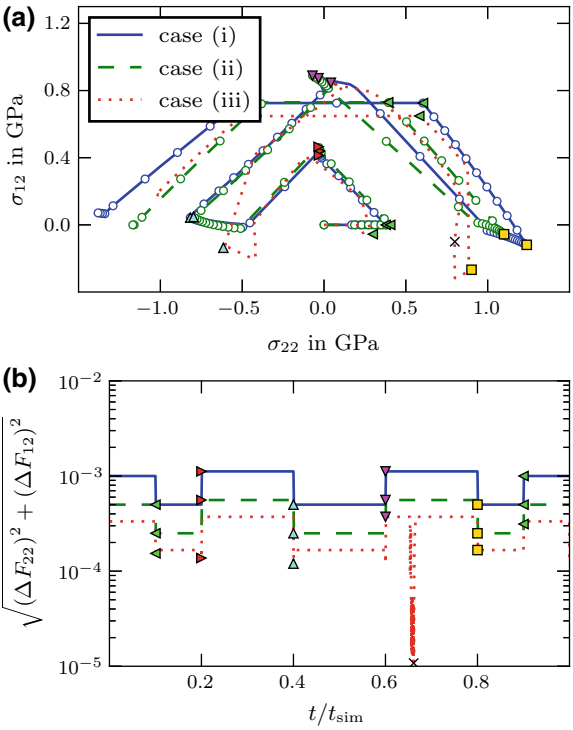

Fig. 24.7 Influence of the interaction matrix on: **a** the stress path in the butterfly test for different numbers of increments and **b** the norm of the prescribed deformation increment for the rate-dependent formulation based on the OM-viscosity function. The three different interaction matrices are indicated by case (i), (ii) and (iii), in agreement with Table 24.3. The filled symbols denote changes in the deformation path consistent with Fig. 24.5a

In case (iii), associated with the four-parameter interaction matrix, the stress path predicted by the rate-dependent formulation differs significantly from the results of the rate-independent formulation. A noticeable difference is already observed in the first part of the loading cycle, corresponding to a constrained uniaxial tensile loading, in which $F_{12} = F_{21} = 0$. Here, non-zero shear stresses σ_{12} of considerably different magnitude develop for both the rate-dependent and rate-independent formulation, as depicted in Fig. 24.8b. These stresses can be attributed to the above mentioned constraint in combination with the activation of the slip systems given in Table 24.4. While the four-parameter interaction matrix provokes the activation of five slip systems in the rate-independent formulation, eight slip systems are active in the rate-dependent formulation, as shown in Fig. 24.8a. Note that for the latter the eight hardening variables ε_α do not evolve identically. On the contrary, the simulations conducted with the interaction matrices (i) and (ii), identical slip along the same set of active systems is determined. Thus, the high-symmetry of the initial orientation is preserved during the first part of the loading cycle and the constraint is automatically fulfilled.

Comparing the complete stress paths obtained for the rate-dependent and the rate-independent formulations in case of the interaction matrix (iii) once again, it becomes apparent that the different slip activity during the initial stage of the non-proportional

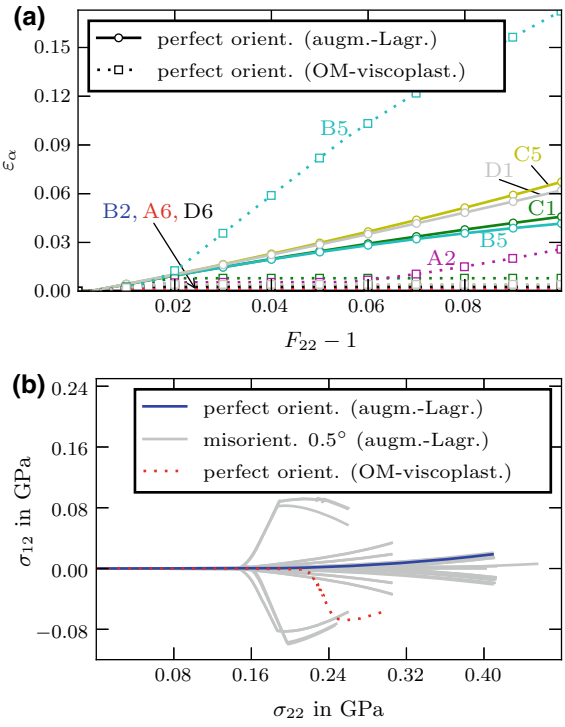

Fig. 24.8 **a** Evolution of the hardening variables under constrained uniaxial tension, **b** influence of initial misorientation on stress path under constrained uniaxial tension during the initial stage of the non-proportional deformation path

Table 24.4 Hardening variables ε_α at $F_{22} = 1.1$ in constrained uniaxial tension during the initial stage of the non-proportional loading

	B2	C1	A6	A2	B5	C5	D6	D1
augm.-Lagr.	–	0.04587	–	–	0.04160	0.06728	9.8×10^{-6}	0.06205
OM-viscoplast.	0.00155	0.00797	0.00154	0.02586	0.17239	0.00369	0.00285	0.00419

test results in a more complex stress path for the rate-dependent formulation. This observation is also reflected in a different history of the prescribed deformation increments shown in Fig. 24.7b, which is obtained by the adaptive procedure mentioned above. However, the sudden decrease in the increment size, indicated by a black cross in Fig. 24.7a, b, is not linked to any sharp change in the stress path. It is rather caused by rapidly changing shear components of the deformation gradient, determined from corresponding zero stress condition, to allow for a constant slip activity.

Similar to the approach employed in Sect. 24.3.1, a sensitivity analysis is conducted to investigate the deviation of the stress paths during the initial constrained uniaxial tensile loading. To this end, the initial orientation is perturbed employing (24.31) and (24.32) and choosing $\alpha = 0.5°$. A wide range of stress paths is obtained for selected perturbed initial orientations employing the rate-independent augmented Lagrangian formulation. The corresponding results are illustrated in

Fig. 24.8b together with the uniaxial stress path of the perfectly oriented single crystal simulated employing the rate-dependent OM-viscosity function. The striking similarity in the results of the two formulations is the sudden change of the shear stress σ_{12}, which is observed immediately at the initiation of plastic flow in the rate-independent formulation for some perturbed initial orientations. In the rate-dependent result however this sudden deviation from uniaxial tension is shifted to higher stresses.

Due to the fact, that the loading axis is aligned with a direction of high symmetry for the perfect cube orientation $\{\varphi_1, \Phi, \varphi_2\} = \{0°, 0°, 0°\}$—yielding up to eight potentially active slip systems—the stress response obtained either experimentally or from numerical simulations is rather sensitive to small misorientations [61, 68]. As mentioned above the interaction matrix in case (iii) initially provokes the activation of this set of eight slip systems associated with the high symmetry orientation in the rate-dependent formulation (see Fig. 24.8a and Table 24.4). However, at an uniaxial stretch $F_{22} \approx 1.02$, several slip systems are deactivated and concentrated slip on system B5 is observed, which accompanies the sudden change in the shear stress σ_{12} in the response of the rate-dependent model.

The strong sensitivity of the actual stress path to small initial misorientations, illustrated in Fig. 24.8b, indicates an unstable orientation, which is also supported by two results found in the literature. Firstly, the combinatorial search conducted in [67] for a single crystal—with an anisotropic hardening law (based on a six-parameter interaction matrix)—under incompressible, uniaxial tension loading in cube orientation revealed that there exist three different slip system solutions. One corresponds to the activation of eight systems, while the other two only activate four systems. This is consistent with the results presented in [72], where it was also found that the Taylor ambiguity problem occurs if anisotropic hardening is included in the model for fcc single crystals. Secondly, it has been reported in [72] that the value of the rate-sensitivity exponent influences the stability of a crystallographic orientation. In particular, crystallographic orientations which are stable in simulations carried out by rate-independent formulations can become unstable in the corresponding rate-dependent formulation, if the viscous parameters are not chosen such that they are able to recover the rate-independent limit. The choice of viscous parameters and the Taylor ambiguity problem are therefore regarded as the key factors for the significant deviations in the stress path and slip activity obtained by the rate-independent and rate-dependent formulations. The large difference in the plastic slip activity may also be amplified due to application of the iterative procedure to determine the non-zero shear components of deformation gradient, which eventually leads to an unsymmetric plastic slip. The initial variation in stress path clearly has an influence on the subsequent evolution of the stress along the remaining non-proportional deformation path. Thus, it cannot be expected that the stress path obtained by the rate-dependent formulation in Fig. 24.7 returns to the one of the augmented Lagrangian formulation in Fig. 24.6 for the interaction matrix employed in case (iii).

24.4 Constrained Tension Test

To further illustrate the robustness of the rate-independent, augmented Lagrangian formulation, it is tested within the finite element solution of a spatially inhomogeneous finite deformation boundary value problem. In particular, a constrained tension test is simulated employing a tensile specimen with a geometrical imperfection. The corresponding dimensions are given in Fig. 24.9, where the imperfection is introduced in terms of two symmetrical notches reducing the width of the specimen at its center to 90% of the original width. Along the lower edge of the specimen the displacement in 2-direction is fixed, while at the upper edge a proportionally increasing displacement is homogeneously prescribed. Additionally, the influence of two different types of boundary conditions is studied. Firstly, a clamped condition, in which the displacement in 1-direction $u_1 = 0$ is prescribed at both edges and secondly, a free lateral contraction condition, for which the displacement in 1-direction $u_1 = 0$ is only enforced at points A and B in Fig. 24.9, is considered. In either case, the displacement in 3-direction is also fixed for the entire specimen. The geometry of the specimen is discretized with 400 three-dimensional linear hexahedral elements, denoted as C3D8 according to ABAQUS conventions. The material model outlined in Sect. 24.2 with Taylor-type hardening, (24.11), is employed in the simulation. The corresponding material parameters are given in Table 24.5. With this model at hand, the influence of the initial orientation of the crystal on the force displacement curve is studied first. Therefore, four different initial orientations with respect to loading axis, namely $\{\varphi_1, \Phi, \varphi_2\} = \{30°, 45°, 0°\}$; $\{0°, 0°, 0°\}$; $\{0°, 45°, 30°\}$ and $\{289°, 163.6°, 42.5°\}$ are chosen, where the Schmid factor m of the most favor-

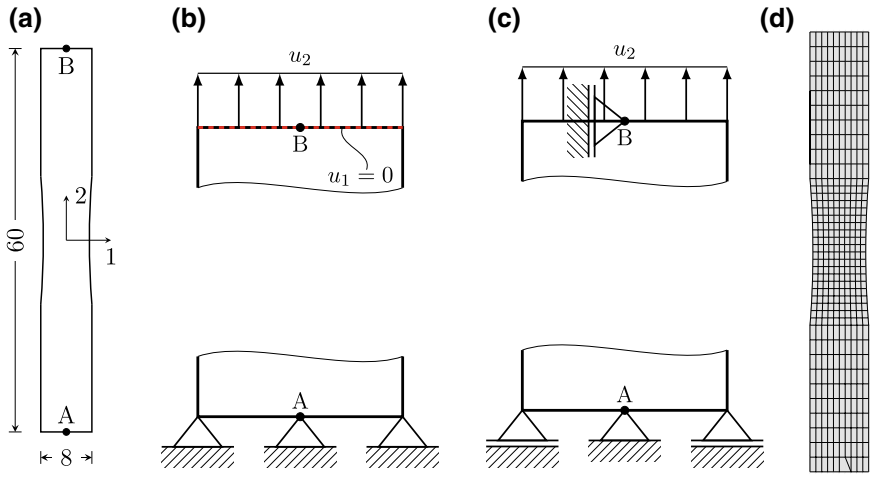

Fig. 24.9 **a** Geometry of a mildly notched tensile specimen of unit thickness with a notch radius of 125 mm and an initial reduction the of specimen width to 90%, **b** clamped and **c** free contraction boundary conditions, **d** finite element mesh

Table 24.5 Material parameters employed in the constrained tension test

κ in GPa	μ in GPa	Y_0 in GPa	ΔY in GPa	h
49.98	21.1	0.06	0.049	10

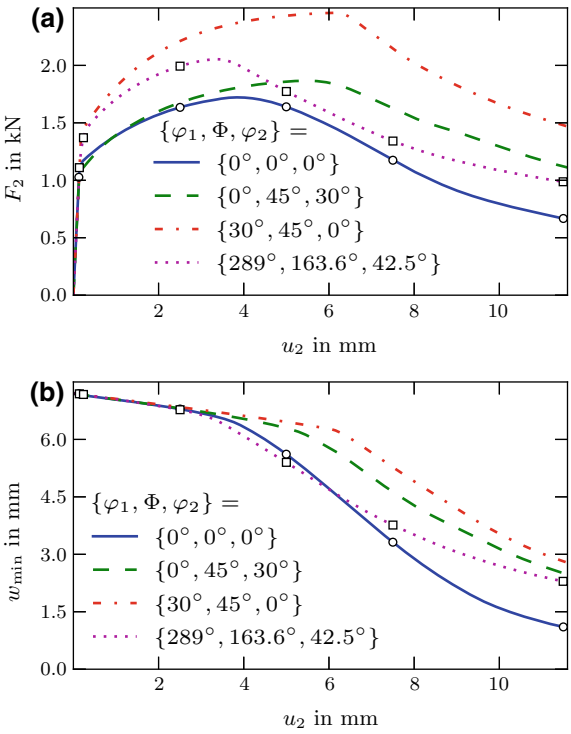

Fig. 24.10 Influence of the initial orientation on the overall force-displacement curve (**a**) and the minimal width $w_{\min}$ of the specimen measured in 1-direction (**b**). Symbols indicate the deformation at which field distributions of the logarithmic strain LE_{22} are shown in Fig. 24.12

ably orientated slip systems take the values of $m = 0.3291$; $m = 0.4082$; $m = 0.4183$; $m = 0.5$, respectively, if the crystal is deformed under homogeneous uniaxial tension. Consistent with the Schmid factors, the orientation $\{30°, 45°, 0°\}$ requires the highest force to activate the plastic flow, as shown in Fig. 24.10a. For the orientation $\{289°, 163.6°, 42.5°\}$, a considerably lower force is required at initial yield, but the plastic flow is accompanied by strong initial hardening, leading to almost the same force level as the former orientation (Fig. 24.10a).

Besides the influence of the initial orientation on the initial yield and the hardening behavior, the onset of necking and localization of the deformation is also strongly affected by the choice of initial orientation. While the force-displacement curves for the orientations $\{0°, 0°, 0°\}$ and $\{0°, 45°, 30°\}$ show a rather smooth transition to the geometrically-induced softening, more rapid drops in the applied force are observed for the other two orientations. A similar trend is observed for the respective minimal width of the specimen $w_{\min}$ measured in 1-direction, shown in Fig. 24.10b, where

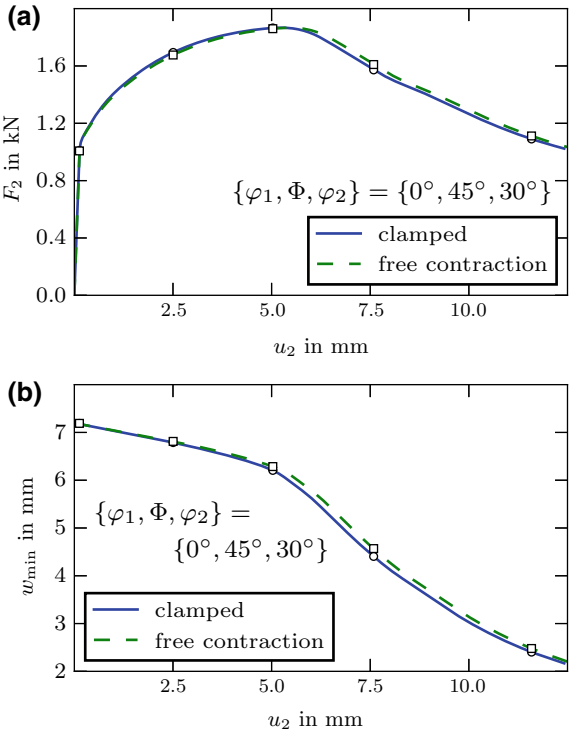

Fig. 24.11 Influence of the boundary conditions on the overall force-displacement curve (**a**) and the minimal width $w_{\min}$ of the specimen measured in 1-direction (**b**). Symbols indicate the deformation at which field distributions of the logarithmic strain LE_{22} are shown in Fig. 24.13

the former two orientations continuously deviate from the initially linear relation between $w_{\min}$ and u_2, while especially the orientation $\{30°, 45°, 0°\}$ is characterized by a sudden change in the specimen width. In each case, the deformation at which the deviation from this linear relation occurs, does not coincide with the maximum applied force, but happens, as expected, at considerably smaller deformations. The deformed specimen geometry and the spatial distribution of the logarithmic strain in longitudinal direction, i.e. (LE_{22}) are illustrated in Fig. 24.12, where the latter is computed from

$$\mathrm{LE} = \frac{1}{2} \ln \left(\mathbf{F} \cdot \mathbf{F}^{\mathrm{T}} \right). \tag{24.34}$$

The evolution of the strain fields further confirms the important influence of the initial orientation on the mode of localization (symmetric/unsymmetric). In case of the highly symmetric crystal orientation, $\{0°, 0°, 0°\}$, the strain field is symmetric even during necking. The location, at which the highest strain is observed, is shifted rapidly from the notch surface, for the elastic solution, shown on the left in the top row of Fig. 24.12, to the center of the specimen during elastic-plastic loading. In contrast, the strain field of the initial orientation $\{289°, 163.6°, 42.5°\}$ shows a smooth transition at the initiation of plastic deformation. While during the initial stages of elastic-plastic loading a rather large volume experiences pronounced deformation,

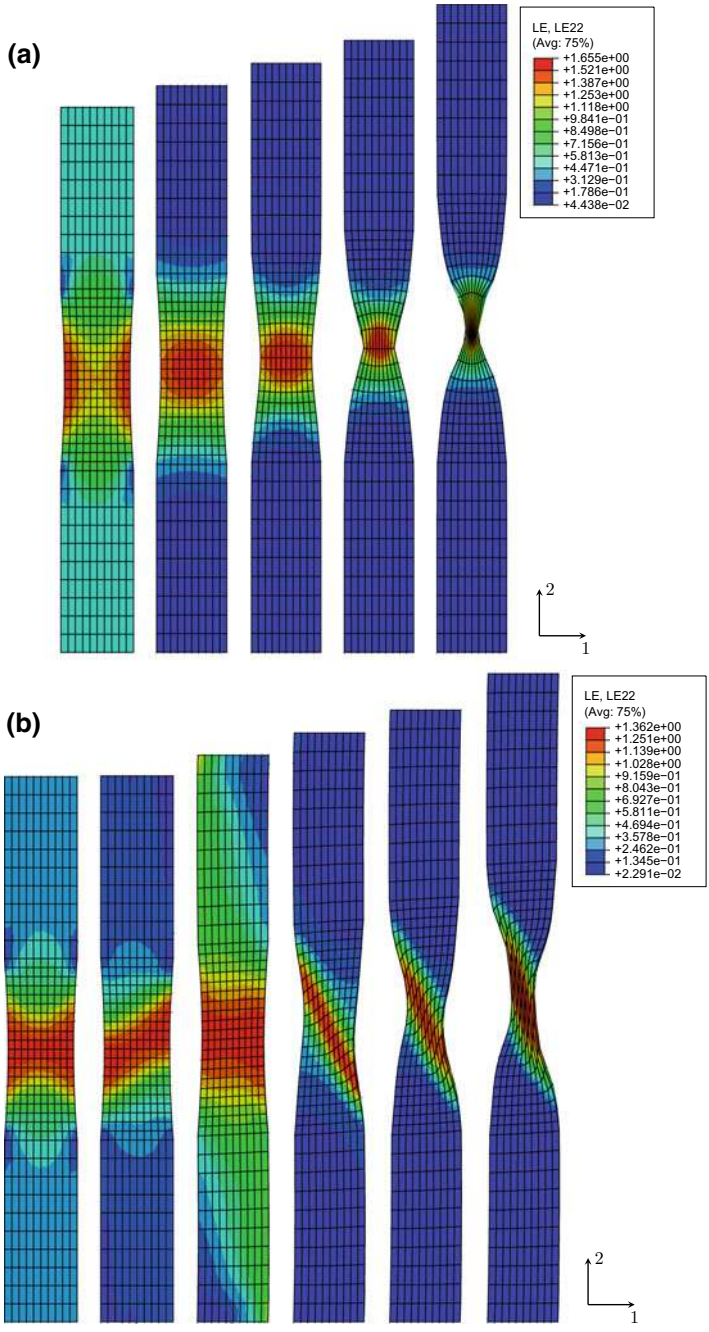

Fig. 24.12 Influence of the initial crystal orientation on the evolution of the logarithmic strain LE_{22}, **a** $\{\varphi_1, \Phi, \varphi_2\} = \{0°, 0°, 0°\}$ and **b** $\{\varphi_1, \Phi, \varphi_2\} = \{289°, 163.6°, 42.5°\}$

the deformation eventually localizes within a band. Interestingly, the inclination of the deformation band changes during the loading history due to the reorientation of the crystal.

Motivated by similar studies presented in [81], the influence of the boundary conditions indicated in Fig. 24.9 shall now be analyzed. Inspecting the respective force-displacement curves, depicted in Fig. 24.11a, only minor differences are observed for these two scenarios. In particular, the clamped condition leads to a slight increase of the required force at moderate elongations ($u_2 \leq 5$ mm) and to an earlier localization, compared to the free lateral contraction condition. Especially, the latter observation is also clearly visible in the evolution of the minimal specimen width, see Fig. 24.11b. Although the influence of the boundary condition is not as pronounced as reported in [81], the main characteristic, namely the earlier localization for the clamped condition is consistent with the results from the literature. The reason why the current simulation only shows a small sensitivity with respect to the boundary condition is that the reference case employed a double slip formulation, while the current model includes all primary slip systems of the fcc material. Moreover, inspecting the strain fields in Fig. 24.13 reveals that the clamped condition has significant influence only in the initial loading stages, where it leads to the development of a localization band immediately after plastic yielding—an effect that is absent in the free lateral contraction case. However, as the prescribed deformation is increased the strain fields become increasingly similar, although they differ in absolute values of LE_{22}.

Finally, it is worth emphasizing two aspects that pertain to all of the numerical tensile test studies. Firstly, although significant deformation increments can occur at the Gauss point level for elements within a developing deformation band, the material routine, in fact, did not require a reduction in the global time step. This again emphasizes the robustness of the augmented Lagrangian formulation, also in the context of inhomogeneous deformation states. Secondly, it is well-known that the formation of localization bands in the geometrically-induced softening regime leads to spurious mesh-dependencies of numerical results. The reason is that in *local* formulations—which lack the notion of an intrinsic length scale — localization zones degenerate to discontinuities surfaces, whose predicted widths solely depend on the spatial resolution of the finite element mesh. Generalized continuum formulations have been proposed in the literature that circumvent this problem and also naturally incorporate size effects, cf. [82–85] for gradient extended formulations and [86–89] for micromorphic formulations. However, the application of the proposed material model within the framework of a generalized continuum formulation is beyond the scope of the current contribution.

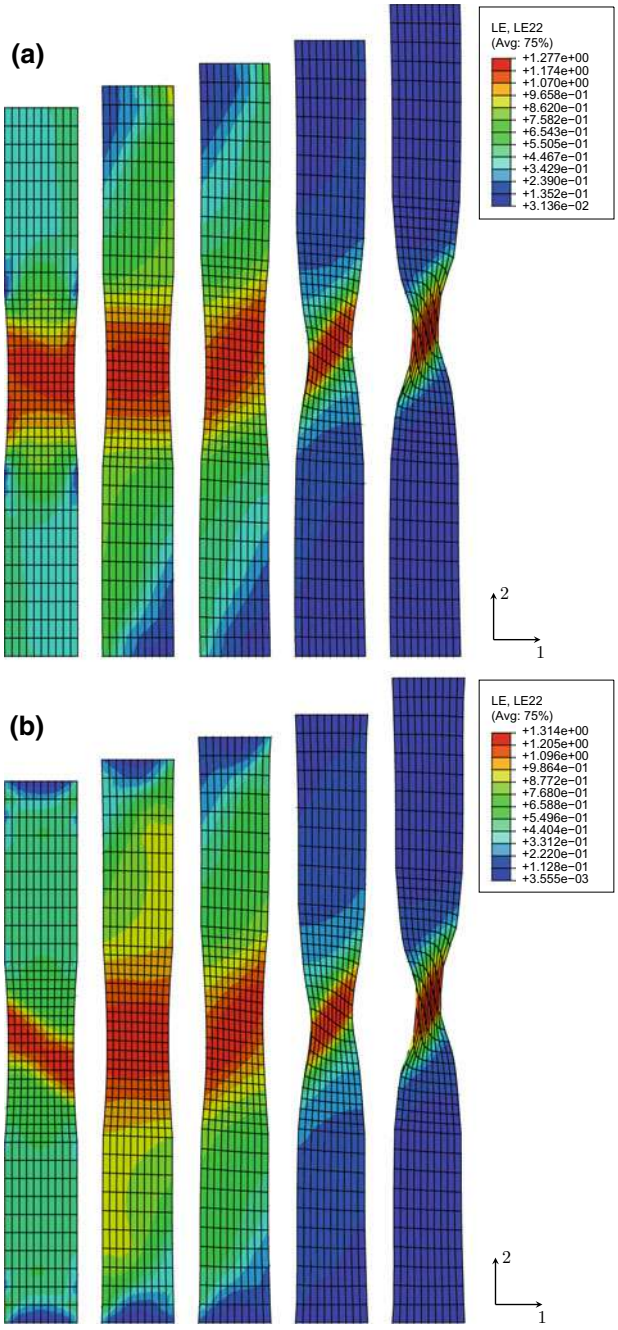

Fig. 24.13 Influence of the boundary conditions on the evolution of the logarithmic strain LE_{22} for an initial orientation $\{\varphi_1, \Phi, \varphi_2\} = \{0°, 45°, 30°\}$. **a** free lateral contraction and **b** clamped condition

24.5 Conclusions

In the current contribution, a material model for face-centered cubic single crystals, suitable for finite deformations, was discussed. Four different formulations were considered accounting for both rate-dependent and rate-independent flow behavior. Furthermore, a nonlinear anisotropic hardening law based on an interaction matrix has been incorporated, which accounts for the interaction of different slip systems in a phenomenological manner. The robustness of the corresponding stress update algorithms was assessed under homogeneous deformation states employing proportional and non-proportional loading histories. In the rate-independent case the augmented Lagrangian based formulation, originally proposed in [35], proved to be very robust, while the rate-dependent model adopted from [61] provided convincing results. However, increasing the complexity of the hardening law by choosing the parameters in the interaction matrix increasingly different from Taylor-type hardening, had a strong impact on the performance of the corresponding algorithms, resulting in a strong reduction of the prescribed deformation increment size. But this observation can readily be explained by the fact that such anisotropic interaction matrices induce an evolution of the shape of the elastic domain and not only its size, complicating the stress update considerably. Thus, the successful application of these two stress-update algorithms even in the case of anisotropic hardening emphasized their robustness.

In order to assess the performance of the rate-independent, augmented Lagrangian formulation under inhomogeneous deformations, an implementation of this model as a user-defined material subroutine (UMAT) into the finite element program ABAQUS has been employed in the simulation of a single crystalline, mildly notched tensile specimen. Herein, a strong influence of the initial orientation on the deformation and localization behavior was observed. Even during the formation of localization bands in the specimen—resulting in substantial deformation increments at the Gauss point level—an adjustment of the global time step was not necessary, confirming the robustness of the augmented Lagrangian formulation in connection with a Taylor-type hardening law also under inhomogeneous deformation states.

Having identified robust numerical frameworks for both the rate-dependent and the rate-independent case, current research efforts are focused on model extensions towards the inclusion of martensitic phase transformation and twinning by means of analytical homogenization approaches. Furthermore, a comparison with experimental results at the single crystal scale is sought, from which the constitutive parameters will be identified.

Acknowledgements The authors gratefully acknowledge the Deutsche Forschungsgemeinschaft (DFG, German Research Foundation) for funding the research in the framework of the Collaborative Research Center "TRIP-Matrix-Composite", (project number 54473466—SFB 799, subproject C10).

References

1. O. Bouaziz, H. Zurob, M. Huang, Steel Res. Int. **84**(10), 937 (2013)
2. T. Nanda, V. Singh, V. Singh, A. Chakraborty, S. Sharma, Proc. Inst. Mech. Eng. Part L J. Mater. Des, Appl. (2016)
3. C. Lesch, N. Kwiaton, F. Klose, Steel Res. Int. **88**(10), 1700210 (2017)
4. S. Martin, S. Wolf, U. Martin, L. Krüger, Solid State Phenomena **172–174**, 172 (2011)
5. S. Wolf, Temperatur- und dehnratenabhängiges Werkstoffverhalten einer hochlegierten CrMnNi-TRIP/TWIP-Stahlgusslegierung unter einsinniger Zug- und Druckbeanspruchung. Dissertation, Technische Universität Bergakademie Freiberg (2012) (in German)
6. S. Martin, Deformationsmechanismen bei verschiedenen Verformungstemperaturen in austenitischem TRIP/TWIP-Stahl. Dissertation, Technische Universität Bergakademie Freiberg (2013) (in German)
7. S. Wolf, S. Martin, L. Krüger, U. Martin, Mater. Sci. Eng.: A **594**, 72 (2014)
8. S. Martin, S. Wolf, S. Decker, L. Krüger, U. Martin, Steel Res. Int. **86**(10), 1187 (2015)
9. C. Ullrich, S. Martin, C. Schimpf, A. Stark, N. Schell, D. Rafaja, Adv. Eng. Mater. **21**(5), 1801101 (2019)
10. S. Prüger, A. Seupel, M. Kuna, Int. J. Plast. **55**, 182 (2014)
11. S. Prüger, Thermomechanische Modellierung der dehnungsinduzierten Phasenumwandlung und der asymmetrischen Verfestigung in einem TRIP-Stahlguss. Dissertation, TU Bergakademie Freiberg, Freiberg (2016) (in German)
12. A. Seupel, M. Kuna, in *XIV International Conference on Computational Plasticity. Fundamentals and Applications, COMPLAS 2017*, ed. by E. Oñate, D. Owen, D. Peric, M. Chiumenti (2017), pp. 576–587
13. S. Turteltaub, A. Suiker, Int. J. Solids Struct. **43**, 4509 (2006)
14. S. Turteltaub, A. Suiker, J. Mech. Phys. Solids **53**, 1747 (2005)
15. D. Tjahjanto, S. Turteltaub, A. Suiker, Continuum Mech. Thermodyn. **19**(7), 399 (2008)
16. D. Tjahjanto, S. Turteltaub, A. Suiker, S. van der Zwaag, Philos. Mag. **88**(28/29), 3369 (2008)
17. V. Kouznetsova, M. Geers, Mech. Mater. **40**(8), 641 (2008)
18. M. Lee, S. Kim, H. Han, Int. J. Plast. **26**(5), 688 (2010)
19. R. Stringfellow, D. Parks, G. Olson, Acta Metall. Mater. **40**(7), 1703 (1992)
20. S. Gupta, Micromechanical modeling of martensitic phase transformation in steels based on non-local crystal plasticity. Dissertation, Ruhr-Universität Bochum (2014)
21. S. Gupta, A. Ma, A. Hartmaier, Int. J. Solids Struct. **155**, 213 (2018)
22. R. Khan, F. Zahedi, A. Siddiqui, Proc. Manuf. **5**, 772 (2016)
23. R. Khan, T. Pervez, S. Qamar, Mech. Mater. **95**, 83 (2016)
24. C. Sun, N. Guo, M. Fu, S. Wang, Int. J. Plast. **72**, 186 (2016)
25. S. Wong, M. Madivala, U. Prahl, F. Roters, D. Raabe, Acta Mater. **118**, 140 (2016)
26. M. Madivala, A. Schwedt, S. Wong, F. Roters, U. Prahl, W. Bleck, Int. J. Plast. **104**, 80 (2018)
27. T. Park, L. Hector, X. Hu, F. Abu-Farha, M. Fellinger, H. Kim, R. Esmaeilpour, F. Pourboghrat, Int. J. Plast. (2019)
28. G. Olson, M. Cohen, Metall. Trans. A **6**(4), 791 (1975)
29. M. Zecevic, M. Upadhyay, E. Polatidis, T. Panzner, H. Van Swygenhoven, M. Knezevic, Acta Mater. **166**, 386 (2019)
30. F. Roters, P. Eisenlohr, L. Hantcherli, D. Tjahjanto, T. Bieler, D. Raabe, Acta Mater. **58**(4), 1152 (2010)
31. F. Roters, Advanced Material Models for the Crystal Plasticity Finite Element Method-Development of a general CPFEM framework. Habilitation (RWTH, Aachen, 2011)
32. F. Roters, M. Diehl, P. Shanthraj, P. Eisenlohr, C. Reuber, S. Wong, T. Maiti, A. Ebrahimi, T. Hochrainer, H.O. Fabritius, S. Nikolov, M. Friák, N. Fujita, N. Grilli, K. Janssens, N. Jia, P. Kok, D. Ma, F. Meier, E. Werner, M. Stricker, D. Weygand, D. Raabe, Comput. Mater. Sci. **158**, 420 (2019)
33. M. Knezevic, M. Zecevic, I. Beyerlein, R. Lebensohn, Comput. Meth. Appl. Mech. Eng. **308**, 468 (2016). https://doi.org/10.1016/j.cma.2016.05.025

34. A. Guery, F. Hild, F. Latourte, S. Roux, Mech. Mater. **100**, 55 (2016). https://doi.org/10.1016/j.mechmat.2016.06.007
35. M. Schmidt-Baldassari, Comput. Meth. Appl. Mech. Eng. **192**(11), 1261 (2003)
36. E. Busso, G. Cailletaud, Int. J. Plast. **21**(11), 2212 (2005)
37. O. Casals, S. Forest, Comput. Mater. Sci. **45**(3), 774 (2009)
38. S. Forest, M. Rubin, Eur. J. Mech. A. Solids **55**, 278 (2016)
39. E. Kröner, Arch. Ration. Mech. Anal. **4**(1), 273 (1959)
40. E. Lee, J. Appl. Mech. **36**(1), 1 (1969)
41. J. Mandel, Int. J. Solids Struct. **9**(6), 725 (1973)
42. C. Miehe, M. Lambrecht, Commun. Numer. Methods Eng. **17**(5), 337 (2001)
43. H. Ledbetter, S. Kim, in *Handbook of Elastic Properties of Solids, Liquids and Gases*, vol. 2, Chap. 8, ed. by M. Levy (Academic Press, Cambridge, 2001), pp. 107–122
44. S. Ranganathan, M. Ostoja-Starzewski, Phys. Rev. Lett. **101**, 055504 (2008)
45. R. Mahnken, Commun. Numer. Methods Eng. **21**(8), 405 (2005)
46. P. Franciosi, A. Zaoui, Acta Metall. **30**(8), 1627 (1982)
47. C. Miehe, Int. J. Solids Struct. **33**(20), 3103 (1996)
48. C. Miehe, J. Schröder, J. Schotte, Comput. Meth. Appl. Mech. Eng. **171**(3–4), 387 (1999)
49. C. Miehe, J. Schröder, Int. J. Numer. Methods Eng. **50**(2), 273 (2001)
50. L. Méric, G. Cailletaud, J. Eng. Mater. Technol. **113**(1), 171 (1991)
51. M. Khadyko, S. Dumoulin, G. Cailletaud, O. Hopperstad, Int. J. Plast. **76**, 51 (2016)
52. D. Bertsekas, *Constrained Optimization and Lagrange Multiplier Methods*. No. 4 in Optimization and Neural Computation (Athena Scientific, 1996)
53. A. Fischer, Optimization **24**(3–4), 269 (1992)
54. C. Kanzow, H. Kleinmichel, Comput. Optim. Appl. **11**(3), 227 (1998)
55. P. Perzyna, Revue de Physique Appliquée **23**(4), 445 (1988)
56. L. Méric, G. Cailletaud, M. Gaspérini, Acta Metall. Mater. **42**(3), 921 (1994)
57. C. Gérard, B. Bacroix, M. Bornert, G. Cailletaud, J. Crépin, S. Leclercq, Comput. Mater. Sci. **45**(3), 751 (2009)
58. F. Šiška, S. Forest, P. Gumbsch, D. Weygand, Modell. Simul. Mater. Sci. Eng. **15**(1), S217 (2007)
59. F. Šiška, D. Weygand, S. Forest, P. Gumbsch, Comput. Mater. Sci. **45**(3), 793 (2009)
60. C. Ling, B. Tanguy, J. Besson, S. Forest, F. Latourte, J. Nucl. Mater. **492**, 157 (2017)
61. A.M. Cuitiño, M. Ortiz, Modell. Simul. Mater. Sci. Eng. **1**(3), 225 (1993)
62. S. Prüger, B. Kiefer, A comparative study of integration algorithms for finite single crystal (visco-)plasticity (Submitted)
63. A. Bertram, M. Kraska, Arch. Mech. **47**(2), 203 (1995)
64. P. Steinmann, E. Stein, Comput. Meth. Appl. Mech. Eng. **129**(3), 235 (1996)
65. J. Schröder, C. Miehe, Comput. Mater. Sci. **9**(1), 168 (1997)
66. J. Raphanel, G. Ravichandran, Y. Leroy, Int. J. Solids Struct. **41**(22), 5995 (2004)
67. M. Ben Bettaieb, O. Débordes, A. Dogui, L. Duchêne, C. Keller, Int. J. Plast. **32-33**, 184 (2012)
68. H. Petryk, M. Kursa, Int. J. Numer. Methods Eng. **104**(3), 157 (2015)
69. H. Akpama, M. Ben Bettaieb, F. Abed-Meraim, Int. J. Numer. Methods Eng. **108**(5), 363 (2016)
70. H.J. Bunge, *Texture Analysis in Materials Science—Mathematical Methods* (Cuvillier Verlag, Göttingen, 1993)
71. J. Chaboche, Int. J. Plast. **24**(10), 1642 (2008)
72. T. Mánik, B. Holmedal, Int. J. Plast. **55**, 152 (2014)
73. Z. Bažant, B. Oh, ZAMM—J. Appl. Math. Mech. (Zeitschrift für Angewandte Mathematik und Mechanik) **66**(1), 37 (1986)
74. U. Kocks, C. Tome, H.R. Wenk, *Texture and Anisotropy*, 2nd edn. (Cambridge University Press, Cambridge, 2000)
75. D. Mohr, M. Oswald, Exp. Mech. **48**(1), 65 (2008)
76. R. McMeeking, Int. J. Solids Struct. **18**(3), 199 (1982)
77. A. Rieger, Zur Parameteridentifikation komplexer Materialmodelle auf der Basis realer und virtueller Testdaten. Dissertation, Universität Stuttgart (2005) (in German)

78. G. Scheday, Theorie und Numerik der Parameteridentifikation von Materialmodellen der finiten Elastizität und Inelastizität auf der Grundlage optischer Feldmeßverfahren. Dissertation, Universität Stuttgart, Stuttgart (2003) (in German)
79. I. Doghri, *Mechanics of Deformable Solids: Linear, Nonlinear, Analytical and Computational Aspects* (Springer, Berlin, Heidelberg, 2000)
80. C. Gérard, G. Cailletaud, B. Bacroix, Int. J. Plast. **42**, 194 (2013)
81. E. de Souza Neto, D. Peric, D. Owen, *Computational Methods of Plasticity* (Wiley, Hoboken, 2008)
82. S. Bargmann, B. Reddy, B. Klusemann, Int. J. Solids Struct. **51**(15–16), 2754 (2014)
83. M. Ekh, S. Bargmann, M. Grymer, Acta Mech. **218**(1–2), 103 (2011)
84. J. Mayeur, D. McDowell, Int. J. Plast. **57**, 29 (2014)
85. B. Kiefer, T. Waffenschmidt, L. Sprave, A. Menzel, Int. J. Damage Mech. **27**(2), 253 (2018)
86. S. Forest, in *Generalized Continua and Dislocation Theory: Theoretical Concepts, Computational Methods and Experimental Verification*, ed. by C. Sansour, S. Skatulla, CISM Courses and Lectures (Springer Vienna, Vienna, 2012), pp. 181–287
87. S. Forest, K. Ammar, B. Appolaire, N. Cordero, A. Gaubert, in *Plasticity and Beyond: Microstructures, Crystal-Plasticity and Phase Transitions*, ed. by J. Schröder, K. Hackl, C.I.S.M. International Centre, for Mechanical Sciences (Springer Vienna, Vienna, 2014), pp. 131–198
88. S. Wulfinghoff, E. Bayerschen, T. Böhlke, Int. J. Plast. **51**, 33 (2013)
89. G. Hütter, Int. J. Solids Struct. **110–111**, 15 (2017)

Index

H. Biermann and C. G. Aneziris (eds.), *Austenitic TRIP/TWIP Steels and Steel-Zirconia Composites*, Springer Series in Materials Science 298,
https://doi.org/10.1007/978-3-030-42603-3